UNIVERSITY OF OKLAHOMA

GRADUATE COLLEGE

CARBON DIOXIDE AND WATER INJECTION-INDUCED FRACTURING: IMPLICATIONS FOR CARBON GEOSEQUESTRATION

A THESIS

SUBMITTED TO THE GRADUATE FACULTY

in partial fulfillment of the requirements for the

Degree of

MASTER OF SCIENCE

By

BLESSED CHARLES AMANKWAH AMOAH

Norman, Oklahoma

2024

CARBON DIAOXIDE AND WATER INJECTION-INDUCED FRACTURING:

IMPLICATIONS FOR CARBON GEOSEQUESTRATION

A THESIS APPROVED FOR THE

MEWBOURNE SCHOOL OF PETROLEUM AND GEOLOGICAL ENGINEERING

BY THE COMMITTEE CONSISTING OF

Dr. Chandra S. Rai, Chair

Dr. Deepak Devegowda

Dr. Mark Curtis

ACKNOWLEDGMENT

My graduate school journey has been worthwhile and valuable due to my association with Dr. Chandra Rai. Thank you, Dr. Rai, for admitting me into the Integrated Core Characterization Center research group and shaping my character and scientific judgment with your kind but solemn words and encouragement to work hard. You were patient and forgiving even with mistakes I should not have made, and I am grateful for that. Although demised, Dr. Carl Sondergeld's great impact on me behooves that I express my deepest appreciation for his inspiration and challenge to be a master in my subject knowledge. Moreover, I appreciate the invaluable guidance and input of Dr. Deepak Devegowda and Dr. Mark Curtis throughout my research and academics.

To Dr. Son Thai Dang, your intellectual prowess and passion for research have motivated me greatly to aspire for excellence. Thank you for going beyond yourself to guide, teach and mentor me to do meaningful research work. I would like to thank Micaela Langevin and Gary Stowe for their help in troubleshooting and fixing problems which occurred during my laboratory experimentations. To my colleagues, Felipe Adriao Cruz, Sidi Mamoudou, Carlos Arengas Sanguino, Rishabh Pandey, Abdelali Guezei and Mohammad Aljishi, thank you for your contributions toward my research work.

I would also like to express my gratitude to the staff members and faculty of the Mewbourne School of Petroleum and Geological Engineering especially to those who supported me academically and non-academically. A big thank you to Dean Sergent who has been a wonderful mentor to me.

To crown it all, my heartfelt gratitude goes to my family, friends, and loved ones whose prayers, encouragement and support have led to the realization of my dream.

TABLE OF CONTENTS

ACKNOWLEDGMENT iv
ABSTRACT xiv
1. INTRODUCTION 1
1.1 Background 1
1.2 Motivation 6
1.3 Research Objectives 7
1.4 Synopsis of thesis 8
2. LITERATURE REVIEW 9
2.1 Carbon Sequestration 11
2.1.1 Biotic Sequestration 12
2.1.1.1 Terrestrial sequestration 12
2.1.1.2 Oceanic sequestration 13
2.1.2 Abiotic Sequestration 14
2.1.2.1 Chemical/Mineral Sequestration 14
2.1.2.2 Oceanic sequestration 15
2.1.2.3 Geological Carbon Sequestration 15
2.2 Geological Carbon Sequestration: Case Studies 19
2.3 Fracture Mechanics 21
2.4 Fundamentals of Microseismicity 24
2.5 Laboratory Fracturing Studies and Microseismic Experiments 30
3. EXPERIMENTAL PROCEDURE 36
3.1 Equipment and materials 36
3.2 Triaxial Fracturing Unit 36
3.3 Pumping Unit 38
3.4 Fluid System 38
3.5 Acoustic Emission (AE) Monitoring System 38
3.1 Sample selection: 42
3.2 Sample Characterization 42
3.2.1 Circumferential Velocity Analysis (CVA) 42
3.2.2 Porosity and Permeability 47
3.2.3 Mineralogy 47
3.2.4 Dynamic Elastic Properties 49
3.3 Experimental Procedure 49

3.4 Experimental conditions 52
3.5 Fracture Permeability 52
3.6 Fracture Morphology 53
3.6.1 Fractured Plug Sectioning and Sample Preparation 53
3.6.2 SEM Imaging and Stitching 54
4. RESULTS AND DISCUSSION 56
4.1 Pressure and AE response to fluid injection 56
4.2 AE event location and fracture dimension 72
4.3 Focal mechanism solution 90
4.4 AE spectral analysis 95
4.5 AE source parameters 100
4.6 Fracture morphology 110
4.7 Fracture permeability 118
5. CONCLUSIONS 124
6. REFERENCES 127
7. APPENDIX A: EXPERIMENTAL CONDITIONS 136
8. APPENDIX B: PRESSURE AND AE RESPONSES 137
9. APPENDIX C: AE LOCATION AND FRACTURE DIMENSION 143
10. APPENDIX D: AE SPECTRAL ANALYSIS AND SOURCE PARAMETER ESTIMATION 153

LIST OF TABLES

Table 1. Summary of storage capacity in different formations 16

Table 2. Summary of experimental studies involving the impact of different fluid types on rock geomechanics 32

Table 3. Summary of experimental studies involving the impact of CO_2 on rocks at different experimental conditions (stresses, flow rate, petrophysics). 34

Table 4. Results of circumferential velocity analysis (CVA) 46

Table 5. Average porosity and permeability values of rock samples used for experiment. 47

Table 6. Mineral compositon of samples measured using Fourier Transform Spectroscopy (FTIR) 48

Table 7. Dynamic elastic properties of samples 49

Table 8. Experimental conditions 52

Table 9. Summary of experimental results 68

Table 10. Properties of water and CO_2 at 68^{o}F and 500 – 2500 psi. Data was obtained from NIST. 69

Table 11. Summary of results for AE events location 89

Table 12. S1 focal mechanism results 92

Table 13. S2 focal mechanism results 93

Table 14. S3 focal mechanism results 94

Table 15. Summary of S1 plugs used for fracture permeability measurement. 119

Table 16. Walsh correlation constant and coeficient of correlation for left- and righ- wing fractured plugs. 122

LIST OF FIGURES

Figure 1. Carbon geosequestration. Note: Adapted from Enverus Energy Transition 2

Figure 2. Factors affecting the feasibility of carbon geosequestration 3

Figure 3. Left: schematic diagram of a leak off test. Right: injection pressure versus time (Nghiep et al. 2017) 4

Figure 4. Phase behavior of pure CO_2 and the envelope of pressure and temperature in sedimentary basins. Adapted from Zhao et al. 2015 5

Figure 5. Natural and human drivers behind the increasing average global temperature. Human factors contribute the most to the rise in temperature (Hayhoe, 2018). 10

Figure 6. Location of sites where activities related to CO_2 sequestration are planned or underway (Metz et al. 2015) 11

Figure 7. Stresses on a rock (a) Cartesian coordinate system (b) cylindrical coordinate system. The first subscript depicted denotes the direction of force and the second denotes the plane of action of the force. 22

Figure 8. An elastic body with volume V and internal surface (discontinuity) Σ..... 27

Figure 9. Fault geometry used in earthquake studies. The fault plane with normal vector n̂ separates the foot wall and the hanging wall (not shown). 28

Figure 10. Basic types of faults. Schematic is based on Eakins 1987 28

Figure 11. Polarity of P waves recorded at different receiving stations. The fault plane and auxiliary plane make up the nodal planes. Events are either in compression or dilatation (Stein and Wysession, 2003). 30

Figure 12. Schematic of the experimental setup. CO_2 may be replaced with water depending on the experimental condition. 36

Figure 13. Triaxial stress cell. Axial piston provides vertical stress, the confining vessel supplies the minimum horizontal and the flat jacks applythe maximum horizontal stress..... 37

Figure 14. Acoustic Emission monitoring system. Trigger and continuous acquisition systems receive data in parallel from the pre-amplifer. 39

Figure 15. Typical example of signals acquired by one channel in an experiment. Individual events will be extracted from this signal and further processed for AE attributes. 40

Figure 16. A window for one of the recording systems of the continuous acquisition system.. The waveform length, voltage range, input impedance and sampling rate are variable. 41

Figure 17. Processing window to acquire events. Amplitude threshold is one of the extraction parameters that can be used to acquire events. Appropriate settings are to be set by the user. 42

Figure 18. Schematic of CVA in plan view showing the transmitting and receiving transducers mounted on the sample. The sample is rotated clockwise in 10^o incrmenets and velocity is measured. Adapted from Chitrala's thesis (2012) 43

Figure 19. Laboratory apparatus for circumferential velocity analysis. (A) is the support frame; (B) is the mounted sample on the rotatable base; (C) is the pre-amplifier; (D) is he pulse generator; (E) is the oscilloscope with waveform averaging capabilities; (F) is the high voltage amplifier. Adapted from Aso's thesis (2009) 44

Figure 20. CVA results for S1 samples. 45

Figure 21. CVA results for S2 samples. 46

Figure 22. CVA results for S3 samples. 46

Figure 23. Summary of mineralogy for samples used in experiment. 48

Figure 24. Schematic of test sample. Sample is completed with a 0.25″ OD steel tubing which is cemented in place with epoxy. Injectate comes out from only the perforation. Injection depth is about half the sample length. Attached sensors on the copper jacket pick up AEs during fracturing. 51

Figure 25. Diagram of jacketed sample mounted in the traixial cell. (A) copper jacket (B) bottom metal spacer (C) elastomer (D) clamp (E) copper wire (F) epoxy (G) sensor. 51

Figure 26. Schematic of plug extraction from fractured rock samples. The red line shows the fracture trace. 53

Figure 27. Schematic of plug sectioning for fracture morphology study. Red line shows the fracture trace. The far right image shows the direction of fracture propagation. 54

Figure 28. Model 1060 Fischione broad beam argon mill used for final polishing sample surface prior to SEM imaging. 54

Figure 29. FEI Helios Nanolab 650 scanning electron microscope. (1) pressurized vacuum chamber (2) electron column used to focus and illuminate specimen (3) electron gun to produce electron beam (4) control panel. 55

Figure 30. SEM image of S1A. It has an average grain size of 127 µm. 56

Figure 31. Injection pressure (black line) and cumulative AE events (red dots) versus time for sample S1A. The blue line shows constant flow rate of 10 cc/min until pump shut-in where it drops to zero. 58

Figure 32. Full waveform of amplitude vs time recorded for one channel for sample S1A. It shows AE activity as a function of time. It appears to have two regions of intence AE release. The first region can be attributed to breakdown and fracture propagation and the latter to pump shut-in. 58

Figure 33. Injection pressure (black line) and cumulative AE events (red dots) versus time for sample S1E. The blue line shows constant flow rate of 10 cc/min until pump shut-in where it droped to zero. 60

Figure 34. Full waveform of amplitude vs time recorded for one channel for sample S1E. It shows AE activity as a function of time. AEs due to breakdown and pump shutin are indistinguishable suggesting that fracture closure occurred right after breakdown. 60

Figure 35. SEM image of S2. It has an average grain size of about 290 µm. 61

Figure 36. Injection pressure (black line) and cumulative AE events (red dots) versus time for sample S2A. The blue line shows constant flow rate of 10 cc/min until pump shut-in where it drops to zero. 62

Figure 37. Full waveform of amplitude vs time recorded from one channel at about the same time when injection started for sample S2A. It shows AE activity as a function of experimental time. The first region can be attributed to breakdown and fracture propagation and the latter to pump shutin. 62

Figure 38. Injection pressure (black line) and cumulative AE events (red dots) versus time for sample S2B. The blue line shows constant flow rate of 10 cc/min until pump shut-in where it drops to zero. 63

Figure 39. Full waveform of amplitude vs time recorded from one channel at about the same time when injection started for sample S2B. It shows AE activity as a function of experimental time. AEs due to breakdown and pump shutin are indistinguishable suggesting that fracture closure occurred right after breakdown. 64

Figure 40. SEM image of S3. It has an average grain size of about 63 µm. Visual observation indicates a poorly sorted grain deposition. 64

Figure 41. Injection pressure (black line) and cumulative AE events (red dots) versus time for sample S3A. The blue line shows constant flow rate of 10 cc/min until pump shut-in where it drops to zero. 65

Figure 42. Full waveform of amplitude vs time recorded from one channel at about the same time when injection started for sample S3A. It shows AE activity as a function of experimental time. AEs due to breakdown and pump shutin are indistinguishable suggesting that fracture closure occurred right after breakdown. 66

Figure 43. Injection pressure (black line) and cumulative AE events (red dots) versus time for sample S3B. The blue line shows constant flow rate of 10 cc/min until pump shut-in where it drops to zero. 67

Figure 44. Full waveform of amplitude vs time recorded from one channel at about the same time when injection started for sample S3B. It shows AE activity as a function of experimental time. AEs due to breakdown and pump shutin are indistinguishable suggesting that fracture closure occurred right after breakdown. 67

Figure 45. P_b for sandstones used in this study. 69

Figure 46. Cumulative AE events for sandstones used for experimentation 71

Figure 47. Plot of AEs located in sample S1A fractured with water. The located events are shown in blue, the sensors in orange and the fracture is traced in broken red line. (a) plan view of AE hypocenter showing a one wing fracture. (b) and (c) are lateral views. 75

Figure 48. Physical observation of induced fractures in sample S1A fractured with water. The fracture is delineated by the broken red line. (a) and (b) show the side view. (c) and (d) show the bottom and top view. 76

Figure 49. Plot of AEs in sample S1E fractured with water. (a) plan view of AE hypocenter showing a bi wing fracture. (b) and (c) are lateral views. 77

Figure 50. Physical observation of induced fractures in sample S1E fractured with CO_2. The fracture is delineated by the broken red line. (a) and (b) shows the side view. (c) and (d) shows the bottom and top view. 78

Figure 51. Plot of AEs located in sample S1G fractured with water. (a) plan view of AE hypocenter showing a bi wing fracture. (b) and (c) are lateral views. 79

Figure 52. Physical observation of induced fractures in sample S1G fractured with CO_2. The fracture is delineated by the broken red line. (a) and (b) shows the side view of the sample. (c) and (d) shows the bottom and top view of the sample. 80

Figure 53. Plot of AEs located in sample S2A fractured with water. (a) plan view shows a bi-wing fracture. (b) and (c) are lateral views. 81

Figure 54. Physical observation of induced fractures in sample S2A fractured with CO_2. Top images show the side view. Bottom images show the bottom and top view. 82

Figure 55. Plot of AEs located in sample S2B fractured with CO_2. (a) plan view. (b) and (c) are lateral views. 83

Figure 56. Physical observation of induced fractures in sample S2B fractured with CO_2. Top images show the side view. Bottom images show the bottom and top view. 84

Figure 57. Plot of AEs located in sample S3A fractured with CO_2. (a) plan view. (b) and (c) are lateral views. 85

Figure 58. Physical observation of induced fractures in sample S2B fractured with CO_2. Top images show the side view. Bottom images show the bottom and top view. 86

Figure 59. Plot of AEs located in sample S3B fractured with CO_2. (a) plan view. (b) and (c) are lateral views. 87

Figure 60. Physical observation of induced fractures in sample S3B fractured with CO_2. Top images show the side view. Bottom images show the bottom and top view. 88

Figure 61. Waveforms of 16 sensors for an event along with marked polarities. Upward and downward arrows indicate tensile and compressive events respectively. X represents unclear polarities (after Damani 2013) 91

Figure 62. Classification of AE events as tensile, compresive or shear. Shear failure is dominanat. Samples are without CO_2 exposure. 92

Figure 63. Classification of AE events as tensile, compresive or shear. S1G and S1H were exposed to CO_2 for 6 and 8 weeks respectively. Shear failure is dominant. 93

Figure 64. Classification of AE events as tensile, compresive or shear. Shear failure is dominant. 94

Figure 65. Classification of AE events as tensile, compresive or shear. Shear failure is dominant. 95

Figure 66. A waveform showing the arrival time and the 40μs window used for FFT. 96

Figure 67. The amplitude varies with location of sensor and (b) the frequency content of the event varies with location of sensor. 97

Figure 68. Frequency content of different damage mechanisms induced in S1. S2 amd S3 samples. 97

Figure 69. Amplitude versus frequency for S1, S2 and S3 samples. 98

Figure 70. Displacement versus mean amplitude 99

Figure 71. Displacement spectral density. 101

Figure 72. Source parameters for the shear events of S1A 103

Figure 73. Source parameters for the shear events of S1E 104

Figure 74. Source parameters for the shear events of S2A 105

Figure 75. Source parameters for the shear events of S2B 106

Figure 76. Source parameters for the shear events of S3A 107

Figure 77. Source parameters for the shear events of S3B 108

Figure 78. Moment magnitude of water- and CO_2-induced AEs for all tests 110

Figure 79. Sectioning slices for SEM imaging 111

Figure 80. SEM image taken at different regions along a fractured induced by water injection. Fracture propagation is from (a)–(b)..... 112

Figure 81. SEM image taken at different regions along a fractured induced by CO_2 injection. Fracture propagation is from (a)–(b)..... 112

Figure 82. SEM image taken at different regions along a fractured induced by water injection From left to right shows fracture propagation from top to bottom of sample. 114

Figure 83. SEM image taken at different regions along a fractured induced by CO_2 injection From left to right shows fracture propagation from top to bottom of sample. 114

Figure 84. Statistical analysis of primary fracture width (S1 horizontal fracture) 115

Figure 85. Statistical analysis of primary fracture width (S1 vertical fracture)..... 116

Figure 86. S2 SEM image taken at different regions along a fractured induced by water injection. From left to right shows fracture propagation away from borehole. 117

Figure 87. S2 SEM image taken at different regions along a fractured induced by CO_2 injection. From left to right shows fracture propagation away from borehole. 117

Figure 88. Statistical analysis of primary fracture width (S2 horizontal fracture) 118

Figure 89. Fracture permeability (Klinkenberg corrected) as a function of confing pressure for plugs taken from the left side of fractured samples. Samples 1A-1B and 1D-1E were fractured with water and CO_2 respectively..... 120

Figure 90. Fracture permeability (Klinkenberg corrected) as a function of confing pressure for plugs taken from the right side of fractured S1 samples. Samples 1B and 1D-1F were fractured with water and CO_2 respectively..... 120

Figure 91. Fracture permeability (Klinkenberg corrected) as a function of confing pressure for plugs taken from the left side of fractured S3 samples. Samples 3A and 3B were fractured with water and CO_2 respectively..... 121

Figure 92. Permeability as a function of confing pressure for a native sample and a sample exposed to CO_2 for 6 weeks..... 121

Figure 93. Walsh correlation plot for water-induced left- and right-wing fracture permeability. The high correlation coefficient values suggest that the fracture is the main contributor to permeability. 123

Figure 94. Walsh correlation plot for CO_2-induced left- and right-wing fracture permeability. The high correlation coefficient values suggest that the fracture is the main contributor to permeability. 123

ABSTRACT

To safely sequester carbon dioxide (CO_2) in the subsurface, it is vital to maintain the injection pressure below the formation breakdown pressure, which is dominantly governed by lithology, principal stresses, and presence of natural fractures. Injecting CO_2 at pressures below formation breakdown prevents the creation of injection-induced fractures and associated microseismicity which are undesirable occurrences for CO_2 sequestration projects. However, higher injection pressure allows more formation fluids to be displaced, thus enhancing the effective storage capacity of the sequestration zone which benefits CO_2 project economics. Leak-off tests are typically conducted with a water-based fluid to determine the breakdown pressure. But, considering the significant dissimilarity in the fluid properties of water and CO_2 the resulting breakdown pressure (P_b), failure mechanism and extent of damage can vary. In this study, we investigate how different injectates (CO_2 and water) impact rock breakdown pressure and fracturing and the implications for CO_2 sequestration.

Multiple true triaxial fracturing tests were performed on 2.5% KCl brine saturated samples using CO_2 and water. The tests were done on CO_2 non-/exposed samples which were cylindrical with dimensions of 4” in diameter and 5.5” in length. Samples with different petrophysical and elastic properties were used. The injection pressure and acoustic emissions were simultaneously recorded in real time. We mounted an array of sixteen (16) 1 MHz piezoelectric transducers around the samples to capture acoustic emissions (AEs) which were used to calculate the events’ location, and attributes. After the fracturing tests, we took vertical plugs along the main fracture and measured permeability under confining pressure. We also imaged the fractures using the scanning electron microscope (SEM).

For all samples, CO_2 reduced P_b noticeably as compared to water. The percentage by which P_b was reduced varied among the different sandstones. Similar P_b was observed for non-exposed and exposed samples fractured with CO_2. The permeability of fractures induced by CO_2 was consistently one order of magnitude greater than water induced fracture permeability, over the entire range of confining pressure (1000 psi to 4000 psi). Physical examination of the fractured samples revealed that CO_2 fracturing created bi-wing fractures that spanned the entire length of samples, whereas fractures generated by water fracturing traversed only half of the sample length. The number of AEs in CO_2 fracturing was considerably greater, and the AEs had broader distribution perpendicular to the fracture plane, compared to that of water fracturing. CO_2 and water induced AEs had similar moment magnitudes, failure mechanism and frequency. SEM imaging of fractures revealed wider fracture aperture (1.4-6 times), several lose grains, rough fracture edges, secondary branching, and regions of intense microcracking in fractures created by CO_2 injection than by water injection.

Based on the experimental results, we have observed that fracturing with CO_2 occurs at a lower breakdown pressure; therefore, the P_b estimated from leak-off test (using a water based fluid) would be an overestimation of the actual P_b of the formation. Similarity in breakdown pressure of exposed and non-exposed quartz rich rocks means that the geomechanical response of a predominantly quartz rich formation during and before CO_2 injection will likely remain similar. The lower breakdown pressure could be attributed to the lower viscosity and greater percolation ability of CO_2, enabling it to reach pores and crack tips more easily to promote crack propagation. CO_2 fracturing results in larger damage in both fracture propagation extent and permeability due to the sudden expansion of CO_2, which releases energy to further the crack extension. Consequently, generated fractures can propagate over longer distances vertically which can

potentially compromise the integrity of the seal above and below the storage zone. They also have greater transmissivity and thus could facilitate CO_2 leakage by providing a pathway for migration. Therefore, precise knowledge of the formation's P_b during CO_2 injection is essential for optimizing injectivity which consequently will promote accurate project economic evaluation and environmental protection. But the comparability between magnitudes, focal mechanism and frequency of acoustic emissions induced by water and CO_2 injection means that lessons can be learnt from the abundant experience of conventional water injection. Laboratory measurements provide a controlled means to ascertain the true P_b and other geomechanical responses to CO_2 injection. In terms of reservoir stimulation, CO_2 as a fracturing fluid has the potential to lower operations cost, increase production, and minimize environmental impacts.

1. INTRODUCTION

1.1 Background

Global warming is primarily attributed to human activities like burning fossil fuels, incinerating biomass, and deforestation which contribute to greenhouse gases in the atmosphere. While natural factors like volcanic eruptions and solar variations play a role, they are minor compared to anthropogenic causes. Global warming is closely linked to climate change, which has become a growing concern due to indicators such as more extreme weather events, rising sea levels, polar ice melting, and changes in vegetation cover. Since the industrial revolution, the Earth's average temperature has risen by about 1.8°F, with the potential to further increase if significant greenhouse gas reduction is not achieved. On this basis, the Paris Agreement was constituted which aims to limit global warming to well below $2^{o}C$ above pre-industrial levels (Schleussner et al. 2016).

Among the suite of technologies (carbon capture and sequestration, renewable energy, energy efficiency, electric vehicles, bioenergy, carbon pricing etcetera) which have been proposed to combat climate change, geological carbon sequestration is one of the premier methods by which CO_2 can be permanently removed from the atmosphere. In geological carbon sequestration, captured CO_2 from sources such as fossil fuel-based power plants and industrial sites is injected into subsurface geologic storage sites such as depleted oil and gas reservoirs, deep coal seams and saline aquifers (**Figure 1**). These storage sites are intended to permanently (for hundreds to thousands of years) store injected CO_2 without any leakage from the sequestered zone to near-surface ecosystems where humans, plants, and other living things inhabit. Leakage of CO_2, especially in high concentrations, can have serious health, safety, and environmental implications (Qi et al. 1994; Benson et al. 2002; Wang and Jaffe 2004; Oldenburg, 2007; and Siirila et al. 2012).

Moreover, release of CO_2 back into the atmosphere defeats the primary purpose of geosequestration to combat climate change. Hepple and Benson (2005) showed that an average annual leakage rate ≥ 0.01% for largest storage amount (gigatons of carbon) may hinder carbon sequestration as an effective climate change mitigation strategy. Therefore, it is essential to minimize the potential for CO_2 leakage and implement appropriate safety measures to make geosequestration economically viable and environmentally friendly.

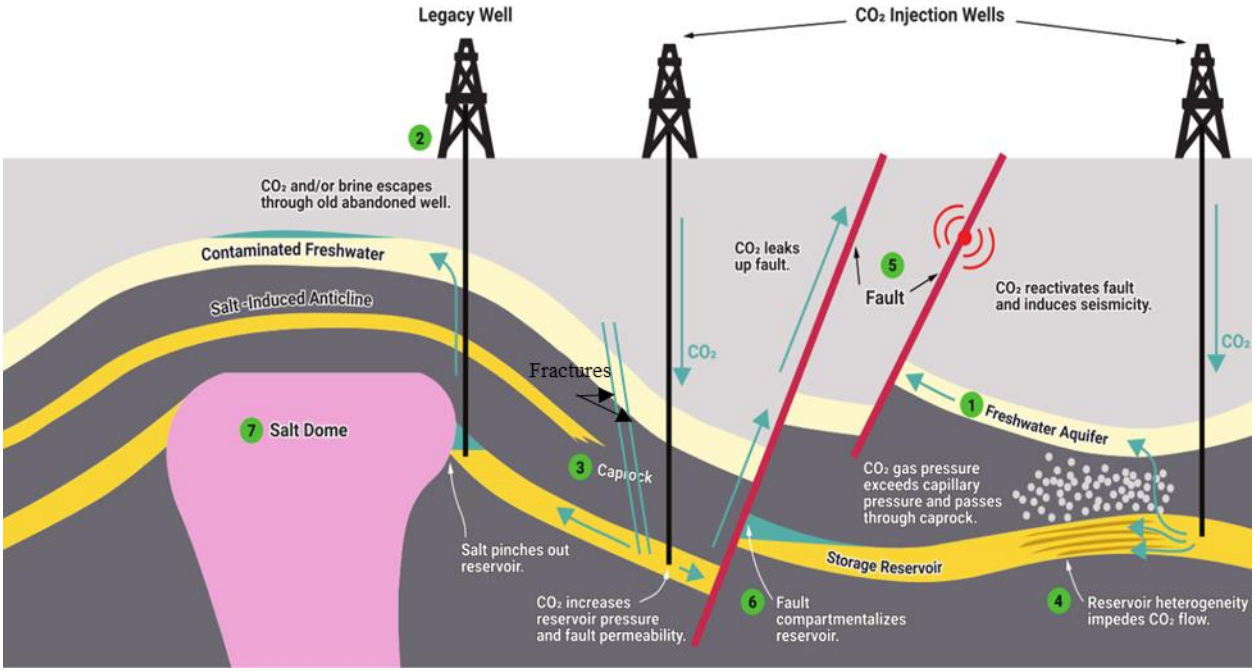

Figure 1. Carbon geosequestration. Note: Adapted from Enverus Energy Transition

Injectivity and formation integrity are major factors (**Figure 2**) that affect the success of CO_2 geosequestration. Injectivity influences the mass of CO_2 per unit time per unit pressure to be pushed into pore space of the formation which is controlled by factors such as injection pressure, reservoir transmissivity, permeability, heterogeneity, and reservoir conditions. At the same reservoir conditions, depleted hydrocarbon reservoirs are expected to see low injection pressures

due to low initial reservoir pressures as compared to full saturated saline aquifers. Higher injection pressure increases the solubility and displacement capacity of CO_2 in existing formation fluids. This consequently increases the effective storage of CO_2 which improves the profitability of the project. However, a possible hazard at high injectivity is the creation of discontinuities such as fractures caused by the over pressurization of the sequestration zone which could lead to the leakage of CO_2.

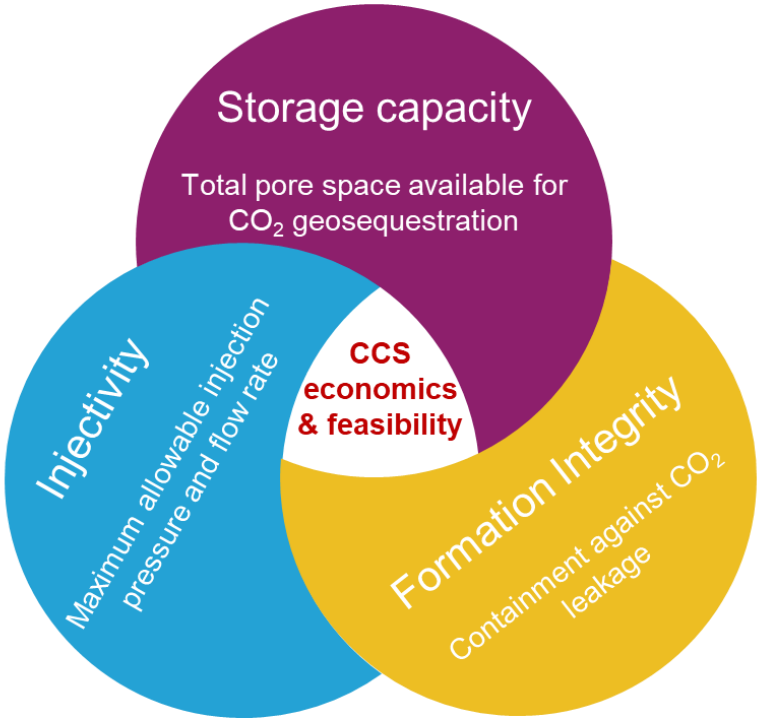

Figure 2. Factors affecting the feasibility of carbon geosequestration

To optimize injectivity, operators perform leak-off test to determine the formation P_b. This test is conducted at the bottom of the casing shoe using conventional water-based fluids (Nghiep et al. 2017). Pressure just below the P_b may serve as the optimal injection pressure as well as the maximum allowable injection pressure at which fluid can be injected into the formation without formation breakdown (fracture generation).

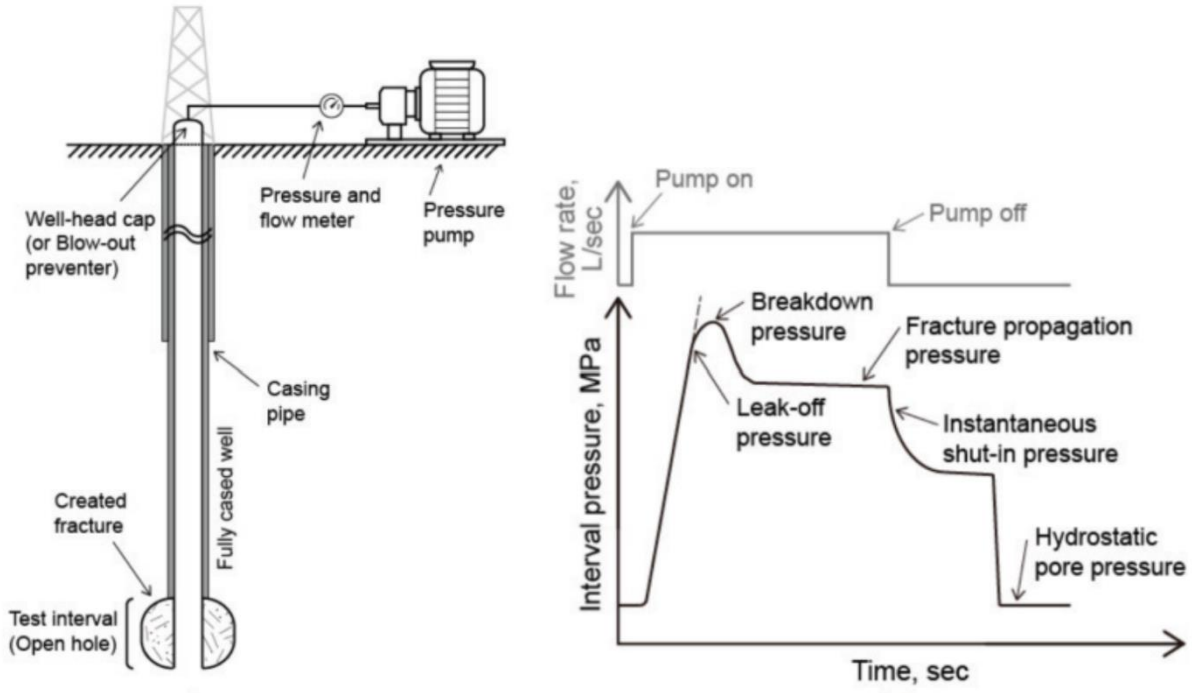

Figure 3. Left: schematic diagram of a leak off test. Right: injection pressure versus time (Nghiep et al. 2017)

CO_2 can exist in distinct phases or a combination of phases depending on its temperature and pressure (**Figure 4**). Above its critical pressure and temperature of 7.39 MPa and 31.04^{o}C respectively, CO_2 exists in the supercritical state where it adopts the properties midway between a gas and a liquid (it expands to fill its container like a gas, but its density resembles that of liquid). In geosequestration, the suitable depth of injection should be deeper than 800 m (Sally and Benson 2004) and considering a hydrostatic pressure gradient of 0.433 psi/ft and geothermal gradient of 1.3 ^{o}F/100 ft, injected CO_2 at this depth is likely to exist in the supercritical or liquid state. CO_2 has low viscosity, low surface tension and high percolation effect (Zhou et al. 2016; Deng et al. 2021) such that its influence on pore pressure cannot be neglected. The viscosity (μ) of CO_2 (μ = 0.0156 – 0.0914 cP) is about an order of magnitude higher than that of water (μ = 1.0006 – 0.9970 cP) at T = 68 ^{o}F and 500 psi $\leq$ P $\leq$ 2500 psi. These properties allow CO_2 to effectively penetrate through interconnected pores, microcracks and crack tips. On the other hand, water has relatively

low percolation power and high viscosity and therefore its property is significantly different from that of CO_2. This difference in properties could influence different fracturing responses which is very important to take into consideration for geosequestration purposes.

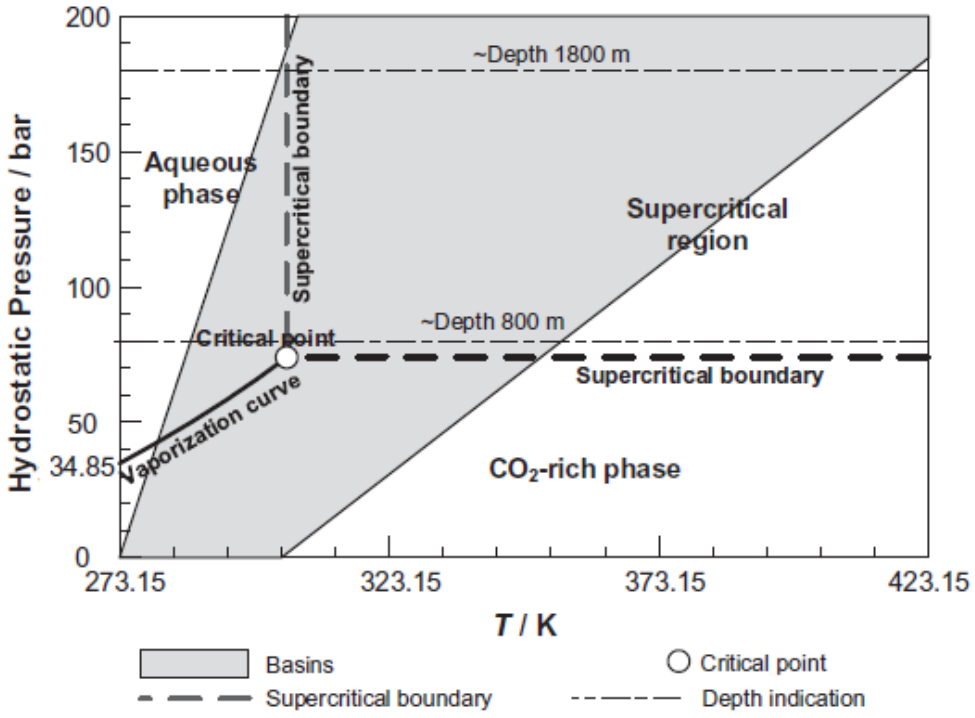

Figure 4. Phase behavior of pure CO_2 and the envelope of pressure and temperature in sedimentary basins. Adapted from Zhao et al. 2015

Fracturing of rocks with aqueous and non-aqueous fluids can either be engineered or occur unintentionally once the breakdown pressure of the formation is exceeded. Depending on multiple factors such as in-situ stresses, presence of natural fractures, bedding planes, rock brittleness index, flow rate, and fluid injected, the fracture complexity can vary significantly from a simple short fracture to a long fracture with multiple secondary and tertiary cracks. To monitor the evolution of fractures, operators typically employ acoustic technology to pick the microseismic emissions resulting from energy release due to the breaking of bonds and creation of new surfaces. The use of this technology involves the acquisition and analysis of microseismic activities caused by shear

slippage along planes of weakness, fluid leak-off or creation of new cracks (Sleefe et al. 1995). The detected seismic signal is a superposition of compressional waves (P-waves) and shear waves (S-waves) with P-wave arriving first at the detector. The signal can be used to determine fracture properties such as length, height, complexity, and seismic attributes such as amplitude, frequency, seismic moment, and energy. The ability of the microseismic technology to provide fracture information in real time has made it a very useful tool to not only improve conventional hydraulic fracturing operation but also monitor the development of fractures in geological formations where CO_2 is being sequestered.

1.2 Motivation

Several studies (Chitrala et al. 2012; Ishida et al. 2012; Zhang et al. 2017; Damani et al. 2018; Li et al. 2019) relating to the use of fracturing fluid with different physical properties (i.e., supercritical CO_2 ($scCO_2$), liquid CO_2 (LCO_2), water and viscous oil) have demonstrated significant differences in geomechanical rock response (breakdown pressure, damage complexity and acoustic emissions). Various authors (Ishida et al. 2012; Zhang et al. 2017; Li et al. 2019) have made consistent observations that the breakdown pressure recorded can be considerably lower with non-aqueous fluids than with aqueous fluids. Kizaki et al. 2013 performed fracturing studies in Inada granite with water and $scCO_2$. At fluid injection rate of 50 cc/min, they observed a 20% decrease in breakdown pressure when $scCO_2$ was used. Zhang et al. (2017) reported that breakdown pressure in shale outcrops was 50% lower with $scCO_2$ fracturing than with water fracturing. The fractures created by $scCO_2$ were more complex, rugged on the surface, had greater fracture density and higher fracture conductivity. Moreover, other scholars including (Jianfeng et al. 2018; Zhou et al. 2018; Shan et al. 2019) observed complex fracture networks in $scCO_2$ fracturing. Zhou et al. (2018) demonstrated using polymethyl methacrylate that $scCO_2$ sudden

phase change is responsible for fracture extension due to the release of stored energy to accelerate fracture growth. Moreover, differences in failure mechanism between $scCO_2$ and water fracturing could be observed in acoustic emissions. For instance, using AE monitoring, Zhou et al. (2018) observed a considerable increase in the energy release rate and cumulative energy during $scCO_2$ fracturing as compared to water fracturing.

It is apparent from the forgoing that if fluids of dissimilar properties are injected into the same rock, the geomechanical response would differ considerably. This then implies that we cannot readily apply our knowledge of fracturing with aqueous fluids to non-aqueous fluids. For geological carbon sequestration, it becomes important that we obtain a fundamental understanding of CO_2 fracturing and microseismic response as that would be very important for the operational success of geosequestration projects. In addition, the potential to inaccurately model the breakdown pressure of the formation due to CO_2 injection raises serious concerns regarding injectivity optimization, economic impact, and CO_2 containment. Health, safety, and environmental concerns cannot be addressed properly unless we have a very good understanding of breakdown pressure, fracture extent, complexity, seismicity, and containment. Thus, industry needs a robust laboratory study in CO_2 fracturing in order to increase feasibility of geosequestration projects.

1.3 Research Objectives

The aim of this experimental investigation is to understand the induced fractures risk due to CO_2 injection. The rock specimens used are cores of sandstones which were pressurized with either CO_2 or water until failure while simultaneously monitoring the acoustic emissions. The breakdown pressure, fracture complexity, morphology, permeability, and seismic attributes were

analyzed. The results were correlated and inferences drawn about the implications of CO_2 fracturing in geosequestration.

1.4 Synopsis of thesis

This thesis is divided into 5 chapters.

Chapter 1 documents background and introduction to geological carbon sequestration and its association with fracturing and microseismic technology for monitoring the fracturing process.

Chapter 2 reviews the concept of carbon capture and storage and provides a background to CO_2 fracturing and microseismicity. It also gives a description of geosequestration field operations and the fracture process of laboratory experiments using aqueos fluids (for example CO_2) and non-aqueos fluids.

Chapter 3 describes the experimental methodology in terms of the instrumentation used, processes followed and experimental conditions .

Chapter 4 details the results and interpretations of the various findings. Analysis based on acoustic emissions, injection pressure profile, seismic attributes analysis, fracture permeability and morphology (using the Scanning Electron Microscopy) are presented.

Chapter 5 lists major findings of this study and their contribution to the field of CO_2 geosequestration.

2. LITERATURE REVIEW

The phenomenon of global warming, characterized by the gradual increase in the Earth's surface temperature, is predominantly ascribed to anthropogenic activities. These activities include the combustion of fossil fuels, alterations in land use, deforestation, and biomass combustion. The substantial release of greenhouse gases into the atmosphere acts to trap solar heat, impeding its dissipation from the Earth's atmosphere. Natural elements, such as volcanic eruptions and fluctuations in solar radiation, also impact global warming. However, their influence is significantly overshadowed by human-induced factors. Since the onset of the industrial revolution in the 19th century, the average global temperature has risen by approximately 1.8 degrees Fahrenheit. This upward trend is poised to escalate unless substantial reductions in greenhouse gas emissions are promptly implemented.

Global warming and the concomitant phenomenon of climate change are intricately intertwined. Concerns regarding global climate have markedly intensified in recent decades. Key indicators of this include alterations in the frequency and severity of extreme weather events such as wildfires, droughts, hurricanes, and floods as well as the rise in sea levels, the diminishing polar ice caps, and shifts in vegetation patterns.

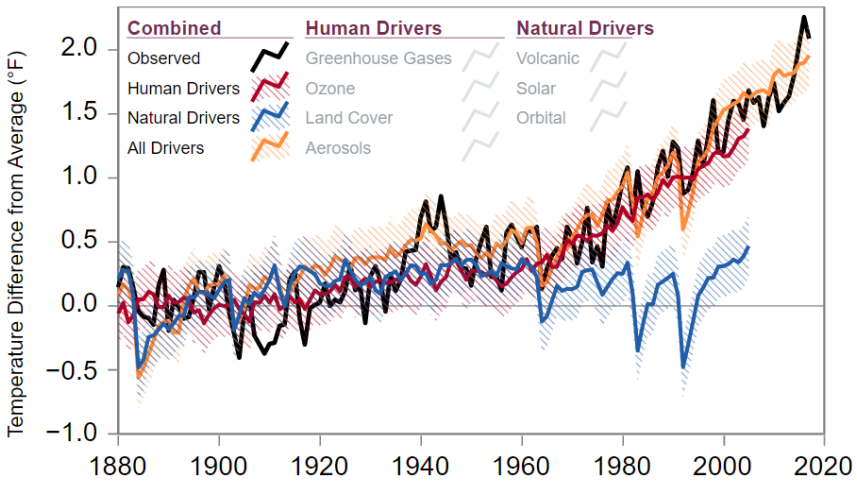

Figure 5. Natural and human drivers behind the increasing average global temperature. Human factors contribute the most to the rise in temperature (Hayhoe, 2018).

These climate concerns pose threats some of which may be irreversible to health, safety, and the environment. For instance, Lee et al. (2023) points out that Greenland and West Antarctic ice sheets may be lost almost entirely and irreversibly over many years at persistent warming levels between 2°C and 3°C. It has been recognized that making efforts to lower CO_2 emissions is necessary (Solomon et al. 2007) since doing so now may result in lower economic and environmental costs than the cost of dealing with the effects of climate change in the future (Clift et al. 2007; Stern et al. 2008). Climate hazards could potentially render the earth less habitable if the rising level of heat-trapping gases is not curbed. Among the various heat-trapping gases (carbon dioxide (CO_2), methane (CH_4), nitrous Oxide (N_2O) and industrial gases), CO_2 which is emitted primarily from the burning of fossil fuels (coal, oil, and natural gas) is the most abundant in the atmosphere. Edenhofer et al. (2014) estimated that CO_2 contributes 76% of the global greenhouse gases. To reverse the rising level of CO_2 (**Figure 5**) actions ought to be taken at an international level. The Intergovernmental Panel on Climate Change (IPCC), consisting of a

hundred and ninety-five members, reports that investing in new technologies (renewables, clean hydrogen, carbon capture and sequestration) is among the ways to reduce the emission of CO_2 (Lee et al. 2023). Reducing the use of fossil fuels through increased energy efficiency and increased use of renewable energy sources are however long-term ways to achieve net-zero carbon emissions. For now, carbon sequestration has been proposed as a major viable technology that can play a role in meeting the climate goals. Metz et al. (2015) shows location of sites around the world where activities related to CO_2 sequestration or planned or underway (**Figure 6**).

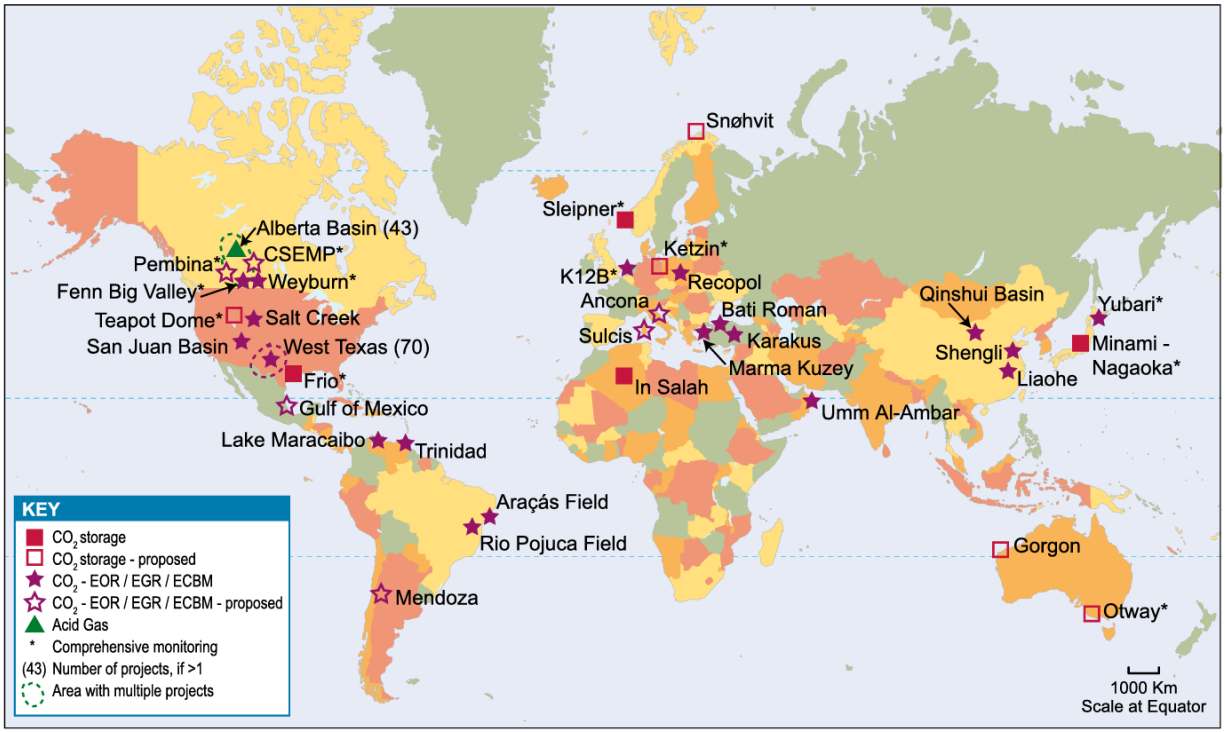

Figure 6. Location of sites where activities related to CO_2 sequestration are planned or underway (Metz et al. 2015)

2.1 Carbon Sequestration

Carbon sequestration is a practical and currently available process that can be employed to bridge the gap between the current atmospheric CO_2 concentration and a net-zero carbon economy. There are multiple biotic and abiotic sequestration mechanisms, each of which vary in

effectiveness, cost, benefits, drawbacks, and time scale of effectiveness. Among the major mechanisms are terrestrial and oceanic sequestration (biotic), chemical/mineral sequestration(abiotic), deep ocean sequestration (abiotic) and geological sequestration (abiotic). Abiotic techniques have the potential to store large amounts of CO_2, but are expensive, have slow proliferation and leakage risk while biotic techniques have finite sink capacity but are cost-effective and instantly applicable (Lal 2008).

2.1.1 Biotic Sequestration

This mechanism involves sequestering CO_2 in life and ecosystems (vegetation, soil, and ocean). The fundamental idea of this mechanism is that carbon bound-up in bodies of organisms is effectively sequestered from the atmosphere (Mistry et al. 2019; Ono et al. 2003). For example, vegetation reduces emissions by removing CO_2 directly from the air by photosynthesis and sequestering it in their tissue, and root systems as well as in forms of organic rich soils. Soil can store carbon as carbonates which are created over several years when CO_2 dissolves in water and percolates through the soil combining with calcium and magnesium to form caliche in arid soils. The ocean absorbs atmospheric CO_2 especially in cold and nutrient rich parts making polar regions effective carbon sinks. Some biotic sequestration techniques are described below.

2.1.1.1 Terrestrial sequestration

The mechanism involves the transfer of carbon into vegetation, soil and wetlands. Of the global anthropogenic CO_2 emitted into the atmosphere per year, terrestrial sinks remove about 60% through photosynthesis and storage of CO_2 in live and dead organic matter (Lal 2007). Aside from the benefit of carbon removal, this technique has other ancillary benefits such as improvement of soil and water quality, increasing crop yield and restoration of damaged ecosystems. Vegetation currently stores carbon at a rate of 6.2 ± 1.8 billion metric tons of CO_2 (Fan et al. 1998) in the form

of lignin and other polymeric compounds. The contribution of vegetation as a CO_2 sink can be increased through programs such as afforestation, reafforestation, and management of degraded temperate tropical forest (Watson et al. 1999; Fang et al. 2001; Lamb et al. 2005). Wetlands are estimated to sequester CO_2 at a rate and in amount which is several factors greater than that of an equivalent area of vegetation (Milne et al. 1997; Garnett et al. 2001). Most of the soil in coastal wetlands is immersed in water and because oxygen diffuses via water relatively slowly, saturated (wet) soils in these wetlands often have little or no oxygen. The poor oxygen concentration results in the slow decomposition and accumulation of dead plants buried in the soil (Nahlik et al. 2016). This results in significant carbon storage although a small amount of carbon is lost back into the atmosphere. Soils can absorb and hold large amounts of carbon in the surface layer of 0.5-1 m depth through various means of land management. Techniques such as planting perennial crops, low or no till practices, planting cover crops, managed livestock grazing and applying plant residue to fields can be utilized. On the contrary, soil carbon can be depleted through processes such as oxidation/mineralization, leaching and erosion (Lal, 2007). Some experts estimate that soil carbon sequestration can be scaled up to sequester about 7 $GtCO_2$ per year at a relatively low cost (Minasny et al. 2017; Batjes 1998). This technique comes with ancillary benefits such as improved soil health, reduced fertilizer use, improved and more stable crop yield (Lal 2004, Pan et al. 2009).

2.1.1.2 Oceanic sequestration

It involves the process of photosynthesis whereby phytoplankton are able to sequester CO_2 by carbon fixation and subsequent sediment sequestration in the ocean (Fuss 2018). However, this process is micro and macro nutrient limited and thus deliberating adding certain nutrients to the ocean could enhance ocean carbon sequestration. Often, iron, which is an essential nutrient for phytoplankton growth is limited in the ocean, so some studies have assessed the importance of

iron fertilization on biotic CO_2 sequestration in the ocean (Martin et al. 1988, Falkowski 1997; Boyd et al. 2004).

2.1.2 Abiotic Sequestration

Contrary to biotic sequestration, this technique does not involve the aid of biological processes/organisms. Rather, it relies on physical, chemical, and engineering processes. Theoretically, it has greater sink capacity. Thus, it has drawn lots of attention (Freund et al. 1997) from several companies in the energy industry. Technologies for CO_2 capture, transport, and injection are being developed and tested at a rapid rate. Examples of such technologies include abiotic oceanic sequestration, mineral carbonation, and geological sequestration.

2.1.2.1 Chemical/Mineral Sequestration

It involves the chemical conversion of CO_2 into geologically and thermodynamically stable minerals carbonates such as $CaCO_3$, and $MgCO_3$. At the industrial level, in order to obtain stable minerals, CO_2 is first purified by passing it through an adsorbent (amine, carbonate solvent, lithium silicate, ceramic, nickel-based compound). The pure CO_2 is reacted with mineral carbonation solutions such as $MgSiO_4$, and $CaSiO_3$ to form stable carbonate rocks (Lal 2007). For instance, aqueous mineral carbonation reaction leading to the formation of calcium carbonate is shown here: $CaSiO_3 + CO_2 \rightarrow CaCO_3 + SiO_2$. Consequently, injecting CO_2 into reactive rocks, such as mafic lithologies which contain high concentrations of divalent cations such as Ca^{2+}, Mg^{2+} and Fe^{2+}, would cause mineralization, which permanently fixes carbon with a negligible risk of CO_2 escape. Formations such as basalts and peridotites are good candidates for in-situ mineral sequestration. Moreover, injection into formations located in offshore environments is more favorable since the likelihood of leakage is inhibited by the overlying seawater. Field scale project such as CarbFix has demonstrated that more than 90% of injected CO_2 into a basaltic formation at a depth of ~

500m and at a temperature of 20-50^{o}C was mineralized within two years (Snæbjörnsdóttir et al. 2020).

2.1.2.2 Oceanic sequestration

Pure CO_2 can be sequestered in the ocean at greater depths to prevent outgassing (Haugan et al. 1992). Liquified CO_2 can be injected below 1000 m depth of the ocean to form a droplet plume, or into depressions of the ocean floor to form a CO_2 Lake, or as a denser CO_2-seawater mixture at 500-1000 m depth (Lal 2008). In high current oceanic environments, it can be injected at depths ranging from 200-400 m considering that the currents will carry the dense CO_2 rich water into deeper regions.

2.1.2.3 Geological Carbon Sequestration

It involves the injection of captured CO_2 into deep geological reservoirs with suitable geologic and reservoir conditions for permanent storage. The four main options for geosequestration are depleted oil and gas reservoirs, saline aquifers, coal seams, and sub-permafrost (Baines et al. 2004; Melnikov et al. 2006; Sheps et al. 2009). These formations can be used for the sole purpose of permanent storage whereby CO_2 is injected without any other benefit rather than to the atmosphere. The other option is for utilization purposes where CO_2 adds additional benefit through enhanced oil recovery, coal bed methane or methane hydrate production (for instance in existing oil and gas reservoirs, coal seams, permafrost). Although not fully developed, geosequestration has matured over many years through field studies. Moreover, this sequestration technique has gained most popularity especially in the oil and gas industry. Several studies have been conducted to estimate the amount of CO_2 that can be sequestered in depleted oil or gas fields at the regional and global level (Bergman and Winter 1995; IEA 1995; Holloway 1997a; Stevens et al. 1999; Bachu 2002). At the global level, the capacity is greater than 1000

Gigatons of carbon (GCT) with brine filled formations having the greatest capacity, followed by depleted oil and gas reservoirs and un-minable coal seams. **Table 1** summarizes the storage capacity in sedimentary basins estimated from the IEA 1995, Stevens et al 1999, and Gunter et al. 1998.

Table 1. Summary of storage capacity in different formations

Formation	Global capacity(GTC)	US capacity (GTC)	Canada capacity (GTC)
Brine formation	87-2700	1-130	>10
Depleted gas reserve	140-310	20-30	4
Depleted oil reserve	40-190	10-14	0.6
Un-minable coal	5-40	4-5	4

Depleted reservoirs have become one of the prime candidate formations for geosequestration. Historically CO_2 was injected into oil fields to improve the recovery efficiency of heavy oils in a process known as CO_2 enhanced oil recovery (CO_2-EOR) and for improved pressure support. Long term storage of CO_2 was not considered by CO_2-EOR operators and thus CO_2 which reached the surface was either recycled or vented. However, in modern times, the technology to permanently store CO_2 has been developed and there are several benefits of using depleted oil and gas reservoir as a sink. Firstly, reservoir characterization (rock type, porosity, permeability, lateral extension cap rock integrity and faults) can be performed with more readily available well, or seismic data without additional expenses. The existence of production and injection wells and gas transportation infrastructure would help to optimize the project from a technical and financial standpoint. Moreover, there is a relatively wide injection pressure range which enables the storage of huge gas amounts for a low compression power, without affecting

the cap-rock integrity. However, a major drawback is that the presence of legacy wells, faults and fractures may serve as leakage path for the escape of injected CO_2.

Saline aquifers are geological formations which contain brine (dissolved salts) which is usually undesirable for human consumption or agriculture. Several properties of saline aquifers have caused it to amass attention as one of the preferred sites for CO_2 sequestration (Baines et al. 2004; Wang et al. 2023) such as large capacity, worldwide distribution, and trapping mechanisms. Some studies indicate their enormous volumetric potential can potentially sequester 20-50 % of the global CO_2 emissions by 2050 (Davidson et al. 2001; Thanh et al. 2022). There are four principal trapping mechanisms for sequestering CO_2 in saline aquifers.

Hydrodynamic mechanism involves the geological time scale trapping as a result of the slow flow velocity (tens of cm/year) of the in-situ brine leading to residence time of millions of years (Finley et al. 2005). Pruess (2004) argues that this is the most likely mechanism for sequestration. Solubility trapping entails the dissolution of injected CO_2 in the aquifer brine which is a function of pressure, temperature, and salinity of the aqueous phase (Metz et al. 2005; Zhao et al. 2010). Regardless of the aqueous phase's mobility, the dissolved CO_2 is retained as long as the physical conditions are unperturbed. Moreover, CO_2-brine mixture is slightly denser (~1%) than in-situ aquifer brine (Bachu et al. 2003) and will eventually sink (in high vertical permeability region), preventing the potential for long-term leakage. This convective effect will also lead to faster rates of dissolution as unsaturated brine replaces CO_2-brine mixture at the plume-formed region. Residual trapping comprises the capture of CO_2 in pore spaces due to capillary forces. As formation water encroaches the tail of a CO_2 plume, part of the CO_2 is trapped by capillary pressure due to relative permeability capillary hysteresis. Holtz (2002) reports that as much as 15-20% of CO_2 can be trapped by this mechanism. Mineral trapping may occur over a long period of time as

a result of rock fluid geochemical interactions. Such interactions at appropriate temperature, pressure, pH and cationic conditions may form stable carbonate minerals thus contributing to the permanent storage of CO_2.

Un-mineable coal seams have a large number of micropores, cleats (fractures) and high affinity to CO_2. Coal can adsorb and/or absorb 1-10 times more CO_2 as it releases methane (CH_4) in exchange (Metz 2005). The use of CO_2 to enhance recovery of methane from coal beds can yield as much as 90% of methane as compared to the conventional recovery of 50% by pressure depletion (Stevens et al. 1999). Provided that it is never mined/disturbed, coal seams hold the potential as an underground storage facility to permanently sequester CO_2. However, a disadvantage of CO_2 adsorption/absorption in coal may be reduction of permeability and consequently injectivity as a result of coal softening in the case of adsorption and coal swelling in the case of absorption (Shi et al. 2005). Maphala et al. (2012) reports chemical and physical changes in coal due to its interaction with CO_2. The changes seen were greater at higher CO_2 exposure time and varied with coals of different maceral composition. Upon saturating bituminous and lignite coal for one week, Ranjith et al. 2012 observed a 4.3% and 9.6% reduction in unconfined compressive strength respectively.

Sub-permafrost is a porous formation below a thick permafrost (ice/frozen ground). Permafrost is impermeable and cannot be considered as a reservoir for CO_2 sequestration. However, it can act as a seal to prevent the escape of CO_2 from formations such as sub-permafrost and cryopegs (Melnikov et al. 2006). Duchkov (2006) reports that permafrost layers in central Siberia can be as thick as 1 km. Moreover, cryogenic porous formations with high pressure and low temperature conditions can enable the formation of stable CO_2 gas hydrates (crystalline solid formed of water and CO_2) (Jadhawa 2006). Such conditions could ensure the effective

sequestration capacity of cryogenic formations and the stability of the sequestered CO_2. There is also the possibility of stable carbonate formation as CO_2 reacts with the sub-permafrost/cryopeg brine. Places such as Alaska and Russia have most of their landmass (>75%) consisting of cryogenic formations (permafrost, sub-permafrost and cryopegs) which may have the potential to sequester several million tons of CO_2.

2.2 Geological Carbon Sequestration: Case Studies

Projects such as Sleipner, Weyburn and In Salah have demonstrated the feasibility of sequestering CO_2 in geologic formations. These projects affirm that site characterization and proper management of the site is essential to the safe and long-term storage of CO_2.

Sleipner (offshore Norway) project was operated by Statoil and partners and was the first industrial scale CO_2 sequestration project in deep saline aquifers (Torp et al, 2004). The field consists of the Utsira Sand which is a saline aquifer and CO_2 injection was done 200 m below the reservoir and 1012 m below sea level. From 1996 to 2006, more than 8 million tons of CO_2 had been sequestered. To track the movement of CO_2 , techniques such as 3D seismic surveying and reservoir simulation were utilized successfully to describe the migration. Other options such as pressure monitoring and observation wells were evaluated and have been suggested to be technically viable. There was negligible reaction of CO_2 with the formation sands from the results of geochemical experiments and modelling studies. Therefore, mineral trapping was limited but the main storage mechanism is the dissolution of CO_2 - solubility of CO_2 was 50 kg/m^3 (Torp et al, 2004). This project provided monitoring results and validity of available models and tools which other companies can use.

The Weyburn CO_2 injection project (Canada) is one of the pilot scale projects used as an experiment to test the theories and ideas relating to CO_2 sequestration and to develop best practices

for future applications. Once a CO_2-EOR project, the Weyburn oil field had the CO_2 sequestration component added to it with an injection rate of ~3 million tons/year and an estimated 50 million tons of CO_2 to be sequestered through the life of field. 4-D seismic, cross well and vertical seismic profiling, and pressure sampling were some techniques used to monitor CO_2 plume migration. Geophones were installed in a monitoring well to assess microseismic activity (Verdon 2011). A few episodic microseismic events (86) were detected at the onset of injection and during increased injection rates over a five-year period: they were characterized as having low dominant frequency (15-80 Hz) and poor signal to noise ratio. The negligible microseismic events suggest that CO_2 plume migration in Weyburn occurs aseismically inducing little to no rock failure. Microseismic event detection can be seen as early warning signs where the event cloud can indicate rock failure and thus the risk of leakage.

The In Salah CO_2 project (Algeria) is an onshore project with injection depth of 1900 m in carboniferous sandstones at the Krechba field. Injection began in 2004 and by 2011, ~4 million tons of CO_2 have been sequestered (Ringrose et al. 2013). Standard oilfield techniques were used for monitoring such as time-lapse seismic, microseismic, wellhead sampling and logging and core analysis, and satellite monitoring among others. Microseismic acquisition using installed geophones in a monitoring well began in 2009, making the In Salah project the first major non-CO_2-EOR carbon geosequestration project to use this technique. The microseismic event rate varied directly with injection rate with a total of 9506 seismic events detected which were attributed to the opening of pre-existing fractures (Stork et al. 2015).

2.3 Fracture Mechanics

At a depth H within the earth, there are three primary stresses which act on the formation and play a huge role in the creation of fractures in the subsurface: these are the vertical and horizontal stresses (maximum and minimum horizontal stresses). For simplicity, the absolute vertical stress can be estimated as

$$\sigma_V = g \int_0^H \rho dH \qquad 1$$

where ρ is the density of the overlaying rock which can be calculated using a density log taken from the surface to the depth of interest. Typical values of density range from 2500 to 2750 kg/m^3. Assuming the overburden consist of sandstone with ρ of 2650 kg/m^3 a common approximation of the gradient of overburden stress is:

$$\frac{d\sigma_V}{d_H} = 9.8 * 2650 = 2.6 * 10^4 \text{ Pa/m} = 1.1 \text{ psi/ft} \qquad 2$$

Considering the effect of pore pressure, Biot (1956) introduced the poroelastic constant α to estimate the effective stress ($\acute{\sigma_V}$) as

$$\acute{\sigma_V} = \sigma_V - \alpha p \qquad 3$$

where p is the pore pressure which can change significantly due to reservoir pressure changes by injection and production.

The original in-situ stress field around a wellbore ((**Figure 7**)) changes due to drilling activities. If a borehole is drilled in a rock in the direction of one of the principal stresses, the near wellbore stresses (in far field) in the cylindrical coordinate system can be expressed by Equations 4-6.

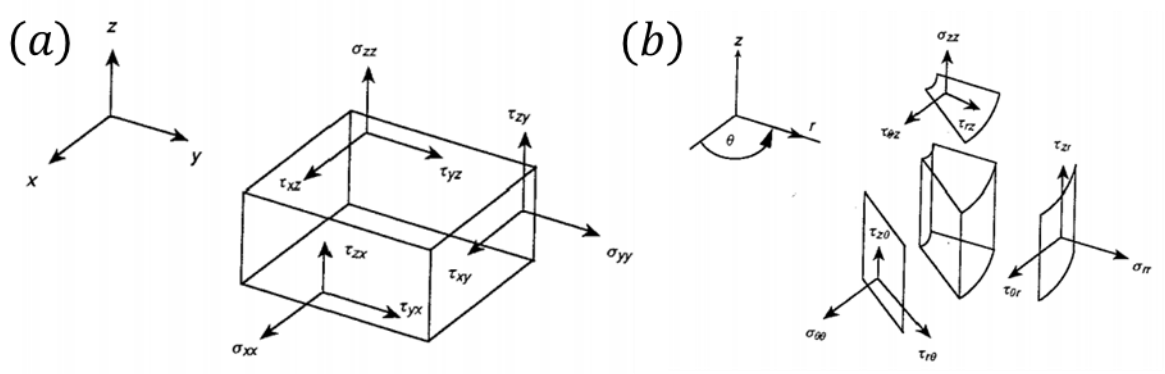

Figure 7. Stresses on a rock (a) Cartesian coordinate system (b) cylindrical coordinate system. The first subscript depicted denotes the direction of force and the second denotes the plane of action of the force.

$$\sigma_r = \frac{1}{2}(\sigma_x + \sigma_y)\left(1 - \frac{r_w^2}{r^2}\right) + \frac{1}{2}(\sigma_x - \sigma_y)\left(1 - \frac{4r_w^2}{r^2}\frac{3r_w^4}{r^4}\right)cos\,(2\theta) \quad 4$$

$$\sigma_\theta = \frac{1}{2}(\sigma_x + \sigma_y)\left(1 - \frac{r_w^2}{r^2}\right) - \frac{1}{2}(\sigma_x - \sigma_y)\left(1 - \frac{3r_w^4}{r^4}\right)cos\,(2\theta) \quad 5$$

$$\tau_{r\theta} = -\frac{1}{2}(\sigma_x - \sigma_y)(1 + \frac{2r_w^2}{r^2} - \frac{3r_w^4}{r^4})sin\,(2\theta) \quad 6$$

For a vertical well, fracture will initiate and propagate horizontally if the vertical stress is the minimum principal stress but will propagate vertically if the vertical stress is not the minimum. Traditionally, the criteria for rock breakdown suggest that when the tangential stress on the wall of the borehole equals the tensile strength of the rock, the pressure of the fluid within the wellbore is that at which the rock will fail. The equation to evaluate the tangential stress and borehole fluid stress can be expressed (Hubbert and Willis,1957) as

$$\sigma_\theta^1 + \sigma_\theta^2 = \sigma_t \; at \; r = R \quad 7$$

where (r, θ) is the cylindrical coordinate system, R is the wellbore radius and r is the radial distance away from the wellbore wall, θ is the tangential angle measured in degree, σ_θ^1 is the tangential stress caused by the horizontal principal stresses (σ_H and σ_h) and σ_θ^2 is stress resulting

from the wellbore fluid pressure. σ_θ^1 varies with θ and reaches peak value in the maximum horizontal stress direction. σ_θ^1 and σ_θ^2 can be expressed as:

$$\sigma_\theta^1 = \frac{\sigma_H + \sigma_h}{2}\left(1 + \frac{R^2}{r^2}\right) - \frac{\sigma_H + \sigma_h}{2}\left(1 + 3\frac{R^2}{r^2}\right)cos\,(2\theta) \quad 8$$

$$\sigma_\theta^2 = \frac{R^2}{r^2}P \quad 9$$

Substituting Equation 8 and 9 into 7 gives

$$P_b = \sigma_t - (3\sigma_h - \sigma_H) \quad 10$$

Equation 10 ignores fluid penetration effect and is thus fit for estimating breakdown pressure when the injectate is an aqueous fluid (water or oil-based fluid). Aqueous fluids have low penetrating power and therefore their effects can be ignored because of relative difficulty for such fluids to effectively penetrate into pores, especially in tight rocks. However non-aqueous fluids like CO_2 have very low viscosity, low surface tension and high percolation effect (Fenghour et al. 1998; Heidaryana et al. 2011; Ishida et al. 2012; Bennour et al. 2014; Zhou and Burbey. 2014; Zhang et al. 2017; Zou et al. 2018;) such that its influence on pore pressure cannot be neglected. Non-aqueous fluids will effectively penetrate interconnected pores from the wellbore wall which will cause additional tangential stress which is given as

$$\sigma_\theta^3 = \alpha\frac{1-2\nu}{1-\nu}\left[\frac{1}{r^2}\int_R^r p(r)rdr - p(r)\right] \quad 11$$

where υ is Poisson's ratio, $\alpha = (1 - C_r/C_b)$, C_r and C_b are rock matrix and rock bulk compressibility and $p(r)$ is the pore pressure at distance r from the center of wellbore. Aside the poroelastic stress (σ_θ^3) induced by the pore pressure, it also reduces the strength of the rock which can be expressed based on Terzaghi effective stress law. Considering this law and the poroelastic stress, Equation 7 can be modified as follows:

$$\sigma_\theta^1 + \sigma_\theta^2 + \sigma_\theta^3 = \sigma_t - p \; at \; r = R \qquad 12$$

The equation shows that increasing pore pressure reduces the breakdown pressure. At $r = R$, the pore pressure at the wellbore wall equal p and the poroelastic stress can be expressed as

$$\sigma_\theta^3 = -P\alpha \frac{1-2\nu}{1-\nu} \qquad 13$$

When p and σ_θ^3 are substituted into Equation 12 the breakdown pressure originally derived by Haimson and Fairhurst (1970) is obtained.

$$P_b = \frac{\sigma_t - 3\sigma_h + \sigma_H}{2 - \alpha(\frac{1-2\nu}{1-\nu})} \qquad 14$$

Equation 14 is suitable for calculating the breakdown pressure for CO_2 fracturing. Comparing Equations 10 and 14, it can be seen that Equation 14 is lower by a factor of $1/[2 - \alpha\left(\frac{1-2\nu}{1-\nu}\right)]$. This implies that fracturing with non-aqueous would have a lower breakdown pressure as compared to aqueous fluids.

2.4 Fundamentals of Microseismicity

Earthquake seismology, which is the study of seismic waves generated in the earth due to slippage along fault planes, is the mother of microseismicity. From the analysis of ground displacement along the San Andreas fault which accompanied the 1906 earthquake, Reid (1910) proposed the elastic rebound theory to explain the phenomenon. The theory refers to the gradual accumulation and release of stress and strain in the earths' crust. For an earthquake to occur, rock masses along a fault plane slowly deform due to shear stress and rupture along the fault causing a sudden release of previously accumulated energy in the form seismic waves.

Seismic waves in the earth can be generated at a source by natural events such as an earthquake or man-made events such as hydraulic fracturing. The resulting waves propagate through the earth and are recorded at a receiving station. The seismic waves recorded provide information on the speed of the wave, arrival time, location, nature of the source and the medium of travel. The hypocenter location of the source is found from the arrival time of seismic waves and it is often shown as the epicenter (the point on the earth surface directly above the source) in earthquake seismology. The amplitude of the wave is a measure of the size of the deformation which is given in terms of seismic moment or magnitude. Moreover, its radiation pattern suggests the type of displacement caused during the ground motion: damage may be by tension, compression, or shear.

The displacement, $u(t)$ detected on a seismograph can be written as a convolution in the time domain as:

$$u(t) = x(t) * e(t) * q(t) * i(t) \qquad 15$$

where $x(t)$ is the source time function, $e(t)$ and q(t) represent earth structure effects and i(t) represents the response of the seismometer. Through Fourier transform, the convolution can be expressed in the frequency domain by deconvolution as a product of four factors in equation 15 as:

$$U(\omega) = X(\omega)E(\omega)Q(\omega)I(\omega) \qquad 16$$

In equation 16, $X(\omega)$ is the source function, $E(\omega)$ represents the effect of reflections, geometrical spreading, and seismic wave conversions at different boundaries along the ray path, $Q(\omega)$ gives inelastic wave attenuation, and $I(\omega)$ stands for instrument response.

Considering an idealized seismic source from a fault process within a medium, a displacement discontinuity (u) across an internal surface ∈ as shown in **Figure 8** can be expressed as (Nowack, 2023)

$$u_n(\vec{x},\, t) = \int_{\Sigma} d\Sigma(\vec{x}^t)[\Delta u_i\,(\vec{x}^t, t)]c_{ijpq}v_j \; * \frac{\partial G_{np}}{\partial x_q^t}(\vec{x}, \vec{x}^t, t) \tag{17}$$

where $\Delta u_i(\vec{x}^t, t)]c_{ijpq}v_j$ is the moment tensor density m_{pg}, * is the time convolution, $d\Sigma(\vec{x}^t)$ is an element of the fault surface and $\frac{\partial G_{np}}{\partial x_q^t}$ represents the propagation process from the source to receiver. Equation 17 can be rewritten as:

$$u_n(\vec{x},\, t) = \iint_{\Sigma} d\Sigma\,(x^t)[m_{pq} * G_{np,q}] \tag{18}$$

The integral of Equation 18 yields a simplified equation below:

$$u_n(\vec{x},\, t) = M_{pg} * G_{np,q} \tag{19}$$

where the moment tensor M_{pg} is given by (Lay and Wallace, 1995) and each element represents a couple in the local source cartesian coordinate system:

$$M = \begin{matrix} M_{11} & M_{12} & M_{13} \\ M_{21} & M_{22} & M_{23} \\ M_{31} & M_{32} & M_{33} \end{matrix} \tag{20}$$

and $G_{np,q}$ can be written as:

$$G_{np}(\vec{x}, \vec{x}^t) = \frac{\gamma_n\gamma_p}{4\pi\rho\alpha^2 R}\delta\left(t - \frac{R}{\alpha}\right) + \frac{\gamma_n\gamma_p - \delta_{np}}{4\pi\rho\beta^2 R}\delta\left(t - \frac{R}{\beta}\right) \tag{21}$$

where γ is a unit vector from the source $\vec{x}$ to the receiver $\vec{x}^t$, and R = $|\vec{x} - \vec{x}^t|$.

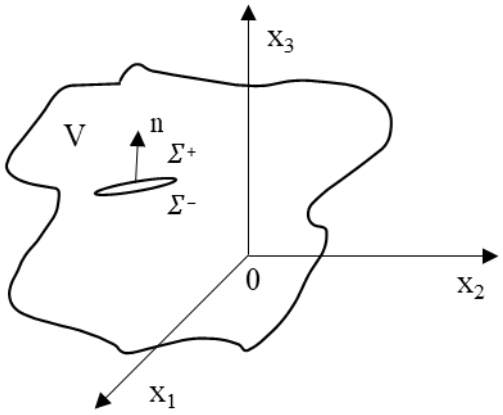

Figure 8. An elastic body with volume V and internal surface (discontinuity) Σ

When a fault occurs, its geometry can be described in terms of the direction of slip along the plane and the orientation of the fault plane. The normal vector $\hat{n}$ characterize the fault plane while the slip angle gives the direction of motion whereby the upper part of the fault (hanging wall block) moved relative to the lower part (foot wall block) (**Figure 9**). The slip angle λ represents the direction of motion. In the geographic coordinate system, a fault strike ϕ_f is defined as the angle measured clockwise from the north to the x_1 axis. Alternatively, the fault's slip and orientation can be defined by giving the normal and slip vectors in a geographic coordinate system. The unit normal and slip vectors are given as follow:

$$\hat{n} = \begin{pmatrix} -\sin\delta\sin\phi_f \\ -\sin\delta\cos\phi_f \\ \cos\delta \end{pmatrix} \quad 22$$

$$\hat{d} = \begin{pmatrix} cos\lambda cos\phi_f + sin\lambda cos\delta sin\phi_f \\ cos\lambda sin\phi_f + sin\lambda cos\delta cos\phi_f \\ sin\lambda sin\delta \end{pmatrix} \quad 23$$

The slip angle λ ranges from 0^o to 360^o. **Figure 10** shows some basic types of faulting in relation to the slip angle. Pure strike slip occurs when λ=0^o or 180^o and two sides of the fault move

horizontally. When λ=-90^o 0r 270^o, the hanging wall slides down to cause normal faulting while at λ=90^o a reverse faulting occurs.

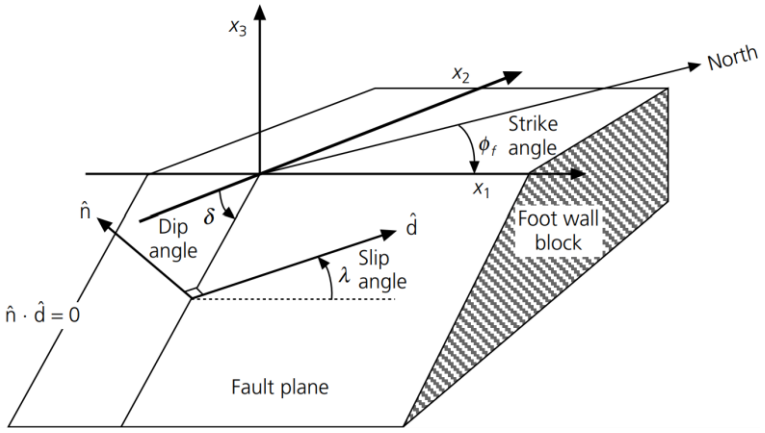

Figure 9. Fault geometry used in earthquake studies. The fault plane with normal vector $\hat{n}$ separates the foot wall and the hanging wall (not shown).

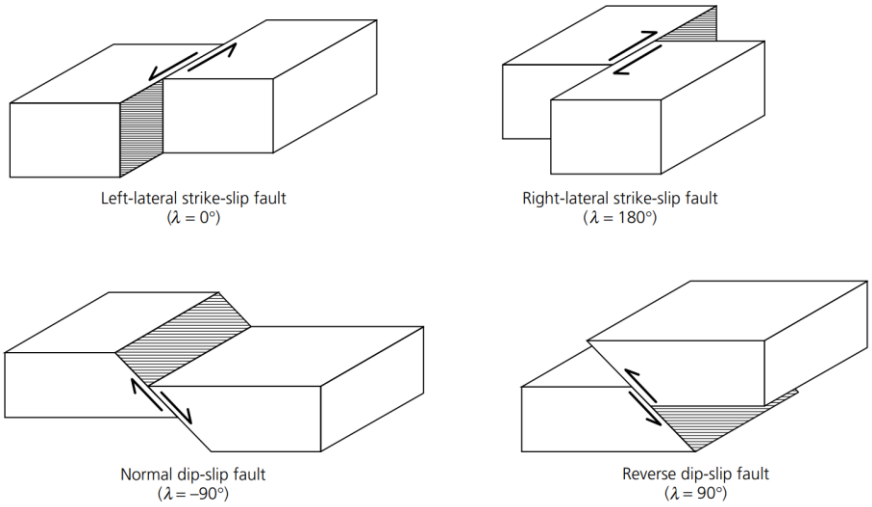

Figure 10. Basic types of faults. Schematic is based on Eakins 1987

The seismic waves recorded during an event such as earthquake can be used to study the geometry of fault by a concept called focal mechanism. This is possible due to the fact that the pattern of radiated energy depends on the fault geometry. One of the simplest methods for studying focal mechanism is the use of the first motion arrival or polarity. The idea is that the polarity recorded at receivers varies due to direction of the waves from the hypocenter. The polarity

(upward or downward first motion) can either be in compression or dilatation. Events in compression signify material near fault moved toward the receiver while dilation means the opposite. The first motions as shown in **Figure 11** define four quadrants (compressional and dilatational) separated along nodal planes (fault and auxiliary planes). If these nodal planes can be found, then the geometry of the fault can be determined. In laboratory studies of acoustic emissions, a similar concept based on polarity can be used for the focal mechanism solution.

Typically, after locating earthquake events, seismologists like to quantify the size of the events for the purpose of discussing their effects on society. The Richter scale was developed by Charles Richter in 1935 to measure the magnitude of events once they've been corrected for reduction due to mode conversions and attenuation. The general form for the magnitude scale is:

$$M = log\left(\frac{A}{T}\right) + F(h, \Delta + C) \quad 24$$

where A is the amplitude of the signal, T is its dominant period, F is a correction for variation of amplitude with earthquake depth (h) and distance (Δ) from the receiver and C is the regional scale factor. A simplified version of Equation 24 based on the seismic moment has been adopted: this equation is expressed as

$$M_w = (log(\mathrm{Mo}) - 9.1)/1.5 \quad 25$$

The seismic moment, M_o can be defined by Equation 26 where μ is rigidity at source depth, $\bar{D}$ is the average slip on the fault and S is the fault area. It is the best measure of earthquake size and energy.

$$M_o = \mu \bar{D} S \quad 26$$

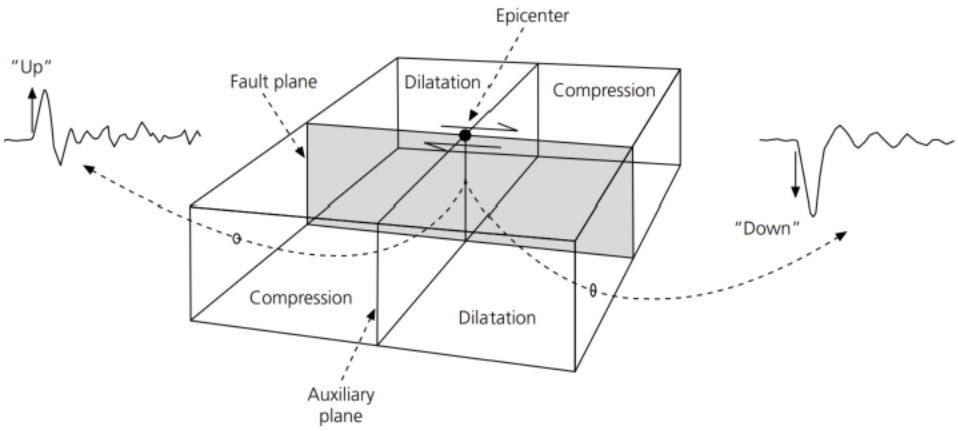

Figure 11. Polarity of P waves recorded at different receiving stations. The fault plane and auxiliary plane make up the nodal planes. Events are either in compression or dilatation (Stein and Wysession, 2003).

2.5 Laboratory Fracturing Studies and Microseismic Experiments

Several authors have undertaken laboratory studies on fracturing with aqueous and non-aqueous (CO_2) fluids in order to investigate different aspects of the process. A brief review of some past experimental studies is discussed in this section.

Ishida et al. (2012, 2016b) studied fracture and acoustic emission behavior induced by the injection of $scCO_2$ and LCO_2 and compared the observations with those of water and viscous oil. They used cubic granite blocks with dimensions of 6.7″ x 6.7″ x 6.7″ and picked AEs using 16 piezoelectric transducers. Breakdown pressure positively correlated with increasing viscosity of injection fluids. The fractal dimensions of resulting microcracks estimated for $scCO_2$ was the highest suggesting that it induces the most cracking three dimensionally by forming sinuous cracks with a greater number of secondary branches. Microscopy images revealed tortuously propagating crack and higher fracture aperture for $scCO_2$.

In like manner, Zhou and Burbey (2014) observed a lower breakdown pressure with $scCO_2$ as compared to water. The fracture aperture was smallest for $scCO_2$ due to fluid leak-off into pores of the unsaturated sample.

Similar observations have been made by Sampath et al. (2018) in coal seams. They observed a 20% reduction in breakdown pressure with LCO_2 and dense network of fractures as compared to water. The time taken till breakdown was 59% higher for LCO_2 than for water due to higher compressibility of CO_2.

Damani et al. (2018) utilized water and oil as injectates to fracture both saturated and unsaturated cylindrical samples of Tennessee sandstone. They documented increased breakdown pressure as injectate viscosity increased regardless of the saturation state. The extent of rock damage quantified using AEs was slightly higher with oil than with water.

Shan et al. (2019) performed true triaxial fracturing on 11.8″ x 11.8″ x 11.8″ shale blocks using water and $scCO_2$ and employed acoustic emission monitoring to study the differences in fracture mechanism between the fluids. From a plot of the number of acoustic emissions against magnitude, they observed greater number of large amplitude events for $scCO_2$ which showed more scattering in their location. Focal mechanism solution suggested more shear and tensile events in the fracture initiation and propagation stages respectively.

Li et al. (2018) carried out true triaxial fracturing experiments on tight sandstones of varying degrees of brittleness and layering using slickwater, LCO_2 and $scCO_2$. Similar to the precedent discussions, they recorded a reduction in breakdown pressure by 18.2% and 30.4% for LCO_2 and $scCO_2$ respectively. CO_2 fracturing in layered rocks yielded more complex fractures (curved macro and micro multi-branch fractures with shattered particles) than in homogeneous rocks. Fracture development increased with increasing brittleness.

In parallel to the observations aforementioned, Zou et al. 2018 reported their findings in 11.8″ x 11.8″ x 11.8″ sandstone outcrops. They investigated the impact of different geological and engineering factors (stress state, fluid type and injection rate) on the growth behavior of fractures.

The results showed a 67% reduction in breakdown pressure and the formation of complex fractures with decreasing fluid viscosity. Increased differential stress and flow rate increased fracture complexity and breakdown pressure respectively. Fracture aperture decreased with decreasing fluid viscosity but the number of shear events were seen to increase.

Aside those discussed above, other authors (Yang et al. 2018; Kizaki et al. 2013; Wang et al, 2017; Zhang et al. 2017) have made similar observations. The tables below summarize some of the findings in literature on the impact of fluid type, fluid viscosity, flow rate, and in-situ stresses on breakdown pressure.

Table 2. Summary of experimental studies involving the impact of different fluid types on rock geomechanics

#	Reference	Sample properties	Findings
1	Ishida et al. 2012	Coal seam; Cylinder (L=3.0″, D=1.5″); Injectate: LCO_2, Water	Breakdown pressure reduced by 20% with LCO_2.
2	Kizaki et al. 2013	Granite; Tuff; Cube (L=5.91″); Injectate: water, $scCO_2$	$scCO_2$ generated lower breakdown pressure and more fracture branching.
3	Ishida et al. 2016	Granite; Cube (L=6.7″); Injectate: viscous oil, water, $scCO_2$, LCO_2	Breakdown pressure positively correlated with viscosity of injectate. AEs and their distribution about the fracture plane increased with decreasing viscosity. $scCO_2$ created more three dimentional cracking.
4	Zhang et al. 2017	Shale; Sandstone; Cube (L=7.87″); Injectate: water, LCO_2, $scCO_2$	Breakdown pressure for $scCO_2$ and LCO_2 was 50% and 15% lower respectively than that of water. $scCO_2$ formed irregular multiple cracks of different lengths and widths. Fractures by LCO_2 are similar to those of $scCO_2$ except the complexity is somewhat lower.

5	Wang et al. 2017	Shale; Cube (L= 7.87″), naturally fractured but fractures were sealed with epoxy; Injectate: $scCO_2$ water	$scCO_2$ breakdown pressure occurred at a much lower pressure than for water in both experimental studies and poroelastic model.
6	Damani et al. 2018	Tennessee sandstone; Cylinder (L=5.5″, D=4.0″); Injectate: water, oil	Breakdown pressure reduced with decreasing injectate viscosity but damage zone extent was larger in oil fractured rocks.
7	Li et al. 2018	Sandstone; Injectate: water, LCO_2, $scCO_2$	Averagely, the breakdown pressure reduced by 18.2% and 30.4% for LCO_2 and $scCO_2$ respectively. Slickwater produced smooth, wide fractures; LCO_2 generated curved fractures with some unevenness, and $scCO_2$ created a complex network of narrow fractures with crushed surfaces. Fracture width follows the order: slickwater > LCO_2 > $scCO_2$.
8	Zou et al. 2018	Sandstone; Cube (L=11.8″); Injectate: x-linked guar, slickwater, $scCO_2$	The results showed as high as 67% reduction in breakdown pressure with $scCO_2$. As compared to x-linked guar and slickwater, $scCO_2$ fracturing promoted complex fracture networks by enhancing bedding plane dilation and natural fracture shearing. Statistical analysis of AE waveforms indicates increasing shear failure with decreasing viscosity.
9	Yang et al. 2018	Granite; Cube (L=6.7″); Injectate: viscous oil, water, $scCO_2$, LCO_2	$scCO_2$ induced significantly more cracks than the other two fluids. Crack surface morphology showed rougher surface than those by other fluids

10	Shan et al. 2019	Shale; Cube, L=11.8″; Injectate: Water, $scCO_2$	Breakdown pressure reduced by 65% with $scCO_2$. AEs had a greater number of large amplitude events and were more scattered in location. They observed more shear and tensile cracking with $scCO_2$ at the crack initiation and propagation stages respectively.

Table 3. Summary of experimental studies involving the impact of CO_2 on rocks at different experimental conditions (stresses, flow rate, petrophysics).

#	Reference	Sample properties	Findings
1	Kizaki et al. 2013	Granite; Tuff; Flow rate (cc/min) = 10,50,150 Stresses (MPa) σ_v, σ_h, σ_H = (12,3,5); (1,3,5)	The greater the differential stress the less the fracture complexity. Pumping rate at 50 cc/min generated more complex fractures at higher breakdown pressure than at 20 cc/min.
2	Zhang et al. 2017	Shale; Sandstone; Horizontal stress difference (MPa) = 0,1,2,3,4	Decreasing horizontal stress difference increased the likelihood of fractures being dictated by weak planes, natural fractures, and bedding. Fracture complexity and density in shale was more than in sandstone due to bedding.
3	Zou et al. 2018	Sandstone; Flow rate (cc/min) = 20, 50 Stresses (MPa) = σ_v, σ_h, σ_H = (25,10,15); (25,10,20)	The greater the differential stress the less the fracture complexity. Pumping rate at 50 cc/min generated more complex fractures at higher breakdown pressure than at 20 cc/min.

4	Li et al. 2018	Sandstone (varying levels of brittleness)	The greater the brittleness, the greater the fracture propagation and complexity. Greater fracture complexity was seen in layered specimens.

3. EXPERIMENTAL PROCEDURE

3.1 Equipment and materials

The experimental setup consists of a triaxial fracturing unit, fluid pumping unit, acoustic emission acquisition and processing systems. A schematic of the experimental setup is shown in **Figure 12**.

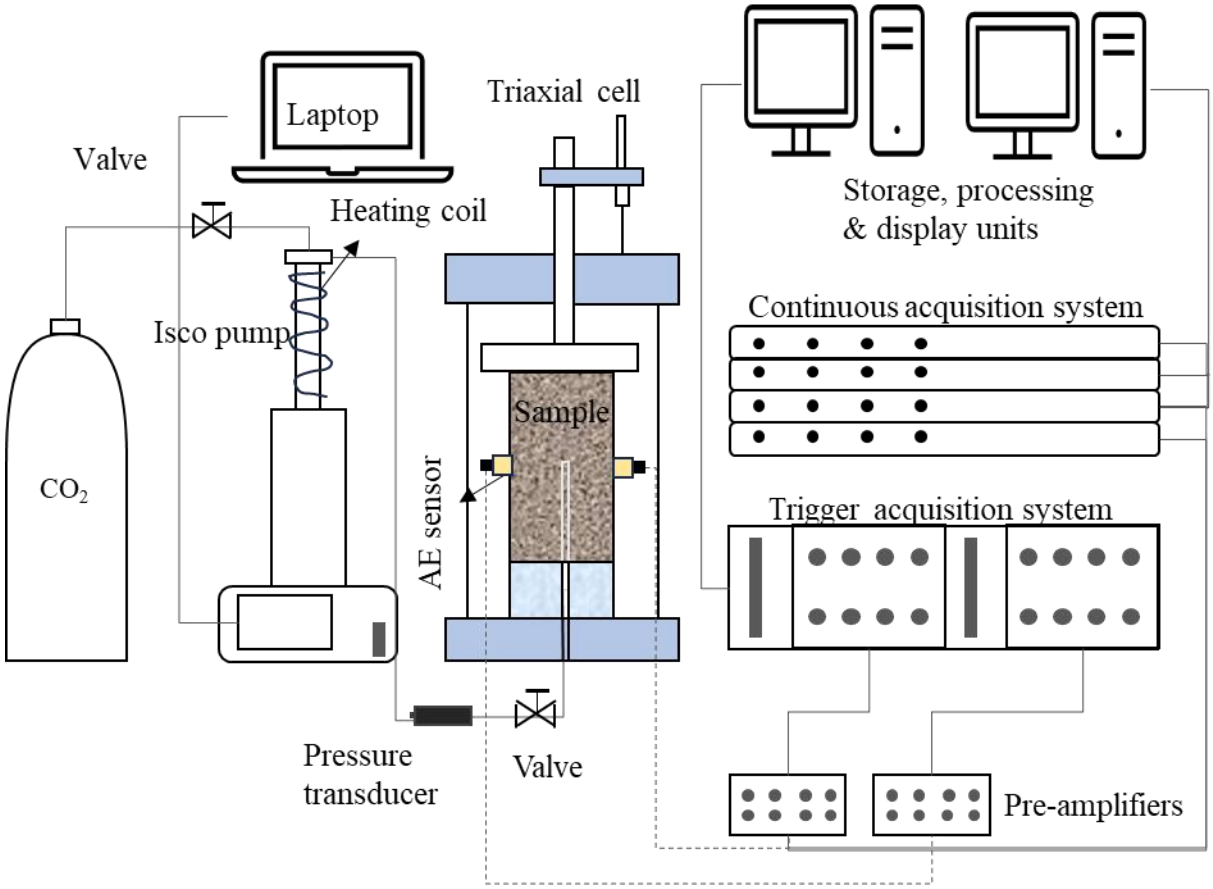

Figure 12. Schematic of the experimental setup. CO_2 may be replaced with water depending on the experimental condition.

3.2 Triaxial Fracturing Unit

The triaxial fracturing unit (**Figure 13**) is a custom-made system designed by New England Research Inc. The unit is servo-hydraulic operated with a computerized system which enables remote control of the stresses applied (up to 20,000 psi) on a rock with dimensions of 4.0″ in

diameter and a variable length. It consists of a pressure vessel with an internal piston for differential stress and servo-hydraulic intensifiers for vertical, minimum, and maximum horizontal stresses. The axial stress is provided by a piston mounted at the top of the confining chamber; the minimum stress is furnished by the fluid (oil) in the confining chamber while the maximum horizontal stress is supplied by a hydraulic actuated flat jacks. It also has an integrated electronics console for servo amplifiers and signal conditioning. For our experiment, we utilized the system to apply true triaxial stresses ($\sigma_V = 1500\,psi, \sigma_H = 3000\,psi, \sigma_h = 500\,psi$) to simulate in-situ conditions for all tests.

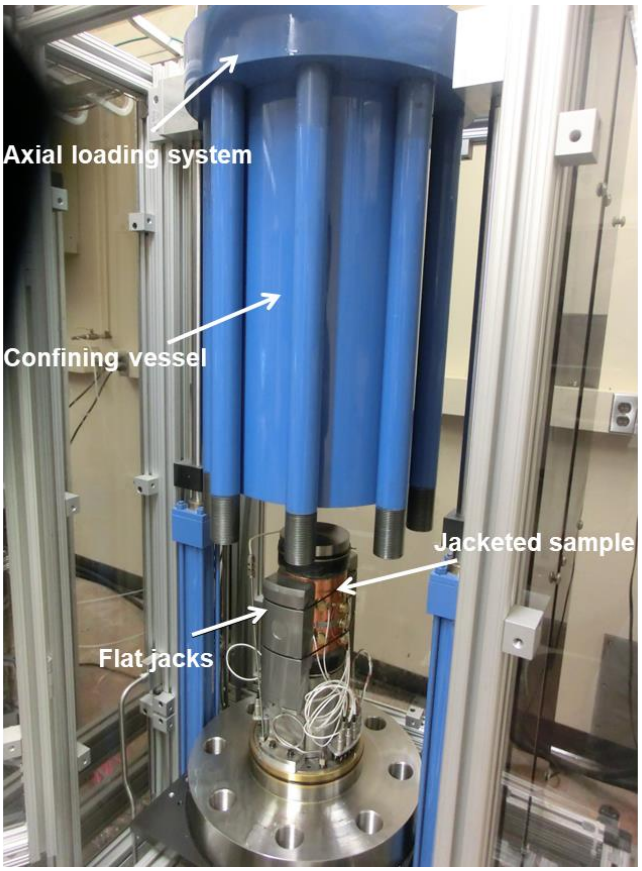

Figure 13. Triaxial stress cell. Axial piston provides vertical stress, the confining vessel supplies the minimum horizontal and the flat jacks applythe maximum horizontal stress.

3.3 Pumping Unit

Teledyne Isco Pump (100DX^{TM}) was used for pumping the injectate (water or CO_2) into the rock sample in the fracturing unit. The pumping system has a maximum pressure capacity of 10,000 psi and flow rate of 50 cc/min with a cylinder capacity of 102.93 cc and a displacement resolution of 9.65 nanoliters/step. We added a couple of other tools to the pumping unit when the experiment involved using CO_2 as the injectate. Some of the tools added include a heating coil to heat CO_2 to about 35^{o}C and a booster pump to increase the pressure of CO_2 in the pump's cylinder. This addition was necessary to have CO_2 in the liquid state during the experiment.

3.4 Fluid System

Water was injected at room temperature and atmospheric pressure, but CO_2 was injected from the pump at about 35^{o}C and a variable pressure depending on sample properties. When the experiment commenced, a valve is opened for the CO_2 to flow to the sample borehole. The pressure and temperature of CO_2 reduce as it expands to fill the gap between the valve and the borehole and contacts the rock at room temperature. We saturated all rock samples with 2.5% KCl brine solution.

3.5 Acoustic Emission (AE) Monitoring System

(a) AE sensor / transducer

Each AE sensor consists of a compressional piezoelectric crystal mounted on a brass conformance button which is machined to fit the curved surface of the sample. The piezoelectric crystal is 0.5″ in diameter and has a resonant frequency of 500 kHz. They are manufactured by Boston Piezo-Optics Inc and have a fine lapped finish and gold plating.

(b) External pre-amplifier

The signals recorded from the AE sensors are fed into a Panametrics - NDT^{TM} model 5660B wide band preamplifier. The preamps have a frequency response between 500 Hz to 40 MHz and

gain settings of 40 and 60 dB. The signal output is passed in parallel to the trigger and continuous acquisition systems (acoustic monitoring system) for filtering and/or recording. A schematic diagram of the AE monitoring system is shown in **Figure 14**.

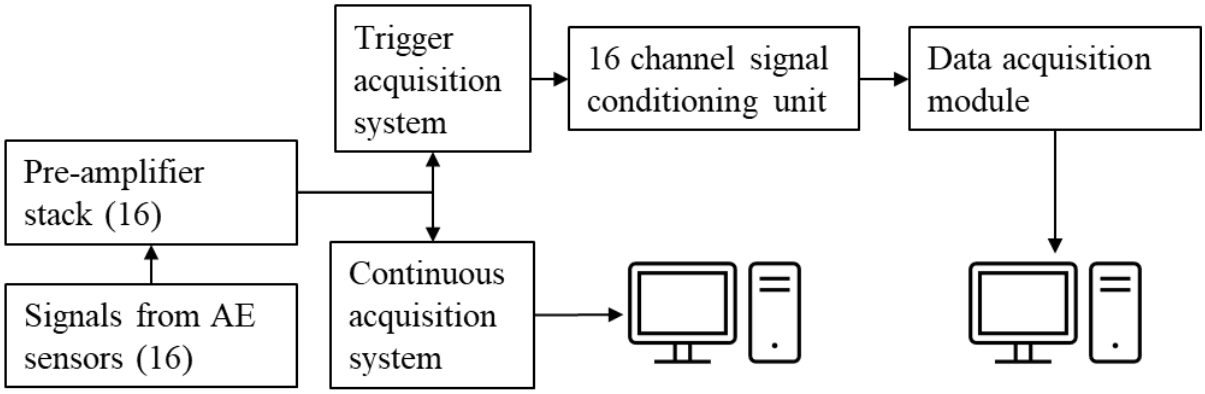

Figure 14. Acoustic Emission monitoring system. Trigger and continuous acquisition systems receive data in parallel from the pre-amplifer.

(c) Acoustic Emission monitoring system

i. Trigger acquisition system

This system consists of a signal conditioning unit and the data acquisition module. The signal conditioning unit amplifies and filters the signals from the external pre-amplifiers. It is designed to condition signals within the range of 20 kHz to 2.3 MHz frequency before they are digitized by an A/D board. It consists of 16 signal cards and 2 controller cards for pre-amplification, signal and trigger gain and filter settings. The internal pre-amplifier can supply up to 42 dB gain in increments of 6 dB. The signals hereafter is fed into the trigger and signal conditioning sections which provide additional amplification and frequency filtering. The trigger threshold has been permanently fixed at ±100 mV by the manufacturer.

The data acquisition module is a 32 channel ICS-645 PCI bus analog input board responsible for sampling the signals. It has a maximum sampling rate of 20 MHz but for our experiments only 16 channels were utilized at a sampling rate of 5 MHz. The control logic of this

module continually fills the circular buffer with fresh data in expectation of a trigger signal. Acquisition stops once a new trigger is received for recording to take place and afterwards resumes to accept new data. This process introduces a dead time during which some signals may be lost especially when acoustic emissions occur in rapid succession.

ii. Continuous acquisition system

Contrary to the trigger acquisition system, the continuous acquisition system relentlessly streams data to the system disk without any interruption (**Figure 15**). It consists of 4 recording systems (1 master and 3 slave computers) with each one recording data from 4 channels. It has the capability to sample data at variable rates (1,2,5 and10 MHz), waveform length, and input impedance (50 **Ω** and 1M**Ω**) (**Figure 16**). Post-acquisition, the signals can be extracted from the data stream and processed using appropriate user specified threshold and window settings. Thus, this eliminates the likelihood of missing events and increases the chances of getting more data to make meaningful interpretations.

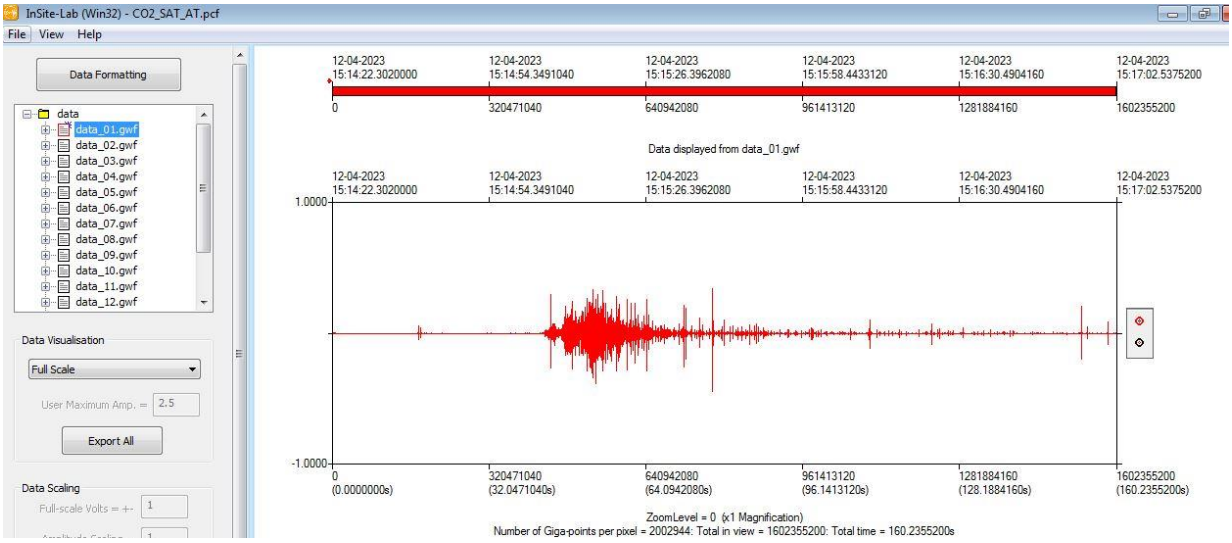

Figure 15. Typical example of signals acquired by one channel in an experiment. Individual events will be extracted from this signal and further processed for AE attributes.

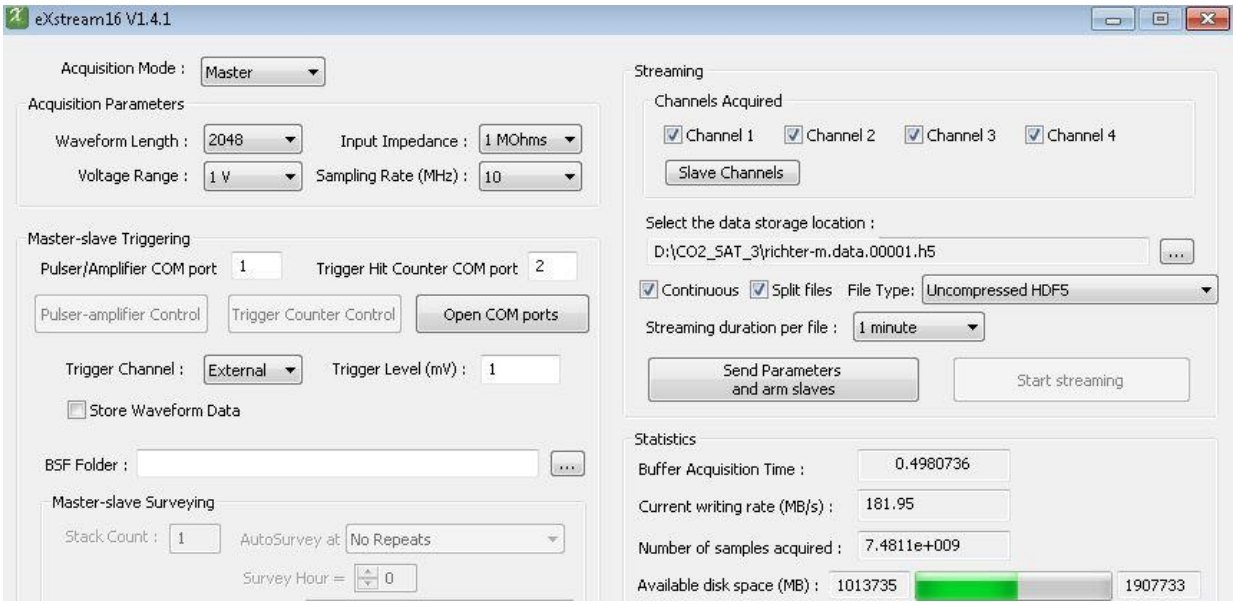

Figure 16. A window for one of the recording systems of the continuous acquisition system.. The waveform length, voltage range, input impedance and sampling rate are variable.

The extraction parameters include amplitude threshold and picking algorithm with each having its own user settings (**Figure 17**).

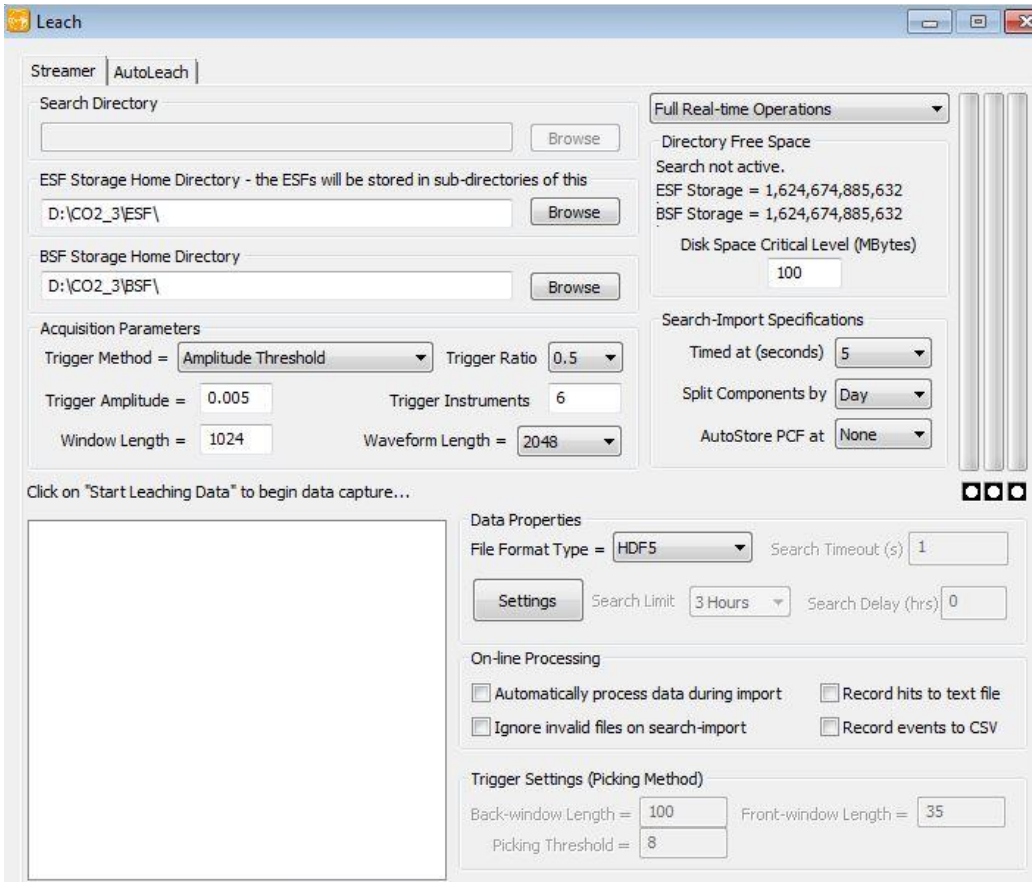

Figure 17. Processing window to acquire events. Amplitude threshold is one of the extraction parameters that can be used to acquire events. Appropriate settings are to be set by the user.

3.1 Sample selection:

Three sandstones having varying petrophysical and elastic properties were chosen for our experiments. The sandstones are labeled as S1, S2 and S3.

3.2 Sample Characterization

3.2.1 Circumferential Velocity Analysis (CVA)

Circumferential velocity analysis is a technique for measuring compressional wave (P-wave) velocity as a function of azimuth on cylindrical samples. The variation in velocity along the azimuth furnishes the magnitude of velocity anisotropy and direction of cracks/discontinuities. P-

wave velocity along cracks is higher than across cracks. An average of the measured velocity is used in a velocity model for locating acoustic emissions. In an isotropic homogenous sample, the P-wave velocity with azimuth is constant. Slight changes in velocity may be due to cracks and small changes in mineralogy.

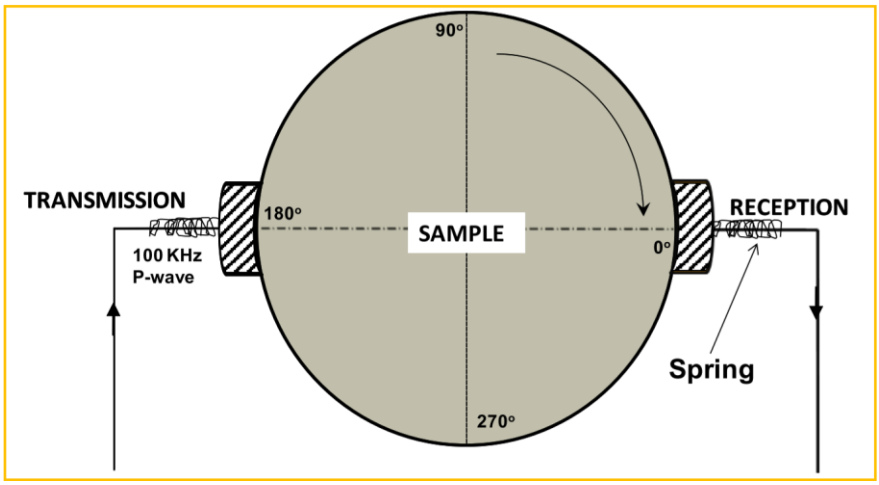

Figure 18. Schematic of CVA in plan view showing the transmitting and receiving transducers mounted on the sample. The sample is rotated clockwise in 10° incrmenets and velocity is measured. Adapted from Chitrala's thesis (2012)

To measure P-wave velocity, the sample is mounted on a rotatable base having two spring loaded P-wave transducers mounted on the sample for transmitting and receiving signals from a pulse generator (**Figure 18**). A 100 kHz sinusoidal signal is sent from the pulse generator into the sample through a transducer and the signal is received at the other end of the sample through another transducer. It is then amplified by a 60 dB pre-amplifier and sent to the oscilloscope for recording. For each velocity measurement, fifty signals are stacked to reduce noise and then amplified on the oscilloscope to enable reading the arrival time. Using the arrival time and diameter of the sample, the velocity of P-wave through the sample can be calculated. With the help of a motor, the sample is turned clockwise in 10° increment for the next measurement to be made until

the sample surface is covered completely. A total of 36 readings were taken on fully saturated samples. Results of CVA measurements will be discussed below.

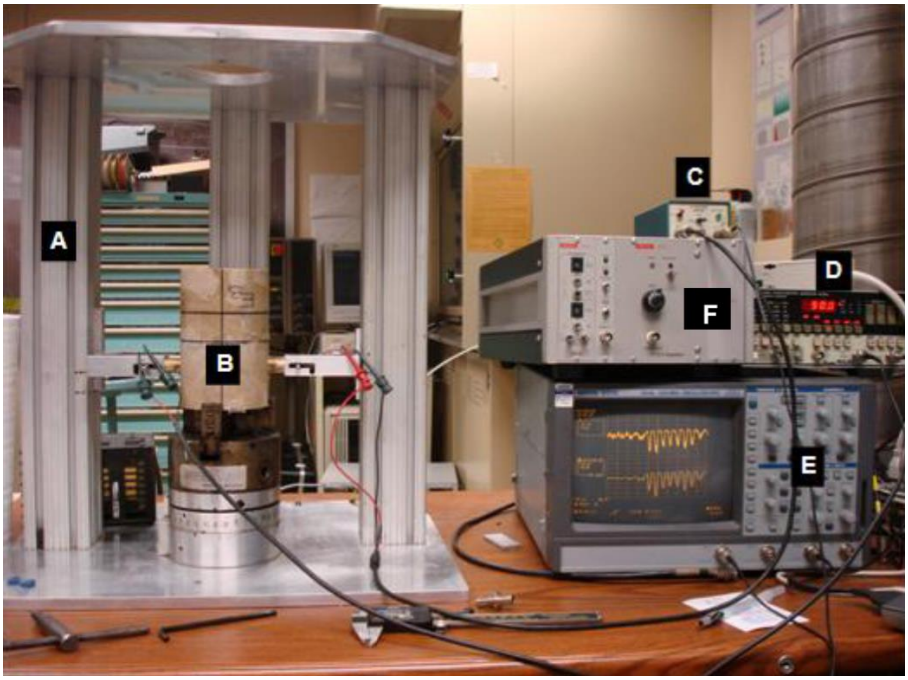

Figure 19. Laboratory apparatus for circumferential velocity analysis. (A) is the support frame; (B) is the mounted sample on the rotatable base; (C) is the pre-amplifier; (D) is he pulse generator; (E) is the oscilloscope with waveform averaging capabilities; (F) is the high voltage amplifier. Adapted from Aso's thesis (2009)

The CVA results for S1-S3 sandstone samples are presented in **Figure 20-22**. There is small variation in Vp as a function of azimuth (anisotropy ≤ 10%). Although there is some degree of anisotropy, an average V_p is used in an isotropic velocity model to simplify the process of locating acoustic emissions (**Table 4**).

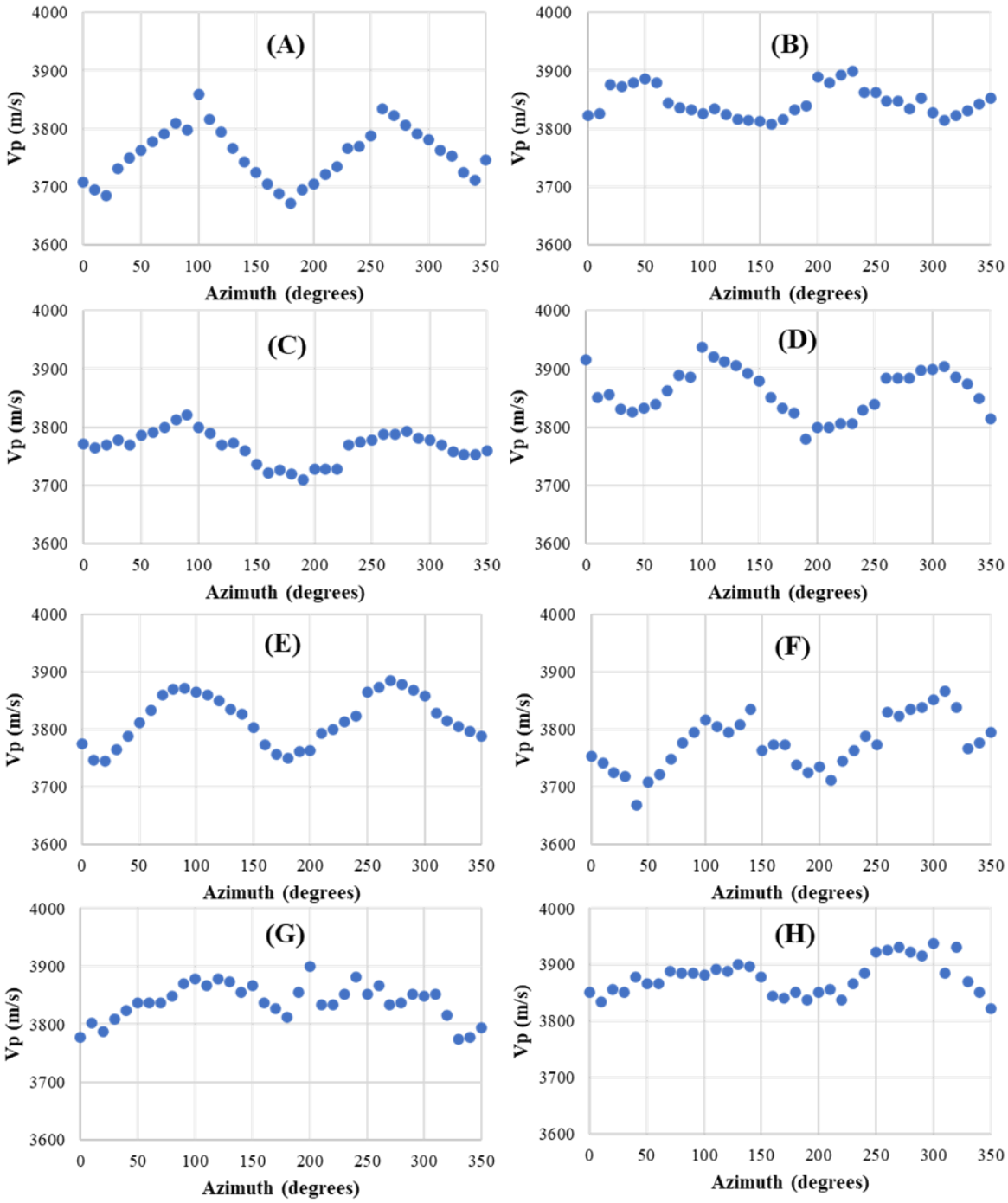

Figure 20. CVA results for S1 samples.

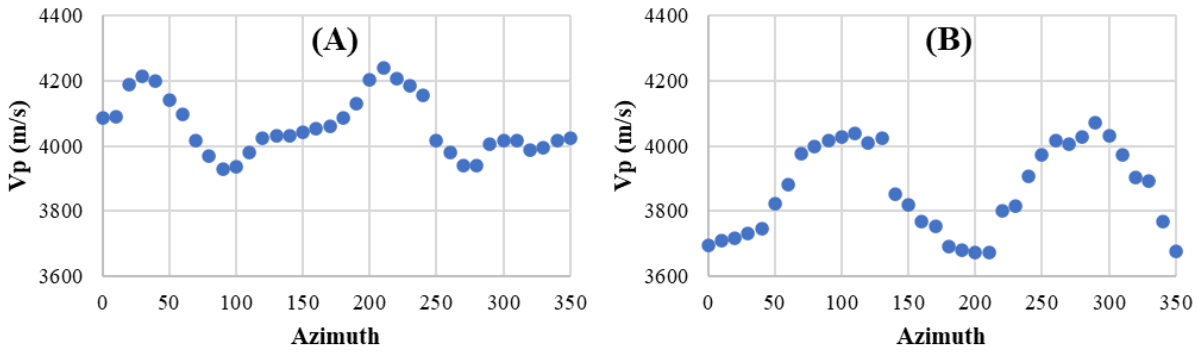

Figure 21. CVA results for S2 samples.

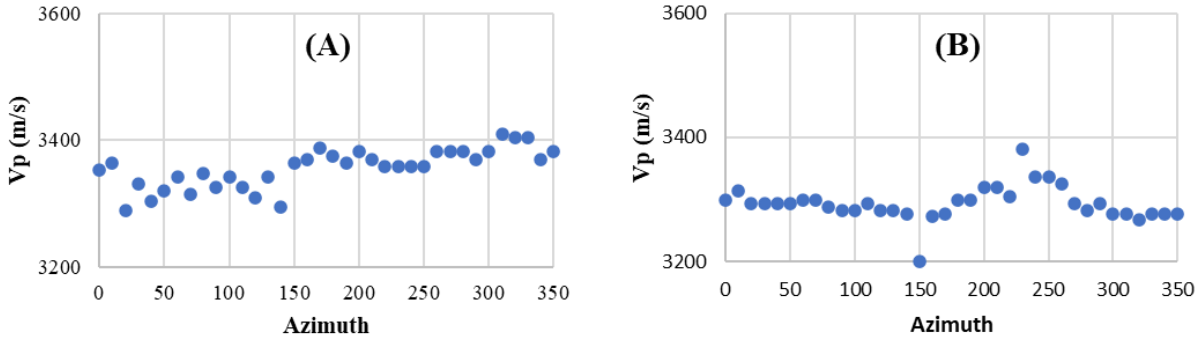

Figure 22. CVA results for S3 samples.

Table 4. Results of circumferential velocity analysis (CVA)

Sandstone	Sample ID	Compressional Wave (P-Wave) Velocity (m/sec)				
		Min	Max	Average	Difference (max- min)	Anisotropy [(Difference/min)*100]
S1	A	3671	3859	3754	188	5.1
	B	3808	3899	3845	91	2.4
	C	3709	3766	3821	57	1.5
	D	3780	3936	3860	156	4.1
	E	3745	3884	3817	139	3.7
	F	3668	3867	3776	199	5.4
	G	3773	3900	3840	127	3.4
	H	3823	3938	3878	115	3.0
S2	A	3929	4238	4062	309	7.9
	B	3674	4072	3866	398	10.8
S3	A	3288	3409	3355	121	3.7
	B	3200	3381	3293	181	5.7

3.2.2 Porosity and Permeability

Porosity (ϕ) is defined as the ratio of pore volume to bulk volume expressed as either a fraction or percentage. Mathematically it is expressed as:

$$\phi = \frac{V_{bulk} - V_{grain}}{V_{bulk}} = \frac{V_{pore}}{V_{bulk}} \quad (27)$$

where V_{bulk}, V_{grain}, V_{pore} are bulk, grain and pore volumes respectively. Porosity is measured on 1" dried intact core plugs using automated porosimeter/permeameter (AP 608). The device also has the capacity to measure permeability of rock samples by using an unsteady state pulse decay technique described by Jones (1971). The range of permeability measurement is from 5D – 1μD at varying range of confining pressure up to 9500 psi. Permeability is measured on 1" dried intact or fractured core plugs. The permeability of intact samples (S1, S2 and S3) measured at a confining pressure of 1000 psi is shown in **Table 5**.

Table 5. Average porosity and permeability values of rock samples used for experiment.

Sandstone	Porosity (%)	Permeability (mD) at 1000 psi
S1	6.0	0.015
S2	2.8	0.020
S3	12.2	0.323

Post fracturing, vertical plugs are taken along the fracture on both sides of the sample. The schematic of the plug sectioning for permeability measurement is shown in **Figure 26**.

3.2.3 Mineralogy

The Fourier Transform Infrared Spectroscopy technique was used to measure the mineralogy of samples. It provides an efficient way for quantifying mineralogy by inversion of the absorption spectrum (Sondergeld and Rai, 1993). Detailed description of the technique is provided by Ballard, 2007. The system used in this study can identify and quantify 16 different minerals: quartz, calcite,

dolomite, illite, smectite, kaolinite, chlorite, pyrite, orthoclase, oligoclase, mixed clay, albite, anhydrite, siderite, apatite, and aragonite. **Table 6** shows the detailed mineral composition of the samples used for the experiment. The mineralogy is summarized in **Figure 23**. S1 is predominantly quartz rich with no carbonates while S2 and S3 are composed of quartz, carbonates and clays.

Table 6. Mineral compositon of samples measured using Fourier Transform Spectroscopy (FTIR)

Mineral	**Mineralogy (wt %)**		
	S1	**S2**	**S3**
Quartz	84	58	68
Calcite	0	15	4
Dolomite	0	0	8
Illite	0	0	0
Smectite	0	0	0
Kaolinite	0	0	3
Chlorite	0	0	4
Pyrite	0	0	0
Orthoclase	4	0	0
Oligoclase	0	0	0
Mixed clays	11	18	10
Albite	1	9	0
Anhydrite	0	0	0
Siderite	0	0	3
Apatite	0	0	0
Aragonite	0	0	0

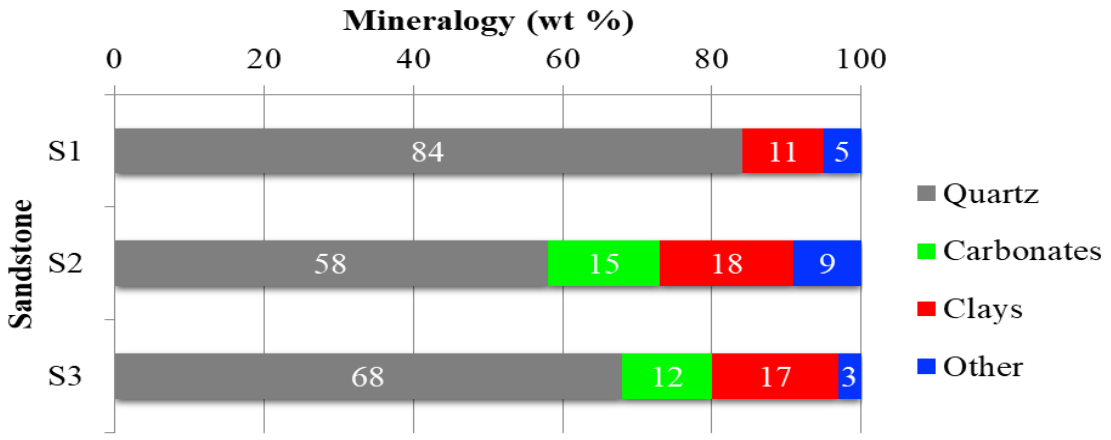

Figure 23. Summary of mineralogy for samples used in experiment.

3.2.4 Dynamic Elastic Properties

Compressional and shear wave velocity (V_p and V_s) and bulk density of the samples were measured to estimate dynamic elastic properties. The samples used were 1" fully saturated intact core plugs. V_p and V_s were taken from 500 to 3000 psi confining pressure. The values reported in **Table 7** reflect Vp and Vs measurements at 500 psi which is same as the confinement pressure during actual experiments.

Table 7. Dynamic elastic properties of samples

Sandstone	Velocity (km/s)		Dynamic properties					
	V_p	V_s	V_p/V_s	Saturated bulk density (g/cc)	Poisson's ratio	Bulk modulus (GPa)	Youngs modulus (GPa)	Shear modulus (GPa)
S1	4.72	1.78	1.77	2.54	0.26	32	46	18
S2	5.5	3.1	1.78	2.27	0.32	41	26	21
S3	3.90	2.00	1.95	2.42	0.28	24	55	10

3.3 Experimental Procedure

Cylindrical rock samples of dimension 4″ in diameter and 5.5″ in length were utilized for the experiments. They were cored from the same block of rock to ensure similarity in properties. To achieve a flat and parallel surface (to allow uniform distribution of applied stresses), samples were polished using a surface grinder with a maximum deviation of ± 0.01″. Each sample had a hole of 0.25″ drilled from the center of the surface to half the sample length; a counterbore of about 0.4″ in diameter and 0.2″ in length is drilled from the center of the surface. The borehole was completed with a steel tubing (0.25″ OD and 0.19″ ID) which had two slots cut 180^o apart about 0.2″ from the base. JB Weld^{TM} epoxy was used to cement the tubing in place and allowed to dry for 24 hours. Groves are cut along the circumference of the tubing to ensure good bonding with the rock.. The

base of the tubing was sealed off to ensure fluid injection only through the perforation. The sample at this stage is saturated in 5000 psi potassium chloride (KCl) brine solution. This step ensures that the clay minerals are stabilized. For CO_2 non-exposed samples, after 72 hours the sample is taken out of the saturation vessel and CVA is performed on it.

Some samples were exposed to CO_2 to investigate the geomechanical impact of the reactivity between CO_2 and the rock mineralogy. To do this, CO_2 was introduced into the saturating vessel at a pressure of 3000 psi and a temperature of 35ºC for a period of time.

Afterwards, the sample is covered with a copper jacket (0.003″ thick) to isolate confining fluid and to act as a point of attachment for the acoustic sensors (**Figure 24**). Two metal spacers with internally mounted transducers are placed on the top and bottom of the sample and the space between the spacer and sample is sealed off with an elastomer and epoxy for 24 hours. Afterward the space between the elastomer and the metal spacer is closed using a copper wire and a clamp. The sample assembly is placed in the triaxial loading system and then an array of 14 acoustic sensors was mounted on the copper jacket at designated locations using ethyl cyanoacrylate glue (**Figure 25**).

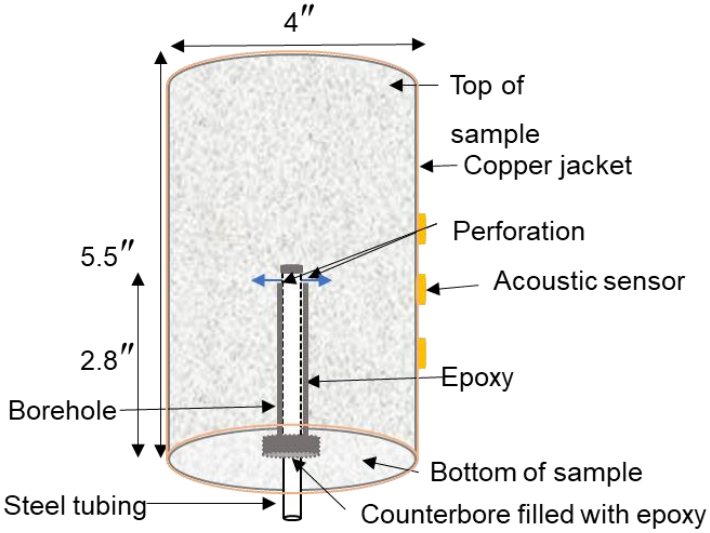

Figure 24. Schematic of test sample. Sample is completed with a 0.25″ OD steel tubing which is cemented in place with epoxy. Injectate comes out from only the perforation. Injection depth is about half the sample length. Attached sensors on the copper jacket pick up AEs during fracturing.

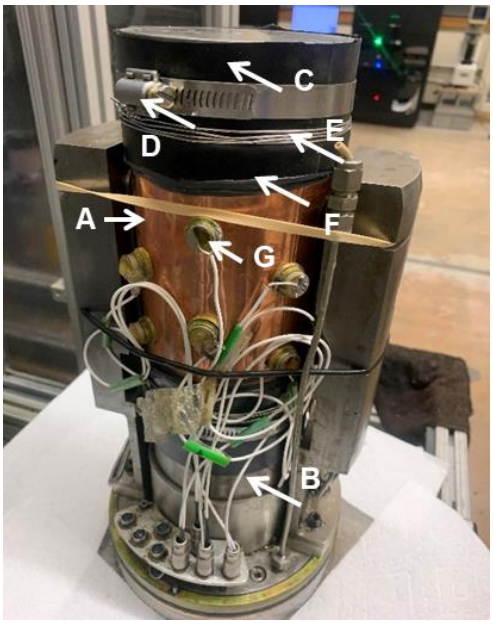

Figure 25. Diagram of jacketed sample mounted in the traixial cell. (A) copper jacket (B) bottom metal spacer (C) elastomer (D) clamp (E) copper wire (F) epoxy (G) sensor.

3.4 Experimental conditions

Table 8 shows the experimental conditions for all samples used for experimentation. Same stresses ($\sigma_h = 500\ psi;\ \sigma_H = 3000\ psi;\ \sigma_V = 1500\ psi$) were applied to all samples. Other test conditions are detailed in Appendix A.

Table 8. Experimental conditions

Sandstone	Sample ID	Length (mm)	Saturation state	Injectate
S1	A	135	Brine	Water
	B	137	Brine	Water
	C	135	Brine	Water
	D	133	Brine	CO_2
	E	134	Brine	CO_2
	F	140	Brine	CO_2
	G	140	Brine+CO_2 (6 weeks exposure)	CO_2
	H	135	Brine+CO_2 (8 weeks exposure)	CO_2
S2	A	131	Brine	Water
	B	137	Brine	CO_2
S3	A	148	Brine	Water
	B	152	Brine	CO_2

3.5 Fracture Permeability

One-inch vertical plugs were taken along the fracture on both sides of borehole for permeability measurement (**Figure 26**). To ensure the plugs do not split due to fracture, a heat shrink rubber was placed around the sample after it is cored. Some plugs, especially those from samples fractured with CO_2 split during either the coring process or post coring before they were secured with a heat shrink tube. Unsplit plugs are cut, polished, and dried for permeability measurements using AP-608™ as described earlier.

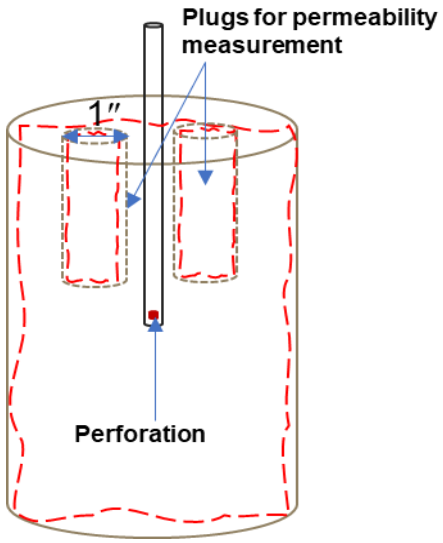

Figure 26. Schematic of plug extraction from fractured rock samples. The red line shows the fracture trace.

3.6 Fracture Morphology

3.6.1 Fractured Plug Sectioning and Sample Preparation

Vertical and horizontal plugs (1″ diameter) were taken from the right and left side of the borehole respectively and close to the borehole as shown in **Figure 27**. The plugs were cut into slices of about 0.2″ thick. The slices were Soxhlet cleaned using 80% toluene and 20% methanol for over 3 days: this was done to remove oil which may have entered from the confining chamber and precipitated salt. Afterward, they are polished using emery papers of increasing grit size (120- to 3000 grit) and ion milled (Fischione™ Model 1060™ **Figure 28**) prior to SEM imaging.

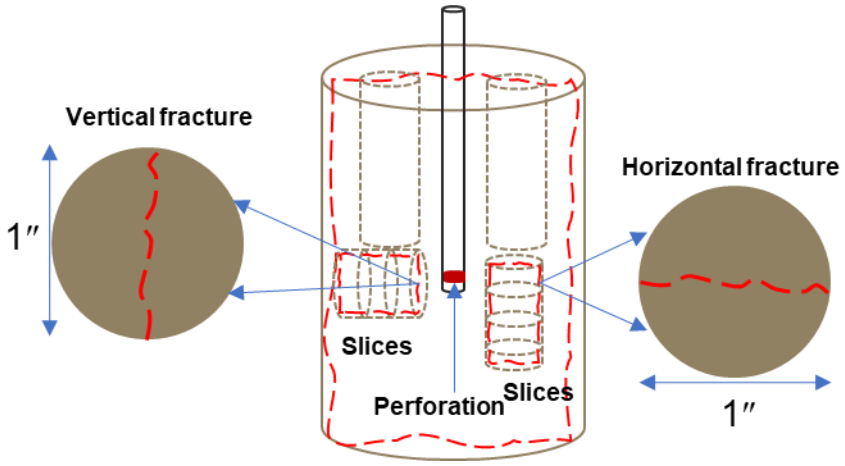

Figure 27. Schematic of plug sectioning for fracture morphology study. Red line shows the fracture trace. The far right image shows the direction of fracture propagation.

Figure 28. Model 1060 Fischione broad beam argon mill used for final polishing sample surface prior to SEM imaging.

3.6.2 SEM Imaging and Stitching

Fracture morphology is studied using images taken using the FEI Helios Nanolab 650 DuelBeam FIB/SEM machine (**Figure 29**). This device can operate in two modes of detection: secondary and backscatter electron modes. The secondary mode detects low energy electrons resulting from the inelastic collision between the incident beam electrons and electrons from the

sample surface while the backscattered mode detects high energy electrons resulting from elastic collision. The secondary mode shows topography while backscattered mode reveals compositional variations. Images (250+ per slice) were taken using the secondary detection mode and the FEI "MAPS" software was used to stitch them together into one large mosaic showing the fracture morphology.

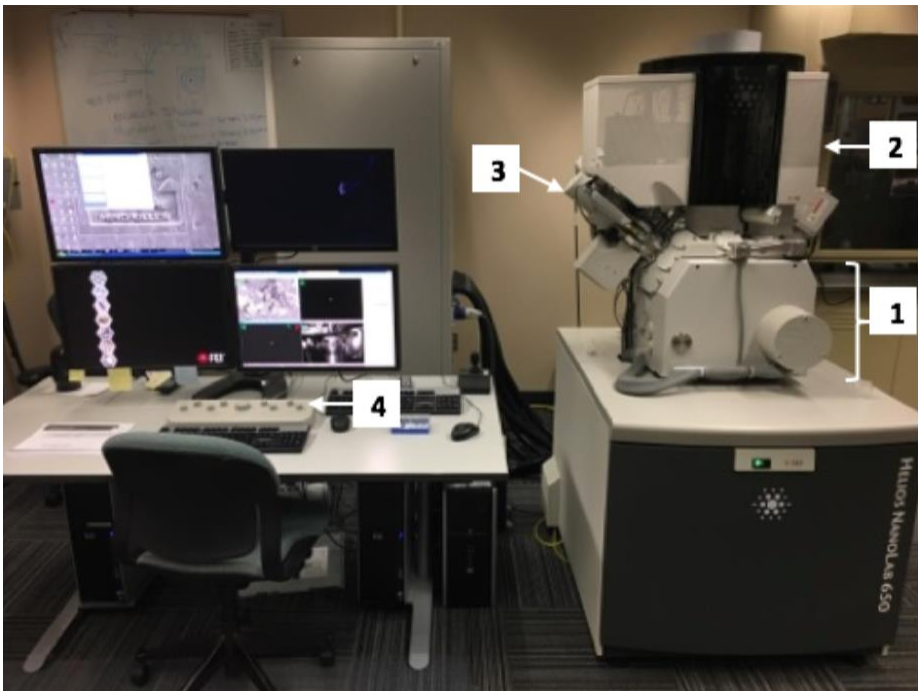

Figure 29. FEI Helios Nanolab 650 scanning electron microscope. (1) pressurized vacuum chamber (2) electron column used to focus and illuminate specimen (3) electron gun to produce electron beam (4) control panel.

4. RESULTS AND DISCUSSION

4.1 Pressure and AE response to fluid injection

Sample S1

S1 has porosity of 6.0% and permeability of 0.015mD rock with mineralogy comprising mostly of quartz and minor amount of mixed clays. It has an average grain size of approximately 127µm (**Figure 30**). Eight (8) samples were used for experimentation out of which two were exposed to CO_2. Three (3) samples were fractured with water and the other five (5) with CO_2. The pressure and AE responses for these tests are discussed below.

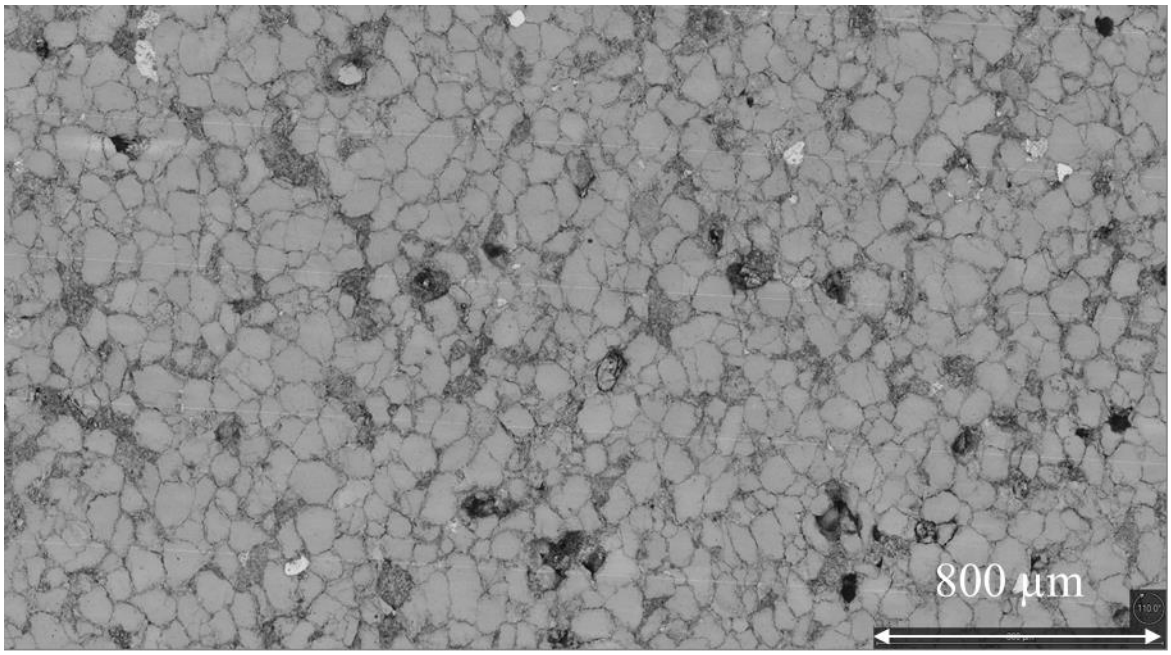

Figure 30. SEM image of S1A. It has an average grain size of 127 µm.

Samples S1A, S1B, andS1C

We carried out water injection test in S1A-S1C. **Figure 31** shows injection pressure and cumulative AE events as a function of time for S1A. An injection rate of 10 cc/min was maintained throughout the test till pump shut-in. As injection pressure began to rise, it increased linearly and rapidly (due to the incompressibility of water) at 144 psi/s until a breakdown pressure of 2158 psi

was reached. At this pressure, the tensile strength of the rock was exceeded, and fractures began to form in the rock leading to its breakdown. After failure, the pressure dropped rapidly and stabilized a little above the minimum horizontal stress (500 psi). Water continued to flow across the fracture surface causing the fracture to remain slightly open till the pump was stopped and the fracture closed. At fracture closure, the pressure dropped slightly to about 500 psi.

Prior to breakdown, recorded AE activity was minimal. But at the time of breakdown, there was a sudden rise in the number of AE events (shown in red in **Figure 31**). The sudden burst of AE events at breakdown was due to the breaking of bonds and creation of new surfaces resulting from rock failure. Post-breakdown, release of AE events stabilized as the fracture partially closed but rose slightly when the pump was stopped and the fracture closed. Fracture closure may result in crushing of asperities along the fracture face which will lead to a slight rise in AEs (Chitrala 2011). In total, 3256 AEs were recorded with most occurring at rock breakdown. **Figure 32** shows the full waveform of AEs for one channel as a function of time. The full waveform appears to have two regions of AE release. The initial region can be attributed to rock breakdown and fracture propagation and the latter to pump shut in. The AE release rate at breakdown till it began to stabilize was ~446 AEs/s. Similar pressure and AE responses were reported by Chitrala 2011; Damani 2013; Goyal et al. 2020.

Other S1 samples (1B and 1C) had similar pressure and AE responses as observed in S1A . Appendix B lists the results for the water injection tests on S1B and S1C.

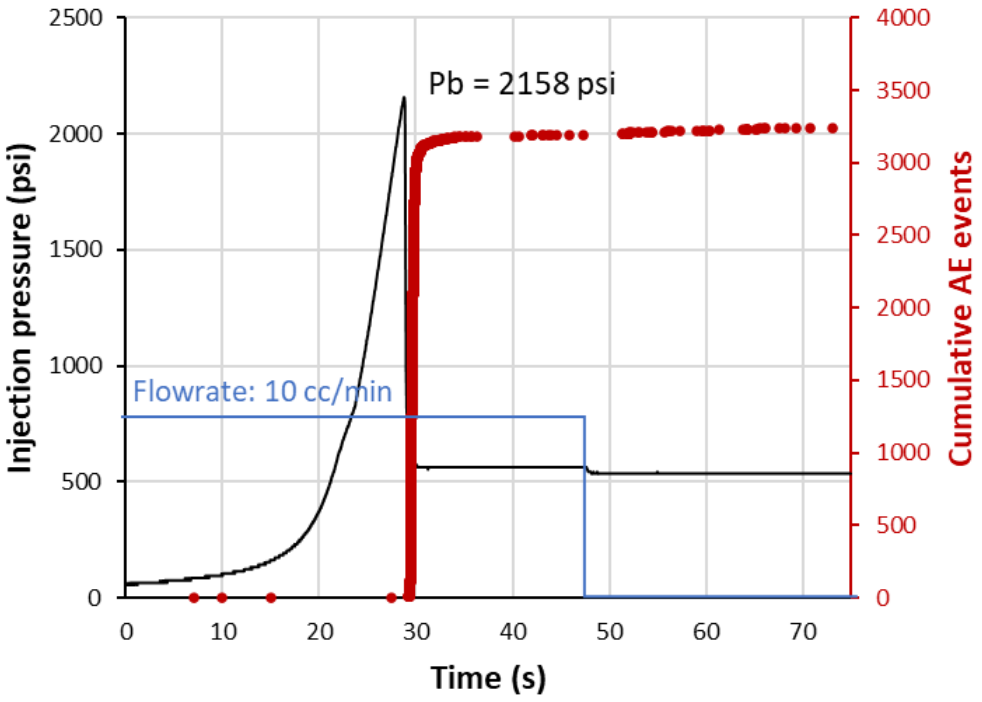

Figure 31. Injection pressure (black line) and cumulative AE events (red dots) versus time for sample S1A. The blue line shows constant flow rate of 10 cc/min until pump shut-in where it drops to zero.

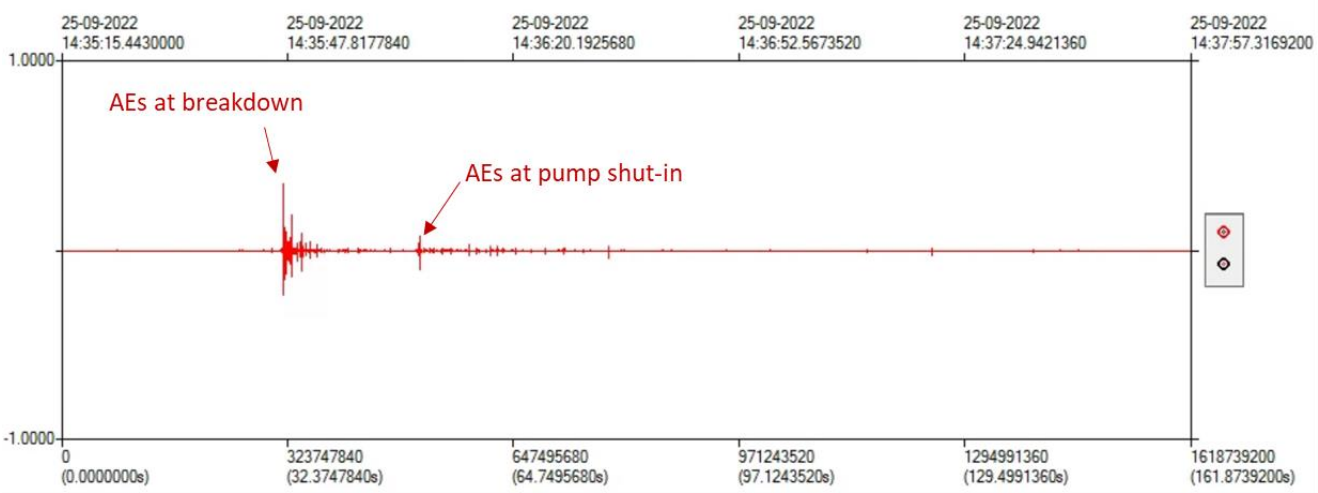

Figure 32. Full waveform of amplitude vs time recorded for one channel for sample S1A. It shows AE activity as a function of time. It appears to have two regions of intence AE release. The first region can be attributed to breakdown and fracture propagation and the latter to pump shut-in.

Samples S1D, S1E, S1F

We carried CO_2 injection test in S1D, S1E, and S1F. **Figure 33** shows injection pressure and cumulative AEs as a function of time for S1D. An injection rate of 10 cc/min was maintained throughout the test till pump shut-in where it dropped to zero. Pumping of CO_2 started at ~1500 psi. This ensures breakdown pressure is reached before the pump runs out of CO_2 and reduces pressure buildup time. The pressure increased slowly (due to the compressibility of CO_2) at 3.6 psi/s until a breakdown pressure of 1846 psi was reached. Following failure, the pressure dropped less rapidly than seen in the tests with water and stabilized at 300 psi above the minimum horizontal stress (500 psi). The increase in the confining pressure is due to CO_2 leak-off through the fracture and the damaged jacket into the confining fluid. Due to the low viscosity of CO_2, fracture closure is likely to occur simultaneously with fluid leak-off instead of pump shut-in as seen in the tests with water.

At breakdown, there was a sudden rise in the number of AEs (**Figure 34**). The sudden burst of AEs at breakdown was due to the breaking of bonds and creating of new surfaces resulting from rock failure. Post-breakdown, the release of AEs reduced and stabilized as the fracture closed. Fracture closure may result in crushing of asperities along the fracture face and thus lead to a slight rise in AEs. In total, 13,594 AEs were recorded with most occurring at rock breakdown. The AE release rate at breakdown till it began to stabilize was ~846 AEs/s.

Other samples (S1D, and S1E) fractured with CO_2 including those exposed to CO_2 (S1F and S1G) had similar pressure and AE responses as observed in S1D. Appendix B lists the results for the CO_2 injection tests for these four samples (S1D through S1G)

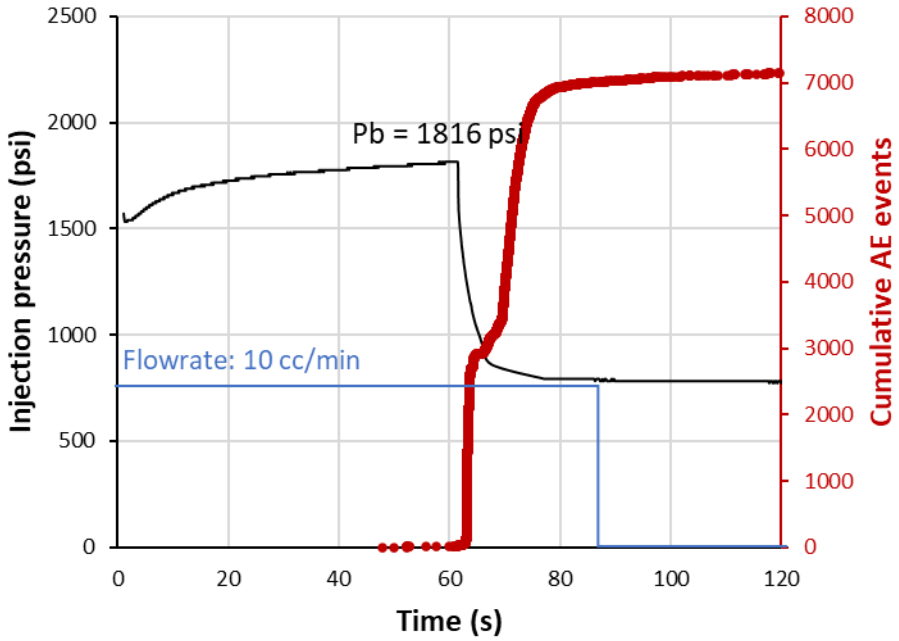

Figure 33. Injection pressure (black line) and cumulative AE events (red dots) versus time for sample S1E. The blue line shows constant flow rate of 10 cc/min until pump shut-in where it droped to zero.

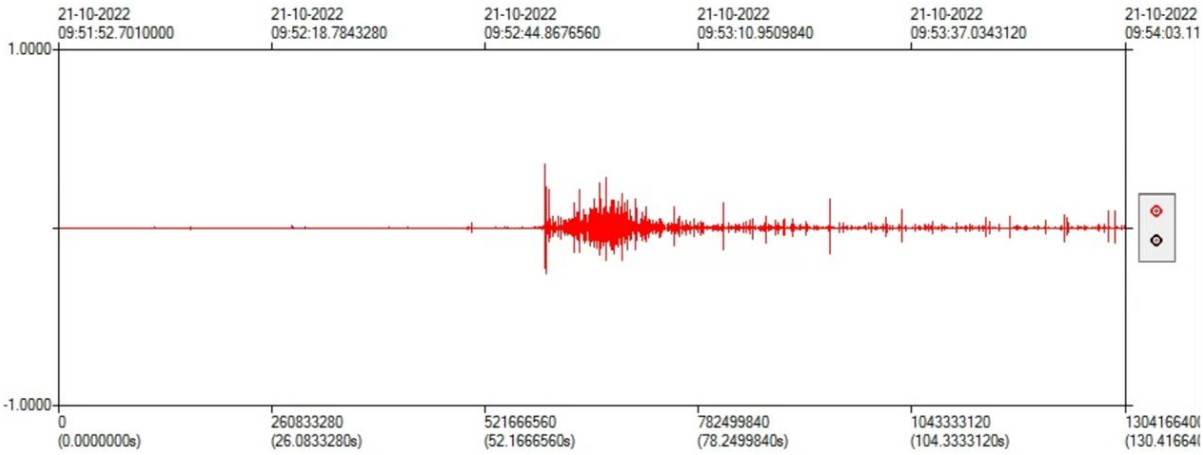

Figure 34. Full waveform of amplitude vs time recorded for one channel for sample S1E. It shows AE activity as a function of time. AEs due to breakdown and pump shutin are indistinguishable suggesting that fracture closure occurred right after breakdown.

Sample S2

S2 has porosity of 2.8% and permeability of 0.015mD with mineralogy comprising of quartz, carbonates, and mixed clays. It has an average grain size of approximately 290 µm (**Figure 35**). Two (2) triaxial fracturing tests were conducted. One test was done with water injection and the other with CO_2 injection.

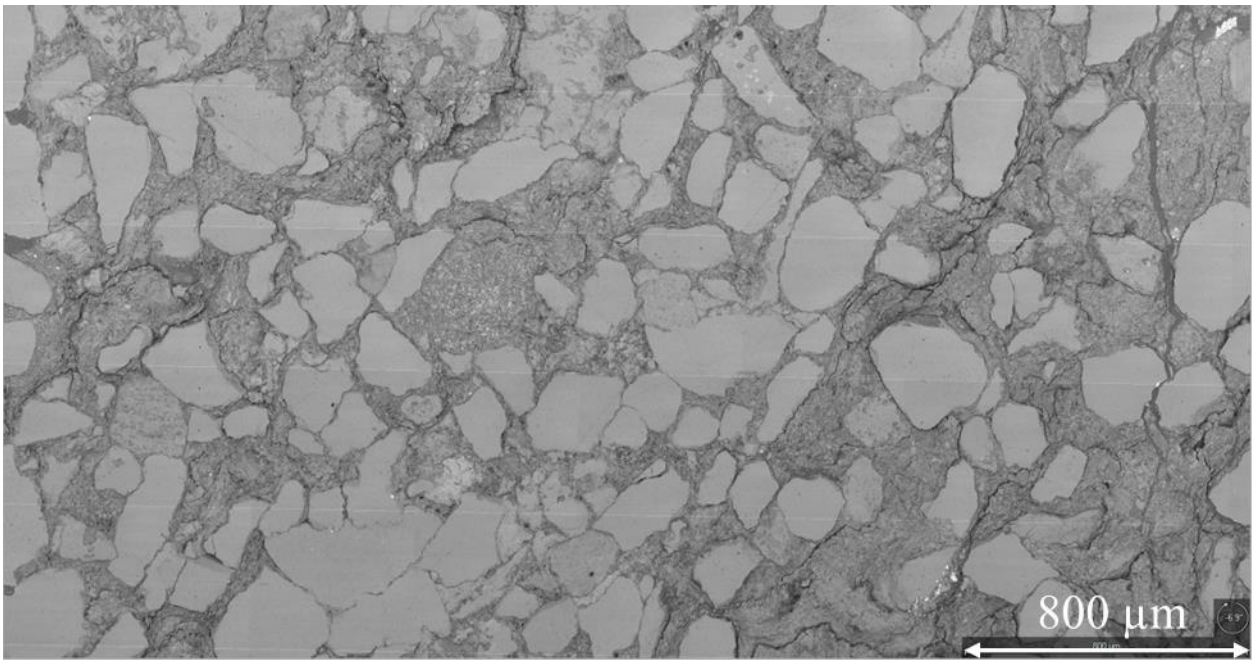

Figure 35. SEM image of S2. It has an average grain size of about 290 µm.

Sample S2A

Figure 36 shows injection pressure and cumulative AE events as a function of time for a test carried out with water as the injectate. The pressure and AE responses are similar to what is discussed in the water injection test for sample S1. Injection pressure rose rapidly at 136 psi/s until a breakdown pressure of 2266 psi was reached. In total, 3648 AEs were recorded with most occurring at rock breakdown.

Figure 37 shows the full waveform of AEs for one channel as a function of time. The AE release rate at breakdown till it began to stabilize was ~359 AEs/s.

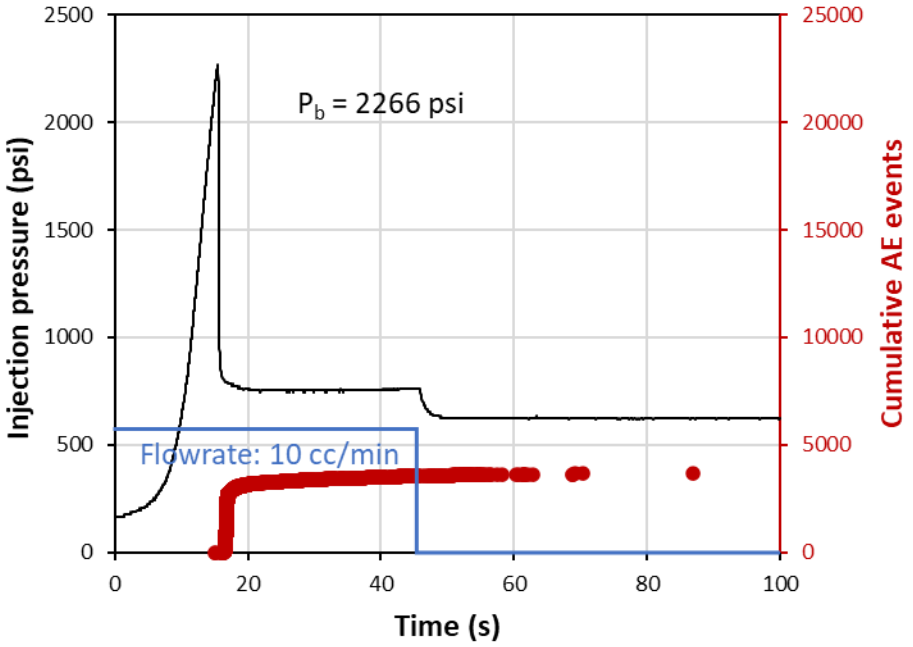

Figure 36. Injection pressure (black line) and cumulative AE events (red dots) versus time for sample S2A. The blue line shows constant flow rate of 10 cc/min until pump shut-in where it drops to zero.

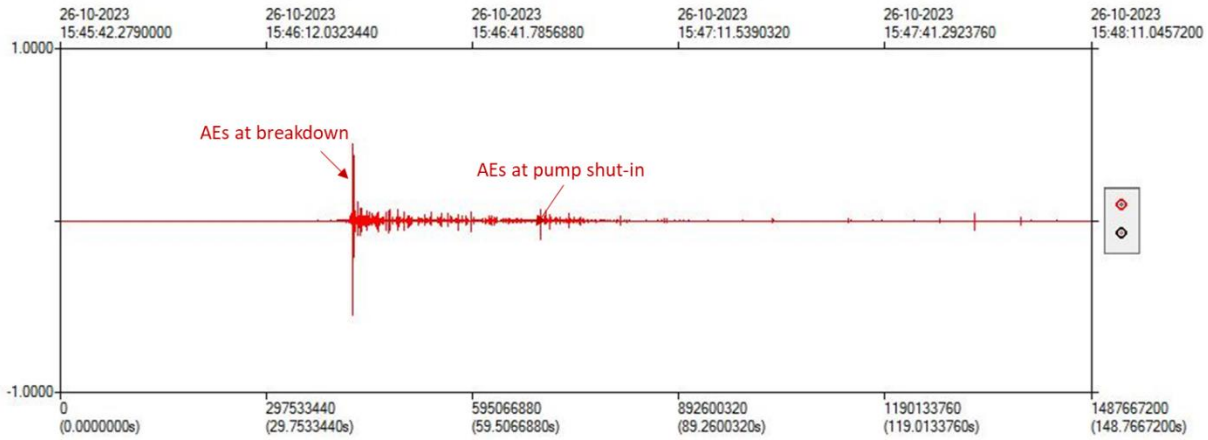

Figure 37. Full waveform of amplitude vs time recorded from one channel at about the same time when injection started for sample S2A. It shows AE activity as a function of experimental time. The first region can be attributed to breakdown and fracture propagation and the latter to pump shutin.

Sample S2B

Figure 38 shows injection pressure and cumulative AEs as a function of time for a test carried out using CO_2 as injectate. The pressure and AE responses are similar to what is discussed in the CO_2 injection test for sample S1. Pumping of CO_2 was initiated at ~1358 psi. The pressure increased slowly (due to the compressibility of CO_2) at 29 psi/s until a breakdown pressure of 2080 psi was reached. In total, 21618 AEs were recorded with most occurring at rock breakdown (**Figure 39**). The AE release rate at breakdown till it began to stabilize was ~1650 AEs/s.

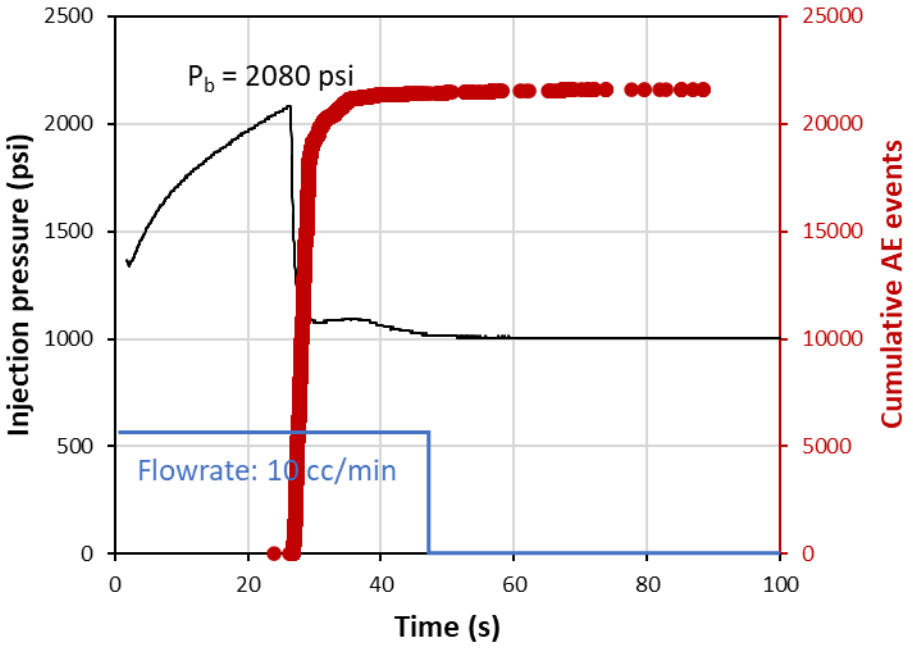

Figure 38. Injection pressure (black line) and cumulative AE events (red dots) versus time for sample S2B. The blue line shows constant flow rate of 10 cc/min until pump shut-in where it drops to zero.

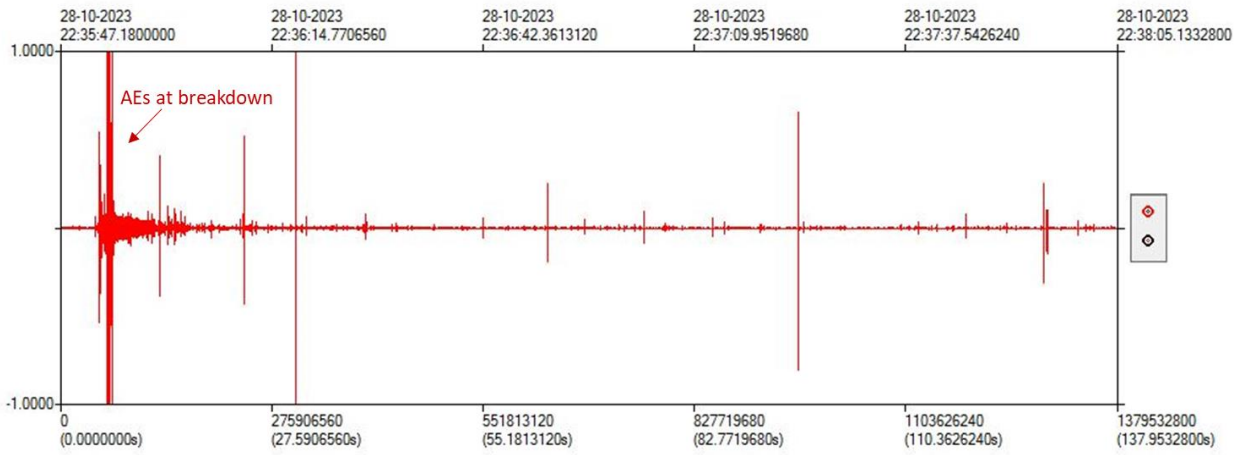

Figure 39. Full waveform of amplitude vs time recorded from one channel at about the same time when injection started for sample S2B. It shows AE activity as a function of experimental time. AEs due to breakdown and pump shutin are indistinguishable suggesting that fracture closure occurred right after breakdown.

Sample S3

S3 has porosity of 12.2% and permeability of 0.293mD with mineralogy comprising of quartz, carbonates, and mixed clays. It has an average grain size of approximately 63 µm (**Figure 40**). Two (2) triaxial fracturing tests were conducted. One test was done with water injection and the other with CO_2 injection.

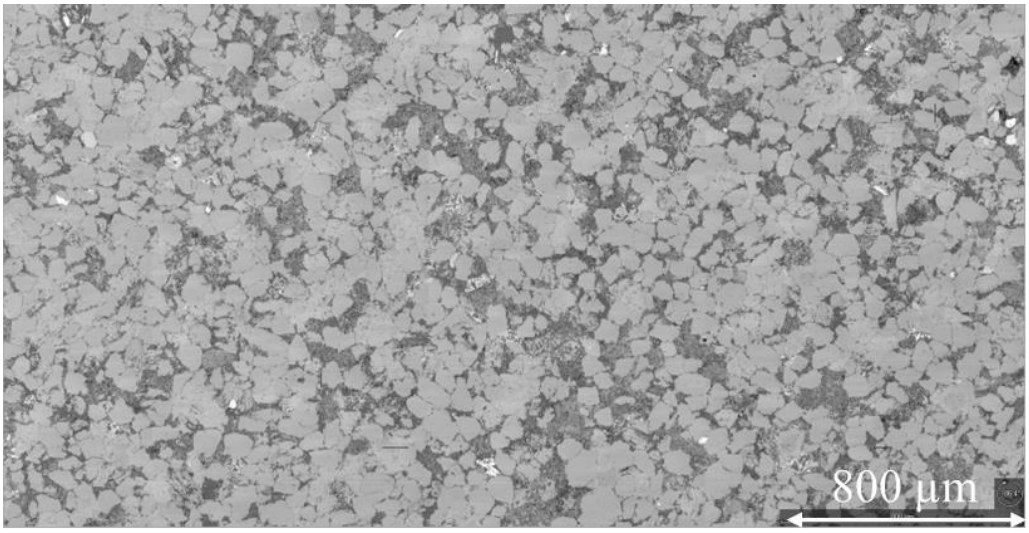

Figure 40. SEM image of S3. It has an average grain size of about 63 µm. Visual observation indicates a poorly sorted grain deposition.

a) Sample S3A

Figure 41 shows injection pressure and cumulative AE events as a function of time for a test carried out with water as the injectate. Injection pressure rose rapidly at 165 psi/s until a breakdown pressure of 1982 psi was reached. In total, 1365 AEs were recorded with most occurring at rock breakdown. The AE release rate at breakdown till it began to stabilize was ~41 AEs/s.

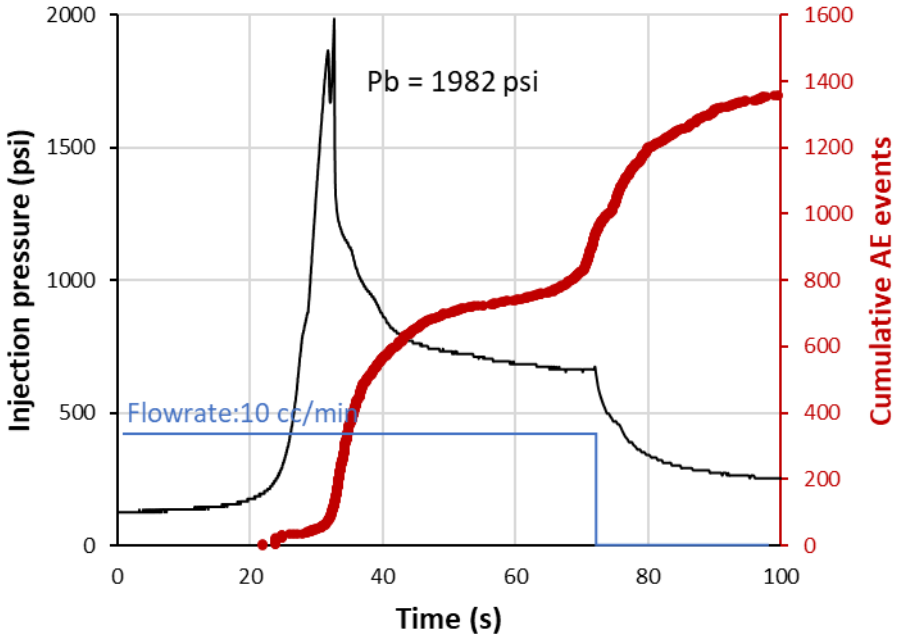

Figure 41. Injection pressure (black line) and cumulative AE events (red dots) versus time for sample S3A. The blue line shows constant flow rate of 10 cc/min until pump shut-in where it drops to zero.

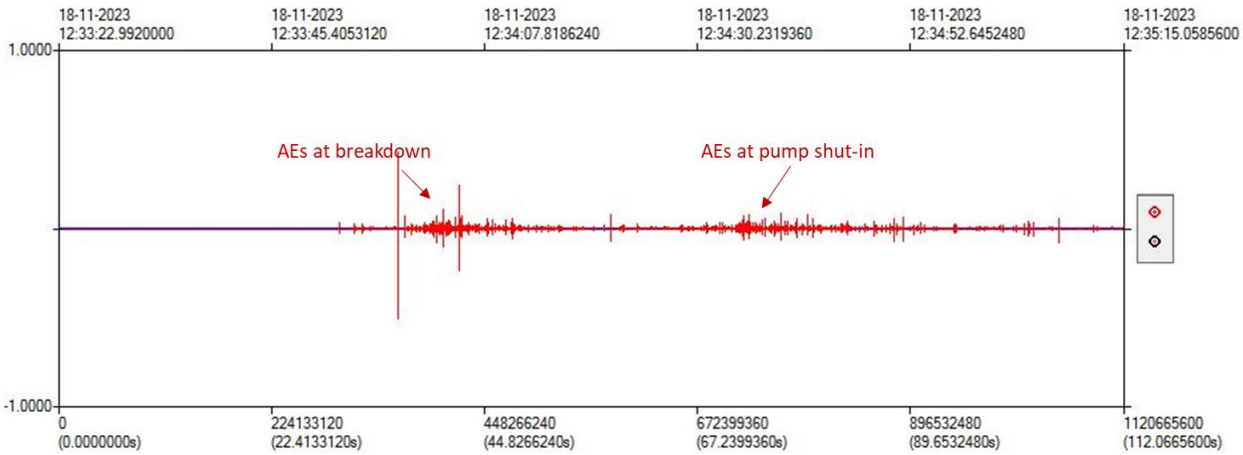

Figure 42. Full waveform of amplitude vs time recorded from one channel at about the same time when injection started for sample S3A. It shows AE activity as a function of experimental time. AEs due to breakdown and pump shutin are indistinguishable suggesting that fracture closure occurred right after breakdown.

b) Sample S3B

Figure 43 shows injection pressure and cumulative AEs as a function of time for a test carried out using CO_2 as injectate. Pumping of CO_2 was initiated at ~1220 psi. The pressure increased slowly at 8.4 psi/s until a breakdown pressure of 1338 psi was reached. In total, 6211 AEs were recorded with most occurring at rock breakdown. The AE release rate at breakdown till it began to stabilize was ~202 AEs/s.

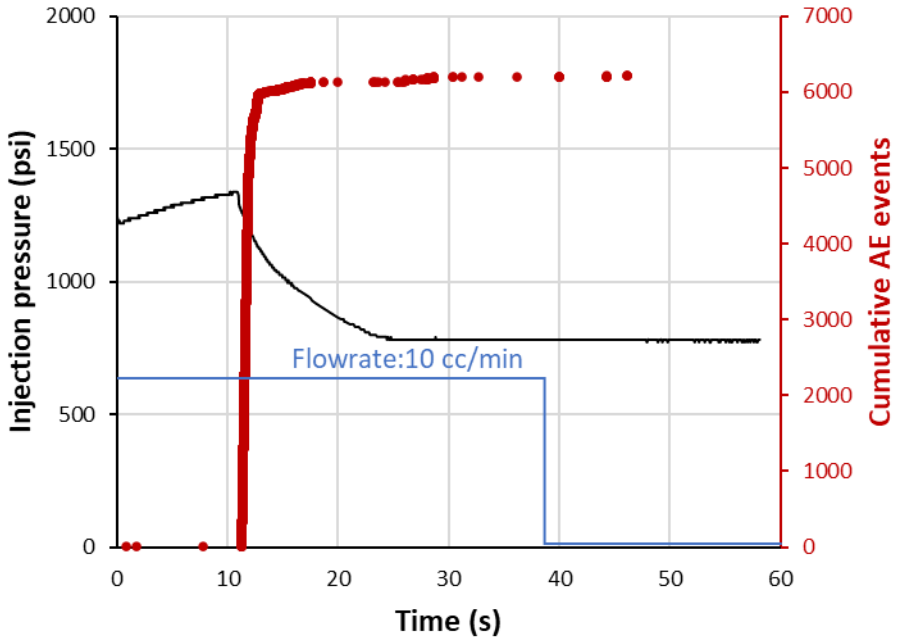

Figure 43. Injection pressure (black line) and cumulative AE events (red dots) versus time for sample S3B. The blue line shows constant flow rate of 10 cc/min until pump shut-in where it drops to zero.

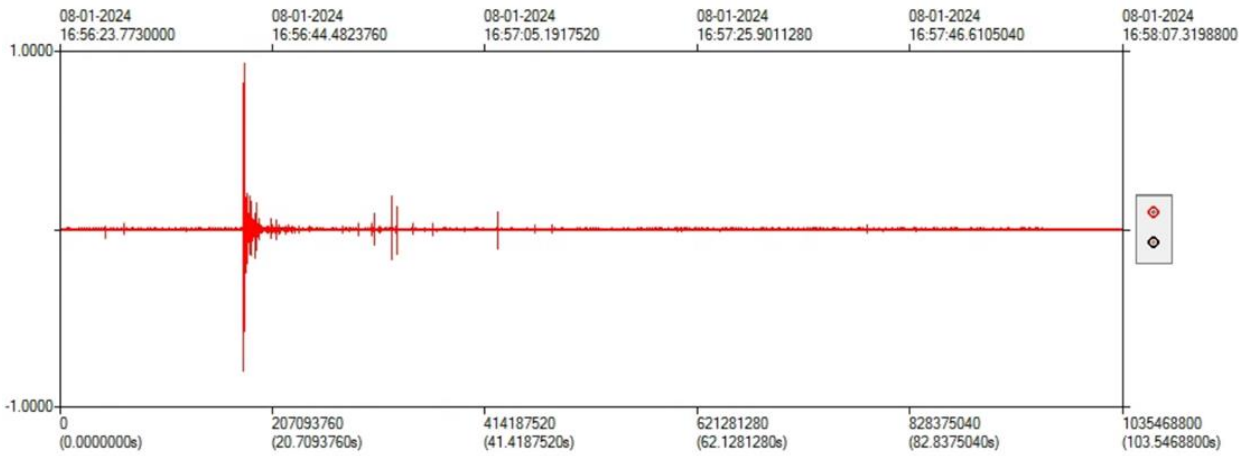

Figure 44. Full waveform of amplitude vs time recorded from one channel at about the same time when injection started for sample S3B. It shows AE activity as a function of experimental time. AEs due to breakdown and pump shutin are indistinguishable suggesting that fracture closure occurred right after breakdown.

Table 9 shows the summary of breakdown pressure and cumulative AE events for all tests. Generally, the breakdown pressure in the tests with CO_2 was less than with water in all sandstones. On average P_b recorded in S1 reduced by ~400 psi (~18%) with CO_2 injection as compared to water injection. In S2 and S3, P_b reduced by 8% and 32% with CO_2 injection (**Figure 45**). Similar observations of reduced P_b with CO_2 injection have been made in several studies (Ishida et al. 2012; Kizaki et al. 2013; Zhang et al. 2017, Amoah et al. 2023). In S1, P_b was similar for samples fractured with CO_2 regardless of whether it was exposed to CO_2. Increasing the length of exposure from 6 to 8 weeks did not change the rocks breakdown pressure. Considering that S1 has negligible amount of carbonate, it would be expected that its reaction with CO_2 would be insignificant to cause dissolution or precipitation and thus alteration of mechanical properties would be unlikely.

A possible explanation for reduced P_b can be attributed to the properties of CO_2. It has very low viscosity, low surface tension and high percolation effect (Fenghour et al. 1998; Heidaryana et al. 2011; Zhou and Burbey. 2014). Data was obtained from the National Institute of Standards and Technology (NIST) to estimate the properties of water and CO_2 at a temperature of 68^{o}F and pressure range of 500 – 2500 psi. The viscosity of CO_2 is at least one order of magnitude lower than that of water (**Table 10**). Owing to these properties, CO_2 effectively penetrates through interconnected pores to increase the pore pressure which consequently reduces the breakdown pressure of the rock. However, water has a higher viscosity and therefore it is relatively ineffective to penetrate into pores.

Table 9. Summary of experimental results

Sandstone	Sample ID	Saturation state	Injectate	Breakdown pressure	Cumulative AE events
S1	A	Brine	Water	2158	3256
	B	Brine	Water	2246	2788

	C	Brine	Water	2334	2184
	D	Brine	CO_2	1846	13594
	E	Brine	CO_2	1816	7196
	F	Brine	CO_2	1884	5684
	G	Brine+CO_2 (6 weeks exposure	CO_2	1856	20052
	H	Brine+CO_2 (8 weeks exposure)	CO_2	1876	26581
S2	A	Brine	Water	2266	3648
	B	Brine	CO_2	2080	21618
S3	A	Brine	Water	1982	1365
	B	Brine	CO_2	1338	6211

Table 10. Properties of water and CO_2 at 68°F and 500 – 2500 psi. Data was obtained from NIST.

Fluid	Compressibility (psi^{-1})	Internal energy (kJ/mol)	Viscosity (cP)
Water	$3.0 – 3.1 \times 10^{-6}$	1.49 – 1.50	0.9976 – 1.0006
CO_2	$9.9 \times 10^{-5} – 4.4 \times 10^{-3}$	10.36 – 18.42	0.0156 – 0.0914

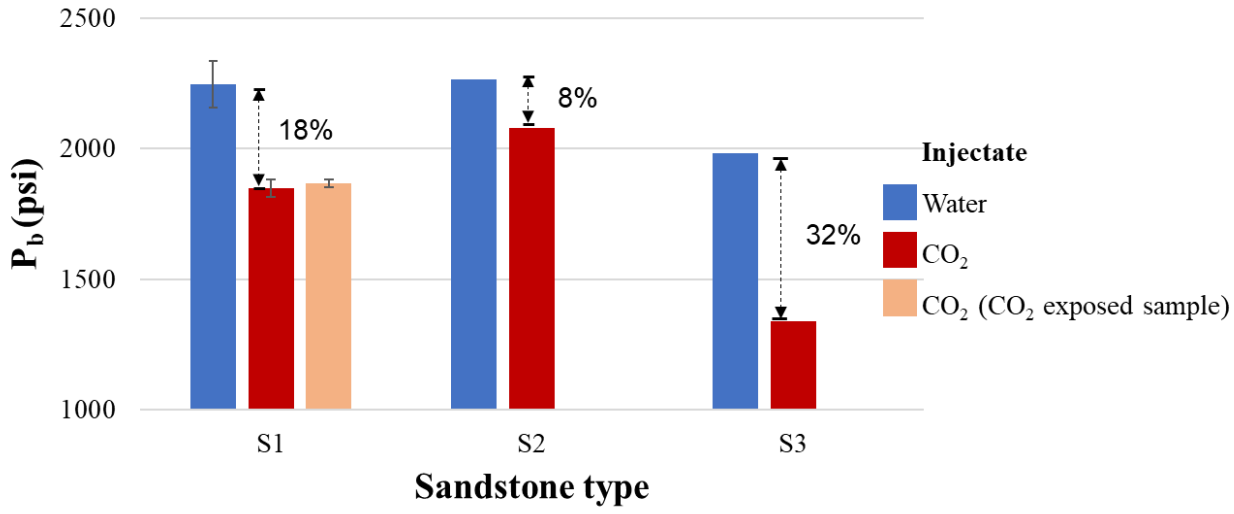

Figure 45. P_b for sandstones used in this study.

Considering the differences in breakdown pressure for S1, S2 and S3, it's clear that each sandstone responds to fluid injection differently due to the differences in rock properties. To investigate the dependence of breakdown pressure on rock properties, we plotted the breakdown pressure of the three samples as a function of shear modulus and Young's modulus. The breakdown pressure is positively and linearly correlated with shear modulus and Young's modulus. The difference in breakdown pressure between water and CO_2 is negatively correlated with both shear and Young's modulus.

A comparison of the total number of acoustic emission events reveals that on average, the number of AE events from the CO_2 tests are 3-6 times more which suggests more cracking activities (**Figure 46**). This increase in the number of AEs can be attributed to the compressibility and internal energy of CO_2 (**Table 10**). When a crack is initiated at the wellbore, a void is created which leads to the sudden expansion of liquid (compressed) CO_2 to gaseous state. The phase change provides expansion work to the crack which facilitates fracture propagation and intense cracking. Span and Wagner (1996) reports ~40 kJ/Kg of released energy when CO_2 pressure dropped from 1160–870 psi at 87.8^{o}F. Thus, CO_2 volume expansion may be converted to large fracture kinetic energy to create extended and multiple fractures which will correspond with greater number AE events. On the contrary, the incompressible nature of water makes it undergo infinitesimal expansion when a void is created after fracture initiation. Therefore, there's negligible expansion work to further crack extension which can explain the fewer number of AE events.

We observe from **Figure 46** that the number of AE events in samples exposed to CO_2 is higher than those without exposure although their breakdown pressures are similar. After CO_2 exposure for 6 weeks, the sample had similar permeability as in the native state (**Figure 92**). This

may indicate no geochemical alterations (precipitation or dissolution of minerals). The likely reason for the increased AE events may be due to the exposed samples achieving higher % saturation as they were subjected to vacuum imbibition before pressure saturation. Higher saturation can provide a greater back pressure which can reduce the time for pressure buildup till breakdown, and consequently increase CO_2 compression in borehole which will yield more energy when decompressed.

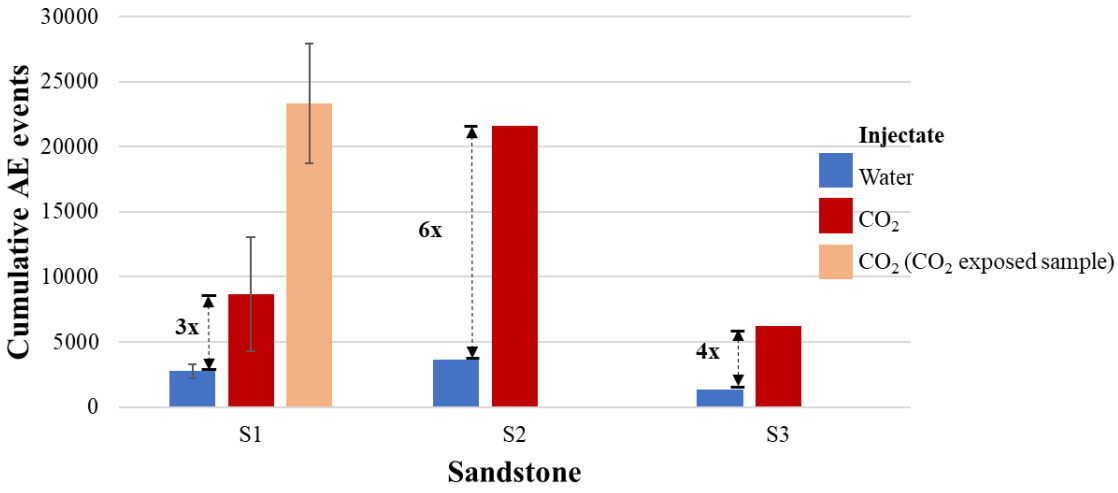

Figure 46. Cumulative AE events for sandstones used for experimentation

4.2 AE event location and fracture dimension

a) AE location algorithm

The AE events obtained from the trigger acquisition system were used for the estimation of hypocenter location. Individual arrival times of signals from 16 sensors were picked automatically using algorithm developed by Ortiz (2010). Using at least 6 arrival times and assuming a homogeneous isotropic velocity model, the Geiger inversion algorithm is used to determine the hypocenter location of each acoustic emission event. The Geiger method uses the first arrivals to determine the event origin time and source location ($x_o\ y_o\ z_o$) such that the sum of the square of the residuals is a minimum where the residual r is equal to the observed time minus the calculated time at ($x_o\ y_o\ z_o$). The algorithm iterates toward the correct location using the magnitudes of the time derivatives (change in time for small changes in $x, y, or\ z$). The Geiger method is an inverse least square problem. The source location is defined by four parameters: $\theta = (t_o, x_o, y_o, z_o)$ where h = (x_o, y_o, z_o).

The time residual r_i is the difference between the calculated arrival times, T_i, and the observed arrivals times, t_i corrected to the time zero of the event, t_o:

$$r_i = t_i - t_o - T_i \qquad 27$$

The use of 16 sensors results in a maximum of sixteen different equations to determine the location depending on the number of sensors that detect the event and has clear first arrival. This leads to an overdetermined problem and thus necessitates the use of an iterative approach to arrive at the best fit model. To simplify this problem, the function relating the arrival times and the location is linearized.

$$\theta = (\theta^* + \Delta\theta) \qquad 28$$

where θ^* is the source location estimate near the true location and $\Delta\theta$ is a small perturbation. The observed times can be approximated by using Taylor series expansion.

$$t_i = t_o{}^* + \Delta t_o + T_i(h^*) + \frac{\delta T_i}{\delta h}\Delta h \quad (29)$$

The time residuals at location h^* are given by

$$r_i(h^*) = t_i - t_o{}^* - T_i(h^*) \quad (30)$$

Combining Equations 29 and 30

$$r_i(h^*) = \Delta t_o + \frac{\delta T_i}{\delta h}\Delta h = \frac{\delta T_i}{\delta \theta}\Delta\theta \quad (31)$$

In matrix notation, the equation above can be expressed as

$$r = A.\Delta\theta \quad (32)$$

where A is a nx4 matrix of partial derivatives. The minimization of the sum of the squared time residuals can be given by

$$b = B.\Delta\theta \quad (33)$$

where $b = A^T r, and\ B = A^T A$.

The location is found by choosing a starting location, then solving the matrix problem for $\Delta\theta$ and then performing repeated iterations with an improved model vector used at each iteration. The result of hypocenter location for all the tests is shown and discussed below. In addition, the fracture dimension is discussed. The fracture on the sample boundary is delineated in two lines.

b) AE location and fracture dimension

Samples S1A, S1B andS1C

The injection fluid for S1A-S1C was water. In S1A, a total of 512 events were recorded out of which 232 (45%) events were located. **Figure 47** shows the plan and lateral views of the located AE events. The plan view shows a narrowly distributed AEs about the fracture plane which appears on the left side suggesting a one-wing fracture formation. The lateral views show an AE cloud that spreads only halfway through the map. Physical observation of the bottom view (**Figure 48**) shows a one wing fracture in the direction of maximum horizontal stress which confirms the observation in the AE maps. No fracture appears on the top and right lateral view of the sample. Moreover, the fracture appears to be thin (barely visible), simple (without multiple branching) and traverses only the lower half of the sample. We made similar observations in S1B and S1C although a bi-wing fracture was formed in those samples (Appendix C).

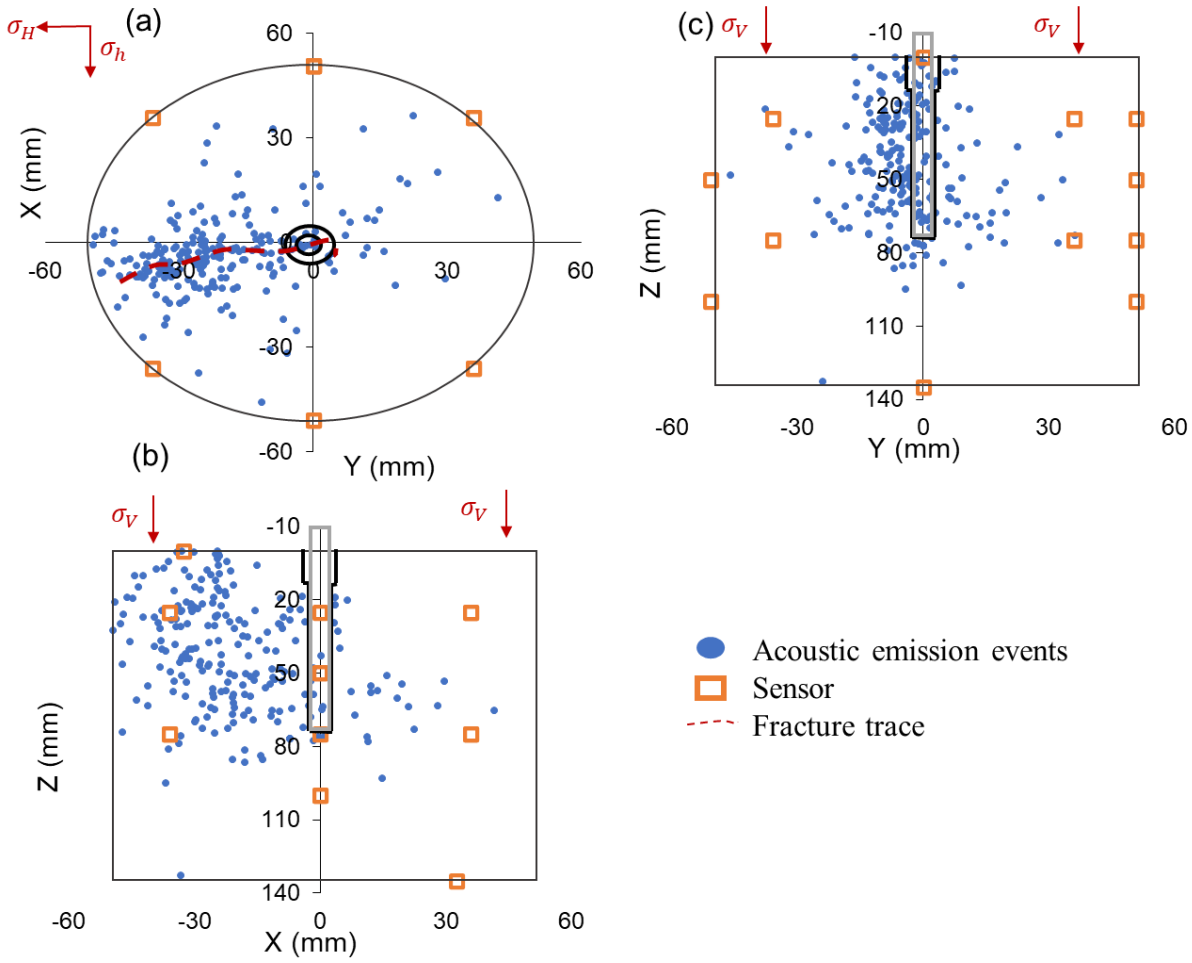

Figure 47. Plot of AEs located in sample S1A fractured with water. The located events are shown in blue, the sensors in orange and the fracture is traced in broken red line. (a) plan view of AE hypocenter showing a one wing fracture. (b) and (c) are lateral views.

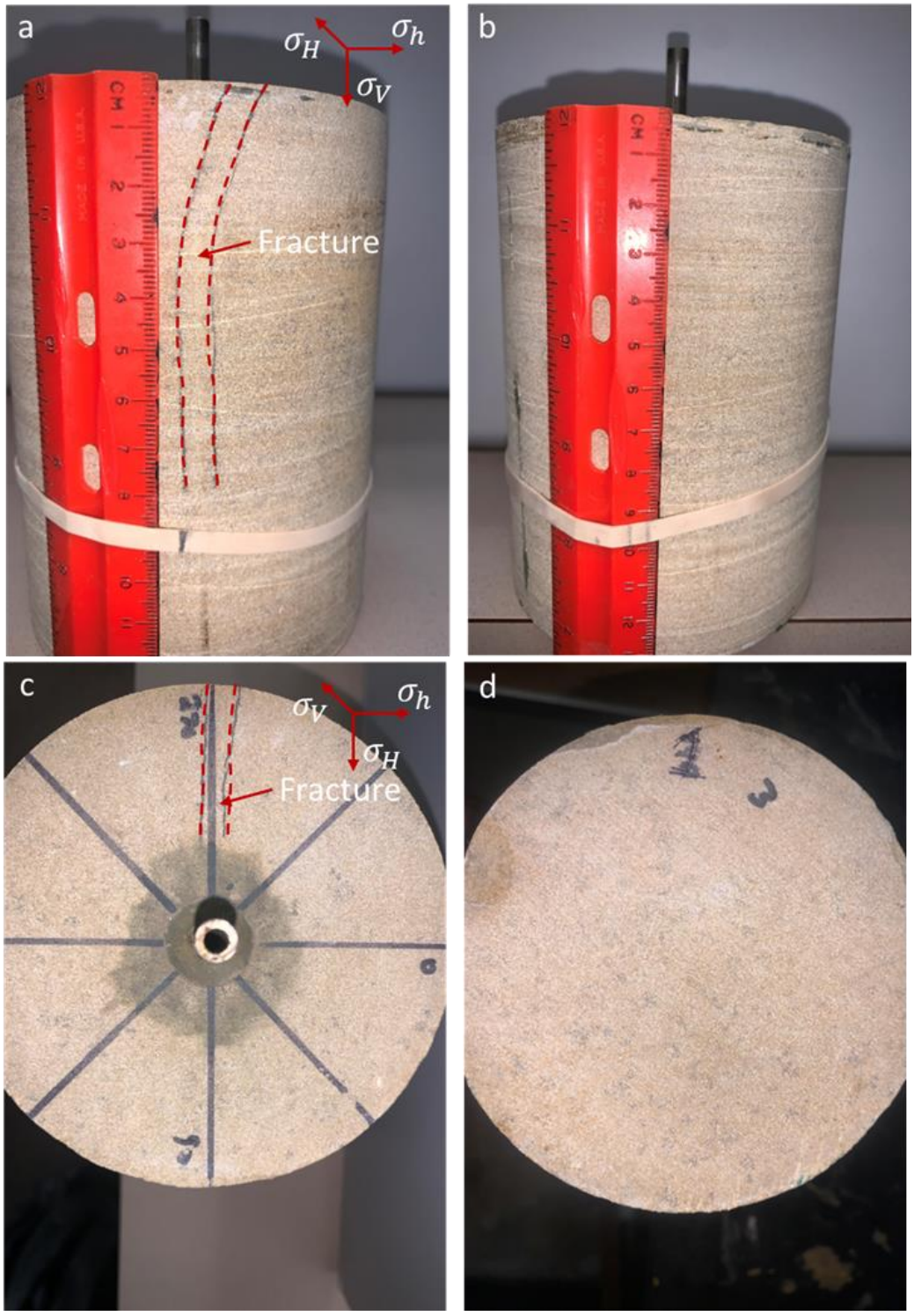

Figure 48. Physical observation of induced fractures in sample S1A fractured with water. The fracture is delineated by the broken red line. (a) and (b) show the side view. (c) and (d) show the bottom and top view.

Samples S1D, S1F, andS1F

The injection fluid for S1D-S1E was CO_2. In S1E, a total of 4650 events were generated out of which only 1048 (23%) events were located.

Figure 49 shows the plan and lateral views of the located AEs. The plan view shows a widely distributed AEs about the fracture plane which spreads from left to right suggesting a bi-wing fracture formation. The lateral views show an AE cloud throughout the length of the map. Physical observation of the bottom view (**Figure 50**) shows a fully develop bi-wing fracture in the direction of maximum horizontal stress. In addition, a fracture can be seen at the top of the sample. The fracture appears to be visible, complex, and traverses the entire length of the sample (**Figure 50**). We made similar observations in S1D and S1F (Appendix C).

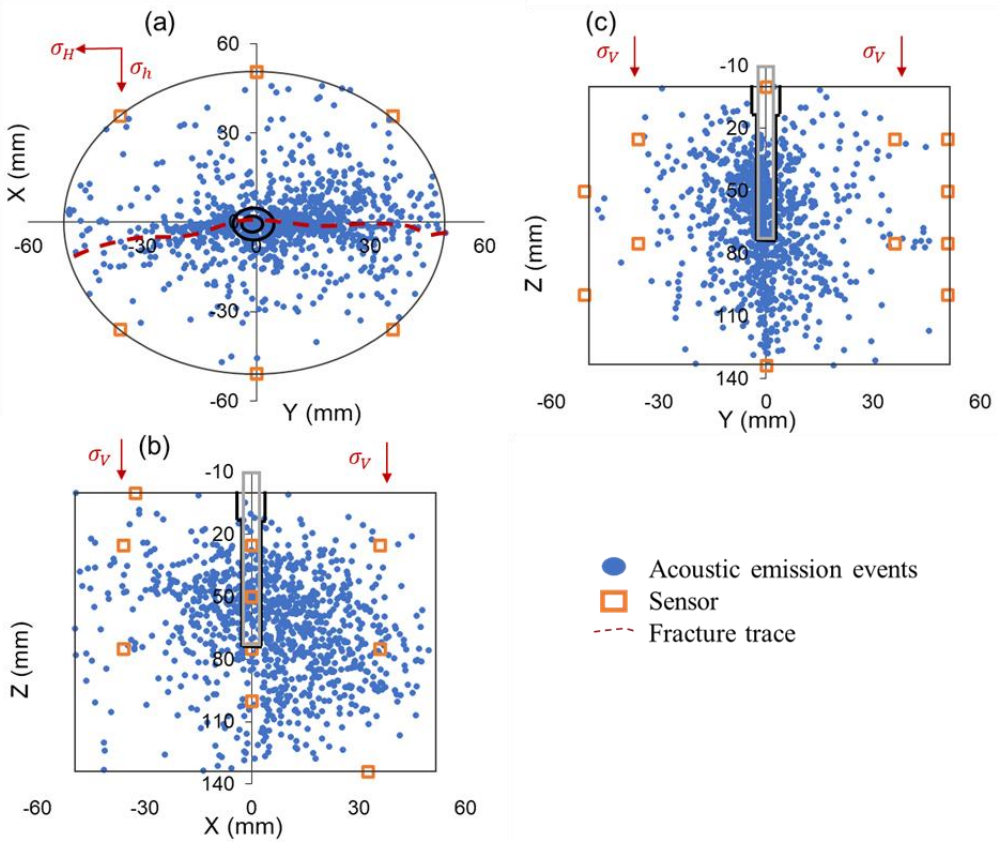

Figure 49. Plot of AEs in sample S1E fractured with water. (a) plan view of AE hypocenter showing a bi wing fracture. (b) and (c) are lateral views.

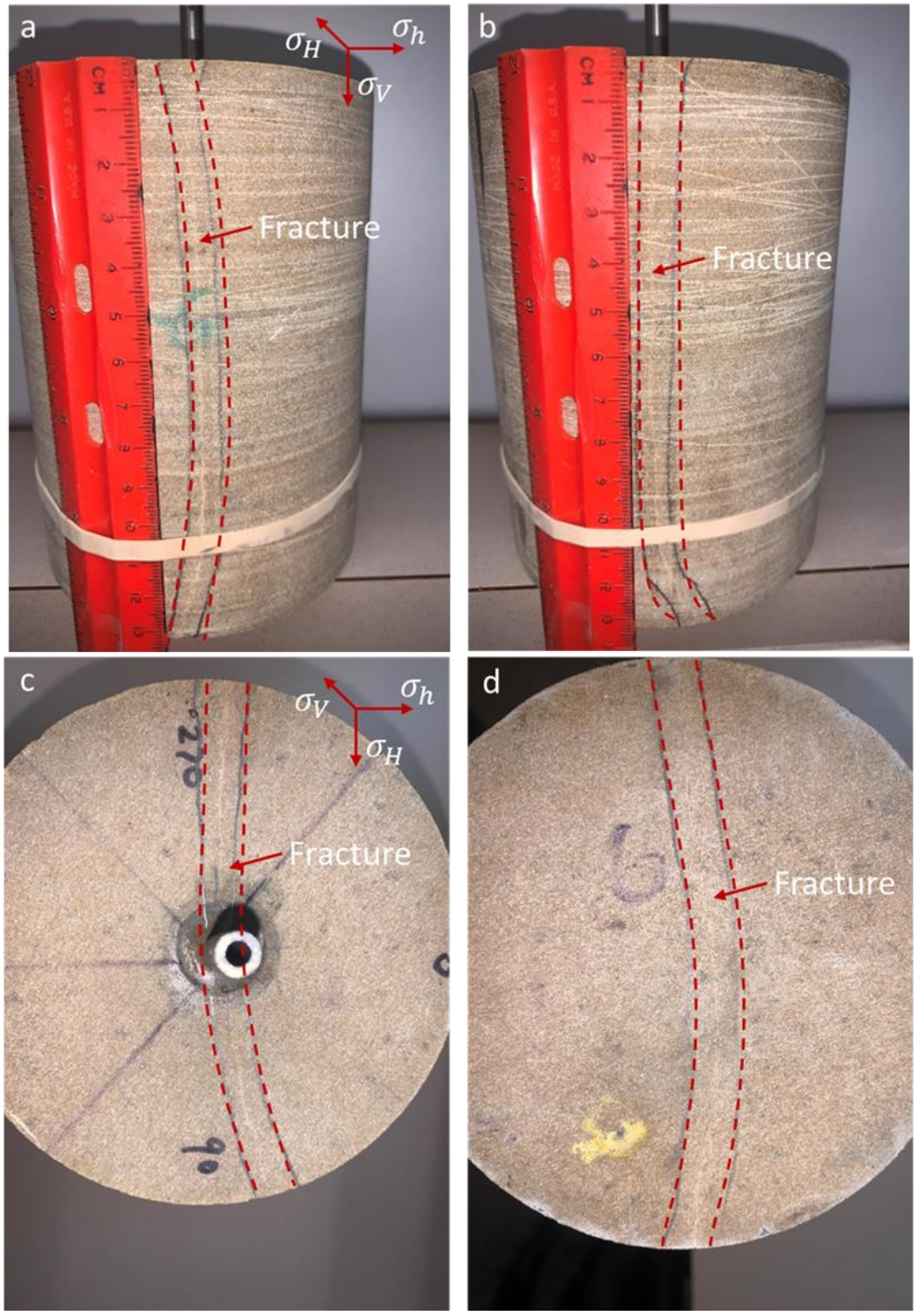

Figure 50. Physical observation of induced fractures in sample S1E fractured with CO_2. The fracture is delineated by the broken red line. (a) and (b) shows the side view. (c) and (d) shows the bottom and top view.

Samples S1G-S1H

This test was done by injecting CO_2 into a sample exposed to CO_2 for 6 and 8 weeks. In S1G, a total of 7279 events were generated out of which 1083 (15%) events were located. The AEs are distributed widely about the fracture plane and spreads from left to right of the plan view and almost throughout the length of the lateral views (**Figure 51**). Physical observation of the bottom view (**Figure 52**) shows a fully develop bi-wing fracture in the direction of maximum horizontal stress. In addition, a fracture appears on the top of the sample. The fracture appears visible, complex, and traverses the entire length of the sample (**Figure 52**). These observations are consistent with those seen in the CO_2 fracturing tests where samples were not exposed to CO_2. We made similar observations in S1H (Appendix C).

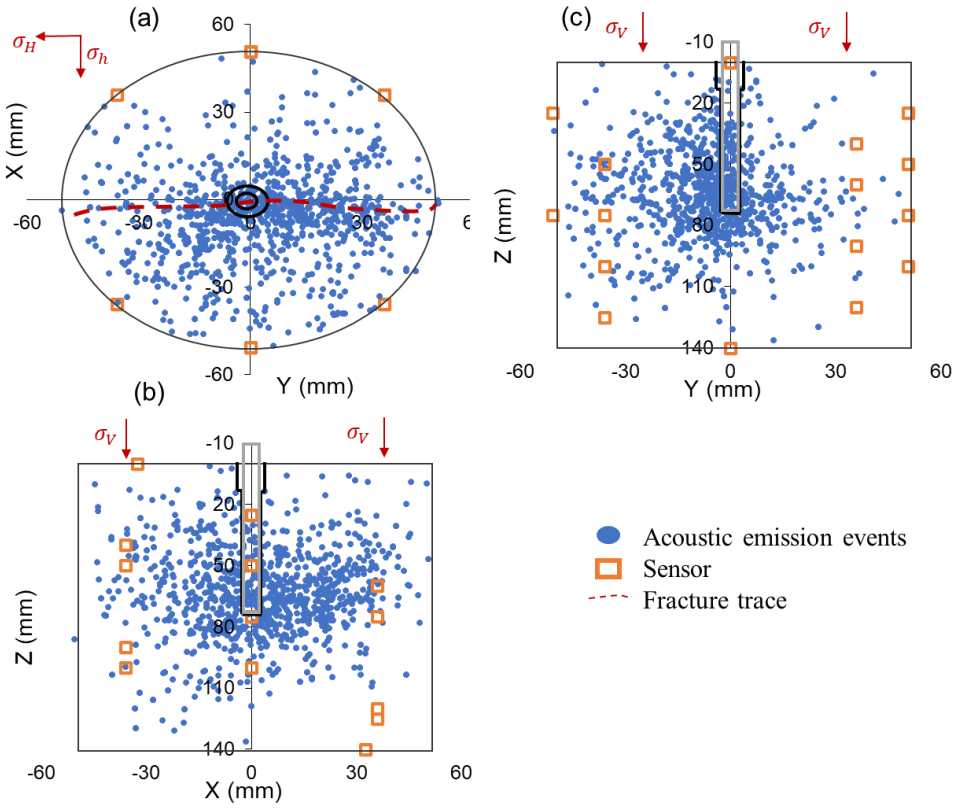

Figure 51. Plot of AEs located in sample S1G fractured with water. (a) plan view of AE hypocenter showing a bi wing fracture. (b) and (c) are lateral views.

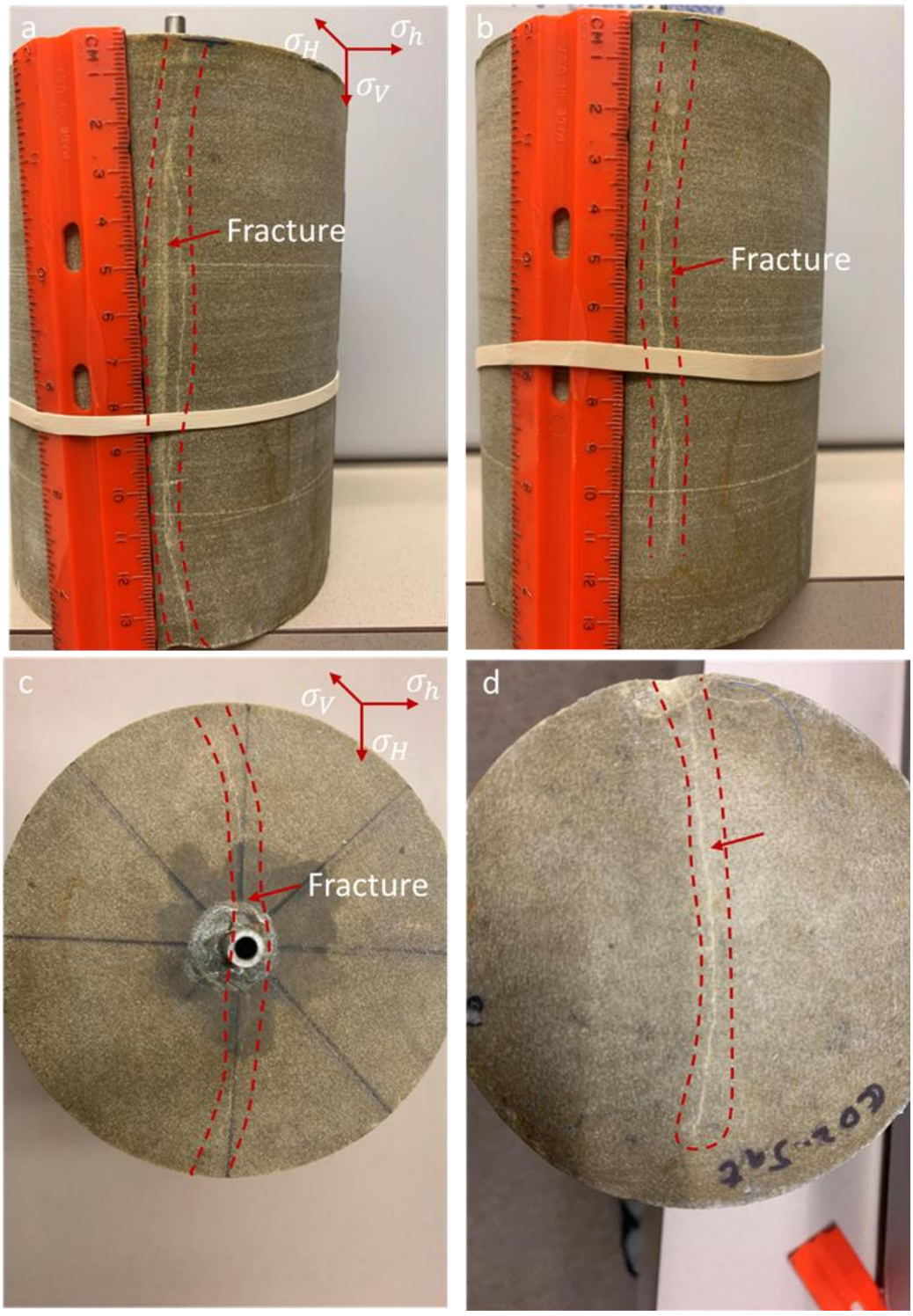

Figure 52. Physical observation of induced fractures in sample S1G fractured with CO_2. The fracture is delineated by the broken red line. (a) and (b) shows the side view of the sample. (c) and (d) shows the bottom and top view of the sample.

Sample S2A

This was a water injection test. A total of 1771 events were recorded out of which 222 (13%) events were located . **Figure 53** shows the plan and lateral views of the located AEs. The AEs are distributed narrowly about the fracture plane and spreads from left to right in the plan view suggesting a bi-wing fracture formation. In the lateral views, the cloud is seen mostly in the middle portion of the map. This may suggest that the fracture did not fully develop to the bottom and top surfaces of the sample. Physical observation of the fractured sample (**Figure 54**) shows no visible fracture signifying that the fracture did not have fully develop to the sample boundary.

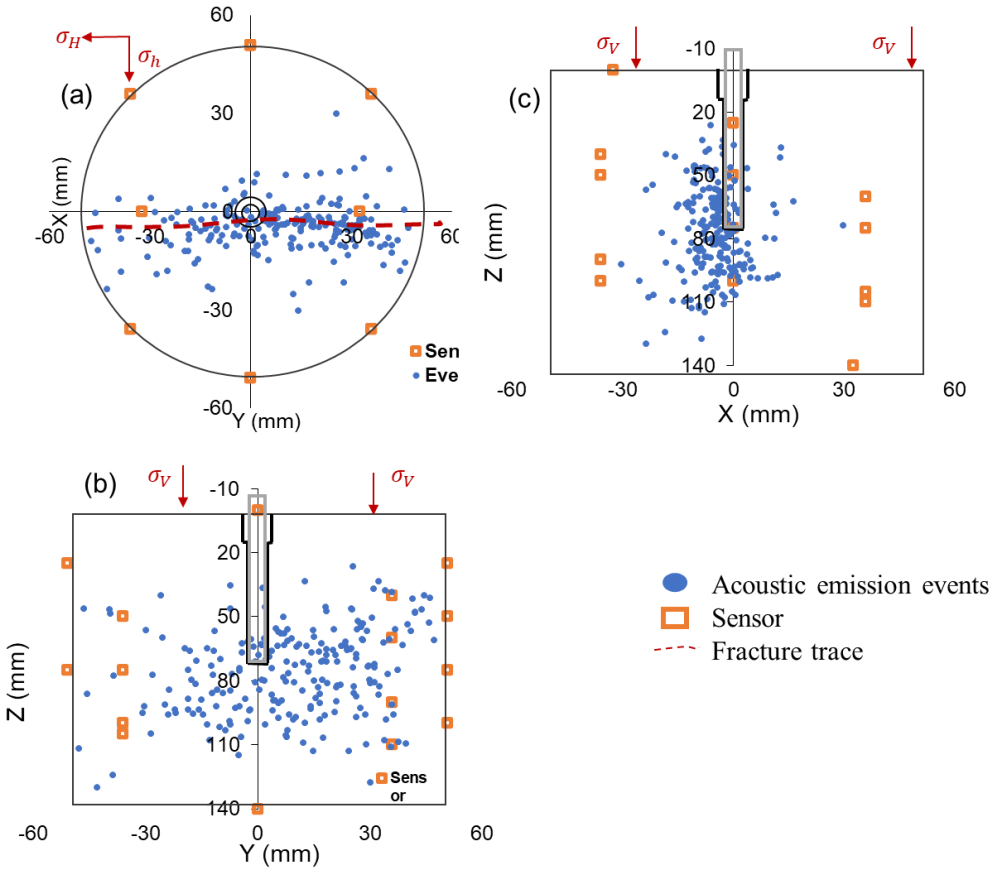

Figure 53. Plot of AEs located in sample S2A fractured with water. (a) plan view shows a bi-wing fracture. (b) and (c) are lateral views.

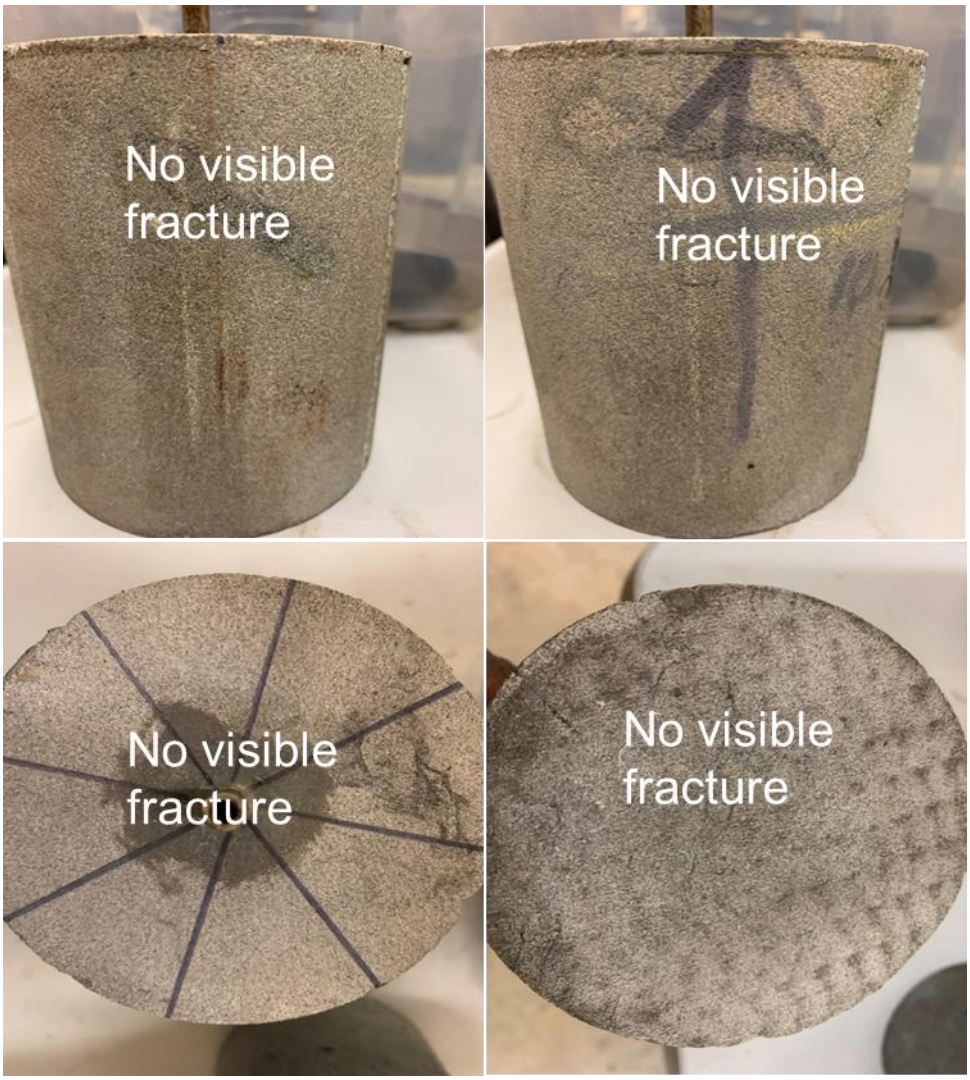

Figure 54. Physical observation of induced fractures in sample S2A fractured with CO_2. Top images show the side view. Bottom images show the bottom and top view.

Sample S2B

This test was done with CO_2 as the injectate. A total of 1573 events were recorded out of which 171(11%) events were located.

shows the plan and lateral views of the located AEs. The AE cloud is scattered such that fracture direction cannot be inferred although a bi-wing fracture was formed. Physical observation of the fractured sample (**Figure 56**) shows a fully develop bi-wing fracture. The fracture appears visible, complex, tortuous and traverses the entire length of the sample.

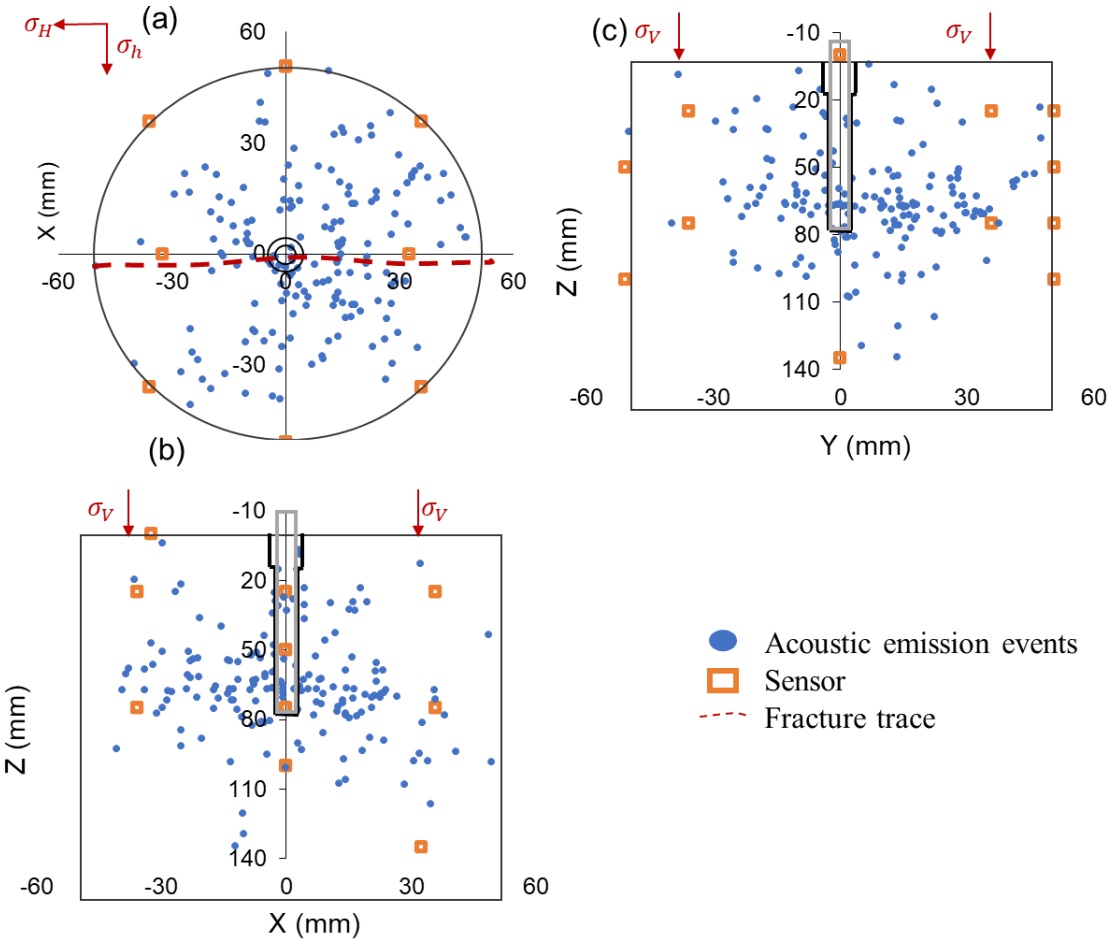

Figure 55. Plot of AEs located in sample S2B fractured with CO_2. (a) plan view. (b) and (c) are lateral views.

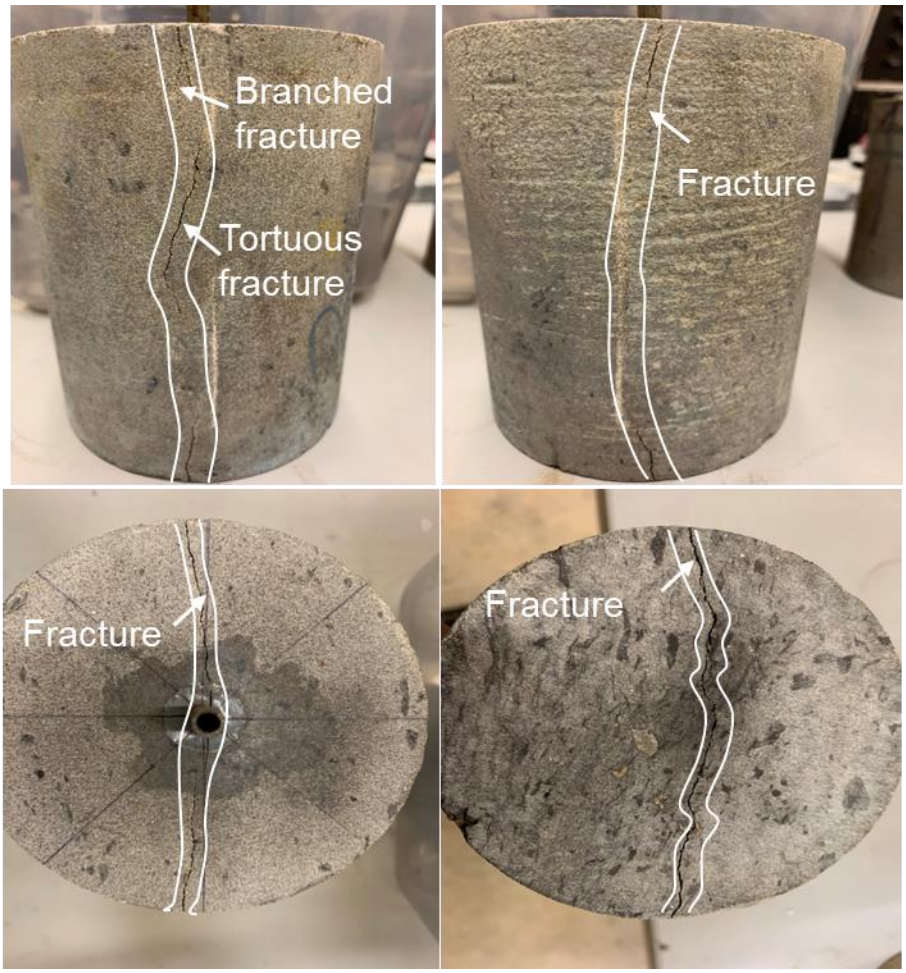

Figure 56. Physical observation of induced fractures in sample S2B fractured with CO_2. Top images show the side view. Bottom images show the bottom and top view.

Sample S3A

This test was done with water as an injectate. A total of 3424 events were recorded out of which 1172 (34%) events were located. **Figure 57** shows the plan and lateral views of the located AEs. The AE cloud suggests a one-wing fracture formation in this sample. Physical observation of the fractured sample (**Figure 58**) shows a poorly developed one-wing fracture.

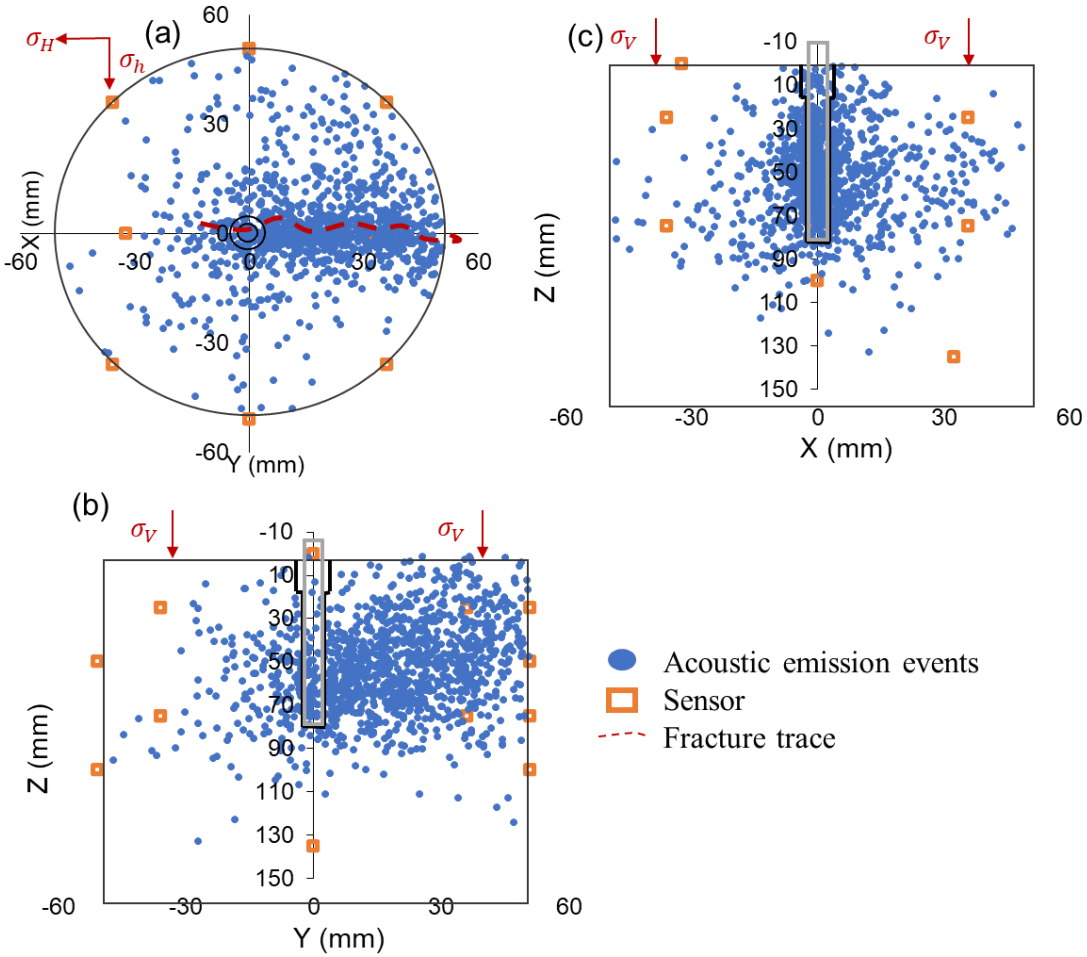

Figure 57. Plot of AEs located in sample S3A fractured with CO_2. (a) plan view. (b) and (c) are lateral views.

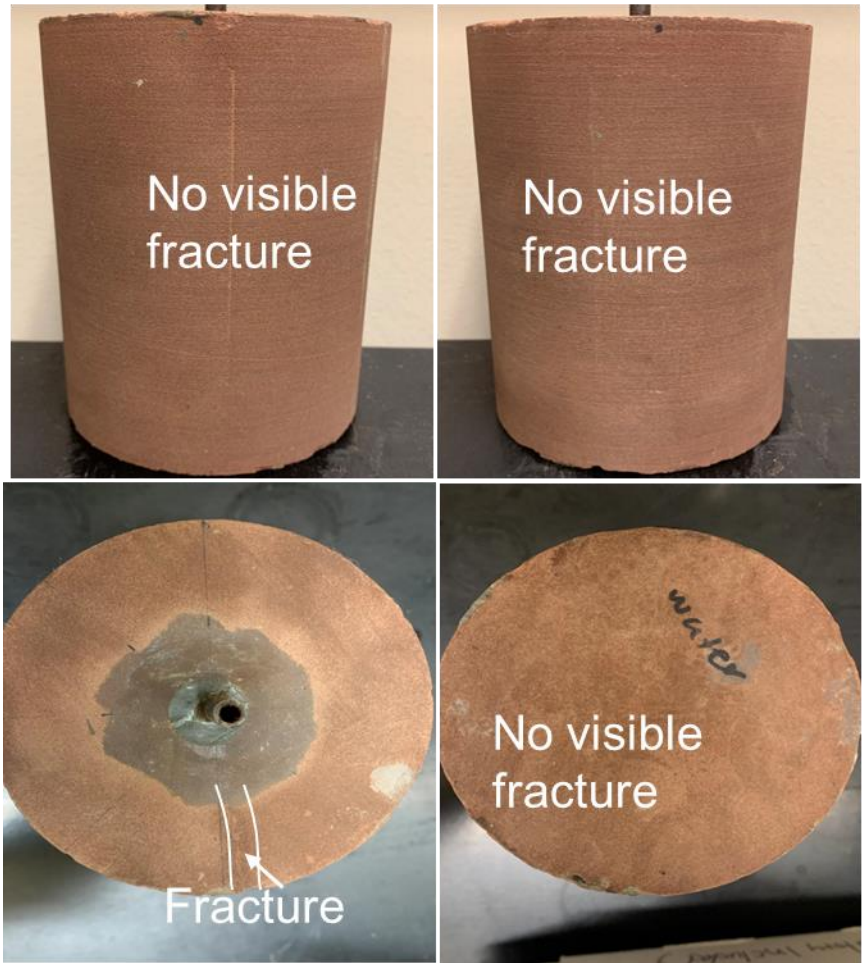

Figure 58. Physical observation of induced fractures in sample S2B fractured with CO_2. Top images show the side view. Bottom images show the bottom and top view.

Sample S3B

This test was done with CO_2 as an injectate. A total of 3067 events were recorded out of which 161 (5%) events were located . **Figure 59** shows the plan and lateral views of the located AEs. The AE cloud is scattered such that fracture direction cannot be inferred although a bi-wing fracture was formed (**Figure 60**). Physical observation of the fractured sample (**Figure 60**) shows a fully develop bi-wing fracture. The fracture appears visible, curved, and traverses the entire length of the sample.

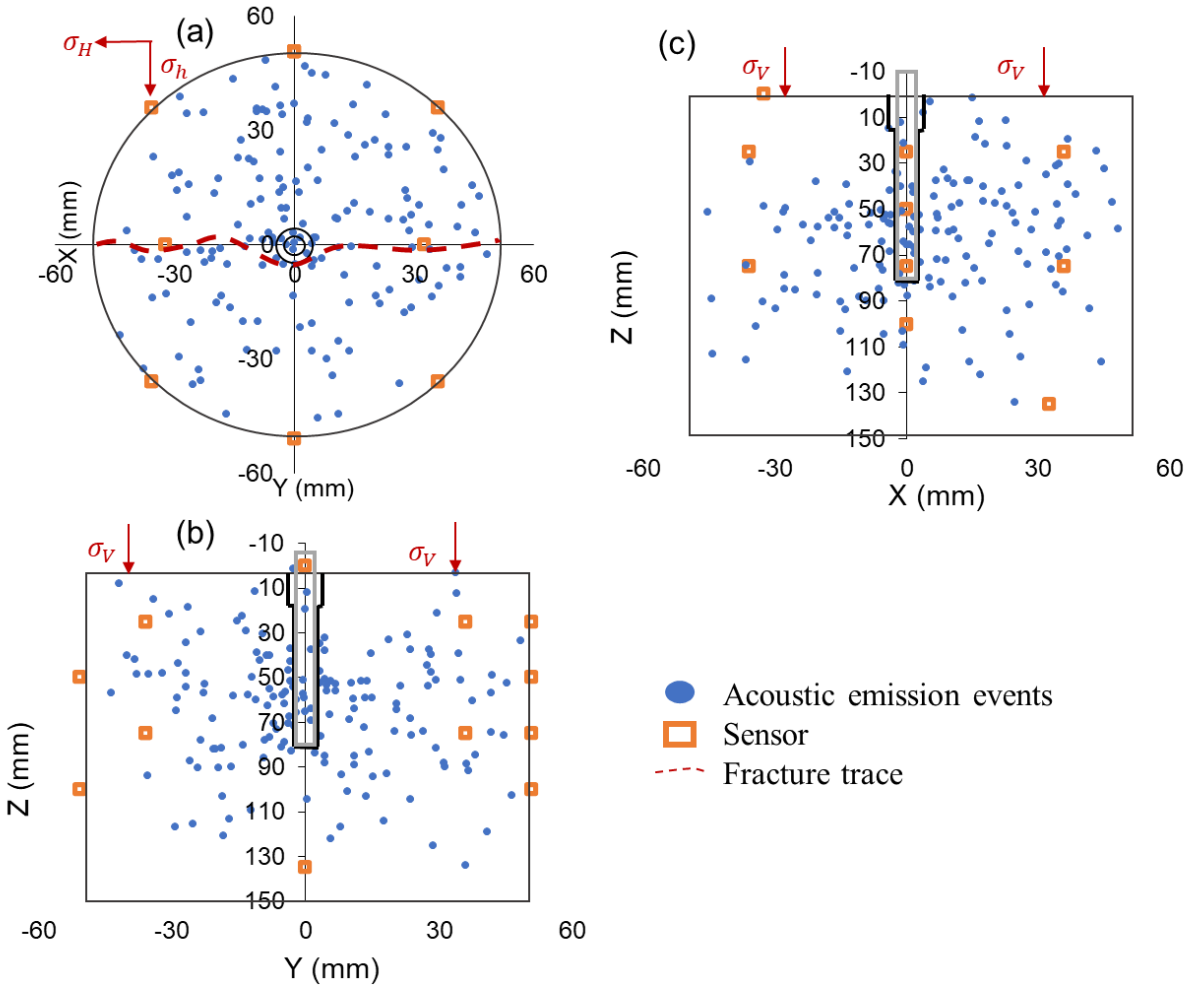

Figure 59. Plot of AEs located in sample S3B fractured with CO_2. (a) plan view. (b) and (c) are lateral views.

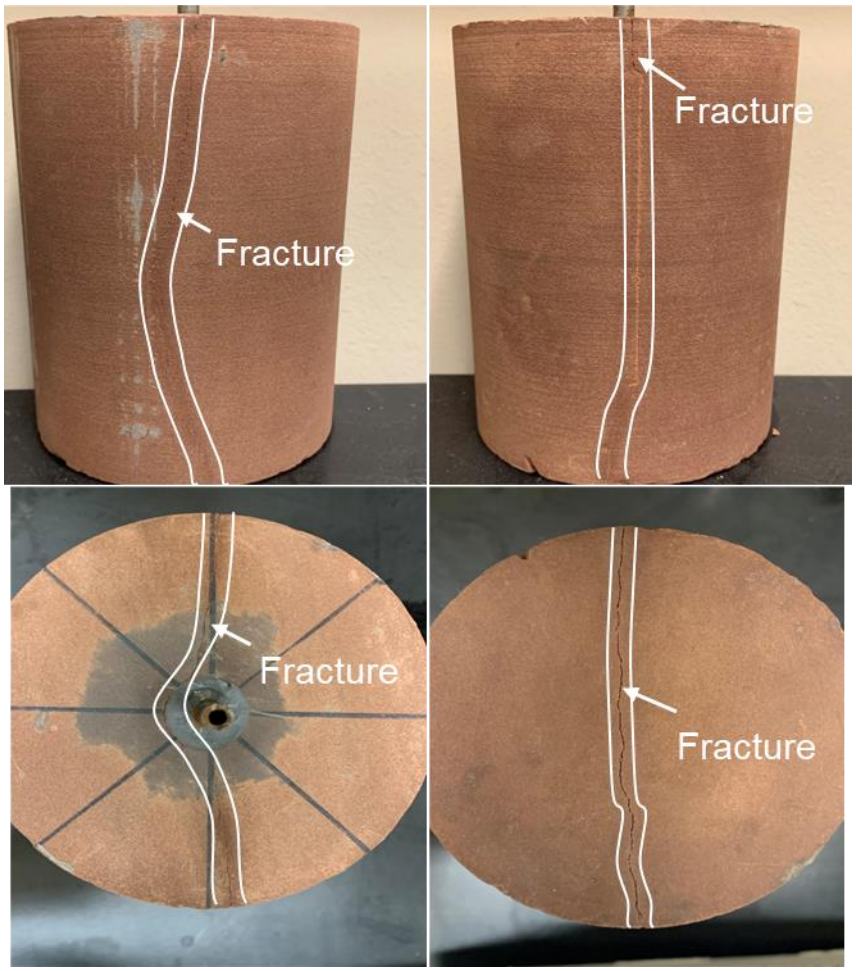

Figure 60. Physical observation of induced fractures in sample S3B fractured with CO_2. Top images show the side view. Bottom images show the bottom and top view.

Generally, we observe a wider spread of AEs and a lower percentage of located events (**Table 11**) in the tests involving CO_2 injection than water injection. This observation may be as a result of the combined effect of higher crack intensity and the complex velocity field within the rock fractured with CO_2. At fracture initiation, compressed (liquid) CO_2 changes phase, resulting in the mixture of liquid and gaseous CO_2, as well as brine in sample. This mixture of fluids complicates the velocity field within the sample, but we assume a uniform and isotropic velocity structure based on measurements from a sample fully saturated with brine. Consequently, the locations of AEs in CO_2-fractured samples could appear more scattered. Moreover, the considerable microcracking activity due to the energy release from decompressed CO_2 could also

contribute to the broader distribution of located AEs. In contrast, samples fractured with water contain only a single fluid, simplifying the velocity patterns and allowing for more precise AE location estimations.

Table 11. Summary of results for AE events location

Sandstone	Sample ID	Saturation state	Cumulative AE events	Number of located events	% of located events
S1	A	Brine	512	232	45
	B	Brine	864	415	48
	C	Brine	1283	684	53
	D	Brine	3176	493	16
	E	Brine	4650	1048	23
	F	Brine	5286	955	18
	G	Brine+CO_2 (6 weeks exposure	7279	1083	15
	H	Brine+CO_2 (8 weeks exposure)	5447	523	10
S2	A	Brine	1771	222	13
	B	Brine	1573	171	11
S3	A	Brine	3424	1172	34
	B	Brine	3067	161	5

4.3 Focal mechanism solution

The radiation pattern of an acoustic wave depends on the fault geometry in an isotropic medium. One of the simplest methods used to study the geometry of a fault known as focal mechanism relies on the first motion (polarity) of acoustic events (Stein and Wysession, 2003). The fundamental idea is that the polarity of AEs for each event varies among acoustic sensors at different directions from the faulting. We classified events as tensile, compressive or shear based on the proportion of positive or negative clear arrivals (polarities). Events which do not meet any of the classification have been named by some authors (Damani, (2013), Chitrala (2011), Falls et al. (1992)) as complex but in this work, they were discarded. The tensile mechanism originates from the separation of surfaces, while compressive mechanisms can arise from pore collapse or fracture closure. Shear mechanisms occur with slippage along a plane of weakness. Most microseismic activity is attributed to shear failure but there is a component of tensile and compressive failure introduced by overriding and failure of asperities along the fracture (Warpinski, 2010).

Prior to the classification, a pensile lead break test was performed on the sensors to check their polarity. We followed the classification technique that an event should be located and should have at least 7 out of 16 clear arrivals to be considered for the focal mechanism solution. If more than 80% of the arrivals for an event are negative, it is called a compressive event and if positive, it is called a tensile event (**Figure 61**). Those that do not qualify to be compressive or tensile are classified as shear events. In this evaluation, it is assumed that the waveforms are recorded under far field condition (source to sensor distance > 10λ) (Aki and Richards, 2002). However, the far field condition is not met in our experiments since the average wavelength (λ) of the acoustic waveforms is 18 mm while the source to sensor distance is only 2λ - 4λ. Due to this limitation, the

focal mechanism reported here are not truly far field and should be used only as a qualitative analysis tool. The focal mechanism results are discussed below.

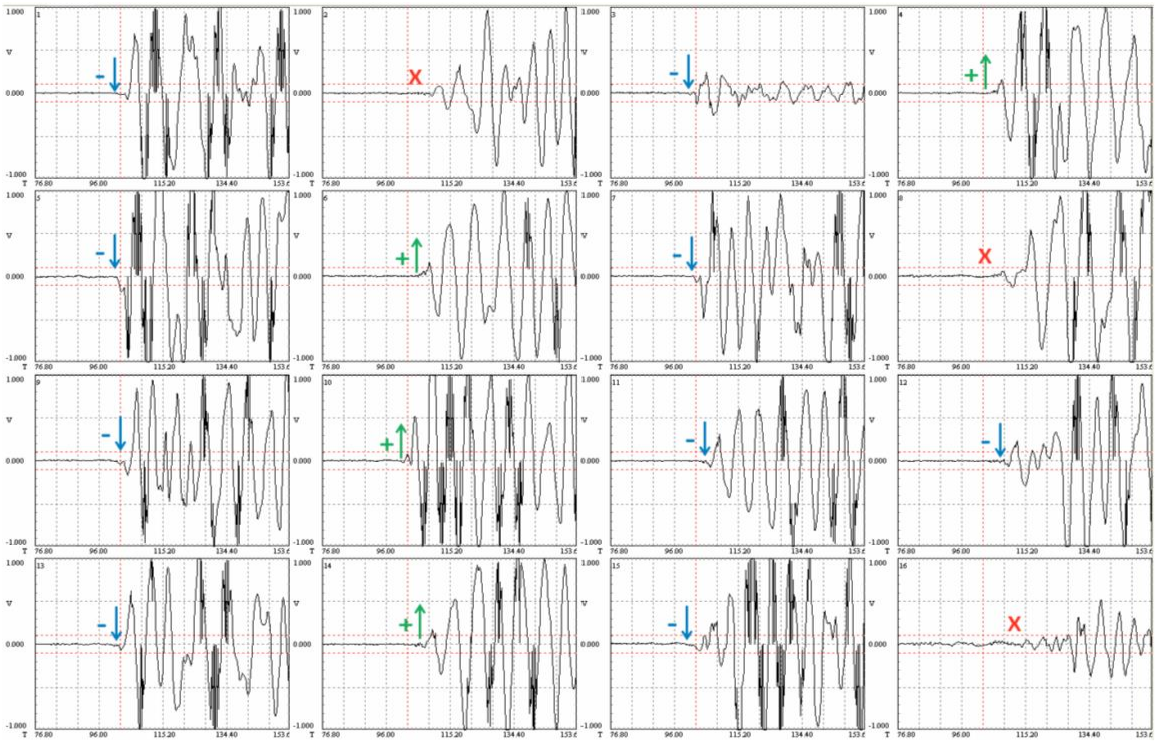

Figure 61. Waveforms of 16 sensors for an event along with marked polarities. Upward and downward arrows indicate tensile and compressive events respectively. X represents unclear polarities (after Damani 2013)

Sample S1

Table 12 shows the results. In all tests, shear events dominate having $\geq 80\%$ of total failure mechanisms. CO_2 injection-induced AEs from samples without exposure have a higher percentage of compressive events as compared to those from the water injection tests. There's negligible difference in the percentage of tensile events in both the test with water and CO_2 (**Figure 62**). Samples exposed to CO_2 have slightly higher percentage of tensile events and lower percentage of compressive events than is seen in samples without exposure (**Figure 63**).

Table 12. S1 focal mechanism results

Sandstone	Sample ID	Saturation state	Injectate	Failure mechanisms			
				Tensile	Compressive	Shear	Total
S1	A	Brine	Water	3	18	164	185
	B	Brine	Water	2	23	282	307
	C	Brine	Water	11	31	374	416
	D	Brine	CO_2	4	54	304	362
	E	Brine	CO_2	11	138	605	754
	F	Brine	CO_2	14	54	342	410
	G	Brine+CO_2	Brine+CO_2 (6 weeks exposure	15	35	361	411
	H	Brine+CO_2	Brine+CO_2 (8 weeks exposure)	23	12	338	373

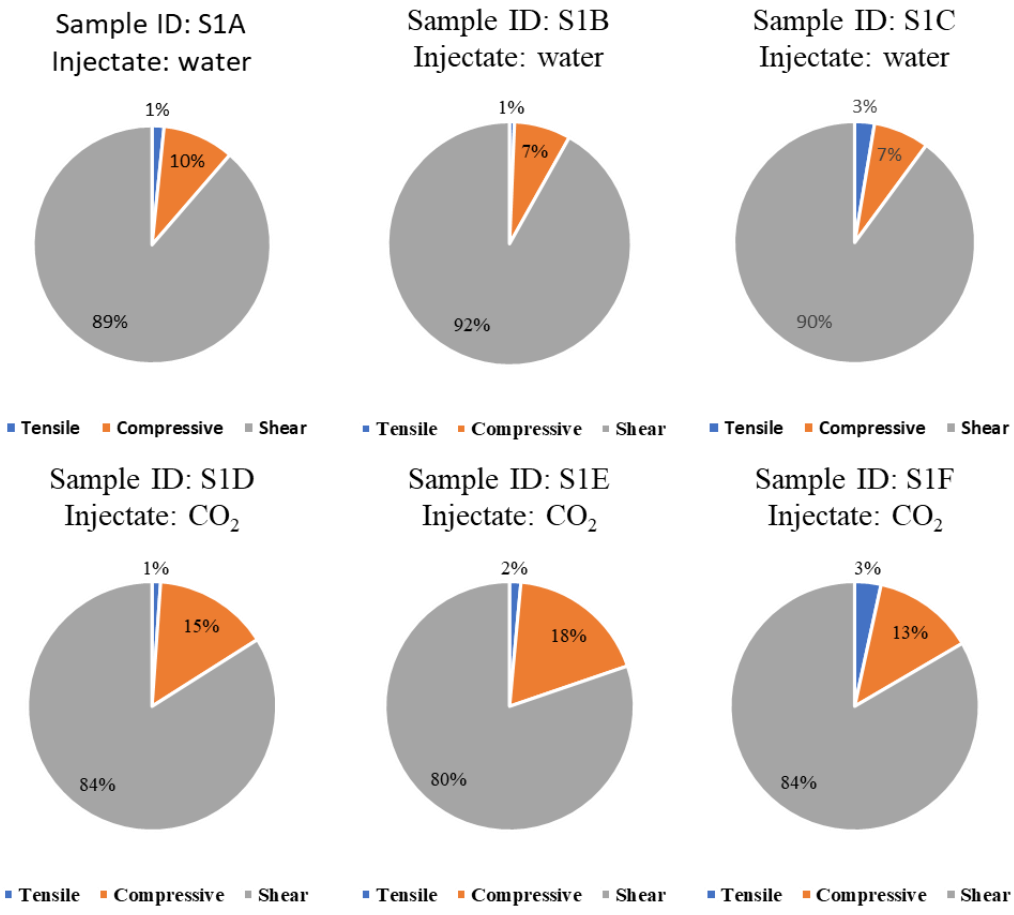

Figure 62. Classification of AE events as tensile, compresive or shear. Shear failure is dominanat. Samples are without CO_2 exposure.

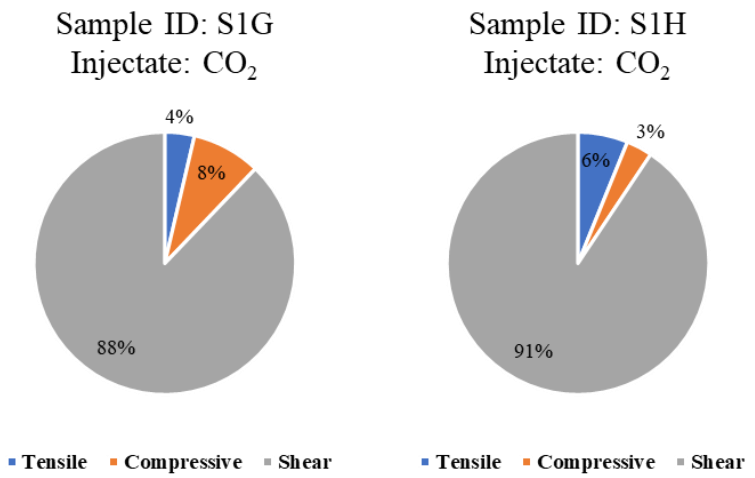

Figure 63. Classification of AE events as tensile, compresive or shear. S1G and S1H were exposed to CO_2 for 6 and 8 weeks respectively. Shear failure is dominant.

Sample S2

Table 13 shows S2 focal mechanism results. In all tests, shear events dominate having ≥ 80% of total failure mechanisms (**Figure 64**). CO_2 injection-induced AEs have a higher percentage of tensile events and no compressive events as compared to those from the water tests.

Table 13. S2 focal mechanism results

Sandstone	Sample ID	Saturation state	Injectate	Failure mechanisms			
				Tensile	Compressive	Shear	Total
S2	A	Brine	Water	13	5	146	164
	B	Brine	CO_2	8	0	57	65

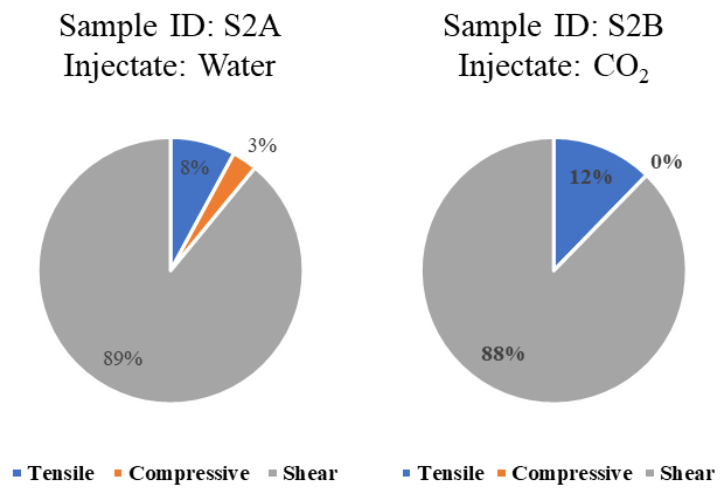

Figure 64. Classification of AE events as tensile, compresive or shear. Shear failure is dominant.

Sample S3

Table 14 shows S3 focal mechanism results. In all tests, shear events dominate having ≥ 80% of total failure mechanisms (**Figure 65**). CO_2 injection-induced AEs have a higher percentage of tensile events and compressive events as compared to those from the water tests.

Table 14. S3 focal mechanism results

Sandstone	Sample ID	Saturation state	Injectate	Failure mechanisms			
				Tensile	Compressive	Shear	Total
S3	A	Brine	Water	45	9	473	527
	B	Brine	CO_2	4	2	34	40

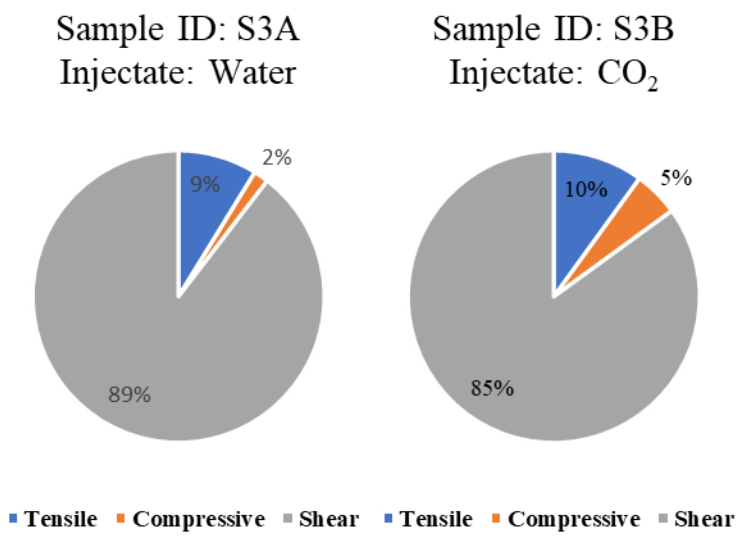

Figure 65. Classification of AE events as tensile, compresive or shear. Shear failure is dominant.

4.4 AE spectral analysis

An expanding area within microseismic monitoring involves the analysis of AE signals' spectra, with the aim of identifying their frequency contents. Ohnaka and Mogi (1981) proposed that distinct cracking mechanisms exhibit unique frequency characteristics. Spasova and Ojovan (2007) utilized the primary frequencies found in AE power spectra to classify AE sources in cementitious wasteforms containing encapsulated aluminum, attributing them to cement matrix hardening (> 2 MHz), cracking (> 100 kHz), and aluminum corrosion (< 40 kHz).

In our investigation, we determined frequency spectra of each AE event by using the Fast Fourier Transform (FFT) to convert the signal from time to frequency domain. The transformation was applied to the portion of the signal corresponding to a 40μs window after the arrival time ensuring analysis on only the P-wave portion of the signal (**Figure 66**). The AE signal has a total of 1024 data points with a time step of 0.2μs between each point. An example of AE signals and their corresponding FFT spectra is illustrated in Appendix D. The frequency spectra reveal one or

more peaks at specific frequencies. The frequency corresponding to the highest peak is referred to as the primary frequency.

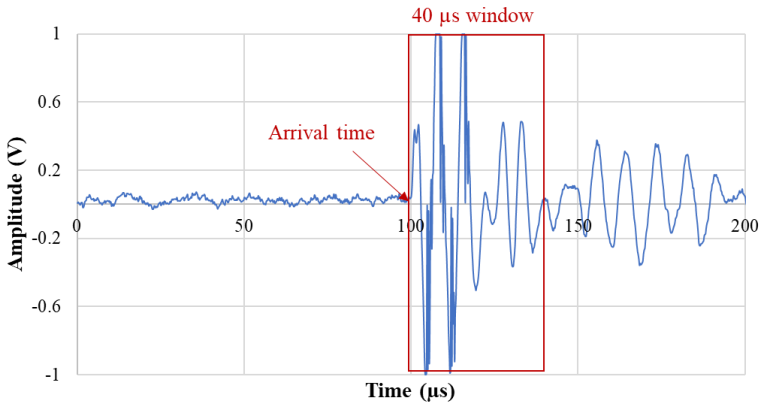

Figure 66. A waveform showing the arrival time and the 40µs window used for FFT.

Upon examination of the frequency spectra, it becomes evident that both the highest peak amplitude and the primary frequency vary depending on the sensor position. An illustrative example is provided in **Figure 67**. This fluctuation in frequency content with azimuthal orientation could stem from the presence of minute, localized regions undergoing intense microcracking or the radiation pattern of the AE source (Sondergeld and Estey, 1982). In **Figure 68,** we observe that microfracturing mechanisms exhibit overlapping primary frequencies. We also observe a weak linear decrease of peak amplitude with primary frequency. This trend is depicted in **Figure 69.**

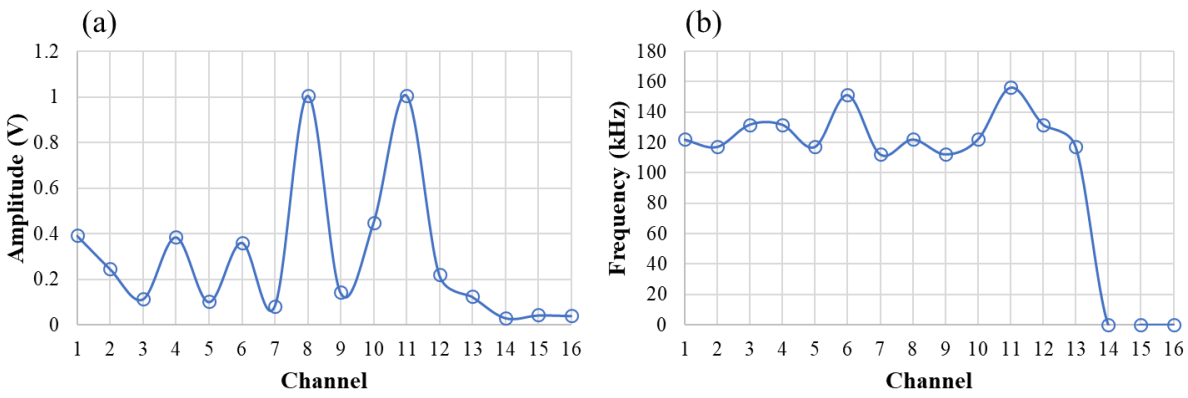

Figure 67. The amplitude varies with location of sensor and (b) the frequency content of the event varies with location of sensor.

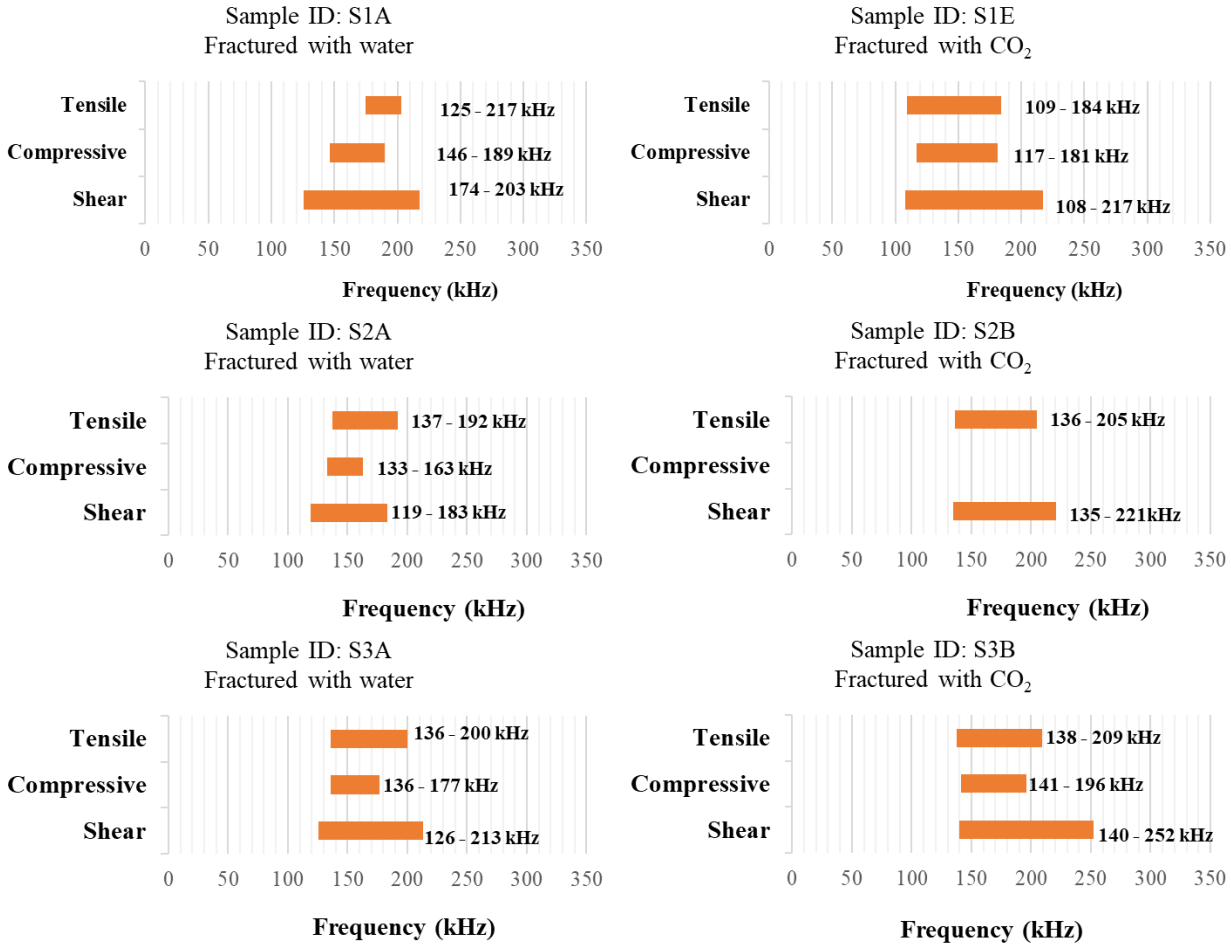

Figure 68. Frequency content of different damage mechanisms induced in S1. S2 amd S3 samples.

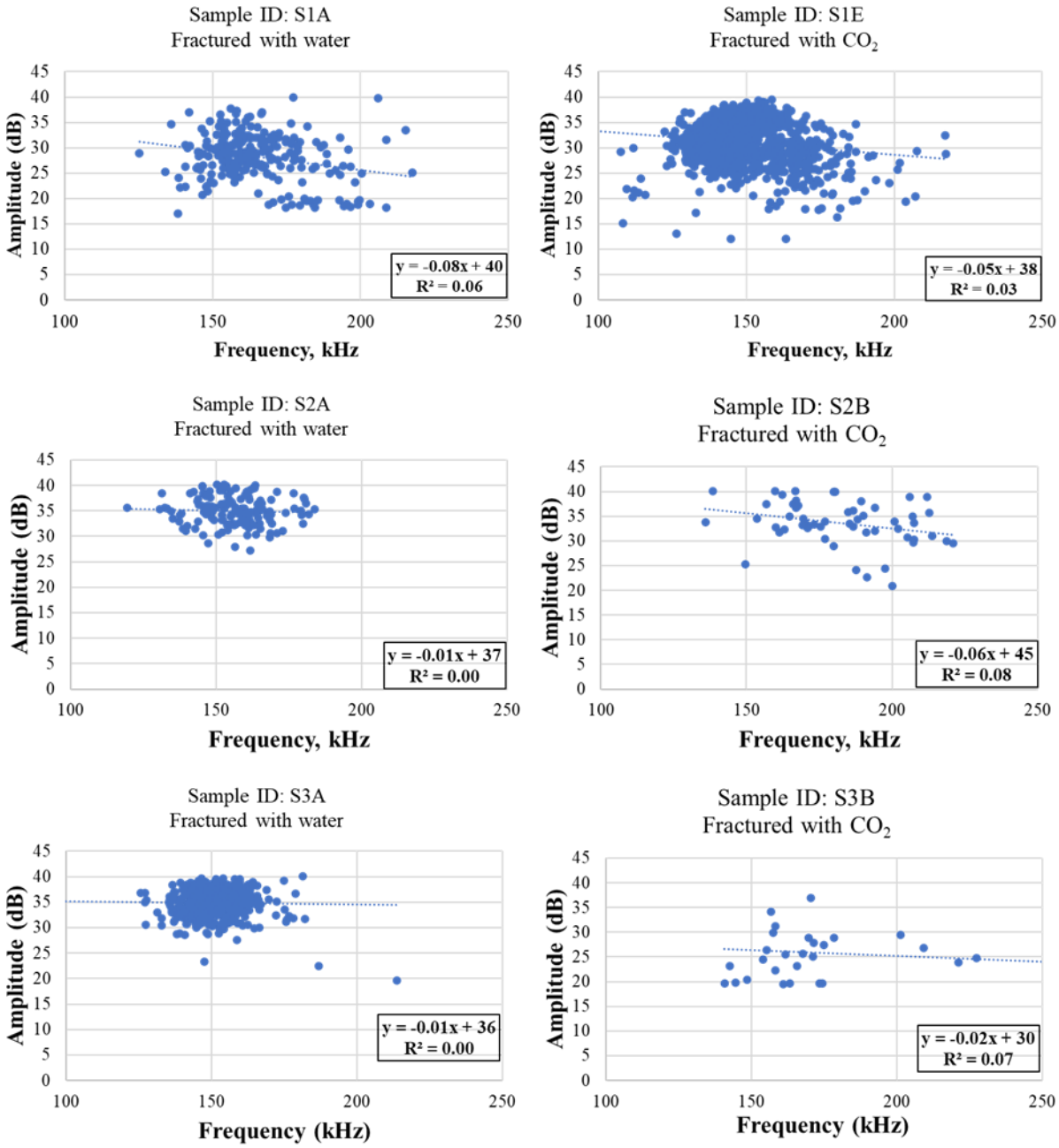

Figure 69. Amplitude versus frequency for S1, S2 and S3 samples.

The amplitude of AEs is inherently related to characteristics of the microcracking process such that it can be correlated with source parameters (explained in the next section) to understand their relationship. In **Figure 70** we have plotted displacement (calculated using Equation 37) versus mean amplitude for the shear events of all tests. Displacement refers to the distance that a

point on the rock surface moves from its original position due to fracturing and it is a measure of the intensity of fracturing. The displacement shows an exponential dependence on mean amplitude (dB) with the exponent between 0.08 – 0.14 for the water induced AEs and 0.08 – 0.13 for the CO_2 induced AEs. These values are similar to those reported by Aso (2009) which ranges from 0.05 – 0.09 for water induced AEs.

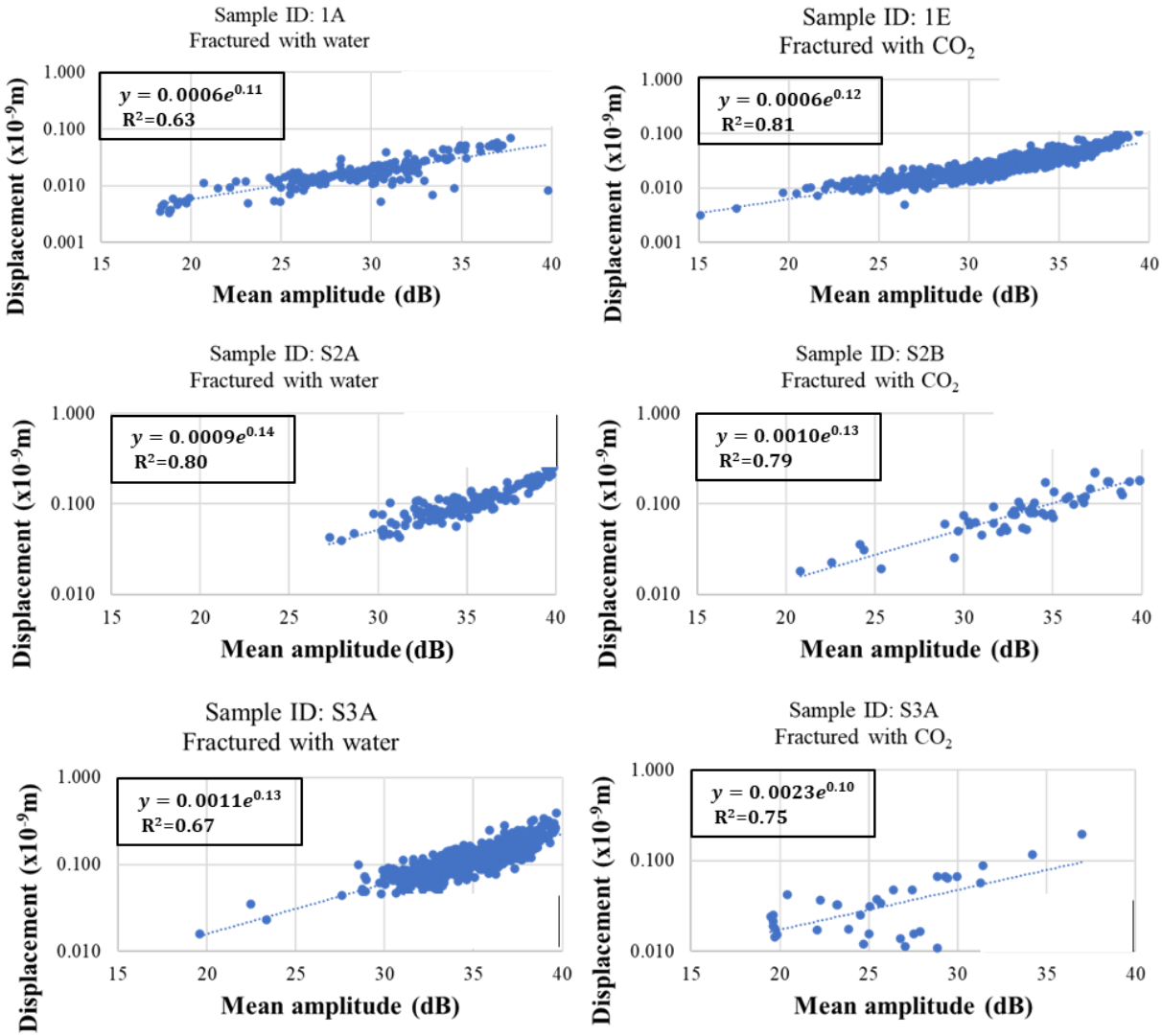

Figure 70. Displacement versus mean amplitude

4.5 AE source parameters

In seismology, the determination of source parameters (source radius, seismic moment, moment magnitude, stress drop, displacement, and radiated energy) is used to assess the strength and dimensions of earthquakes for scientific purposes and to discuss their impact on society. Seismologists utilized seismic waves radiated by earthquakes to study their source geometry and focal depth. We have adopted a similar concept to characterize the shear AE events associated with water and CO_2 fracturing. The basic input obtained from seismic waves for source parameter estimation is the spectra density of the waveform which was computed for all AE signals. The estimated spectra (**Figure 71**) agreed well with the displacement spectra density plot in Aso (2009). Boatwright 1980 shows a relationship between displacement spectral density and frequency as

$$\Omega(f) = \frac{\Omega_o}{[1 + \left(\frac{f}{fc}\right)^{2\gamma}]^{0.5}} \quad 34$$

where Ω_o is the low-frequency displacement spectra plateau; f_c is the corner frequency obtained from the intersection between the high and low frequency asymptotes and γ is the high frequency roll-off given as 1 (Brune, 1970) or 2 (Boatwright, 1980). The corner frequency and the low-frequency displacement spectra plateau can be obtained from a log-log plot of the displacement spectra density versus frequency and used to compute other source parameters.

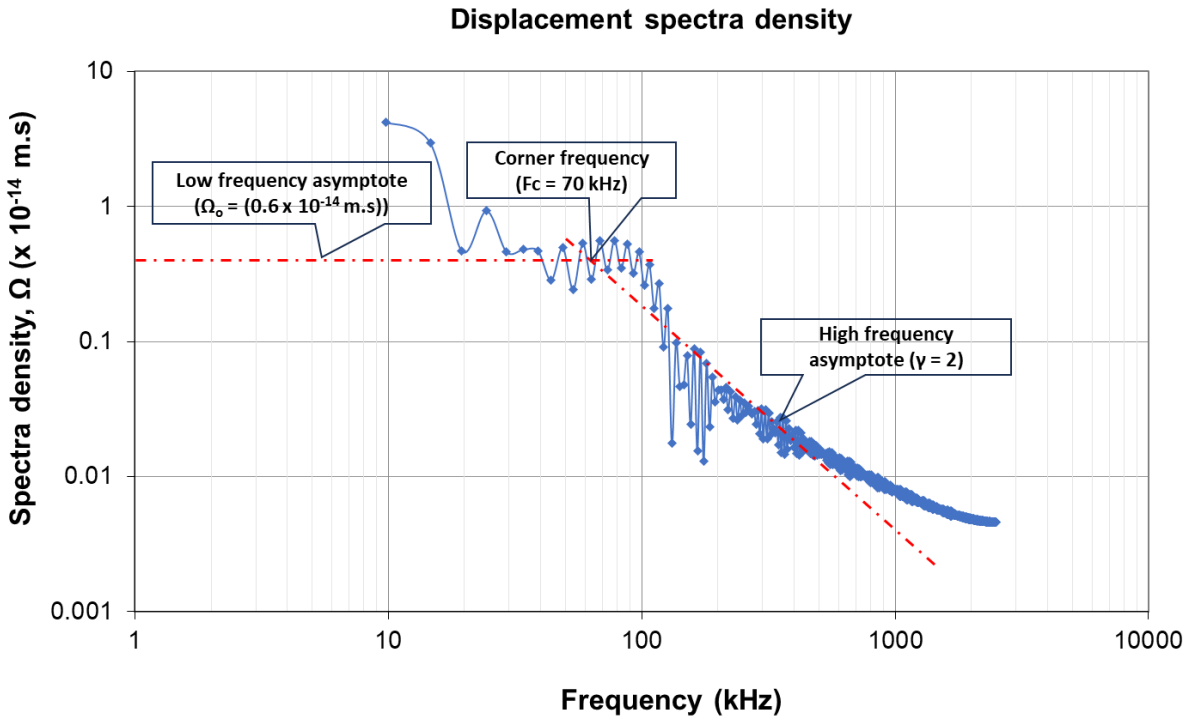

Figure 71. Displacement spectral density.

Assuming a microseismic wave generated by a circular crack generated, Brune (1980) provides an expression to calculate the source radius as a function of corner frequency. The source radius refers to the size of an earthquake source and it helps seismologists to understand the energy release, stress changes and fault process associated with an earthquake. It can be expressed as

$$r = \frac{2.34V_p}{2\pi f_c} \qquad 35$$

where V_p is the p-wave velocity.

The seismic moment, M_o is the best measure of earthquake size and energy, and it describes the faulting process in terms of the rigidity of the medium, history of the slip and fault area (Stein and Wysession 2003). It is given as

$$Mo = \frac{\Omega_o}{R_{o\phi}} 4\pi\rho R V_p{}^3 \qquad 36$$

where $R_{o\phi}$ is the radiation pattern and it is approximated as 0.52, ρ is the density of the medium; and R is the AE source to receiver distance.

In seismology, displacement refers to the shift that occurs along a fault and it is key to understanding energy released. The average displacement for a circular crack (Brune, 1970) is given us

$$D = \frac{M_o}{\pi r^2 \mu} \quad 37$$

where μ is the shear modulus of the rock.

The stress drop is the difference in stress pre- and post-rock rupture and it is a measure of how much stress is released during a rupture of a fault. A high stress drop indicates high energy release and vice versa. It is given as (Lay and Wallace, 1995)

$$\Delta\sigma = \frac{7}{16}\frac{M_o}{r^3} \quad 38$$

The moment magnitude (M_w) and radiated energy (E_o) of an earthquake is given as (Stein and Wysession, 2003)

$$M_w = \frac{\log_{10} M_o - 9.1}{1.5} \quad 39$$

$$E_o = \frac{\Delta\sigma}{2\mu} M_o \quad 40$$

The results from the source parameters estimation are discussed below.

Samples S1A, S1B, and-S1C

S1A-S1C were fractured with water. The source parameters for the located shear AE events of S1A are plotted in **Figure 72**.The corner frequency ranges from 80 – 187 kHz, the high frequency roll-off varies from -2.72 – -1.06, the frequency spectra plateau ranges from $7.7x10^{-5}$ – $3.7x10^{-4}$ x (10^{-14} ms), the source radius varies from 0.007 – 0.018 (m), moment magnitude ranges

from -8.6 – -8.1, the radiated energy ranges from 0.053 – 3.120 ($x10^{-12}$J), the displacement ranges from 0.0081 – 0.0739 ($x10^{-9}$m) and the stress drop ranges from 15 – 207 (N/m^2). These parameters are similar to those estimated for S1B and S1C (Appendix D)

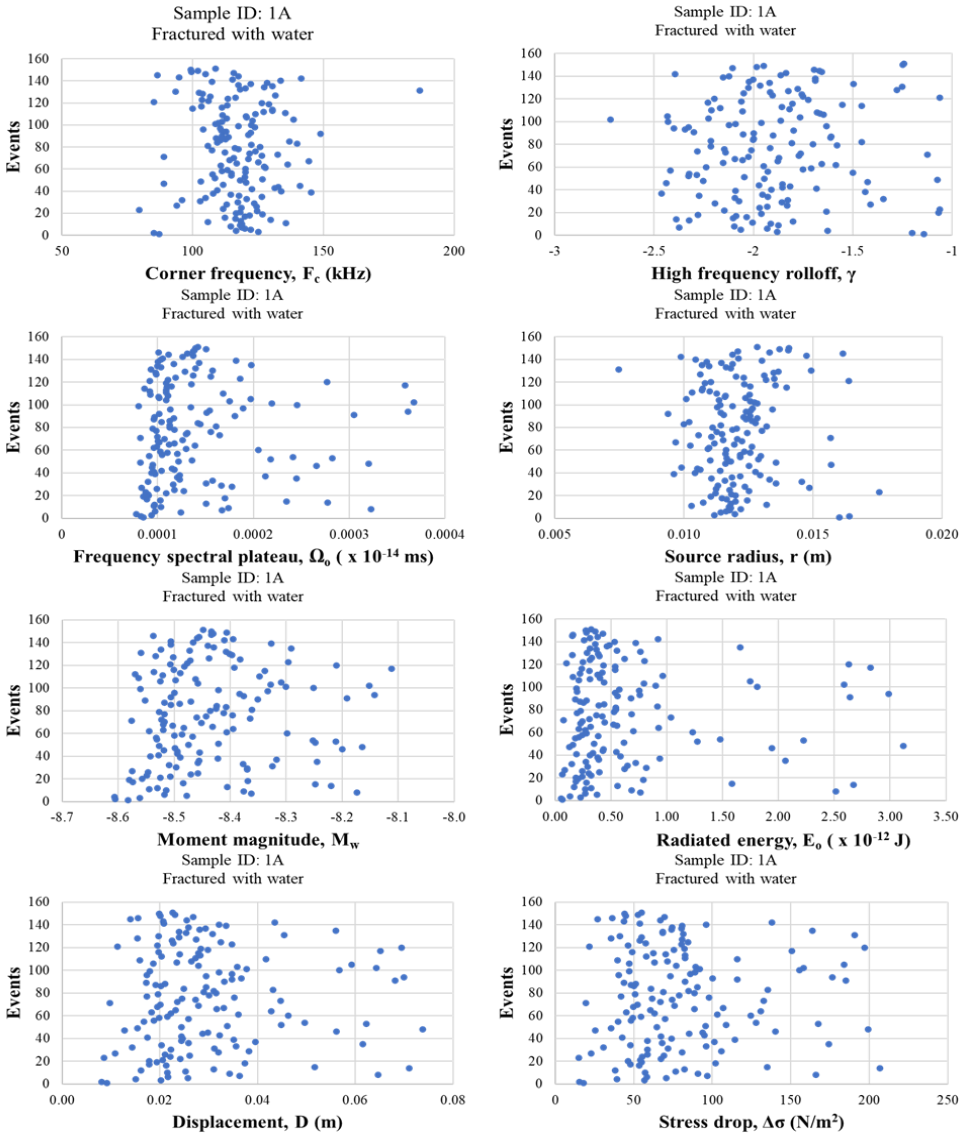

Figure 72. Source parameters for the shear events of S1A

Sample S1D, S1E, S1F, S1G, andS1H

S1D-S1H were fractured with CO_2. The source parameters for the located shear AE events of S1E are plotted in **Figure 73**. The corner frequency ranges from 77 – 148 kHz, the high frequency roll-off varies from -2.70 – -1.06, the frequency spectra plateau ranges from $6.4x10^{-5}$ – $6.0x10^{-4}$ x (10^{-14} ms), the source radius varies from 0.010 – 0.018 (m), moment magnitude ranges from -8.7 – -8.0 (Nm), the radiated energy ranges from 0.059 – 6.304 ($x10^{-12}$J), the displacement ranges from 0.0032 – 0.1092 ($x10^{-9}$m) and the stress drop ranges from 3 – 288 (N/m^2). The other CO_2 fractured samples exhibited similar source parameters (Appendix D).

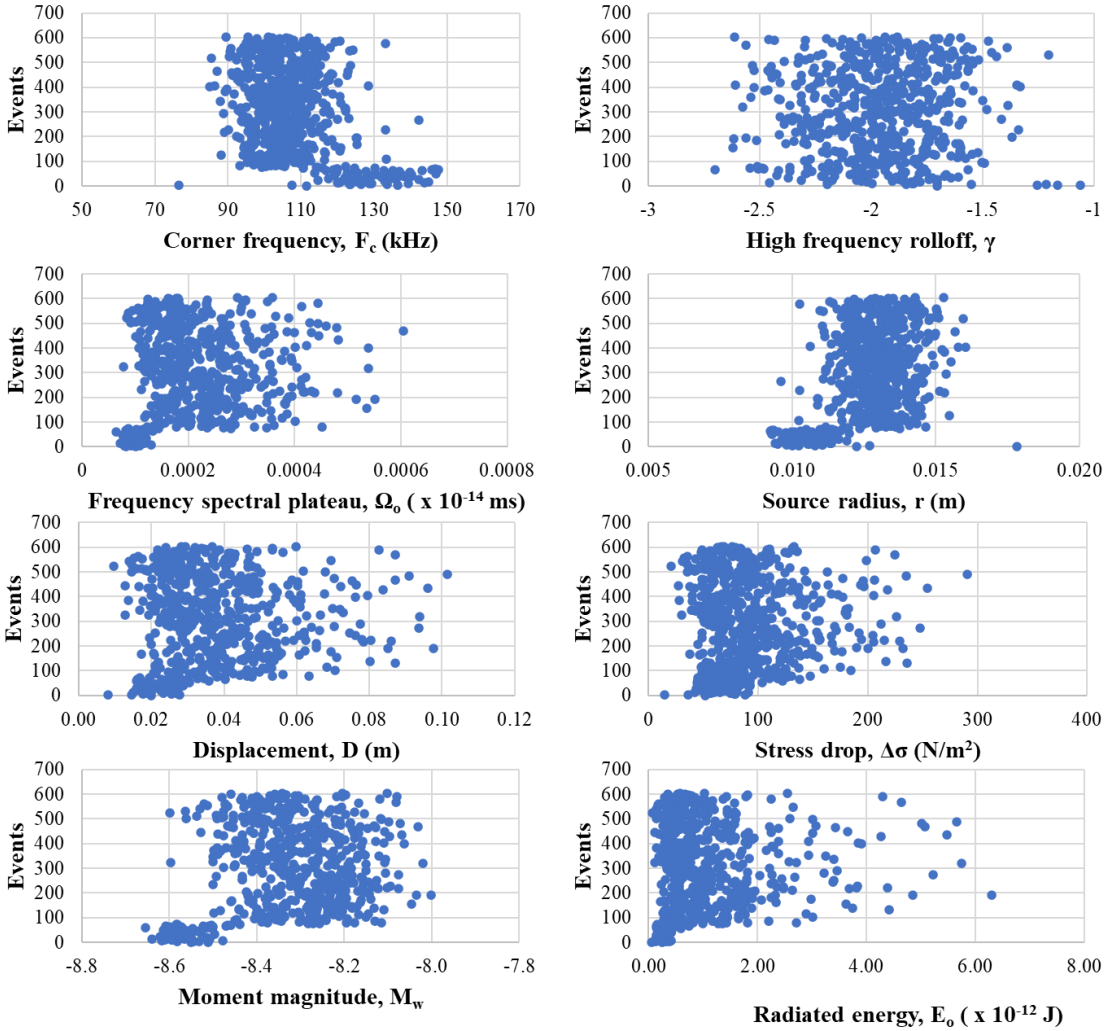

Figure 73. Source parameters for the shear events of S1E

Sample ID: S2A

The source parameters for the located shear AE events of S2A are plotted in **Figure 74**. The corner frequency ranges from 75 – 131 kHz, the high frequency roll-off varies from -2.8 – -1.56, the frequency spectra plateau ranges from $1.2x10^{-4}$ – $9.7x10^{-4}$ x (10^{-14} ms), the source radius varies from 0.011 – 0.020 (m), moment magnitude ranges from -8.4 – -7.9 (Nm), the radiated energy ranges from 0.5 – 35.0 ($x10^{-12}$J), the displacement ranges from 0.0391 – 0.3434 ($x10^{-9}$m) and the stress drop ranges from 40 – 407 (N/m^2).

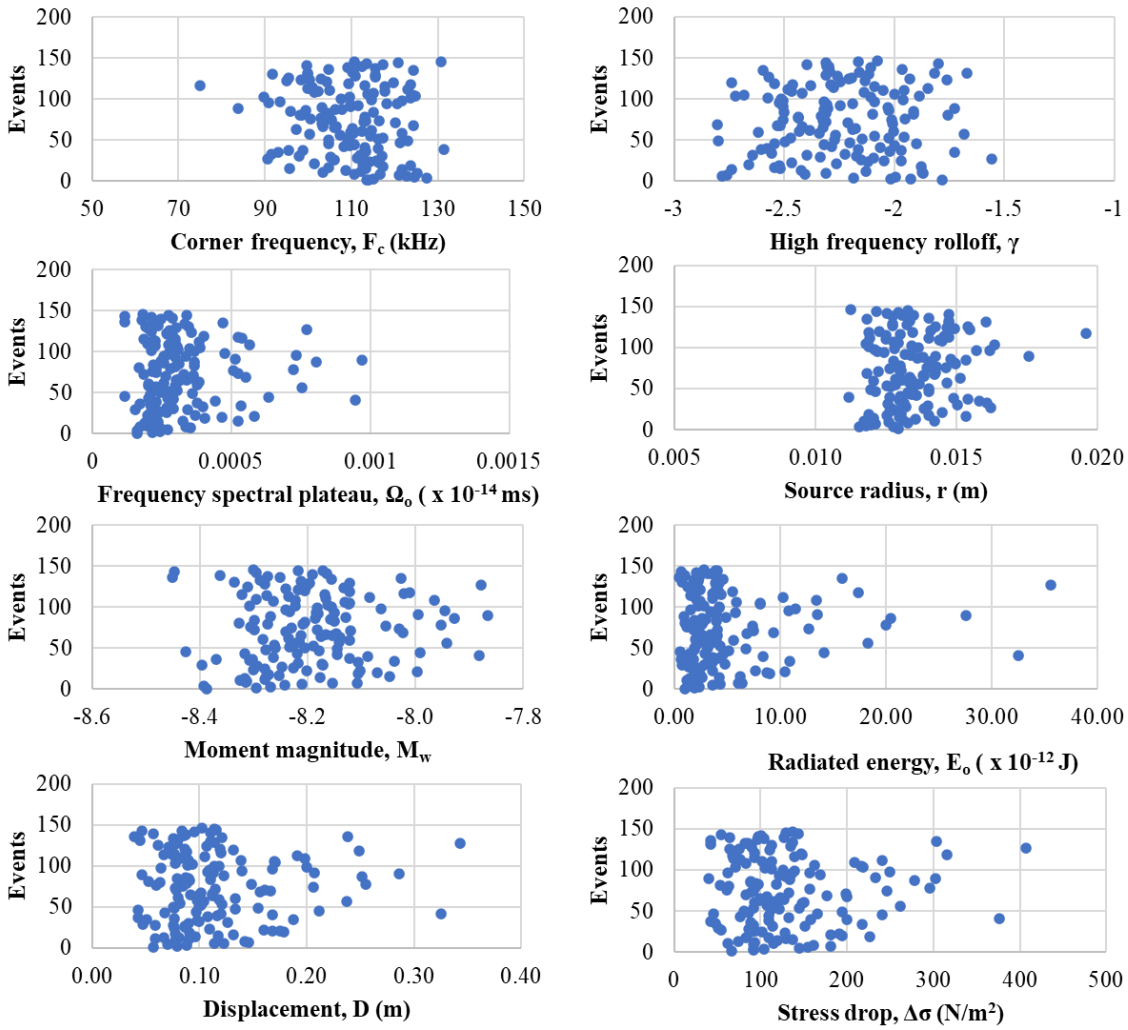

Figure 74. Source parameters for the shear events of S2A

Sample ID: S2B

The source parameters for the located shear AE events of S2A are plotted in **Figure 75**. The corner frequency ranges from 87 – 137 kHz, the high frequency roll-off varies from -2.7 – -1.22, the frequency spectra plateau ranges from $8.0x10^{-5}$ – $1.0x10^{-3}$ x (10^{-14} ms), the source radius varies from 0.011 – 0.020 (m), moment magnitude ranges from -8.5 – -7.8 (Nm), the radiated energy ranges from 0.1 – 34.9 ($x10^{-12}$J), the displacement ranges from 0.0182 – 0.2995 ($x10^{-9}$m) and the stress drop ranges from 15 – 308 (N/m^2).

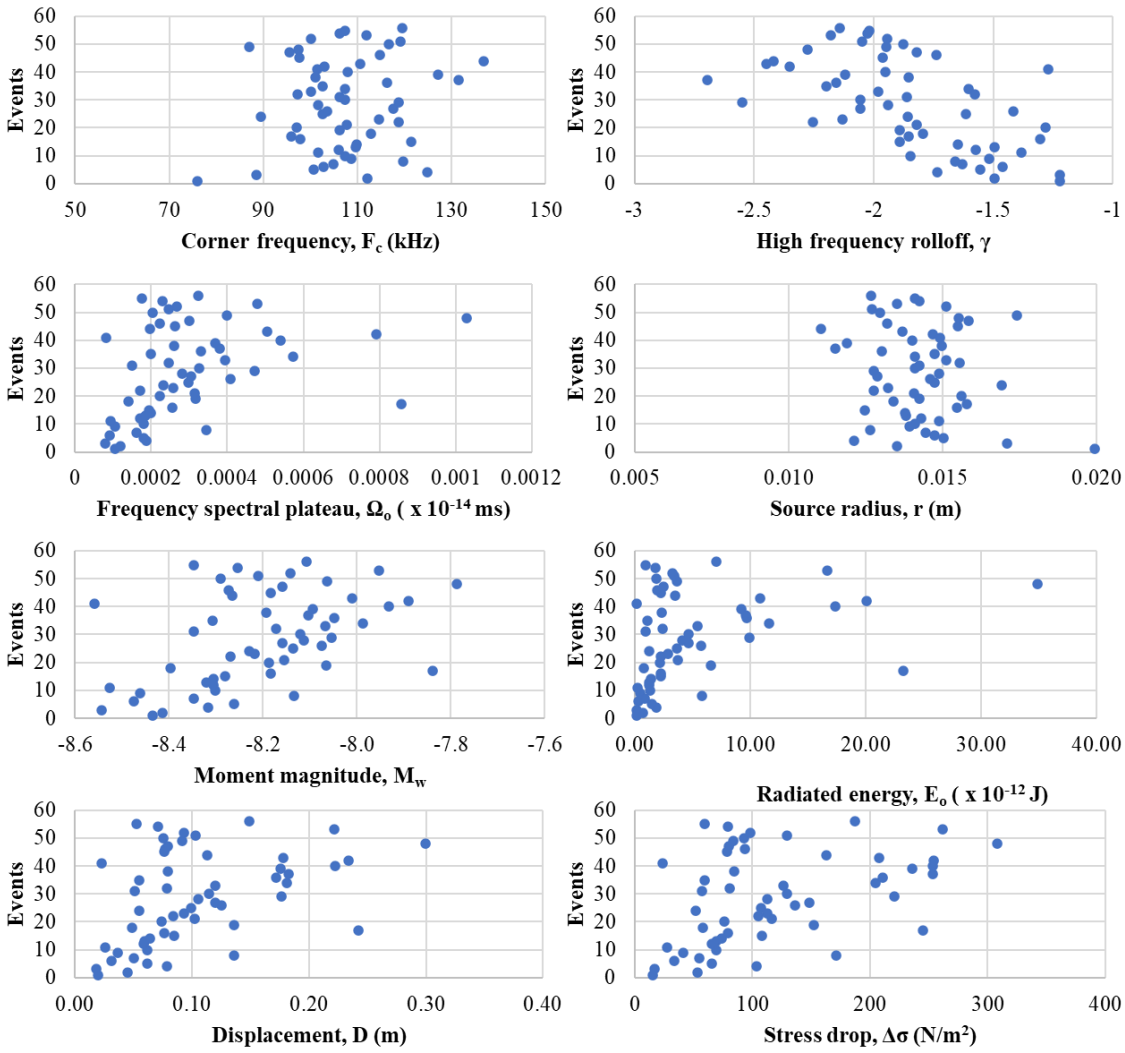

Figure 75. Source parameters for the shear events of S2B

Sample ID: S3A

The source parameters for the located shear AE events of S3A are plotted in **Figure 74**. The corner frequency ranges from 76 – 147 kHz, the high frequency roll-off varies from -3.0 – -1.06, the frequency spectra plateau ranges from $8.4x10^{-5}$ – $7.8x10^{-4}$ x (10^{-14} ms), the source radius varies from 0.010 – 0.020 (m), moment magnitude ranges from -8.5 – -7.8 (Nm), the radiated energy ranges from 0.1 – 47.0 ($x10^{-12}$J), the displacement ranges from 0.0158 – 0.3917 ($x10^{-9}$m) and the stress drop ranges from 11 – 437 N/m^2.

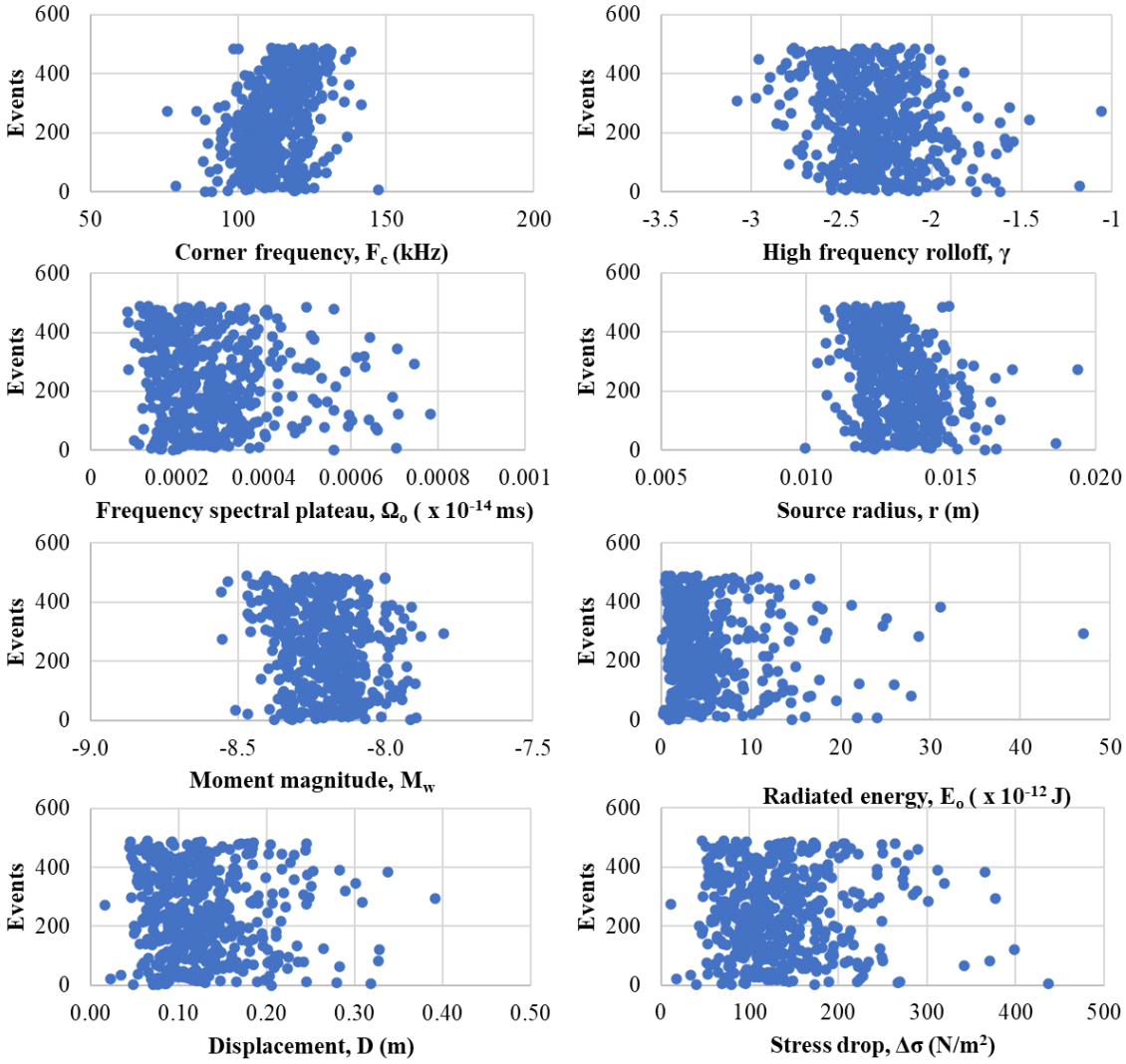

Figure 76. Source parameters for the shear events of S3A

Sample ID: S3B

The source parameters for the located shear AE events of S3A are plotted in

Figure 77. The corner frequency ranges from 76 – 147 kHz, the high frequency roll-off varies from -3.0 – -1.06, the frequency spectra plateau ranges from $8.4x10^{-5}$ – $7.8x10^{-4}$ x (10^{-14} ms), the source radius varies from 0.010 – 0.020 (m), moment magnitude ranges from -8.5 – -7.8 (Nm), the radiated energy ranges from 0.1 – 47.0 ($x10^{-12}$J), the displacement ranges from 0.0158 – 0.3917 ($x10^{-9}$m) and the stress drop ranges from 11 – 437 N/m^2.

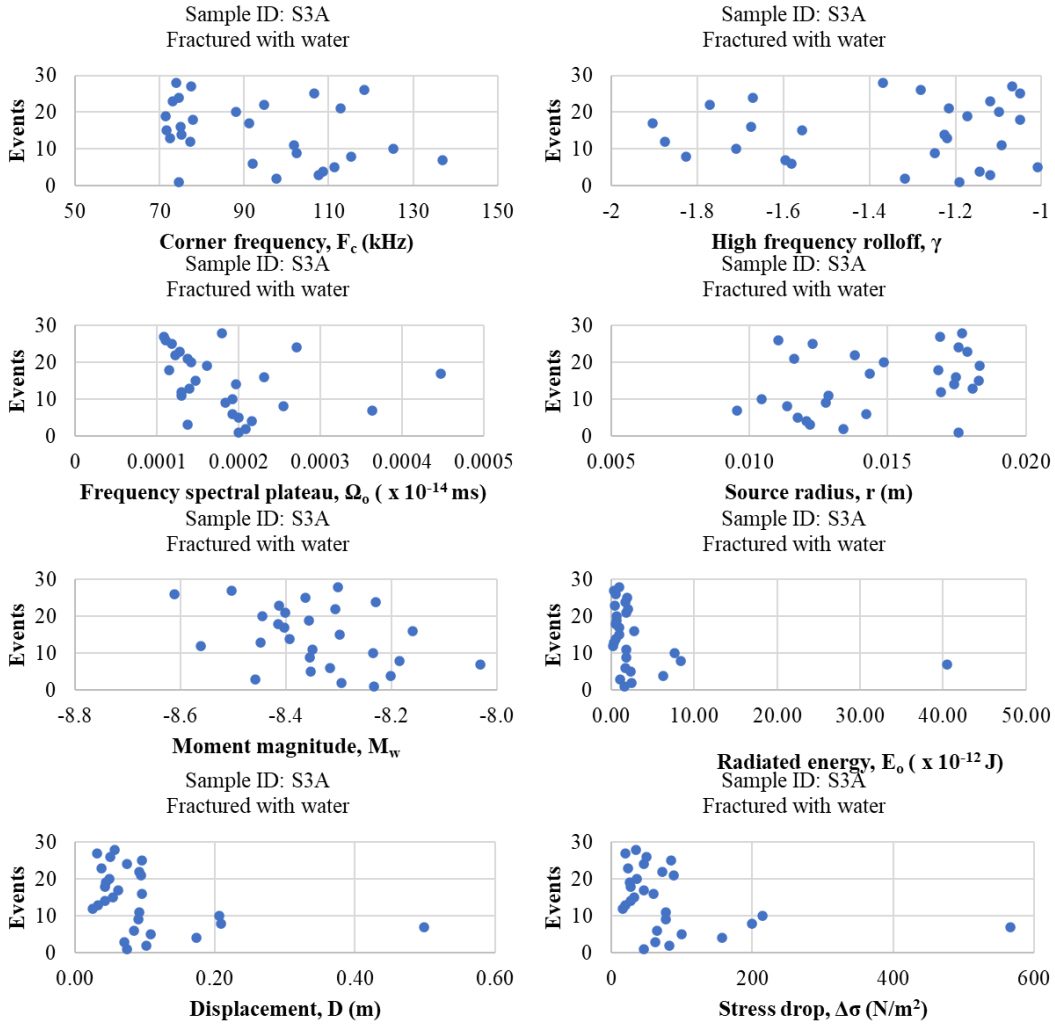

Figure 77. Source parameters for the shear events of S3B

In summary, although there is a considerable amount of scatter in the source parameters, a careful examination shows some degree of similarity in their values. The corner frequency from the tests with water as injectate varies from 80 – 187 kHz, the stress drop has an average value of about 69 N/m^2 and the moment magnitudes averages -8.4. For tests with CO_2 as injectate, corner frequency varies from 73 – 142 kHz, the stress drop has an average value of about 97 N/m^2 and the moment magnitudes averages -8.3. Shear events from the CO_2 tests have slightly lower corner frequency and higher stress drop. The moment magnitudes are similar.

We have further analyzed the magnitudes in a box plot to compare the intensity of fracturing caused by injecting the two different fluids (**Figure 78**). Generally, most events have similar magnitudes ranging from -8.6 – -8.2 in both cases although one can observe slightly higher magnitudes for CO_2 induced AEs (-8.2 – -7.8) in S1. Verdon et al. 2010 observed that few CO_2 induced microseismic events had slightly higher magnitudes than those induced by water, but most events had similarity in magnitudes. This led them to conclude that the comparability between magnitudes induced by water and CO_2 injection means that lessons can be learnt from the abundant experience of conventional water injection.

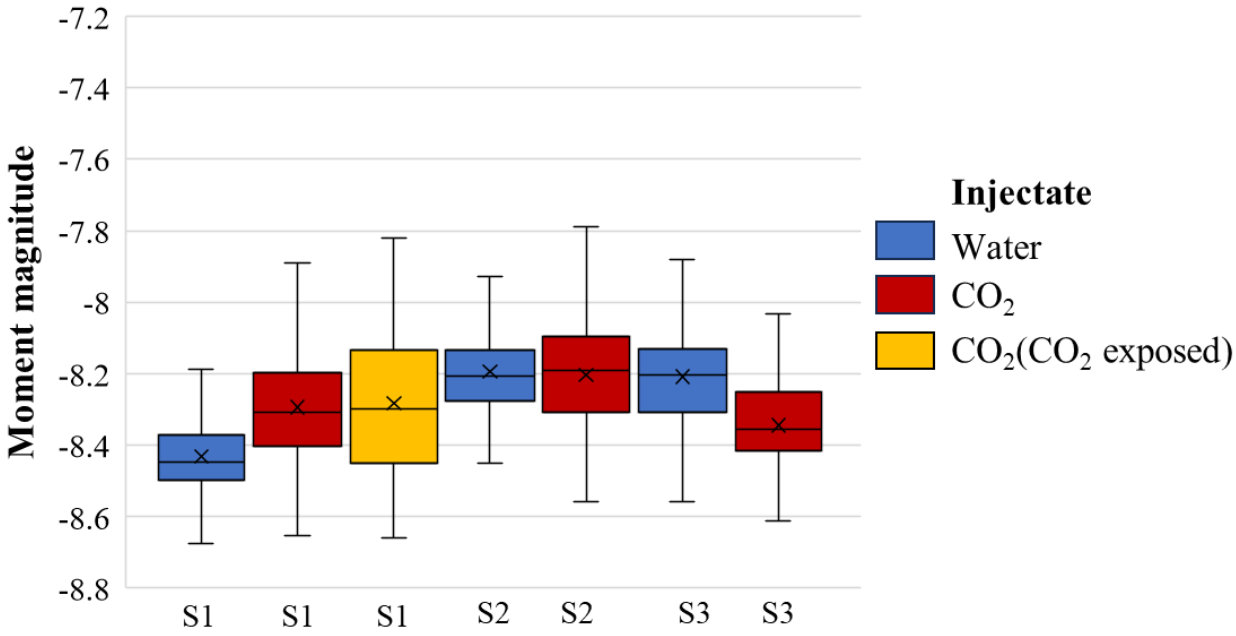

Figure 78. Moment magnitude of water- and CO_2-induced AEs for all tests

4.6 Fracture morphology

The morphology of the induced fractures was examined using Scanning Electron Microscope (SEM), to develop insight into the complexity and mechanism of failure at a microscopic level. The sampling and preparation for this analysis was done according to the procedure explained earlier. Some SEM images are provided here with a description of the fracture morphology and its statistical analysis.

Horizontal fracture: S1

Figure 80 and **Figure 81** represent the images taken along different regions of a sample fractured with water and CO_2 respectively. The slice used for SEM imaging was taken parallel to the borehole and thus images show a horizontal fracture as it moves away from the borehole as depicted in **Figure 79**.

The water injection induced fracture shows a primary fracture with a minimum amount of loose grains and intact/smooth fracture edges. The loose grains can serve as a source of natural

proppants to keep the fracture opened while the smooth fracture edges connote a less violent microcracking process. We can also observe minor branched fracture whereas the primary fracture seems to reduce in width as it moves away from the borehole which can be attributed to decreasing fluid energy due to fluid leak-off.

On the contrary, the CO_2 injection induced fracture shows a primary fracture with relatively greater number of loose grains which is an attribute of intense cracking. We observe relatively greater degree of rough fracture edges, fracture bifurcations into branched fractures and split grains which are likely due to the violent nature of the microcracking process by CO_2. The primary fracture seems to be of uniform width even as it moves away from borehole. The presence of more loose grains in the CO_2 induced fracture suggests less likelihood of fracture closure when stress is applied as compared to water induced fracture.

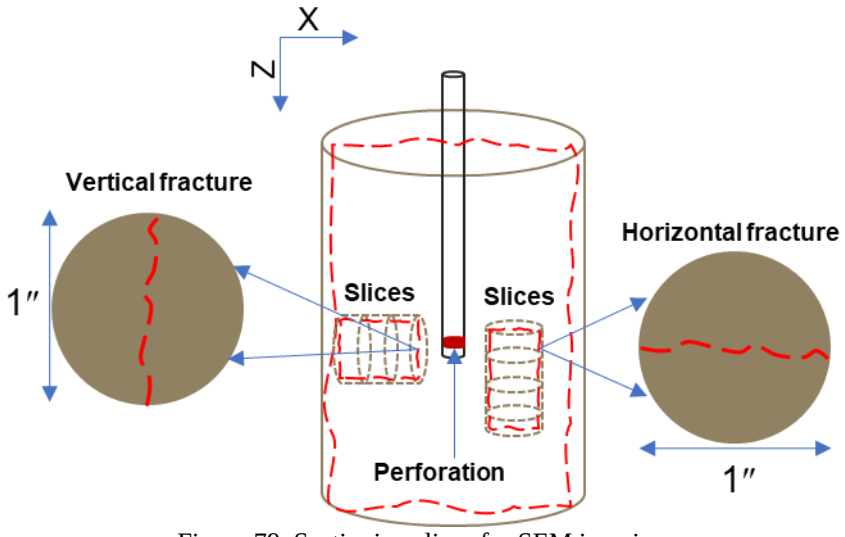

Figure 79. Sectioning slices for SEM imaging

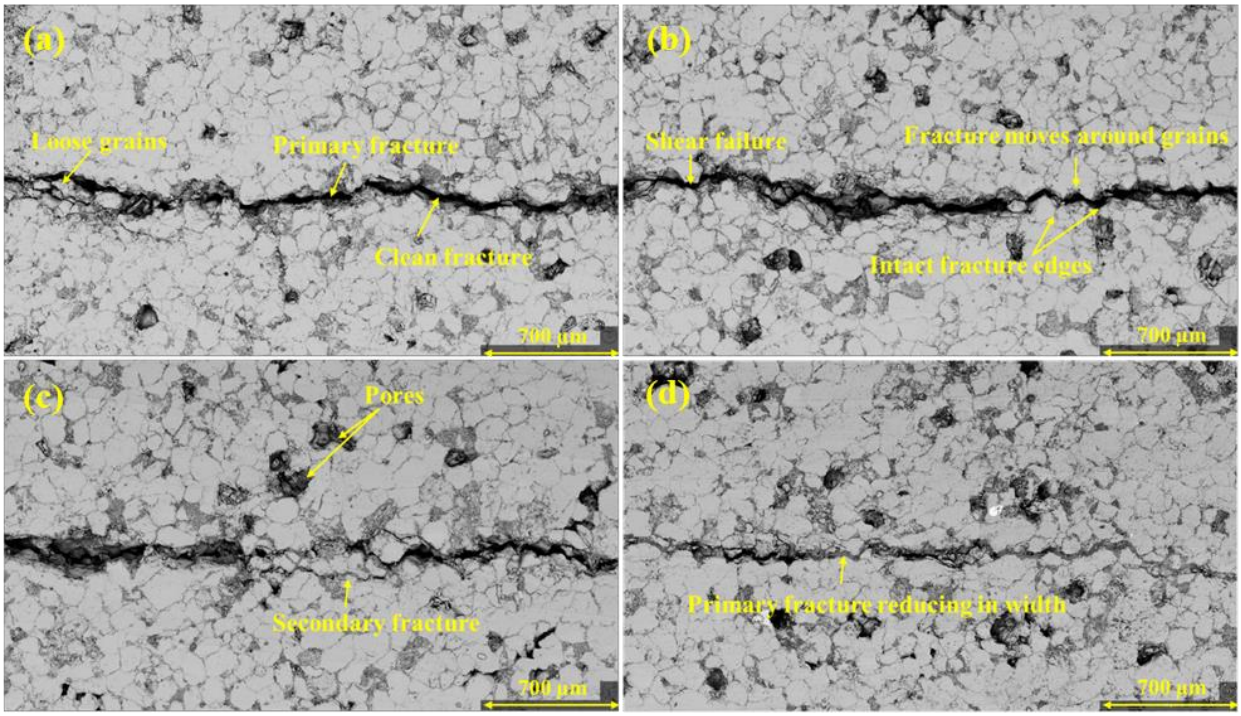

Figure 80. SEM image taken at different regions along a fractured induced by water injection. Fracture propagation is from (a)–(b).

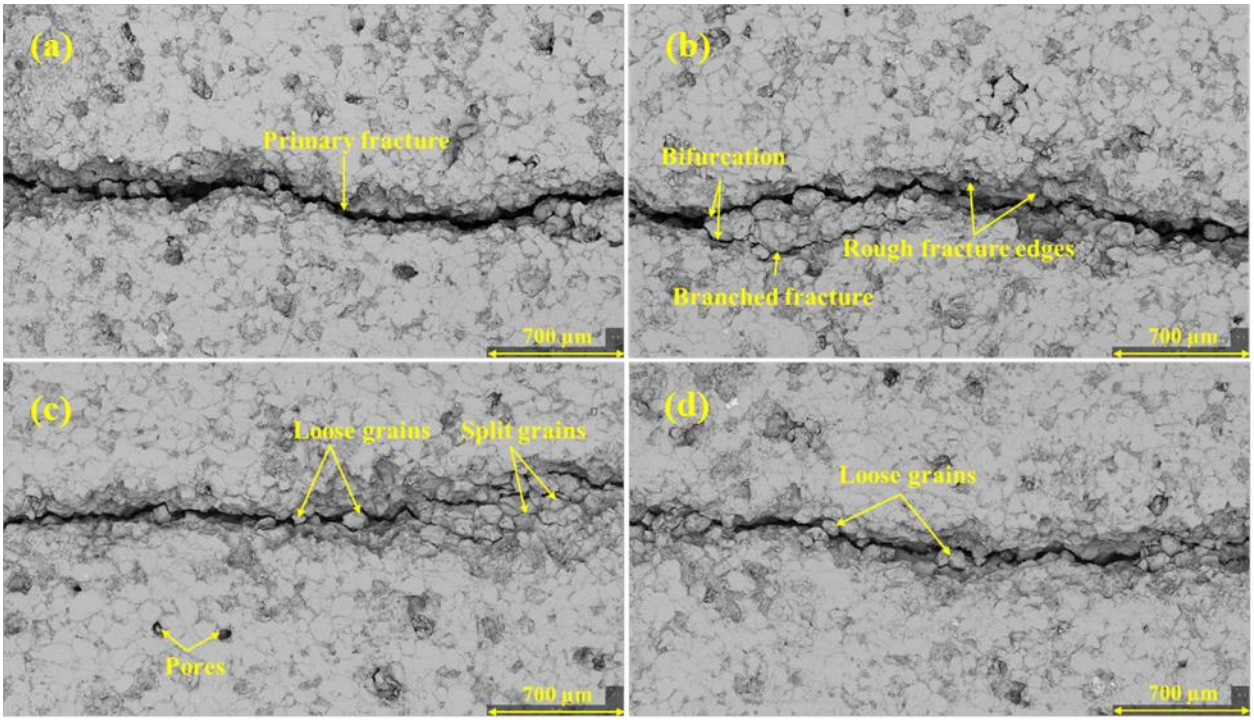

Figure 81. SEM image taken at different regions along a fractured induced by CO_2 injection. Fracture propagation is from (a)–(b).

Vertical fracture: S1

Figure 82 and **Figure 83** represent the images taken along different regions of a sample fractured with water and CO_2 respectively. The slice used for SEM imaging was taken perpendicular to the borehole and thus images show a vertical fracture as it moves away from the injection point to the top of the sample as depicted in **Figure 79**.

The water injection induced fracture shows a primary fracture with some amount of loose and split grains and having both intact/smooth and rough fracture edges at different regions. At the region close to the perforation more damage is seen but this reduces as one moves away.

On the other hand, the fracture generated by CO_2 injection shows a relatively larger primary fracture aperture, greater amount of loose grains, a large region of microcracks, higher number of fracture bifurcations into long branched fractures and split grains suggesting a more violent rock damage by CO_2 as compared to water. Large size fracture aperture can be seen close to the perforation region due to higher fluid energy at depths closer to the perforation.

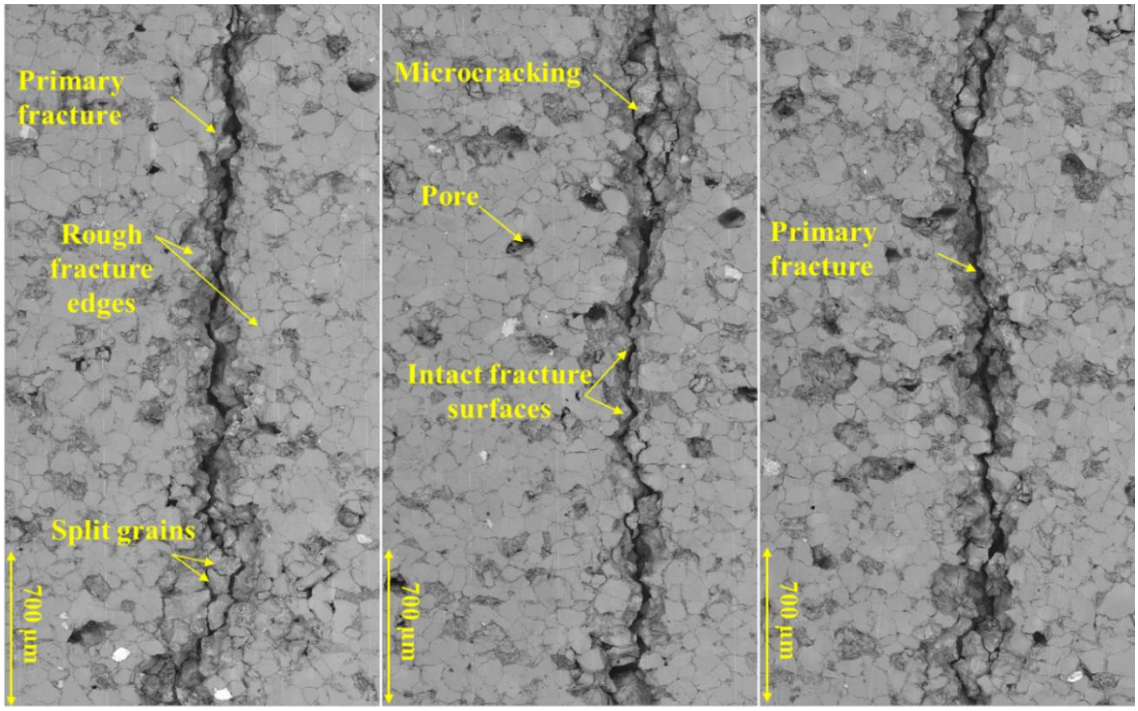

Figure 82. SEM image taken at different regions along a fractured induced by water injection From left to right shows fracture propagation from top to bottom of sample.

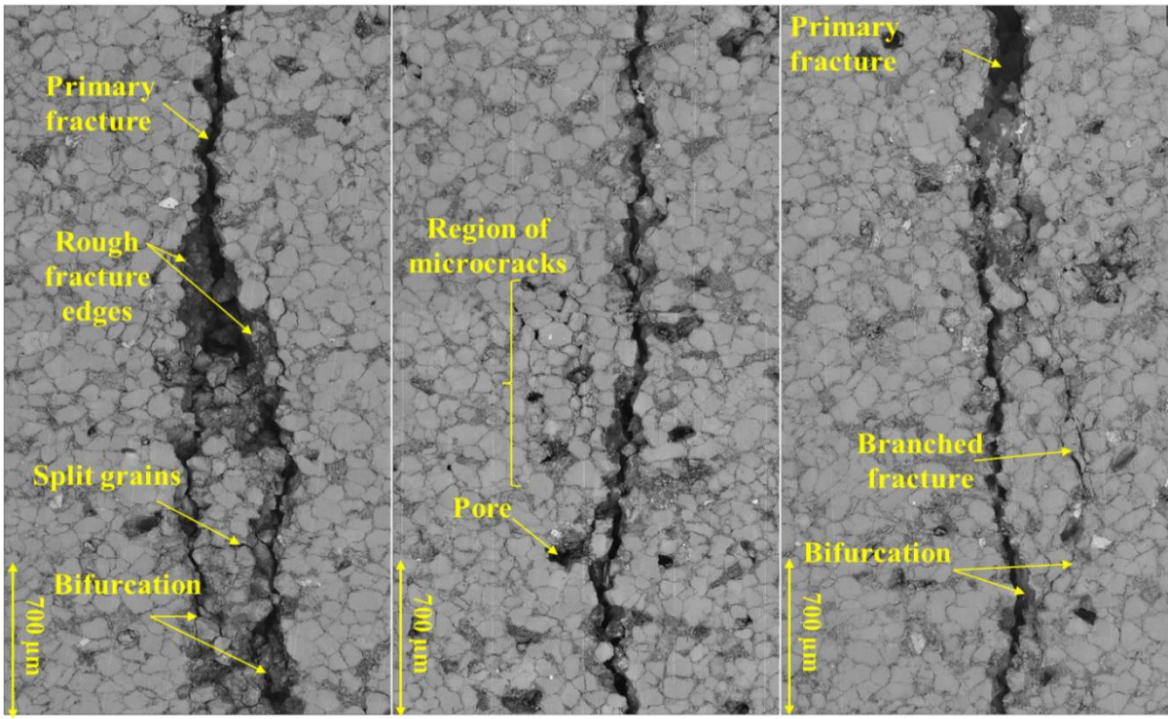

Figure 83. SEM image taken at different regions along a fractured induced by CO_2 injection From left to right shows fracture propagation from top to bottom of sample.

Primary fracture width measurements were obtained from the entire length of the SEM images of the horizontal and vertical slices which are approximately 25 mm in diameter (**Figure 84** and **Figure 85**). This enables an objective and thorough quantitative assessment of the fracture width and its behavior away from the perforation. The width was measured perpendicular to the direction of primary fracture and from its edges at fixed intervals of approximately 0.2 mm. In total about 125 fracture width data points were collected and plotted against distance.

The result obtained for both the horizontal and vertical fracture shows a variation in the primary fracture width signifying an episodic fracture growth. This is expected due to fluid losing energy momentarily after creating a new surface area which reduces fracture width growth and then regaining energy for greater damage due to continuous fluid injection. Spikes in the measurements are as a result of bifurcations or large dislodged grains. The mean width for CO_2 induced fractures is 1.4–2 times that of water as shown in **Figure 84-85**.

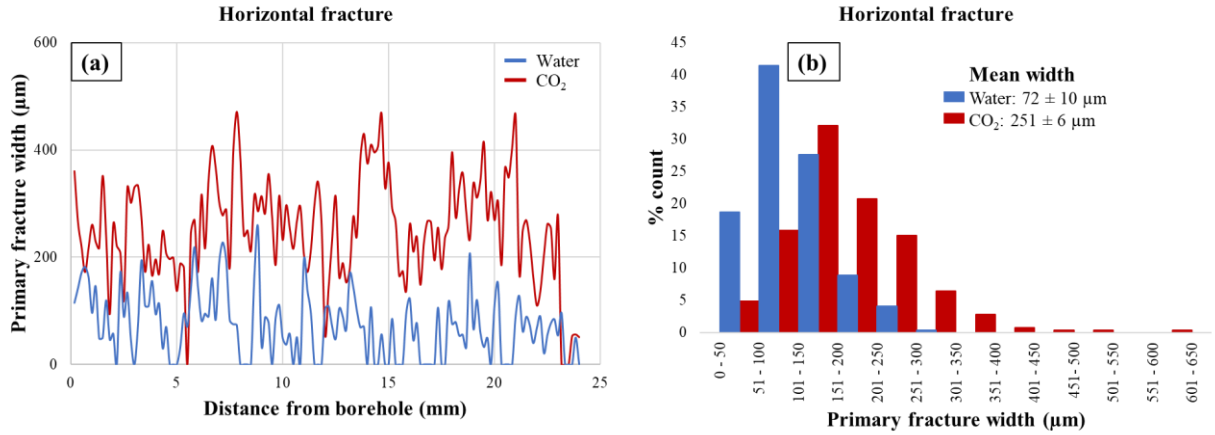

Figure 84. Statistical analysis of primary fracture width (S1 horizontal fracture)

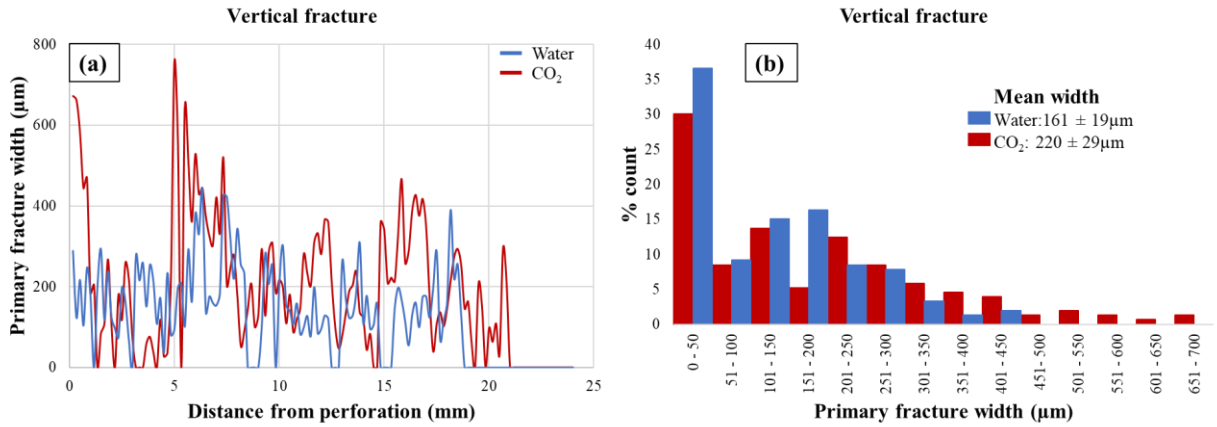

Figure 85. Statistical analysis of primary fracture width (S1 vertical fracture)

Horizontal fracture :S2

Figure 86 and **Figure 87** represent continuous images taken along a fracture induced with water and CO_2 respectively. The fracture was epoxied before imaging using a liquid epoxy. The fracture moves along grain boundaries which are softer due to the presence of clays. The water injection induced fracture shows a thin primary fracture with no loose grains connoting a less violent microcracking process. We can also observe minor branched fractures.

On the contrary, the CO_2 injection induced fracture shows a primary fracture with relatively greater number of loose grains which is an attribute of intense cracking. We observe relatively greater degree fracture bifurcations into a major secondary fracture whose width appears to be greater than seen in the water induced primary fracture. We can observe other branched fractures and split grains which are likely due to the violent nature of the microcracking process. The primary fracture seems to be of uniform width even as it moves away from borehole.

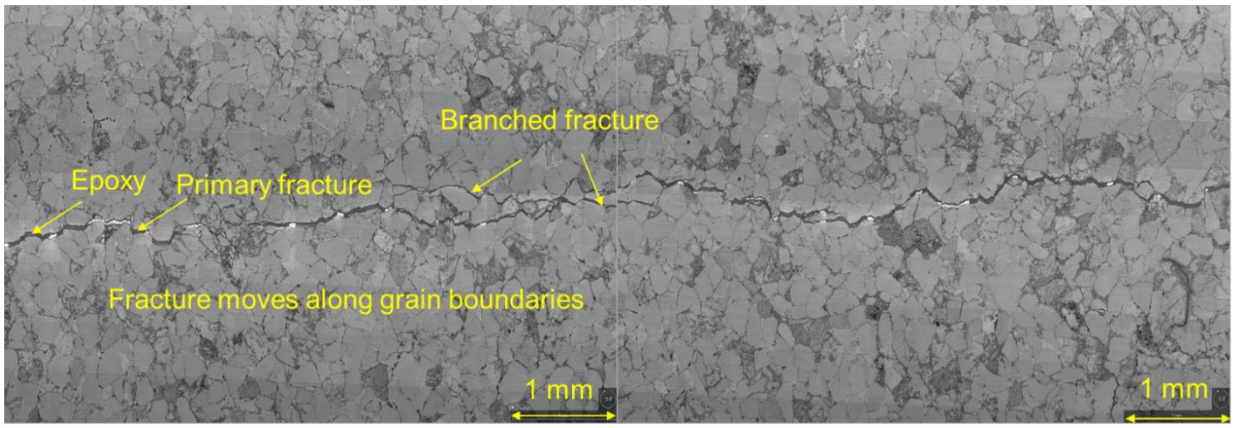

Figure 86. S2 SEM image taken at different regions along a fractured induced by water injection. From left to right shows fracture propagation away from borehole.

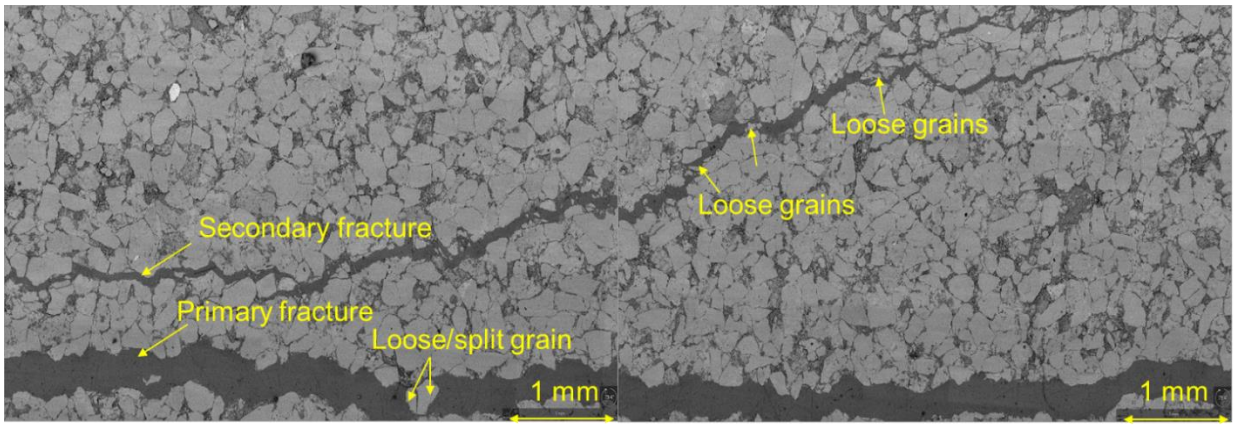

Figure 87. S2 SEM image taken at different regions along a fractured induced by CO_2 injection. From left to right shows fracture propagation away from borehole.

Statistical analysis of the primary fracture width shows episodic fracture growth. The mean width for CO_2 induced fractures is 6.5 times that of water as shown in **Figure 88**.

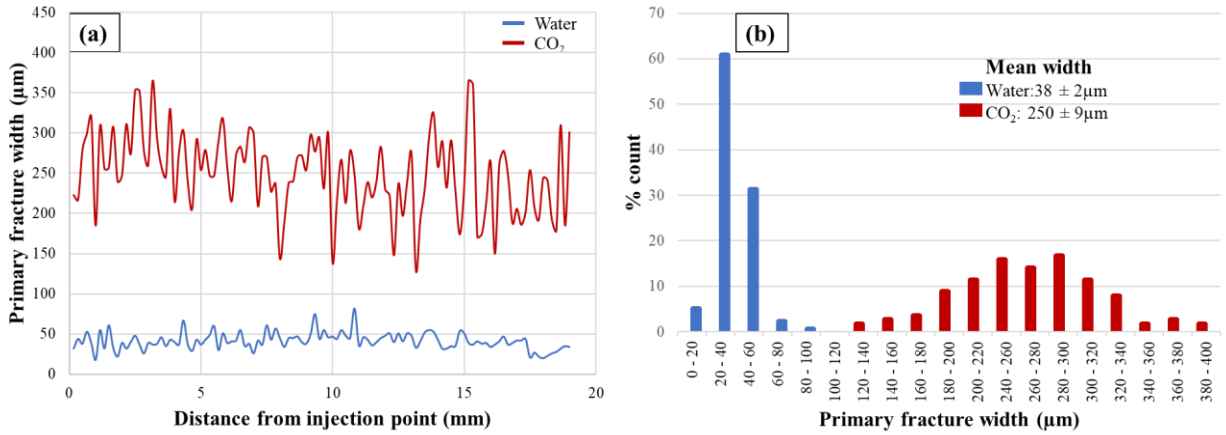

Figure 88. Statistical analysis of primary fracture width (S2 horizontal fracture)

In summary, the observations made for the horizontal and vertical fractures induced by CO_2 shows a wider aperture and greater process zone and thus a higher drainage volume around the fracture which can be detrimental for geological carbon sequestration but beneficial in reservoir stimulation for the production of hydrocarbon resources.

4.7 Fracture permeability

Plugs parallel to the borehole of the fractured sample were taken along the fracture and carefully prepared to carry out permeability (k) measurements as described earlier. We took plugs from the left and right side of the borehole and those which remained unsplit were used for the measurements (**Table 15**). Those that split (mostly CO_2 induced plugs) during the coring or plug preparation steps were not used. In addition, the permeability of a native plug (unfractured) was measured and used for comparison. Permeability was measured using AP 608^{TM} which makes use of the pulse decay technique. **Figure 89-90** shows the result of Klinkenberg corrected permeability as a function of confining pressure (P_c) for the left and right plugs respectively taken from S1 samples. In comparison with the native state, water-induced fracture permeability is 2 orders of magnitude greater and CO_2-induced permeability is 3 – 4 orders of magnitude greater. Moreover,

CO_2-induced fracture permeability is consistently at least 1 order of magnitude higher than water-induced permeability. The pressure dependence of permeability ($\Delta k/\Delta P_c$) (**Table 15**) is higher in CO_2-induced fracture than in water-induced fracture. Permeability for S3 samples (**Figure 91**) shows a similar outcome as described in S1. S2 CO_2 fractured sample didn't remain intact for permeability measurement.

The measured fracture permeability was from naturally propped sample i.e. no artificial proppants were used. The fractures remained opened solely from the self-propping of dislodged grains and the asperities on the fracture surface. The greater the fracture cross sectional area to the flow of fluids, the higher the resulting permeability.

Table 15. Summary of S1 plugs used for fracture permeability measurement.

Sample	Sample ID	Injectate	Permeability measurement		$\Delta k/\Delta P_c$ (µD/psi)	
			Left plug	Right plug	Left plug	Right plug
S1	A	Water	Yes	N/A	4.3	N/A
	B	Water	Yes	Yes	3.3	0.6
	C	Water	N/A	N/A	N/A	N/A
	D	CO_2	Yes	Yes	53	2.5
	E	CO_2	Yes	Yes	55	2.7
	F	CO_2	N/A	Yes	N/A	18
	G	CO_2	N/A	N/A	N/A	N/A
	H	CO_2	N/A	N/A	N/A	N/A

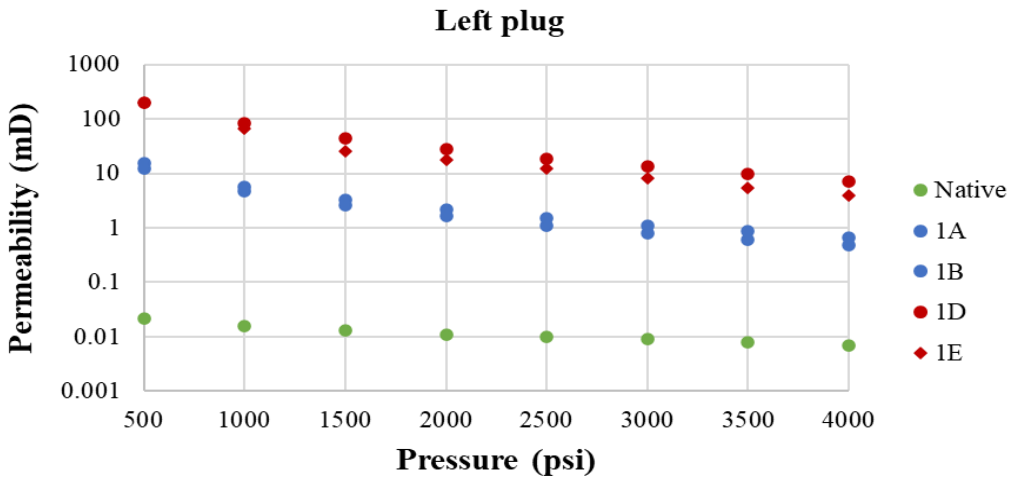

Figure 89. Fracture permeability (Klinkenberg corrected) as a function of confing pressure for plugs taken from the left side of fractured samples. Samples 1A-1B and 1D-1E were fractured with water and CO_2 respectively.

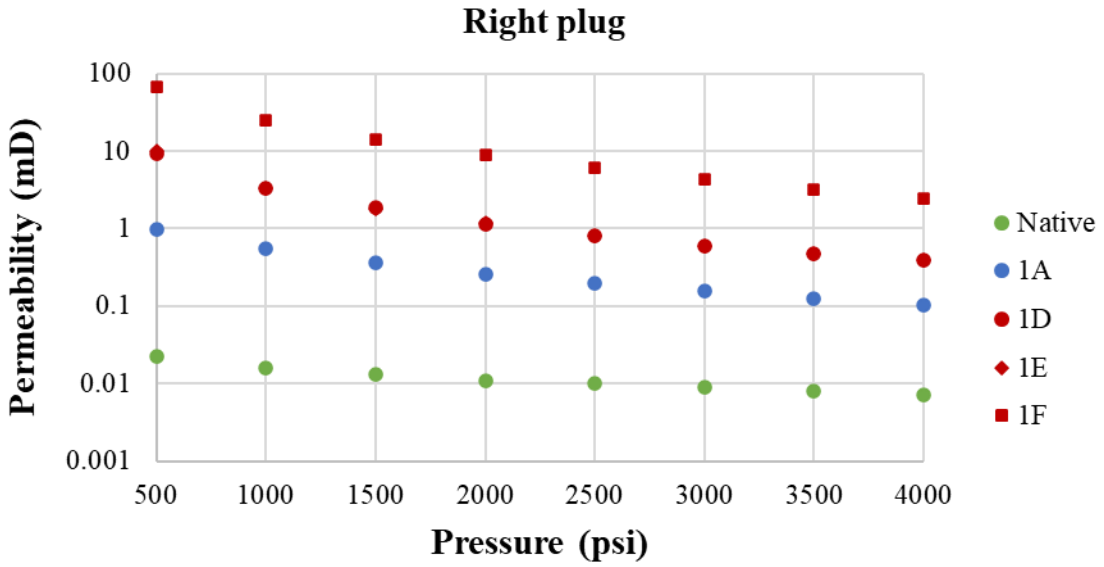

Figure 90. Fracture permeability (Klinkenberg corrected) as a function of confing pressure for plugs taken from the right side of fractured S1 samples. Samples 1B and 1D-1F were fractured with water and CO_2 respectively.

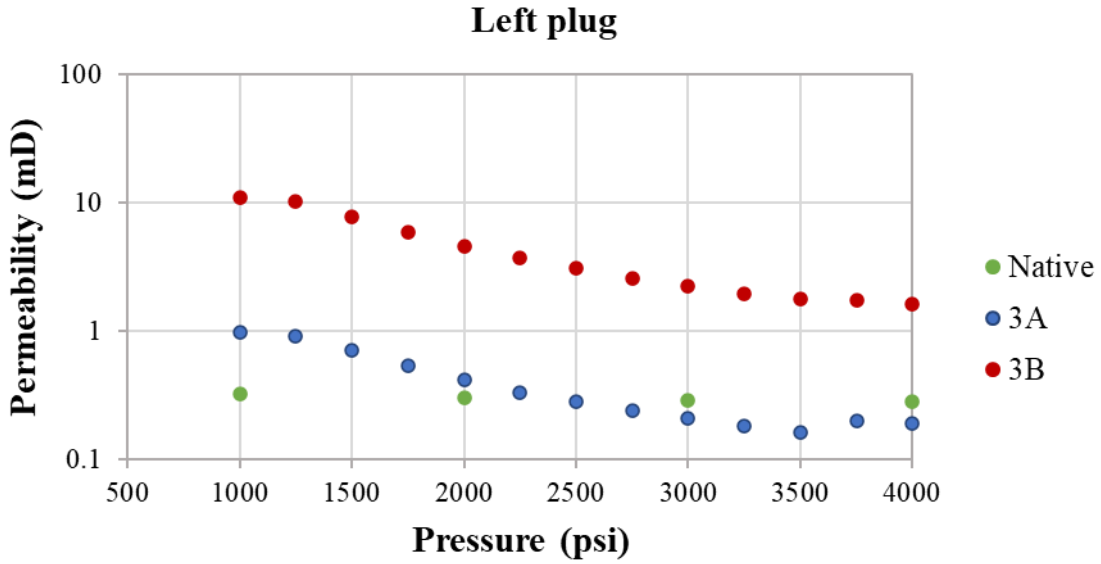

Figure 91. Fracture permeability (Klinkenberg corrected) as a function of confing pressure for plugs taken from the left side of fractured S3 samples. Samples 3A and 3B were fractured with water and CO_2 respectively.

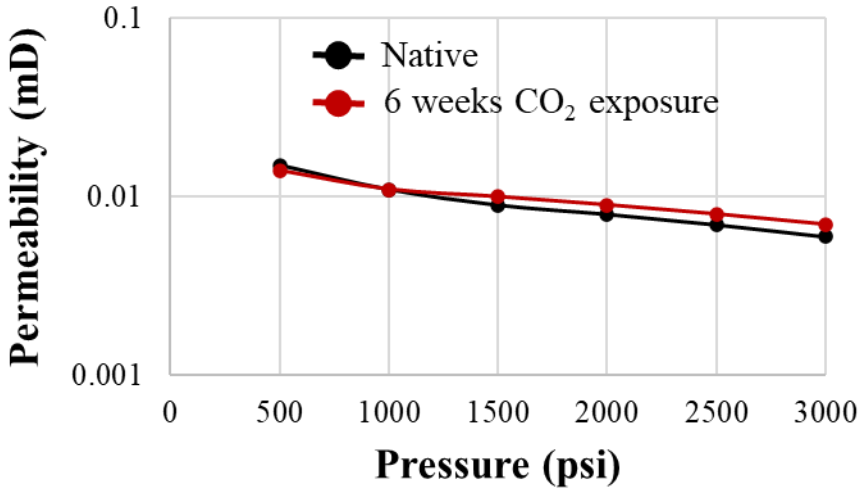

Figure 92. Permeability as a function of confing pressure for a native sample and a sample exposed to CO_2 for 6 weeks.

Walsh (1981) developed a theoretical equation to describe fracture permeability in relation to effective pressure.

$$\frac{K}{K_o} \cong 1 - \frac{\sqrt{2}h}{a_o}\left(\ln\frac{P}{P_o}\right)_e \qquad 41$$

Here, K_o and a_o represent the permeability and half aperture of the fracture, respectively, at a reference pressure value of P_o and h is the rms roughness of the fracture surface. The subscript "e" denotes effective pressure values. When assuming that permeability measurements were taken at nearly atmospheric pore pressure, the effective pressure can be approximated by the confining pressure on the fractured specimen ($P_e \approx P_c$). We normalized our measured values to those at 500 psi, and the outcomes are depicted in **Figure 93** and **Figure 94** for both water and CO_2-fracture induced samples. The data show a strong alignment with Walsh analytical equation. In **Table 16** the calculated Walsh parameters for all S1 tests are listed. The results suggest that the permeability observed in the fractured plugs is primarily influenced by the fracture itself, with minimal impact from the matrix. The resulting values for the slope as shown in **Table 16** are similar to that reported by Kassis and Sondergeld (2010) and Damani (2013). The slope for CO_2-induced fractures is slightly higher than for water-induced fractures.

Table 16. Walsh correlation constant and coeficient of correlation for left- and righ- wing fractured plugs.

Sample/test ID	Injectate	Saturation state	Walsh correlation			
			Left plug		Right plug	
			Constant $[\frac{\sqrt{2h}}{a_o}]$	R^2	Constant $[\frac{\sqrt{2h}}{a_o}]$	R^2
1	Water	Brine	0.306	0.98	N/A	N/A
2	Water	Brine	0.315	0.99	0.254	0.99
3	Water	Brine	N/A	N/A	N/A	N/A
4	CO_2	Brine	0.323	0.99	0.310	0.98
5	CO_2	Brine	0.343	0.98	0.311	0.98

6	CO_2	Brine	N/A	N/A	0.316	0.99
7	CO_2	Brine+CO_2	N/A	N/A	N/A	N/A
8	CO_2	Brine+CO_2	N/A	N/A	N/A	N/A

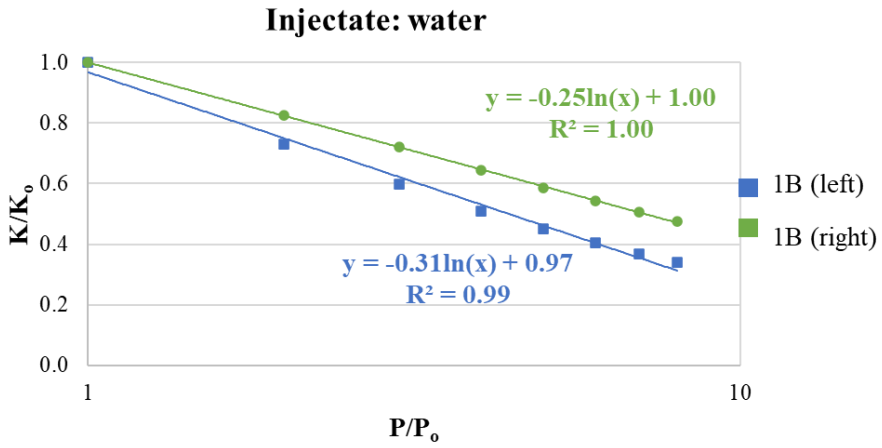

Figure 93. Walsh correlation plot for water-induced left- and right-wing fracture permeability. The high correlation coefficient values suggest that the fracture is the main contributor to permeability.

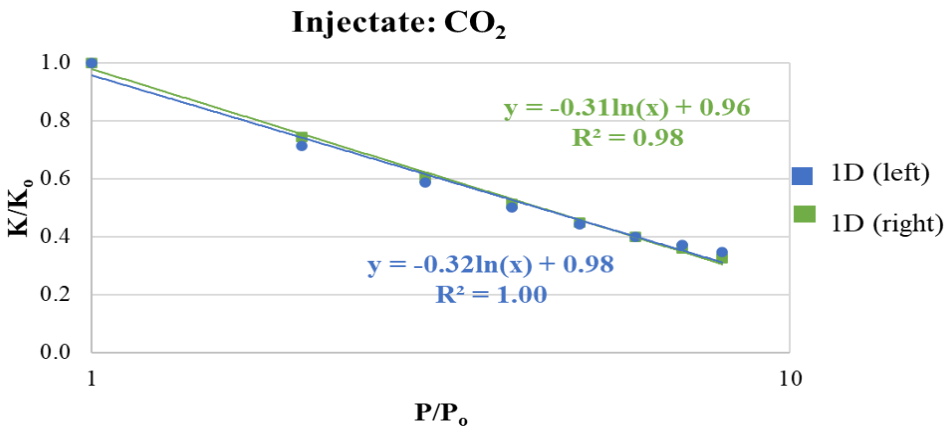

Figure 94. Walsh correlation plot for CO_2-induced left- and right-wing fracture permeability. The high correlation coefficient values suggest that the fracture is the main contributor to permeability.

5. CONCLUSIONS

Laboratory experiments were conducted on 4" x 5.5" cylindrical sandstone samples having varying petrophysical and elastic properties. Some samples were exposed to CO_2 for several weeks prior to measurements. Our over-arching aim was to investigate how CO_2 injection influence sandstone rock fracturing as compared to water and the implication for geosequestration. The following major conclusions can be made.

1) CO_2 injection consistently induced breakdown at a lower pressure than water injection. However, the percentage reduction varied across different rock samples, a variance seemingly linked to the elastic modulus of each rock. Breakdown pressure increases with the modulus. Rocks exposed to CO_2 exhibited similar breakdown pressures to those which were not exposed, indicating minimal geochemical changes likely due to the absence of carbonate minerals.
2) CO_2 injection created fractures that were notably longer, more tortuous, and displayed secondary branching. These fractures propagated in all directions (top, bottom, left, and right sides) of the sample. Microscopic analysis revealed that CO_2-induced fractures exhibited characteristics such as several loose grains, rough edges, secondary branching, and greater process zones.
3) CO_2-induced fracturing induced much more AEs than water-induced fracturing. These AE events had a low percentage of location but a wider distribution around the fracture plane. CO_2 induced AE events had slightly higher event magnitudes in some cases but generally the AE magnitude, focal mechanism and frequency were similar to that of water induced events.

4) CO_2-induced fracture permeability was found to be at least an order of magnitude higher than water-induced fracture permeability. This indicates that CO_2 fractures can be more transmissive to facilitate the migration of fluids.

For geosequestration application, it is important to recognize that CO_2 injection will induce breakdown at a pressure lower than estimated from leak-off tests (using water-based fluid). For quartz-rich sandstone, exposure to CO_2 for a prolong period of time will not change the formations geomechanical response to fluid injection due to minimal geochemical alterations. Therefore, it is expected that the breakdown pressure of the rock after years of injection will remain similar to breakdown prior to injection. Moreover, operators cannot determine the appropriate maximum allowable injection pressure by reducing the estimated breakdown pressure from leak-off tests by a fixed amount since different rocks have difference response to CO_2. Such determination can either underestimate or overestimate the breakdown pressure which can lead to either a non-optimized injectivity or compromising formation integrity. Fractures generated by CO_2 are extensive and transmissive to facilitate CO_2 migration. The insignificant difference of AE magnitudes, focal mechanism and frequency induced by water and CO_2 injection means that some lessons learnt from the abundant experience of conventional water injection can be applied to geosequestration. Understanding the precise breakdown pressure of formations under CO_2 injection is crucial for optimizing injectivity, which in turn will impact economic viability and environmental safety of such operations. Laboratory experiments provide a controlled means to determine rock response to CO_2 injection.

For reservoir stimulation application, CO_2 as a fracturing fluid has the potential to lower operations cost (lower breakdown), increase production (greater stimulated reservoir volume), and minimize environmental impacts (elimination of flow-back water disposal).

6. REFERENCES

1) Aso, I. 2009. Microseismic mapping of hydraulic fractures. Master Thesis, University of Oklahoma. ShareOK. https://shareok.org/handle/11244/331250
2) Bachu, S. 2015. Review of CO_2 storage efficiency in deep saline aquifers. International Journal of Greenhouse Gas Control, 40, 188-202. https://doi.org/https://doi.org/10.1016/j.ijggc.2015.01.007
3) Bachu, S., and Shaw, J. 2003. Evaluation of the CO_2 Sequestration Capacity in Alberta's Oil and Gas Reservoirs at Depletion and the Effect of Underlying Aquifers. Journal of Canadian Petroleum Technology, 42(09). https://doi.org/10.2118/03-09-02
4) Bachu, S., and Stewart, S. 2002. Geological Sequestration of Anthropogenic Carbon Dioxide in the Western Canada Sedimentary Basin: Suitability Analysis. Journal of Canadian Petroleum Technology, 41(02). https://doi.org/10.2118/02-02-01
5) Baines, S. J., and Worden, R. H. 2004. Geological storage of carbon dioxide. Geological Society, London, Special Publications, 233(1), 1-6. https://doi.org/doi:10.1144/GSL.SP.2004.233.01.01
6) Batjes, N. H. 1998. Mitigation of atmospheric CO_2 concentrations by increased carbon sequestration in the soil. Biology and Fertility of Soils, 27(3), 230-235. https://doi.org/10.1007/s003740050425
7) Bennour, Z., Ishida, T., Nagaya, Y., Nara, Y., Chen, Y., Chen, Q., Nakayama, Y., Sekine, K., and Nagano, Y. 2014. Fracture Development and Mechanism in Shale Cores by Viscous Oil, Water and L-CO_2 Injection. 48th U.S. Rock Mechanics/Geomechanics Symposium,
8) Benson, S. M., and Cole, D. R. 2008. CO_2 sequestration in deep sedimentary formations. Elements, 4(5), 325-331.
9) Benson, S. M., Hepple, R., Apps, J., Tsang, C. F., and Lippmann, M. 2002. Lessons learned from natural and industrial analogues for storage of carbon dioxide in deep geological formations. . Lawrence Berkeley National Laboratory Report LBNL-51170.
10) Bergman, P. D., and Winter, E. M. 1995. Disposal of carbon dioxide in aquifers in the U.S. Energy Conversion and Management, 36(6), 523-526. https://doi.org/https://doi.org/10.1016/0196-8904(95)00058-L

11) Biot, M. A. 1956. General solutions of the equations of elasticity and consolidation for a porous material. ASME. J. Appl. Mech. March 1956; 23(1): 91–96. https://doi.org/10.1115/1.4011213
12) Boyd, P. W., Law, C. S., Wong, C. S., Nojiri, Y., Tsuda, A., Levasseur, M., Takeda, S., Yoshimura, T. 2004. The decline and fate of an iron-induced subarctic phytoplankton bloom. Nature, 428(6982), 549-553. https://doi.org/10.1038/nature02437
13) Chitrala, Y. 2011. Laboratory study of fluid induced hydraulic fractures - hypocenter locations, source mechanism, frequency analysis and microscopic observations. Master Thesis, University of Oklahoma. ShareOK.
14) Clift, R. 2007. Climate change and energy policy: The importance of sustainability arguments. Energy, 32(4), 262-268. https://doi.org/https://doi.org/10.1016/j.energy.2006.07.031
15) Damani, A., Sharma, A., Sondergeld, C., and Rai, C. 2012. Mapping of hydraulic fractures under triaxial stress conditions in laboratory experiments using acoustic emissions. In SPE Annual Technical Conference and Exhibition. SPE-159604. SPE.
16) Damani, A., Sondergeld, C. H., and Rai, C. S. 2018. Experimental investigation of in situ and injection fluid effect on hydraulic fracture mechanism using acoustic emission in Tennessee sandstone. Journal of Petroleum Science and Engineering, 171, 315-324. https://doi.org/https://doi.org/10.1016/j.petrol.2018.07.027
17) Davidson, J., Freund, P., and Smith, A. 2001. Putting carbon back in the ground. IEA Greenhouse Gas R and D Programme, Stoke Orchard (United Kingdom). https://doi.org/https://doi.org/
18) Deng, J., Zhao, G., Zhang, L., Ma, H., Song, F., Cao, Q., and Zhang, X. 2021. Simple and accurate calculation model of viscosity for supercritical CO_2. In Journal of Physics: Conference Series (Vol. 2076, No. 1, p. 012030). IOP Publishing.
19) Duchkov, A. D. 2006. Characteristics of Permafrost in Siberia. Kluwer Academic Publishers. https://doi.org/10.1007/1-4020-4471-2_08
20) Eakins, P. R. 1987. Faults and faulting. In Structural Geology and Tectonics (pp. 228-239). Springer Berlin Heidelberg. https://doi.org/10.1007/3-540-31080-0_39

21) Edenhofer, O., Pichs-Madruga, R., Sakona, Y., Minx, J. C., Farahani. E., Kadner, S., Seyboth, K., Adler, A. et al. 2015. Climate change 2014: mitigation of climate change (Vol. 3). Cambridge University Press.
22) Falkowski, P. G. 1997. Evolution of the nitrogen cycle and its influence on the biological sequestration of CO_2 in the ocean. Nature, 387(6630), 272-275.
23) Fan, S., Gloor, M., Mahlman, J., Pacala, S., Sarmiento, J., Takahashi, T., and Tans, P. 1998. A large terrestrial carbon sink in North America implied by atmospheric and oceanic carbon dioxide data and models. Science, 282(5388), 442-446.
24) Fang, J., Chen, A., Peng, C., Zhao, S., and Ci, L. 2001. Changes in forest biomass carbon storage in China between 1949 and 1998. Science, 292(5525), 2320-2322.
25) Finley, R. J., Gustison, S. R., and Leetaru, H. E. 2005. Geological considerations for CO_2 sequestration in a cratonic basin: An assessment of options in the Illinois Basin, USA. In Greenhouse Gas Control Technologies 7 (pp. 1339-1344). Elsevier.
26) Fuss, S., Lamb, W. F., Callaghan, M. W., Hilaire, J., Creutzig, F., Amann, T., Beringer, T., de Oliveira Garcia, W., Hartmann, J., and Khanna, T. 2018. Negative emissions-Part 2: Costs, potentials and side effects. Environmental research letters, 13(6), 063002.
27) Garnett, M. H., Ineson, P., Stevenson, A. C., and Howard, D. C. 2001. Terrestrial organic carbon storage in a British moorland. Global Change Biology, 7(4), 375-388.
28) Haimson, B., and Fairhurst, C. 1969. In-situ stress determination at great depth by means of hydraulic fracturing. ARMA US Rock Mechanics/Geomechanics Symposium,
29) Haugan, P. M., and Drange, H. 1992. Sequestration of $C0_2$ in the deep ocean by shallow injection. Nature, 357(6376), 318-320.
30) Hayhoe, K., Wuebbles, D. J., Easterling, D. R., Fahey, D. W., Doherty, S., Kossin, J. P., Sweet, W. V., Vose, R. S., and Wehner, M. F. 2018. Our changing climate. impacts, risks, and adaptation in the united states: The fourth national climate assessment, volume II.
31) Heidaryan, E., Hatami, T., Rahimi, M., and Moghadasi, J. 2011. Viscosity of pure carbon dioxide at supercritical region: Measurement and correlation approach. The Journal of Supercritical Fluids, 56(2), 144-151.

32) Hepple, R., and Benson, S. 2005. Geologic storage of carbon dioxide as a climate change mitigation strategy: performance requirements and the implications of surface seepage. Environmental Geology, 47, 576-585.
33) Holloway, S. 1996. An overview of the Joule II project the underground disposal of carbon dioxide. Fuel and Energy Abstracts,
34) Holtz, M. H. 2002. Residual gas saturation to aquifer influx: A calculation method for 3-D computer reservoir model construction. SPE Unconventional Resources Conference/Gas Technology Symposium,
35) Hubbert, M. K., and Willis, D. G. 1957. Mechanics of hydraulic fracturing. Transactions of the AIME, 210(01), 153-168.
36) Ishida, T., Aoyagi, K., Niwa, T., Chen, Y., Murata, S., Chen, Q., and Nakayama, Y. 2012. Acoustic emission monitoring of hydraulic fracturing laboratory experiment with supercritical and liquid CO_2. Geophysical Research Letters, 39(16).
37) Ishida, T., Chen, Y., Bennour, Z., Yamashita, H., Inui, S., Nagaya, Y., Naoi, M., Chen, Q., Nakayama, Y., and Nagano, Y. 2016. Features of CO_2 fracturing deduced from acoustic emission and microscopy in laboratory experiments. Journal of Geophysical Research: Solid Earth, 121(11), 8080-8098.
38) Jadhawar, P., Mohammadi, A. H., Yang, J., and Tohidi, B. 2006. Subsurface carbon dioxide storage through clathrate hydrate formation. Advances in the Geological Storage of Carbon Dioxide: International Approaches to Reduce Anthropogenic Greenhouse Gas Emissions,
39) King, M. S. 1969. Static and dynamic elastic moduli of rocks under pressure. In ARMA US Rock Mechanics/Geomechanics Symposium (pp. ARMA-69). ARMA.
40) Kizaki, A., Ohashi, K., Tanaka, H., and Sakaguchi, K. 2013. Effects of vertical stress on fracture propagation using super critical carbon dioxide. ISRM EUROCK,
41) Lal, R. 2004. Soil carbon sequestration impacts on global climate change and food security. Science, 304(5677), 1623-1627.
42) Lal, R. 2008. Carbon sequestration. Philosophical Transactions of the Royal Society B: Biological Sciences, 363(1492), 815-830.
43) Lamb, D., Erskine, P. D., and Parrotta, J. A. 2005. Restoration of degraded tropical forest landscapes. Science, 310(5754), 1628-1632.

44) Lee, H., Calvin, K., Dasgupta, D., Krinner, G., Mukherji, A., Thorne, P., Trisos, C., Romero, J., Aldunce, P., and Barrett, K. 2023. Climate Change 2023: Synthesis Report. Contribution of Working Groups I, II and III to the Sixth Assessment Report of the Intergovernmental Panel on Climate Change.
45) Li, S., Zhang, S., Zou, Y., Ye, L., Ma, X., Ge, Q., Zhou, J., and Zhang, Z. 2018. Experimental study on the features of hydraulic fracture created by slickwater, liquid carbon dioxide, and supercritical carbon dioxide in tight sandstone reservoirs. ARMA US Rock Mechanics/Geomechanics Symposium,
46) Maphala, T., and Wagner, N. J. 2012. Effects of CO_2 storage in coal on coal properties. Energy Procedia, 23, 426-438.
47) Martin, J. H., and Fitzwater, S. E. 1988. Iron deficiency limits phytoplankton growth in the north-east Pacific subarctic. Nature, 331(6154), 341-343.
48) Melnikov, V. P., and Drozdov, D. S. 2006. Distribution of permafrost in Russia. In Advances in the Geological Storage of Carbon Dioxide: International Approaches to Reduce Anthropogenic Greenhouse Gas Emissions (pp. 67-80). Springer Netherlands.
49) Metz, B., Davidson, O., De Coninck, H., Loos, M., and Meyer, L. 2005. IPCC special report on carbon dioxide capture and storage. Cambridge: Cambridge University Press.
50) Milne, R., and Brown, T. 1997. Carbon in the vegetation and soils of Great Britain. Journal of Environmental Management, 49(4), 413-433.
51) Minasny, B., Malone, B. P., McBratney, A. B., Angers, D. A., Arrouays, D., Chambers, A., Chaplot, V., Chen, Z.-S., Cheng, K., and Das, B. S. 2017. Soil carbon 4 per mille. Geoderma, 292, 59-86.
52) Mistry, A. N., Ganta, U., Chakrabarty, J., and Dutta, S. 2019. A review on biological systems for CO_2 sequestration: organisms and their pathways. Environmental Progress and Sustainable Energy, 38(1), 127-136.
53) Nahlik, A. M., and Fennessy, M. S. 2016. Carbon storage in US wetlands. Nature Communications, 7(1), 1-9.
54) Nowack, R. L. 2023. Seismic Sources Represented by Moment Tensors. Introduction to Seismology. https://web.ics.purdue.edu/~nowack/geos557/lecture12-dir/lecture12.htm

55) Oldenburg, C., 2007. Migration mechanisms and potential impacts of CO_2 leakage and seepage. In: Wilson, E.J., Gerard, D. (Eds.), Carbon Capture and Sequestration: Integrating Technology, Monitoring, Regulation. Blackwell Publishing, pp. 127–146.
56) Ono, E., and Cuello, J. L. 2003. Selection of optimal microalgae species for CO_2 sequestration. Proceedings of Second Annual Conference on Carbon Sequestration.
57) Pan, G., Smith, P., and Pan, W. 2009. The role of soil organic matter in maintaining the productivity and yield stability of cereals in China. Agriculture, Ecosystems and Environment, 129(1-3), 344-348.
58) Qi, J., Marshall, J. D., and Mattson, K. G. 1994. High soil carbon dioxide concentrations inhibit root respiration of Douglas fir. New Phytologist, 128(3), 435-442.
59) Ringrose, P., Mathieson, A., Wright, I., Selama, F., Hansen, O., Bissell, R., Saoula, N., and Midgley, J. 2013. The In Salah CO_2 storage project: lessons learned and knowledge transfer. Energy Procedia, 37, 6226-6236.
60) Sampath, K., Perera, M., Ranjith, P., and Stephan, S. 2018. Evaluation of superiority of liquid CO_2 as a non-aqueous fracturing fluid for coal seam gas extraction. ARMA US Rock Mechanics/Geomechanics Symposium,
61) Schleussner, C. F., Lissner, T. K., Fischer, E. M., Wohland, J., Perrette, M., Golly, A., ... and Schaeffer, M. 2016. Differential climate impacts for policy-relevant limits to global warming: the case of 1.5 C and 2 C. Earth system dynamics, 7(2), 327-351.
62) Shan, W., Tiantai, L., Hongkui, G., Xiaoqiong, W., Ning, L., Mingsheng, Z., Shiyu, L., and Yueyue, S. 2019. Comparison of the AE monitoring results between the hydraulic fracturing and sc-CO_2 fracturing. ARMA US Rock Mechanics/Geomechanics Symposium,
63) Sheps, K., Max, M., Osegovic, J., Tatro, S., and Brazel, L. 2009. A case for deep-ocean CO_2 sequestration. Energy Procedia, 1(1), 4961-4968.
64) Siirila, E. R., Navarre-Sitchler, A. K., Maxwell, R. M., and McCray, J. E. 2012. A quantitative methodology to assess the risks to human health from CO_2 leakage into groundwater. Advances in Water Resources, 36, 146-164.
65) Sleefe, G., Warpinski, N., and Engler, B. 1995. The use of broadband microseisms for hydraulic-fracture mapping. SPE Formation Evaluation, 10(04), 233-239.

66) Snæbjörnsdóttir, S. Ó., Sigfússon, B., Marieni, C., Goldberg, D., Gislason, S. R., and Oelkers, E. H. 2020. Carbon dioxide storage through mineral carbonation. Nature Reviews Earth and Environment, 1(2), 90-102.
67) Solomon, S. 2007. Climate change 2007-the physical science basis: Working group I contribution to the fourth assessment report of the IPCC (Vol. 4). Cambridge university press.
68) Span, R., and Wagner, W. 1996. A new equation of state for carbon dioxide covering the fluid region from the triple-point temperature to 1100 K at pressures up to 800 MPa. Journal of physical and chemical reference data, 25(6), 1509-1596.
69) Stern, N. 2008. The economics of climate change. American Economic Review, 98(2), 1-37.
70) Stevens, S., Kuuskraa, V., Spector, D., and Riemer, P. 1999. CO_2 sequestration in deep coal seams: pilot results and worldwide potential Greenhouse Gas Control Technologies. In: Oxford: Pergamon.
71) Stork, A. L., Verdon, J. P., and Kendall, J.-M. 2015. The microseismic response at the In Salah Carbon Capture and Storage (CCS) site. International Journal of Greenhouse Gas Control, 32, 159-171.
72) Thanh, H. V., and Lee, K.-K. 2022. Application of machine learning to predict CO_2 trapping performance in deep saline aquifers. Energy, 239, 122457.
73) Torp, T. A., and Gale, J. 2004. Demonstrating storage of CO_2 in geological reservoirs: The Sleipner and SACS projects. Energy, 29(9-10), 1361-1369.
74) Verdon, J. 2011. Microseismic monitoring and geomechanical modeling of CO_2 storage in subsurface reservoirs. Geophysics, 76(5), Z102-Z103.
75) Wang, B., Wang, X., Chen, Y., Liang, Q., and Zeng, F. 2023. A Review-Dissolution and Mineralization Storage of CO_2 Geological Storage in Saline Aquifers. In SPE Canadian Energy Technology Conference (p. D012S008R001). SPE.
76) Wang, L., Yao, B., Xie, H., Winterfeld, P. H., Kneafsey, T. J., Yin, X., and Wu, Y.-S. 2017. CO_2 injection-induced fracturing in naturally fractured shale rocks. Energy, 139, 1094-1110.

77) Wang, S., and Jaffe, P. R. 2004. Dissolution of a mineral phase in potable aquifers due to CO_2 releases from deep formations; effect of dissolution kinetics. Energy Conversion and Management, 45(18-19), 2833-2848.
78) Watson, R. T., Noble, I. R., Bolin, B., Ravindranath, N. H., Verardo, D. J., and Dokken, D. J. 2000. Land use, land-use change and forestry: a special report of the Intergovernmental Panel on Climate Change. Cambridge University Press.
79) Yang, J., Liang, W., Lian, H., Chen, Y., and Li, L. 2018. Influence of the different fluids on the hydraulic fracturing mechanism of sandy mudstone. ISRM International Symposium-Asian Rock Mechanics Symposium,
80) Zhang, X., Lu, Y., Tang, J., Zhou, Z., and Liao, Y. 2017. Experimental study on fracture initiation and propagation in shale using supercritical carbon dioxide fracturing. Fuel, 190, 370-378.
81) Zhao, H., Fedkin, M. V., Dilmore, R. M., and Lvov, S. N. 2015. Carbon dioxide solubility in aqueous solutions of sodium chloride at geological conditions: Experimental results at 323.15, 373.15, and 423.15 K and 150 bar and modeling up to 573.15 K and 2000 bar. Geochimica et Cosmochimica Acta, 149, 165-189.
82) Zhao, H., Fedkin, M. V., Dilmore, R. M., and Lvov, S. N. 2015. Carbon dioxide solubility in aqueous solutions of sodium chloride at geological conditions: Experimental results at 323.15, 373.15, and 423.15 K and 150 bar and modeling up to 573.15 K and 2000 bar. Geochimica et Cosmochimica Acta, 149, 165-189.
83) Zhao, H., Liao, X., Chen, Y., and Zhao, X. 2010. Sensitivity analysis of CO_2 sequestration in saline aquifers. Petroleum Science, 7, 372-378.
84) Zhou, J., Liu, G., Jiang, Y., Xian, X., Liu, Q., Zhang, D., and Tan, J. 2016. Supercritical carbon dioxide fracturing in shale and the coupled effects on the permeability of fractured shale: An experimental study. Journal of Natural Gas Science and Engineering, 36, 369-377.
85) Zhou, X., and Burbey, T. J. 2014. Fluid effect on hydraulic fracture propagation behavior: a comparison between water and supercritical CO_2-like fluid. Geofluids, 14(2), 174-188.

86) Zou, Y., Li, N., Ma, X., Zhang, S., and Li, S. 2018. Experimental study on the growth behavior of supercritical CO_2-induced fractures in a layered tight sandstone formation. Journal of Natural Gas Science and Engineering, 49, 145-156.

7. APPENDIX A: EXPERIMENTAL CONDITIONS

The experimental conditions for all the samples are displayed in Table A1. The samples were subject to the same triaxial stresses (σ_v=1500 psi, σ_h=500 psi, σ_H = 3000 psi) and flow rate (10 cc/min).

Table A1. Experimental conditions

Sandstone	Sample ID	Dimensions (mm)				State	Injectate
		Length	Diameter	Borehole depth	Injection depth		
S1	A	135	101.6	61	59	Brine	Water
	B	137	101.6	68	66	Brine	Water
	C	135	101.6	64	62	Brine	Water
	D	133	101.6	60	58	Brine	CO_2
	E	134	101.6	59	57	Brine	CO_2
	F	140	101.6	70	68	Brine	CO_2
	G	140	101.6	70	68	Brine+CO_2 (6 weeks exposure)	CO_2
	H	135	101.6	70	69	Brine+CO_2 (8 weeks exposure)	CO_2
S2	A	131	101.6	62	60	Brine	Water
	B	137	101.6	68	66	Brine	CO_2
S3	A	148	101.6	55	53	Brine	Water
	B	152	101.6	63	61	Brine	CO_2

8. APPENDIX B: PRESSURE AND AE RESPONSES

The pressure and AE responses of S1B-S1D, S1F, and S1H are shown in **Figure -B12**.

Sample 1B

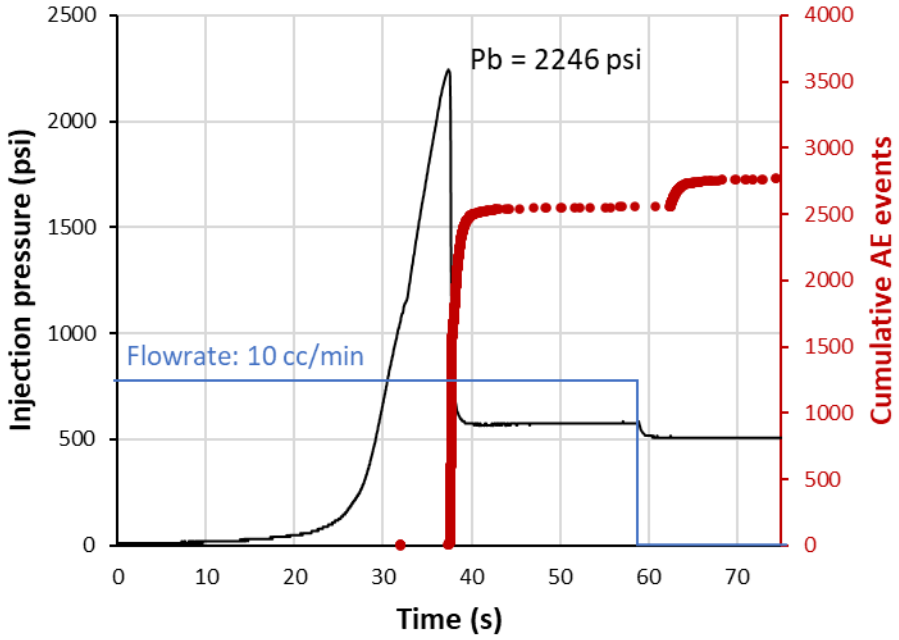

Figure B1. Injection pressure (black line) and cumulative AE events (red dots) versus time for Sample S1B. The blue line shows constant flow rate of 10 cc/min until pump shut-in where it drops to zero.

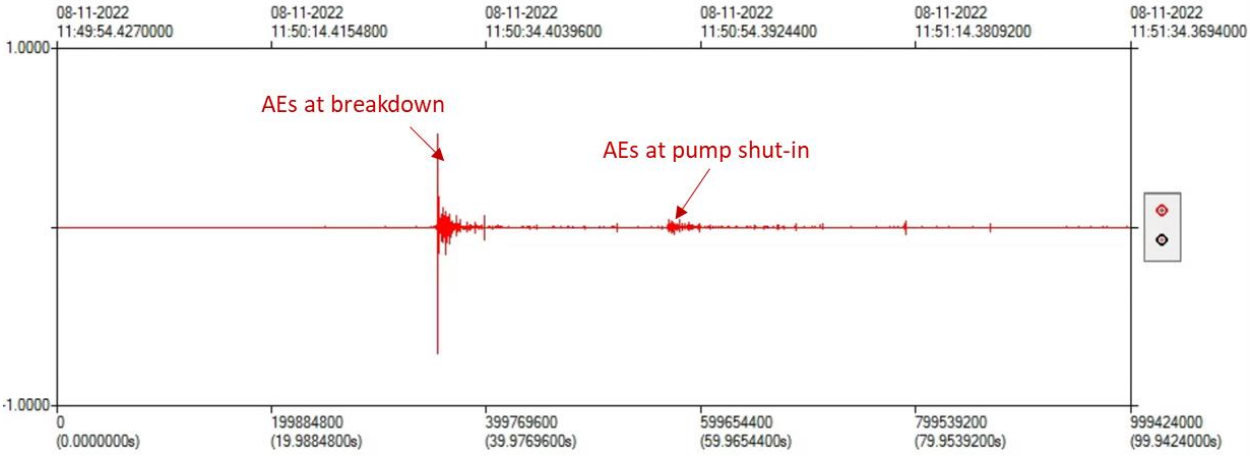

Figure B2. Full waveform of amplitude vs time recorded for one channel at about the same time when injection started for Sample S1B. It shows AE activity as a function of experimental time. The first region can be attributed to breakdown and fracture propagation and the latter to pump shut-in.

Sample ID: 1C

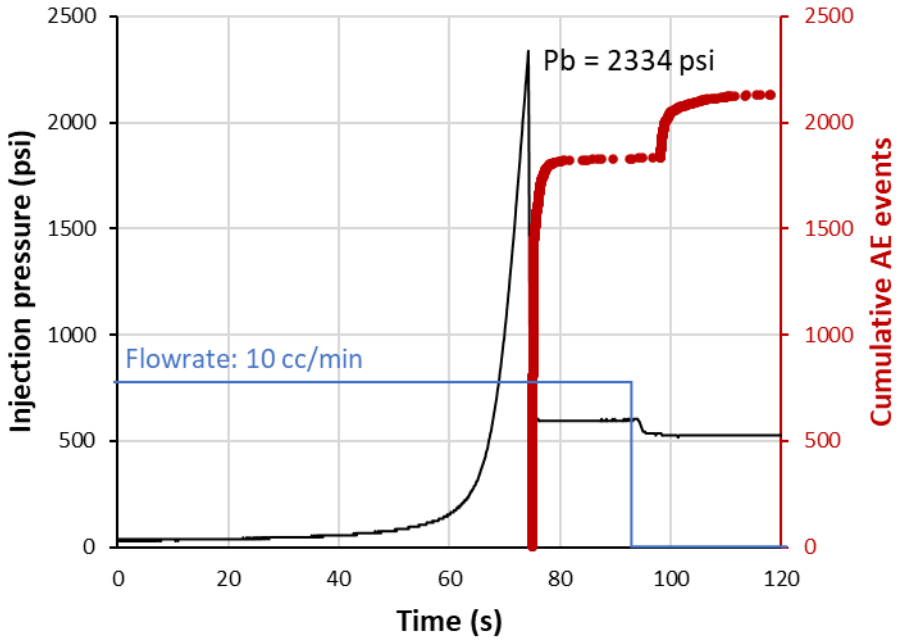

Figure B3. Injection pressure (black line) and cumulative AE events (red dots) versus time for Sample S1C. The blue line shows constant flow rate of 10 cc/min until pump shut-in where it drops to zero.

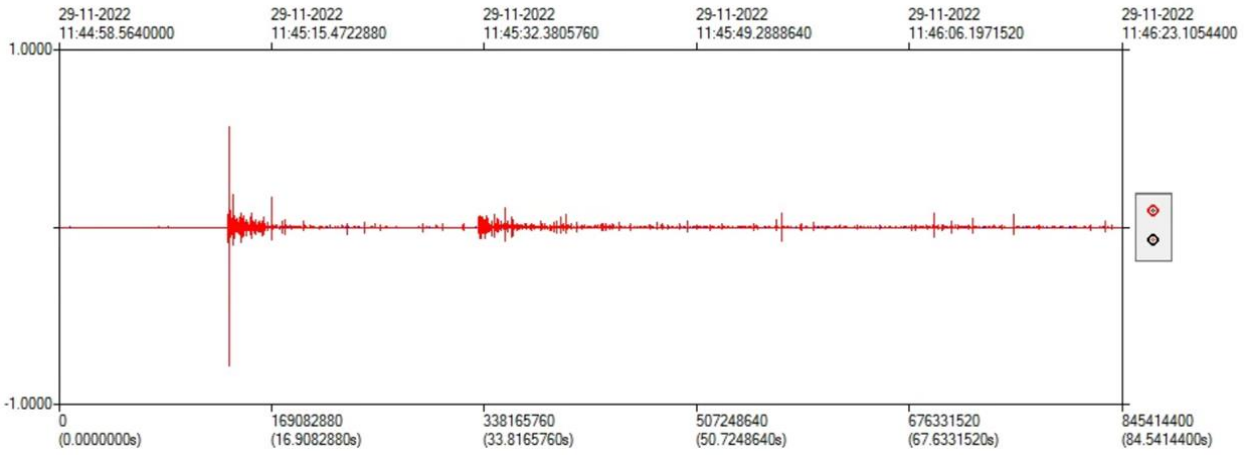

Figure B4. Full waveform of amplitude vs time recorded for one channel at about the same time when injection started for Sample S1C. It shows AE activity as a function of experimental time. The first region can be attributed to breakdown and fracture propagation and the latter to pump shut-in.

Sample 1D

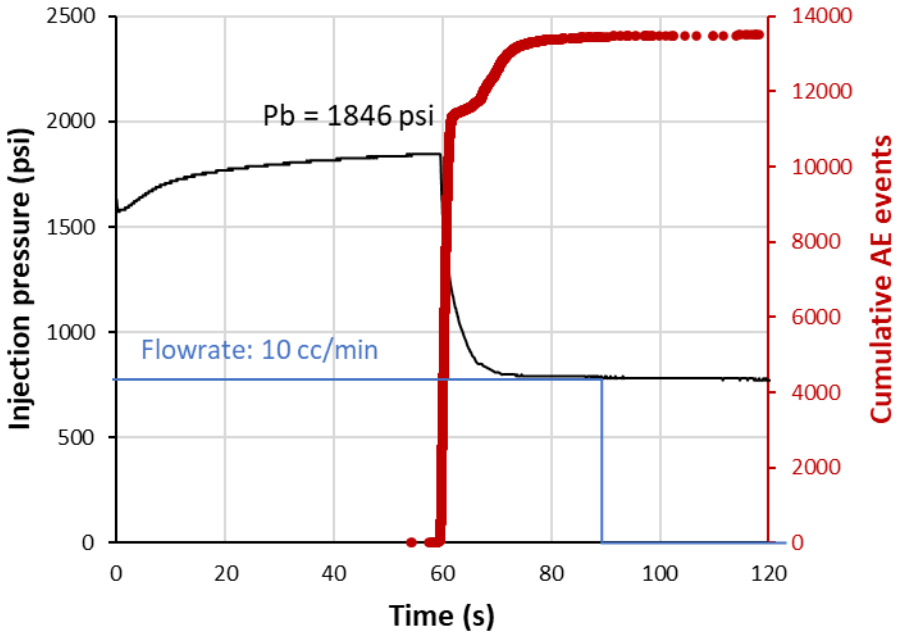

Figure B5. Injection pressure (black line) and cumulative AE events (red dots) versus time for Sample S1D. The blue line shows constant flow rate of 10 cc/min until pump shut-in where it drops to zero.

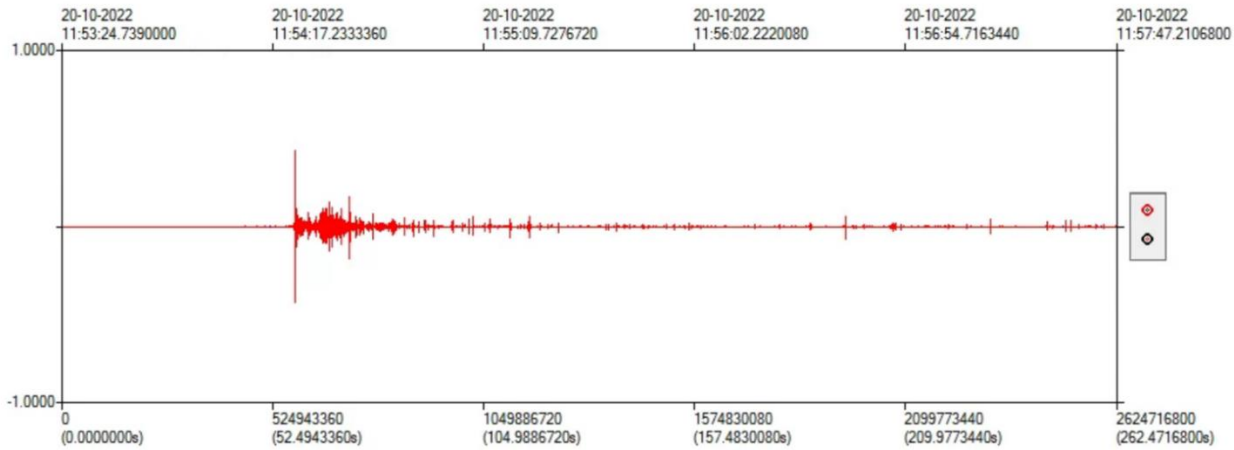

Figure B6. Full waveform of amplitude vs time recorded for one channel at about the same time when injection started for Sample S1D. It shows AE activity as a function of experimental time. The first region can be attributed to breakdown and fracture propagation and the latter to pump shut-in.

Sample 1F

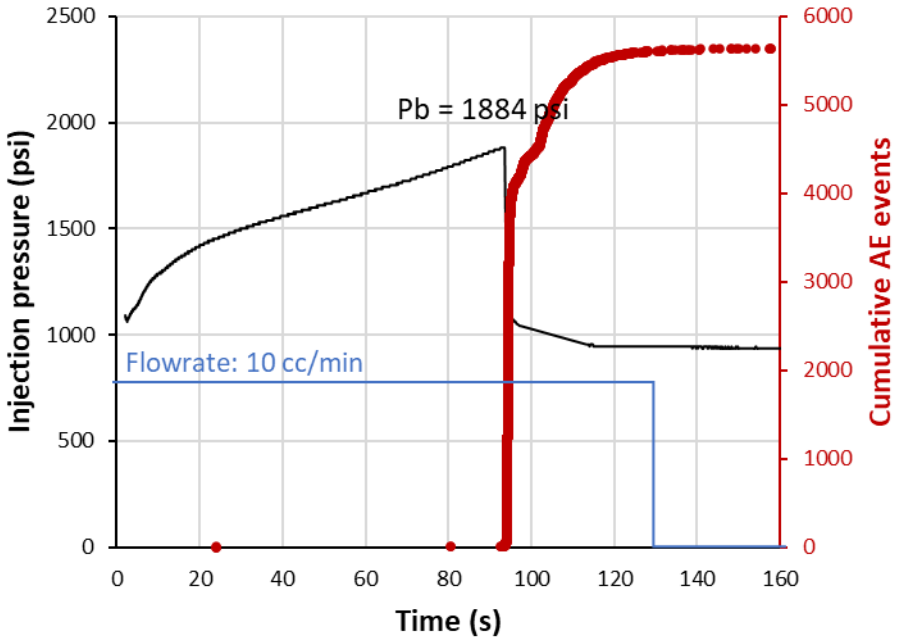

Figure B7. Injection pressure (black line) and cumulative AE events (red dots) versus time for Sample S1F. The blue line shows constant flow rate of 10 cc/min until pump shut-in where it drops to zero.

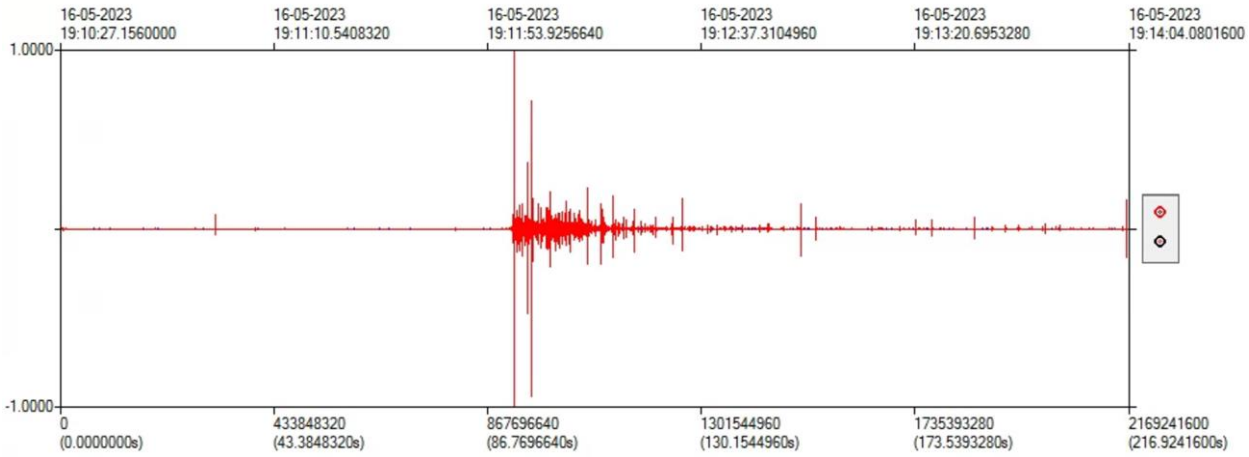

Figure B8. Full waveform of amplitude vs time recorded for one channel at about the same time when injection started for Sample S1F. It shows AE activity as a function of experimental time. The first region can be attributed to breakdown and fracture propagation and the latter to pump shut-in.

Sample 1G

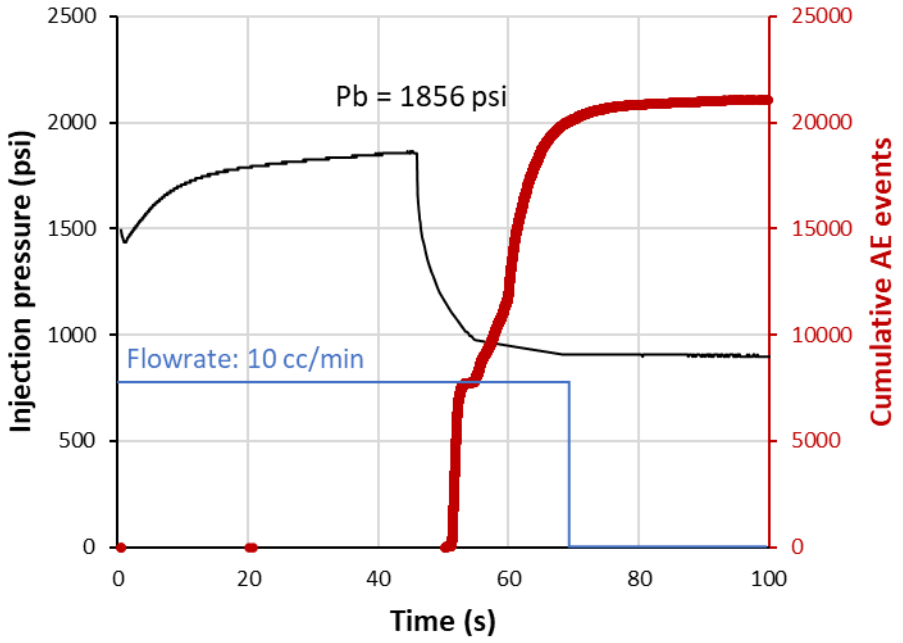

Figure B9. Injection pressure (black line) and cumulative AE events (red dots) versus time for Sample S1G. The blue line shows constant flow rate of 10 cc/min until pump shut-in where it drops to zero.

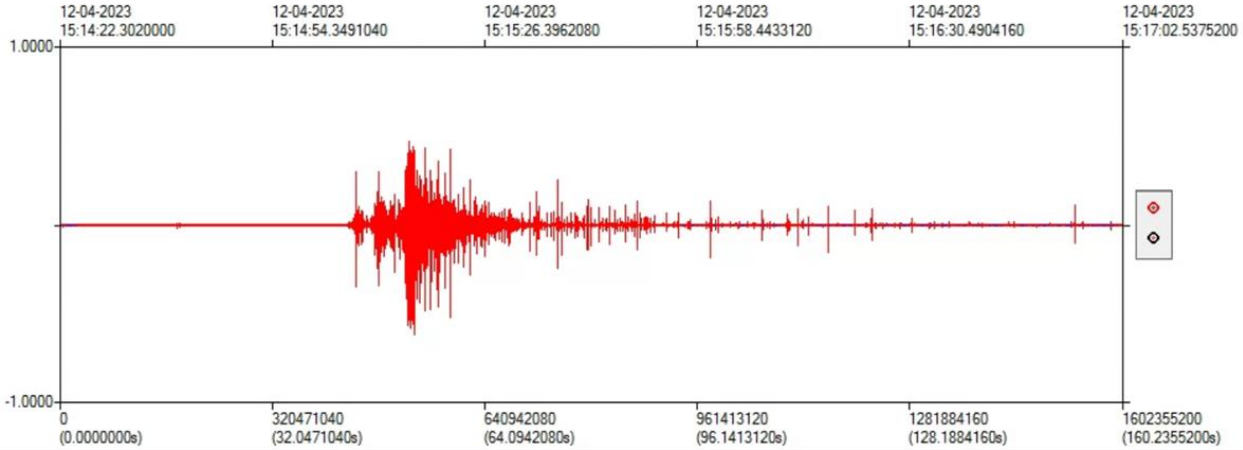

Figure B10. Full waveform of amplitude vs time recorded for one channel at about the same time when injection started for Sample S1G. It shows AE activity as a function of experimental time. The first region can be attributed to breakdown and fracture propagation and the latter to pump shut-in.

Sample 1H

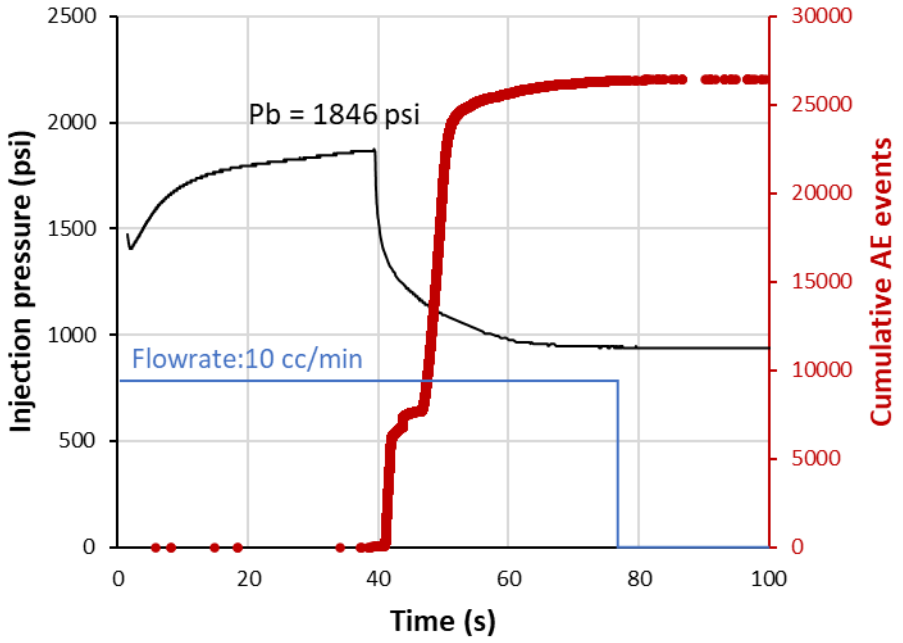

Figure B11. Injection pressure (black line) and cumulative AE events (red dots) versus time for Sample S1H. The blue line shows constant flow rate of 10 cc/min until pump shut-in where it drops to zero.

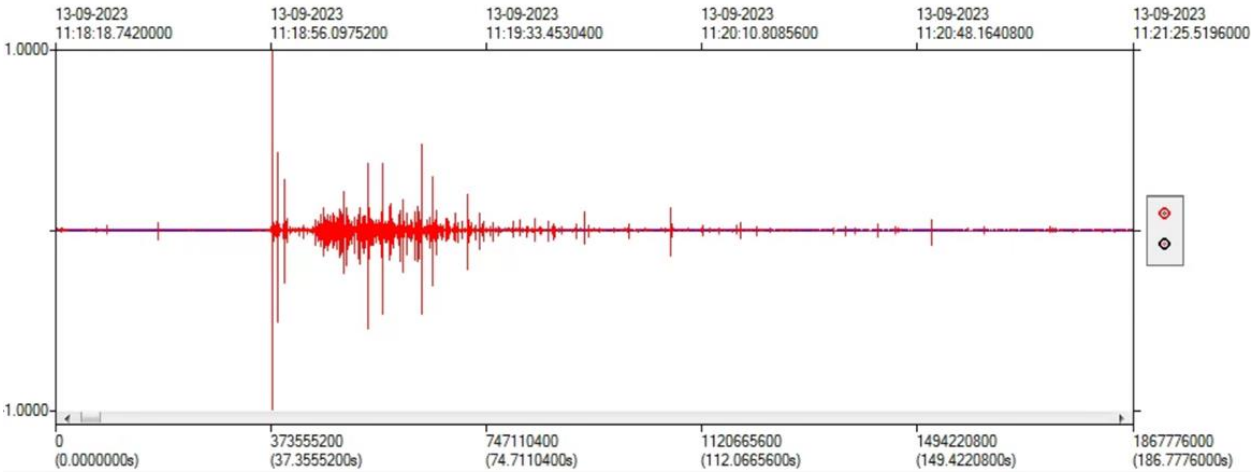

Figure B12. Full waveform of amplitude vs time recorded for one channel at about the same time when injection started for Sample S1H. It shows AE activity as a function of experimental time. The first region can be attributed to breakdown and fracture propagation and the latter to pump shut-in.

9. APPENDIX C: AE LOCATION AND FRACTURE DIMENSION

The AE location and fracture dimensions of S1B-S1D, S1F, and S1H are shown in Figure C1-C10.

Sample 1B

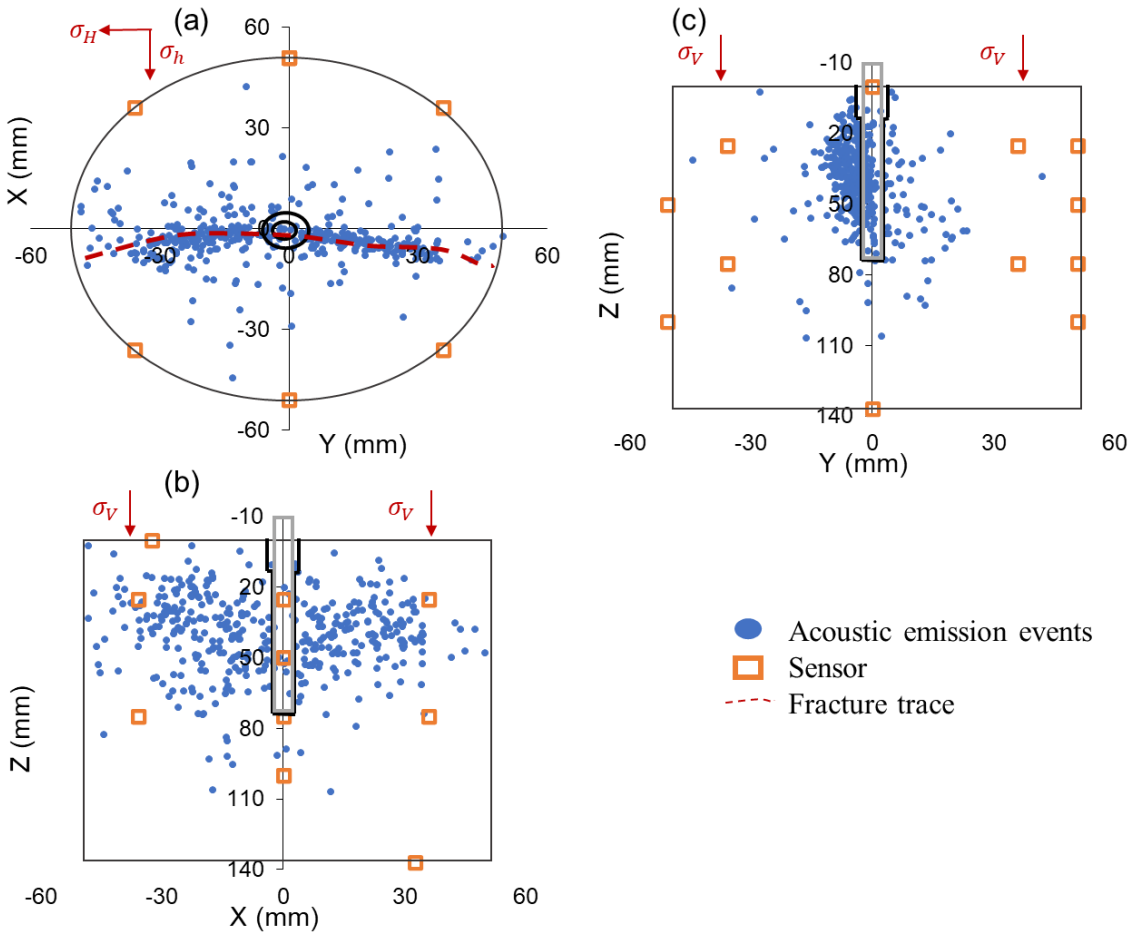

Figure C1. Plot of AEs located in sample S1B fractured with water. The located events are shown in blue, the sesors in orange and the actual fracture trace visible on the bottom surface in red broken line. (a) plan view of AE hypocenter showing a one wing fracture. (b) and (c) are lateral views.

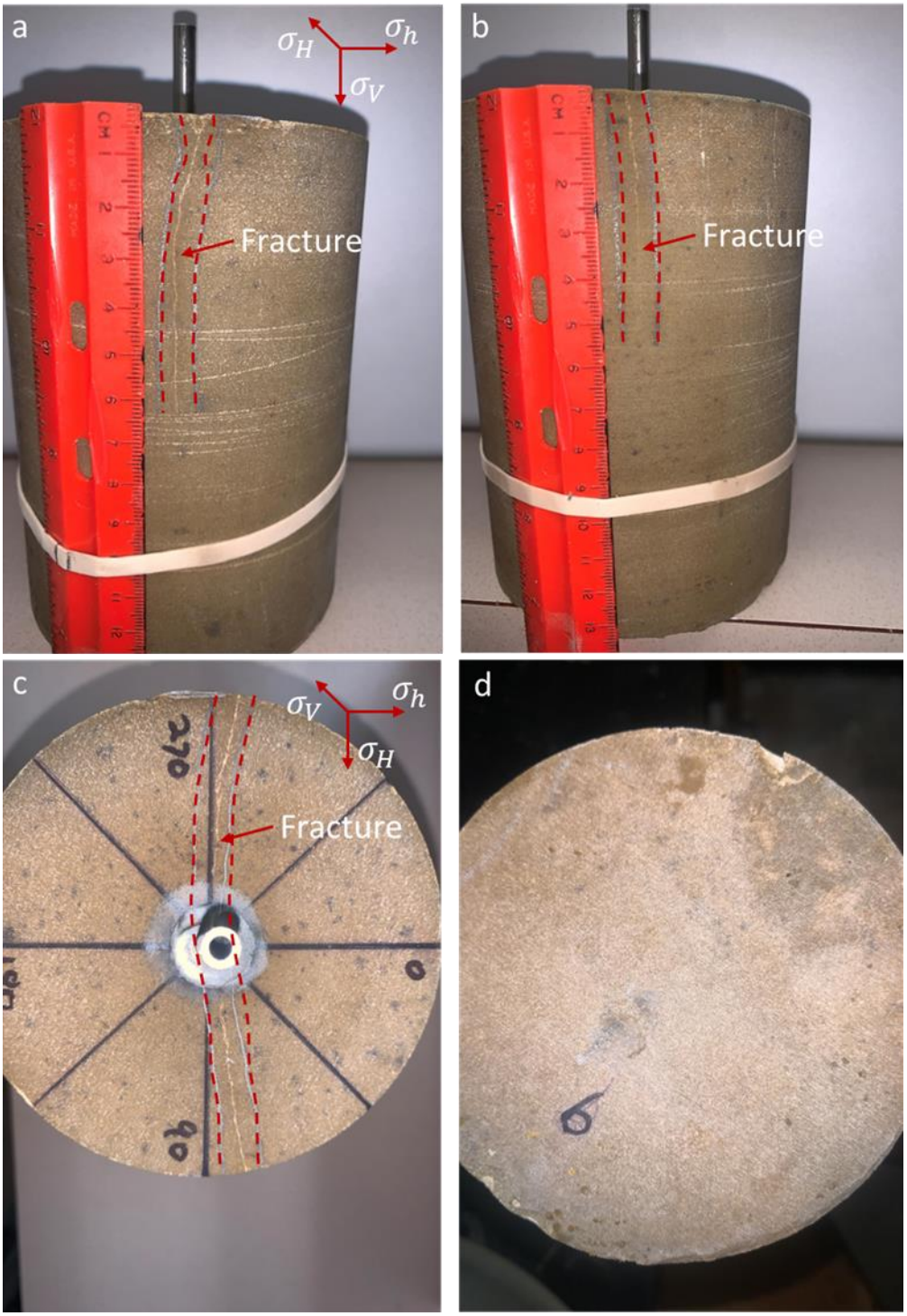

Figure C2. Physical observation of induced fractures in sample S1B fractured with water. The fracture is delineated by the broken red line. (a) and (b) show the side view. (c) and (d) show the bottom and top view.

Sample 1C

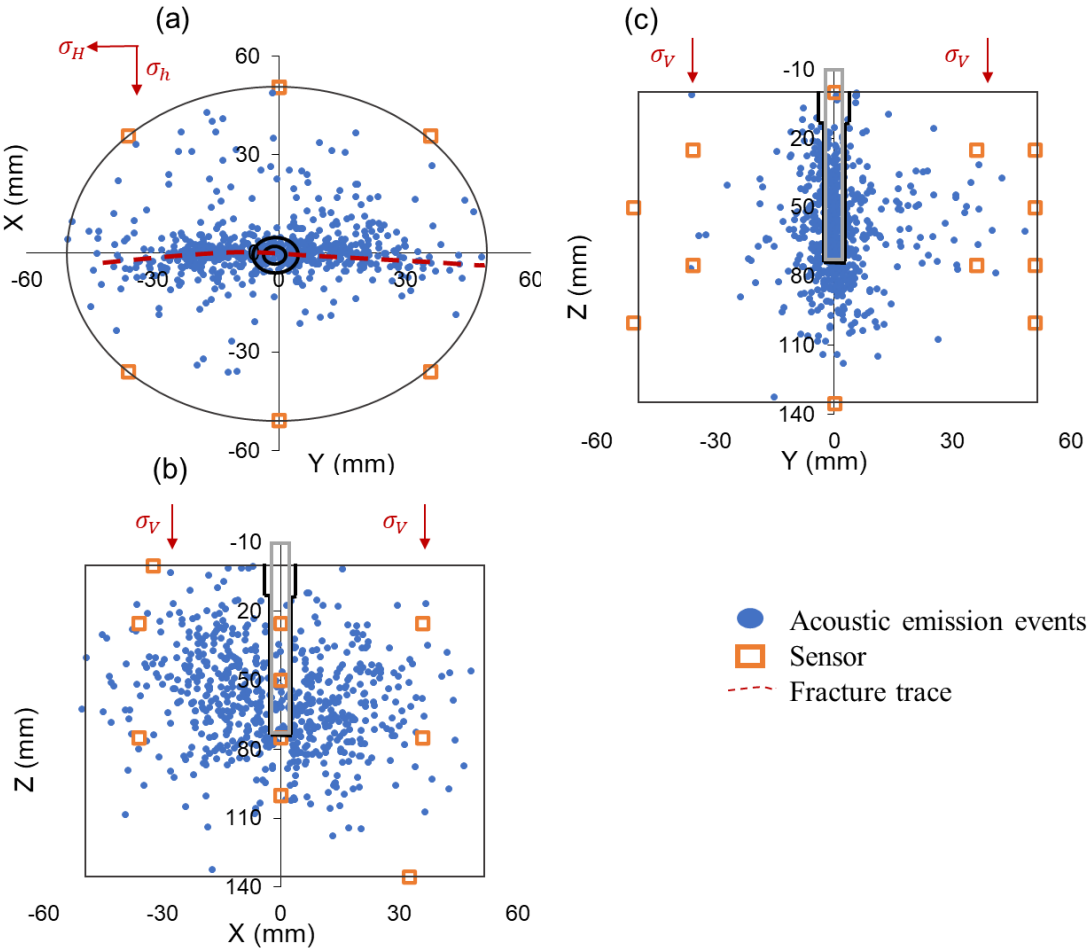

Figure C3. Plot of AEs located in sample S1C fractured with water. The located events are shown in blue, the sesors in orange and the actual fracture trace visible on the bottom surface in red broken line. (a) plan view of AE hypocenter showing a one wing fracture. (b) and (c) are lateral views.

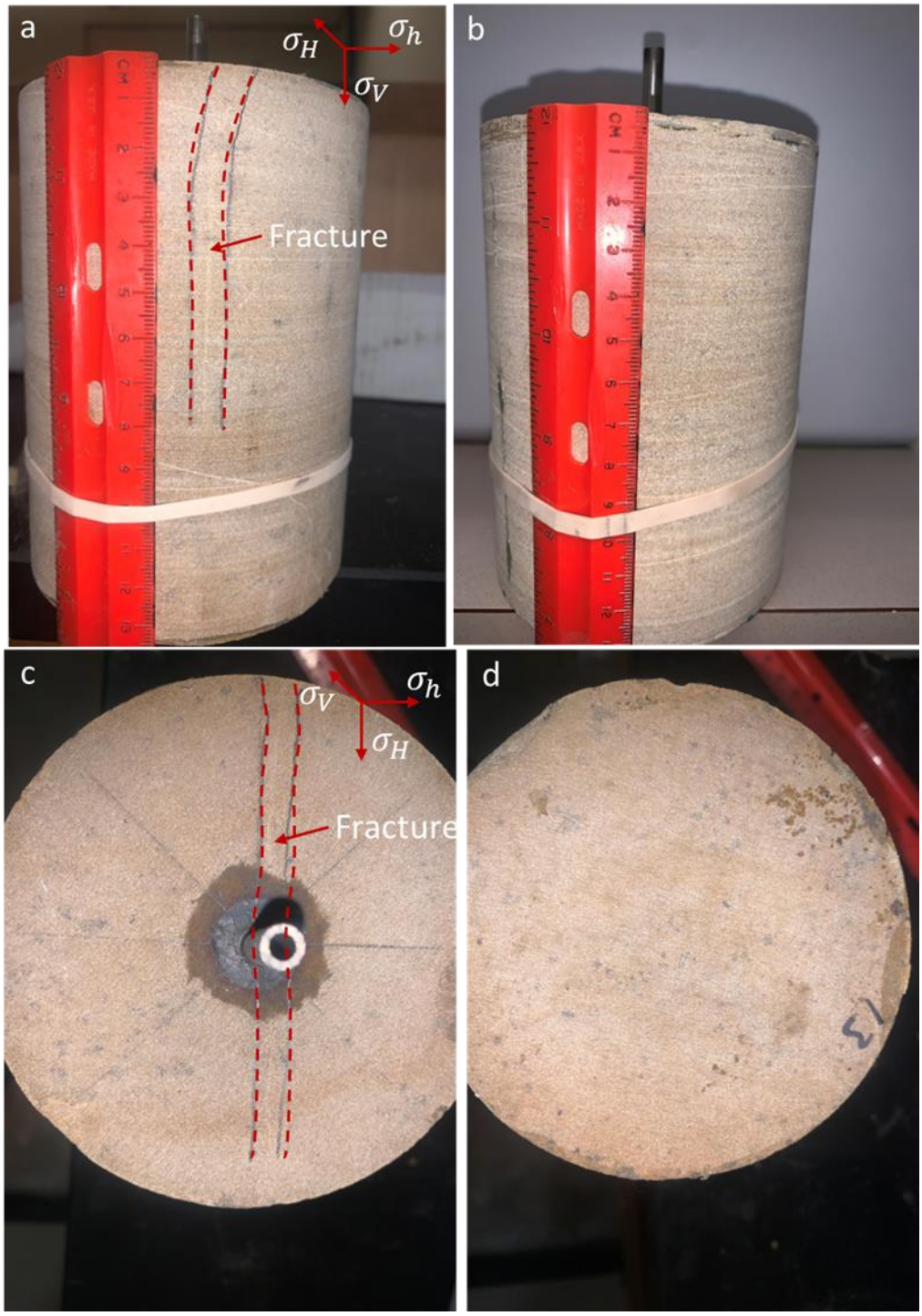

Figure C4. Physical observation of induced fractures in sample S1C fractured with water. The fracture is delineated by the broken red line. (a) and (b) show the side view. (c) and (d) show the bottom and top view.

Sample 1D

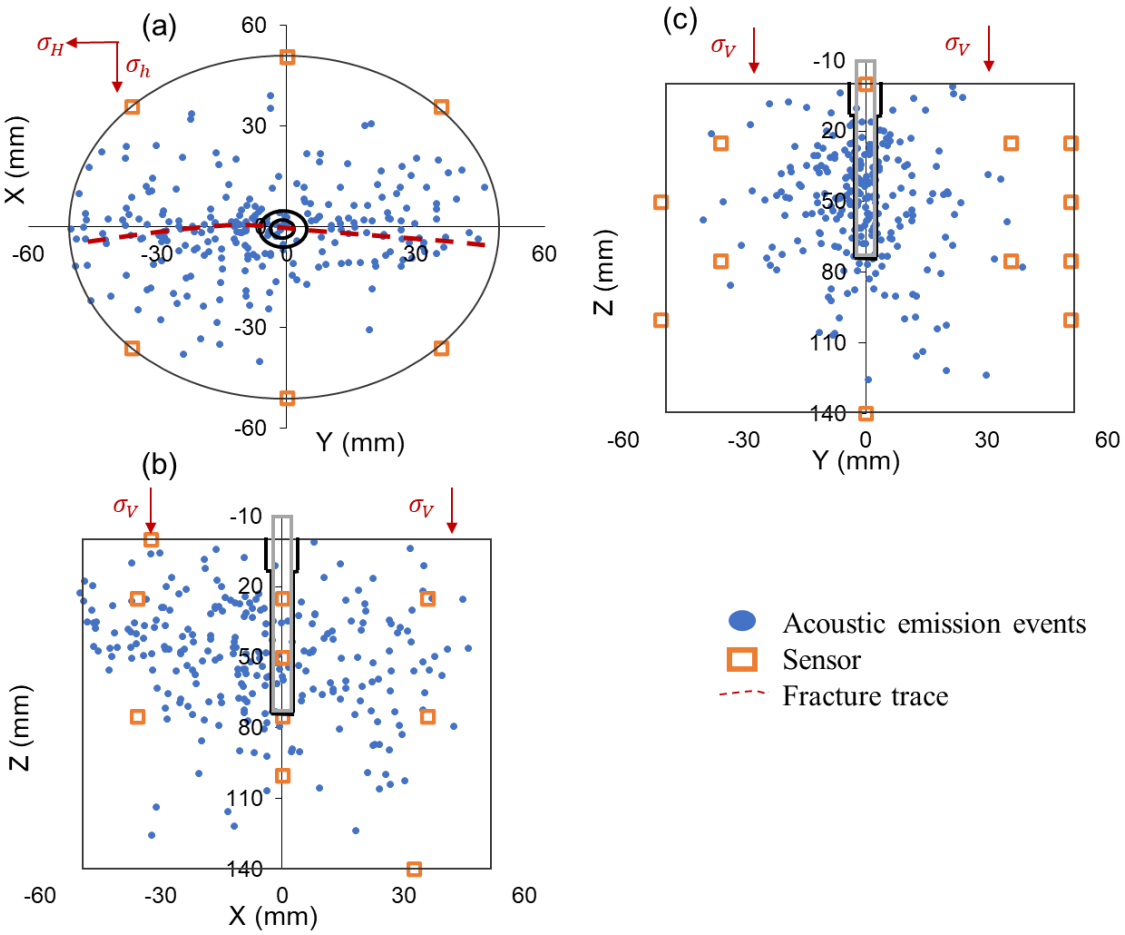

Figure C5. Plot of AEs located in sample S1D fractured with water. The located events are shown in blue, the sesors in orange and the actual fracture trace visible on the bottom surface in red broken line. (a) plan view of AE hypocenter showing a one wing fracture. (b) and (c) are lateral views.

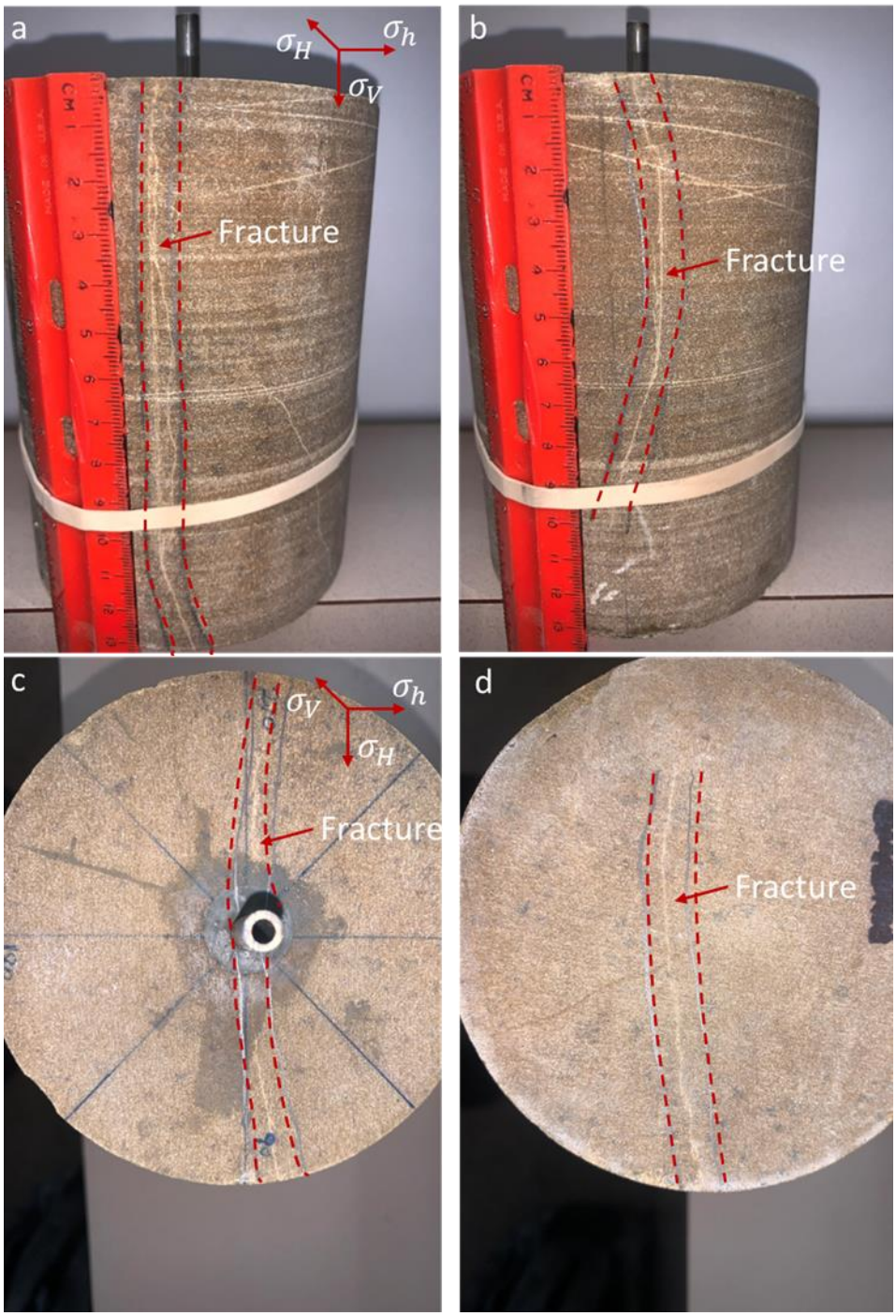

Figure C6. Physical observation of induced fractures in sample S1D fractured with water. The fracture is delineated by the broken red line. (a) and (b) show the side view. (c) and (d) show the bottom and top view.

Sample IF

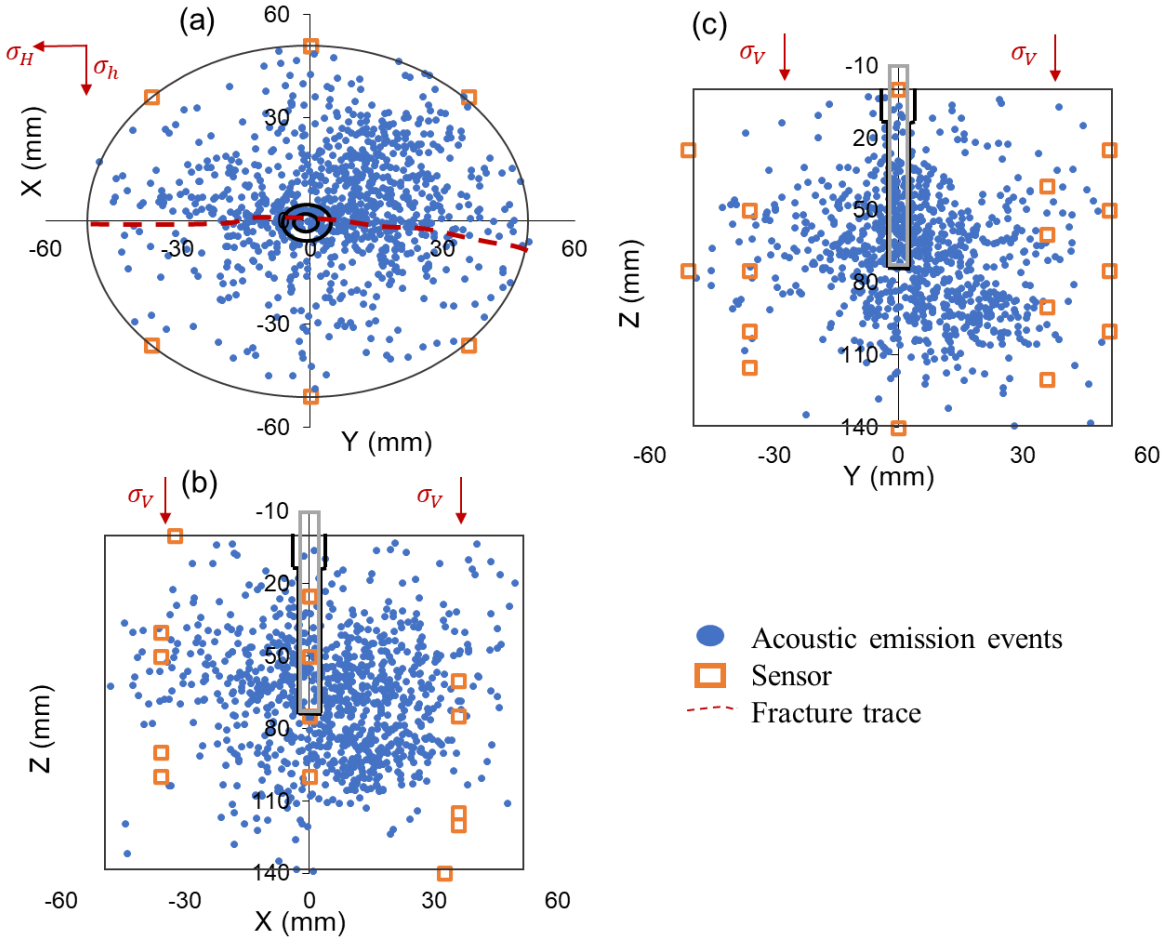

Figure C7. Plot of AEs located in sample S1F fractured with water. The located events are shown in blue, the sesors in orange and the actual fracture trace visible on the bottom surface in red broken line. (a) plan view of AE hypocenter showing a one wing fracture. (b) and (c) are lateral views.

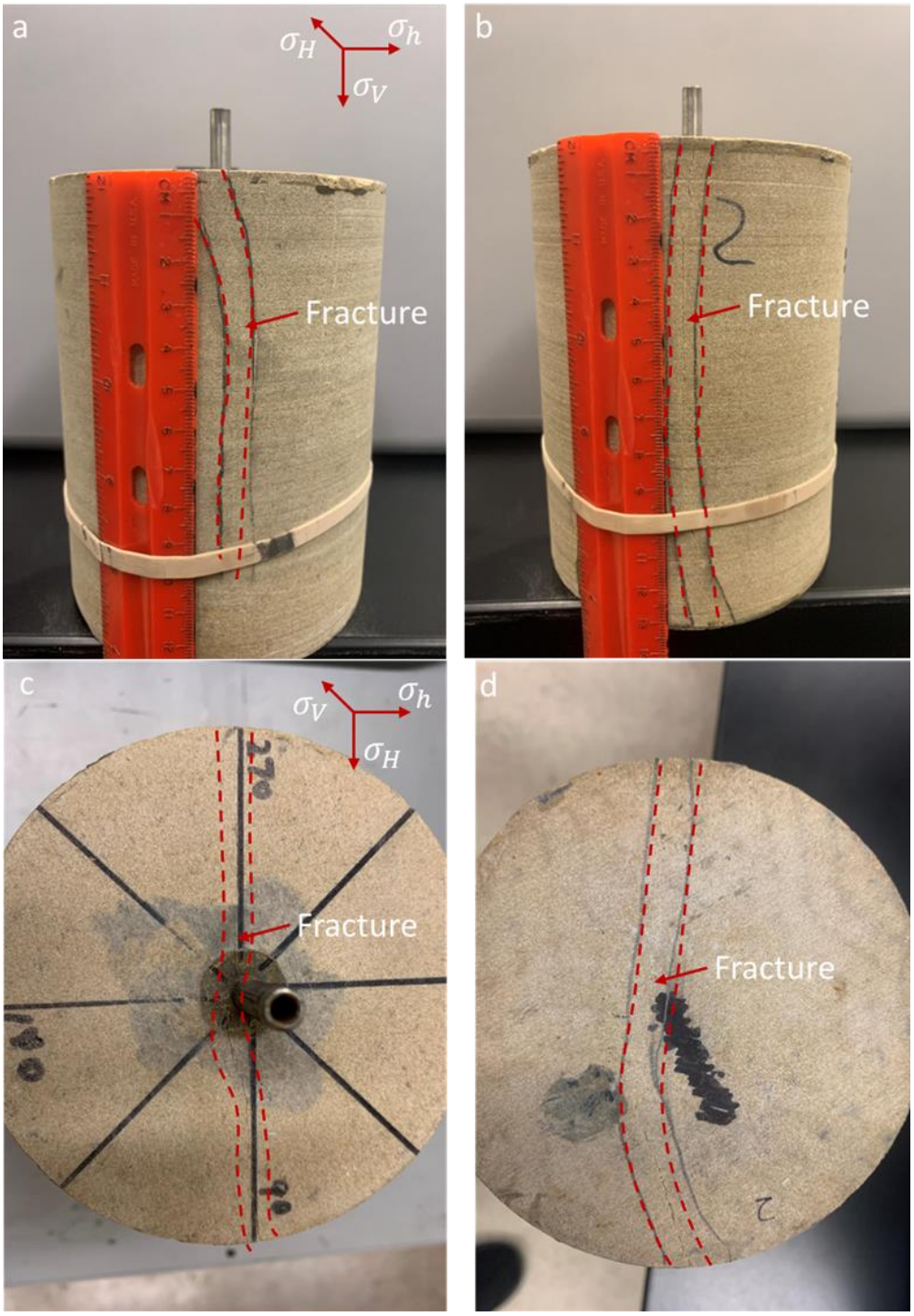

Figure C8. Physical observation of induced fractures in sample S1F fractured with water. The fracture is delineated by the broken red line. (a) and (b) show the side view. (c) and (d) show the bottom and top view.

Sample 1H

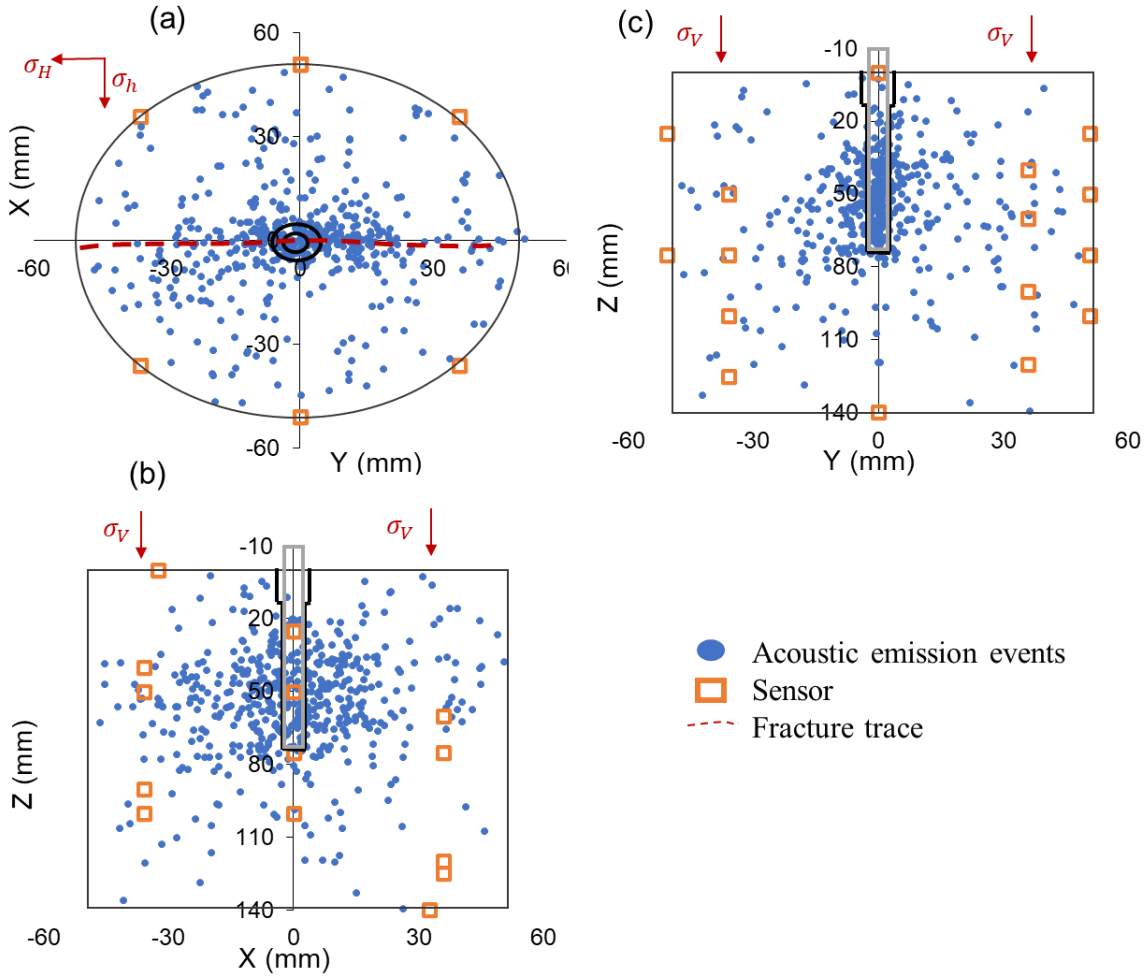

Figure C9. Plot of AEs located in sample S1H fractured with water. The located events are shown in blue, the sesors in orange and the actual fracture trace visible on the bottom surface in red broken line. (a) plan view of AE hypocenter showing a one wing fracture. (b) and (c) are lateral views.

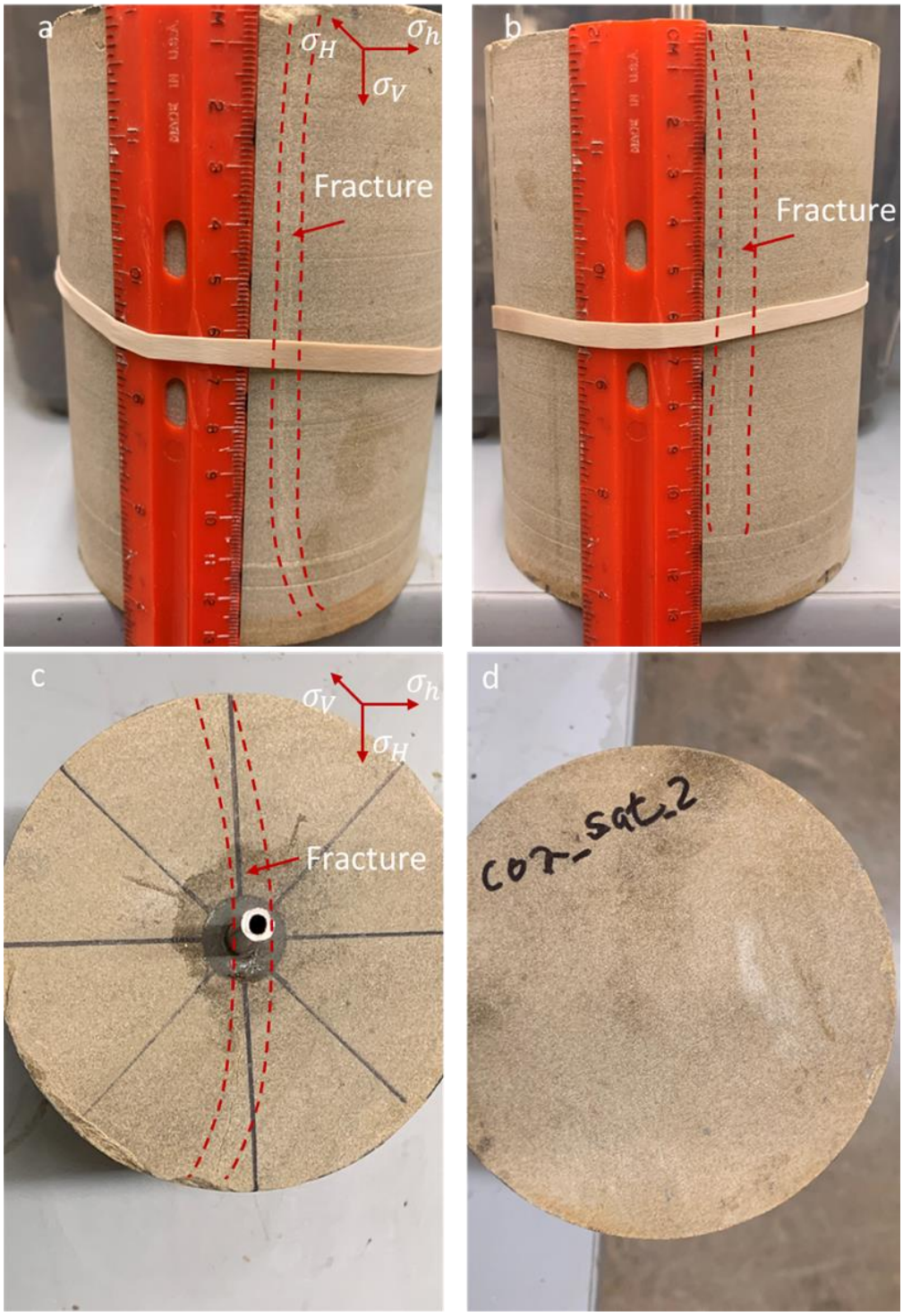

Figure C10. Physical observation of induced fractures in sample S1H fractured with water. The fracture is delineated by the broken red line. (a) and (b) show the side view. (c) and (d) show the bottom and top view.

10. APPENDIX D: AE SPECTRAL ANALYSIS AND SOURCE PARAMETER ESTIMATION

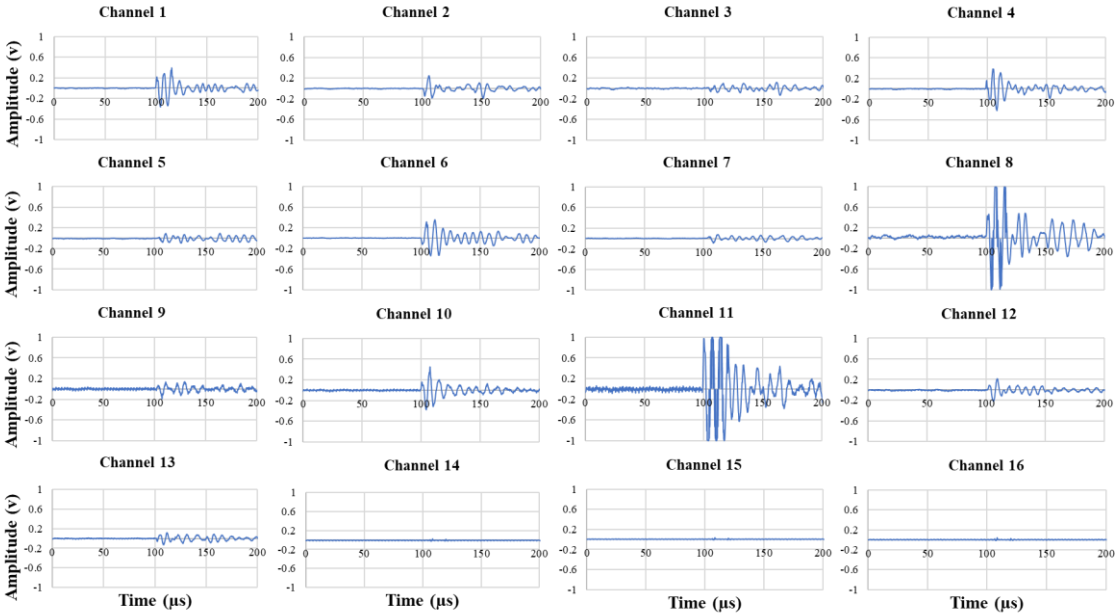

Figure D1. AE signal in time domain. Amplitude versus Time of an AE signal for one event from all 16 sensors.

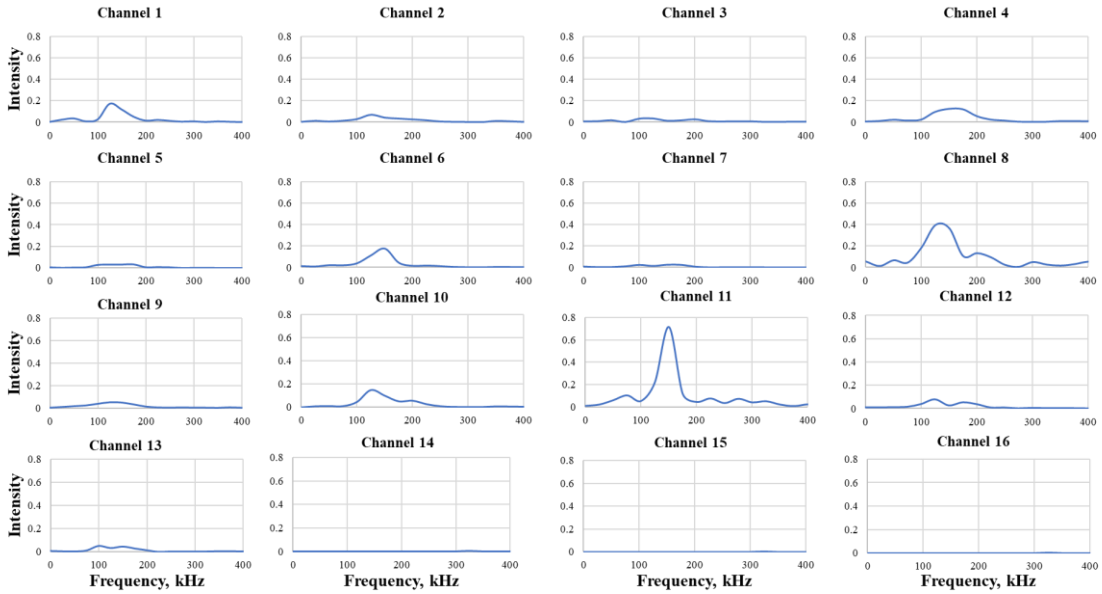

Figure D2. AE singal in frequency domain. Frequency spectra of 40µs window of an AE signal for one event from all 16 channels. They show spectra peaks and associated primary frequency.

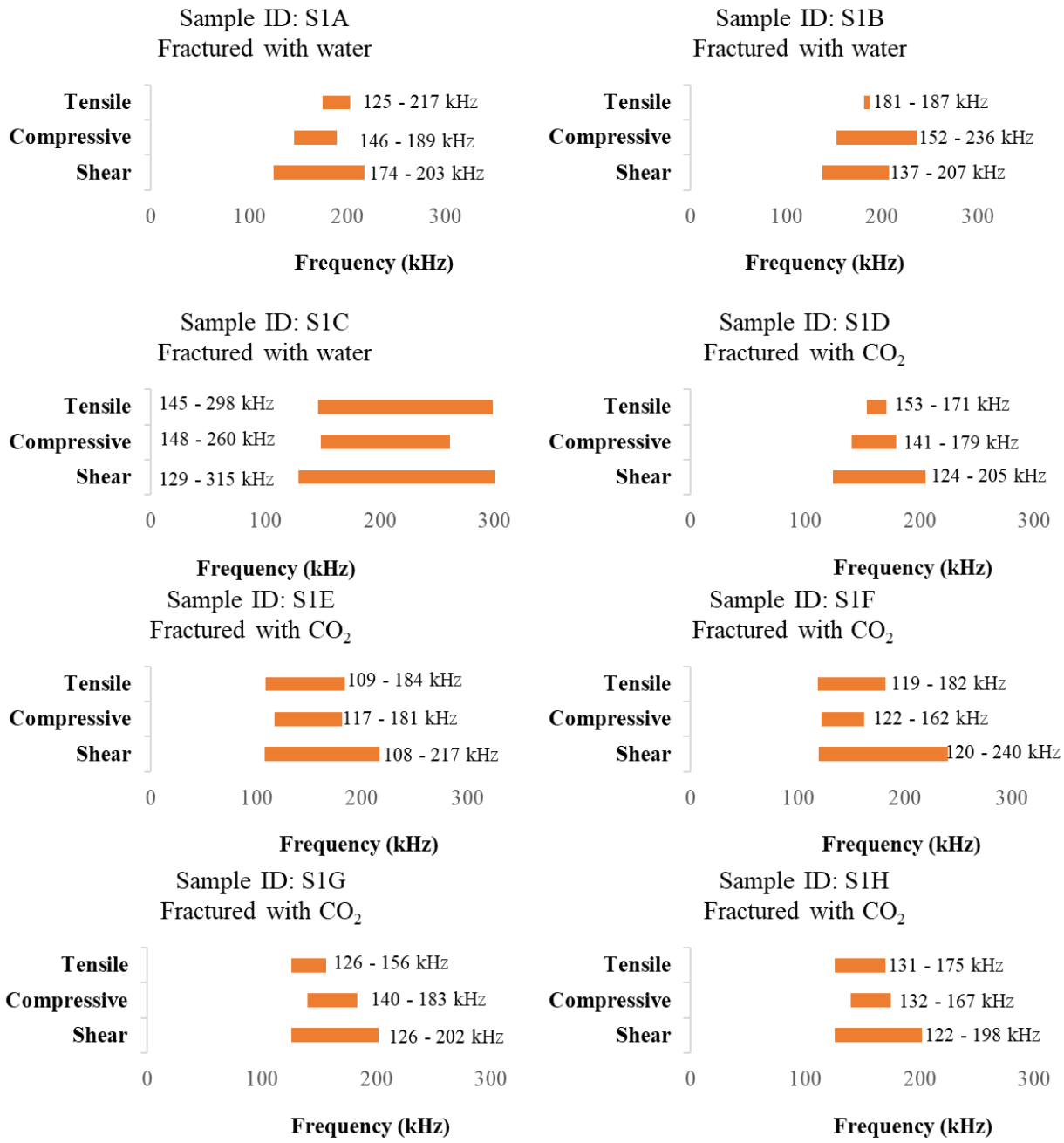

Figure D3. Frequency content of different damage mechanisms induced in S1 samples

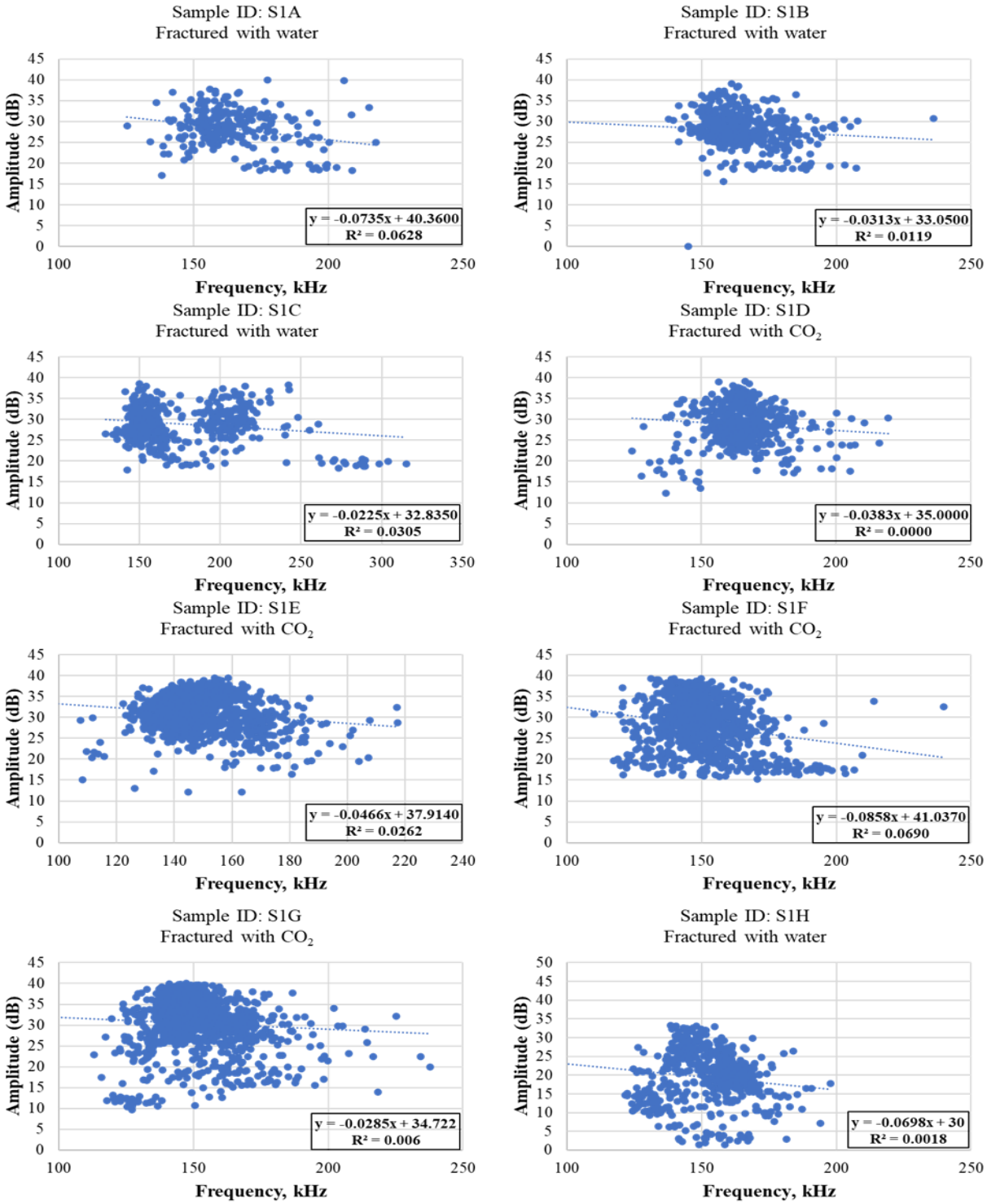

Figure D4. Amplitude versus frequency for S1 samples.

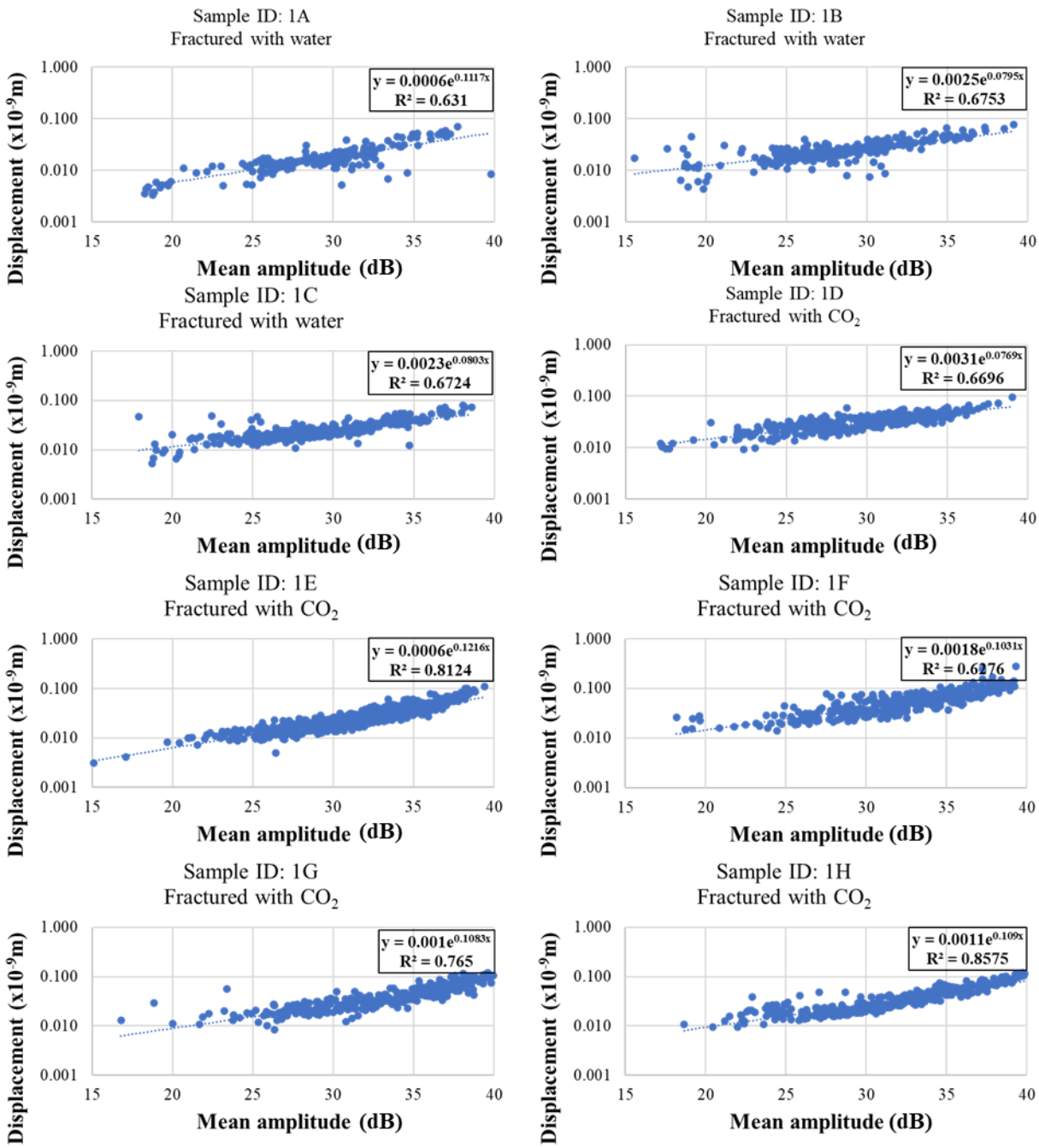

Figure D5. Displacement versus mean amplitude for all samples.

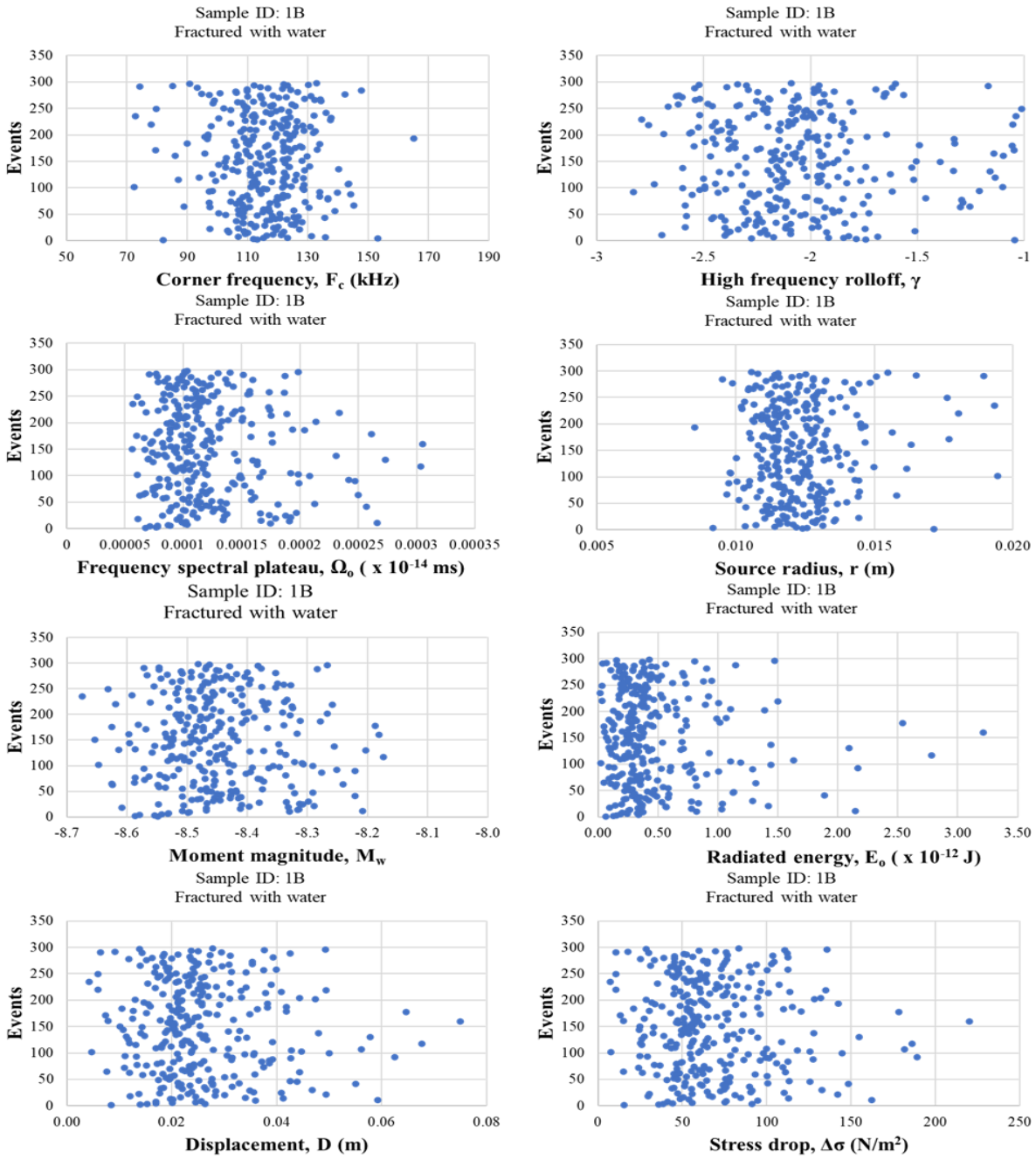

Figure D6. Source parameters for the shear events of S1B

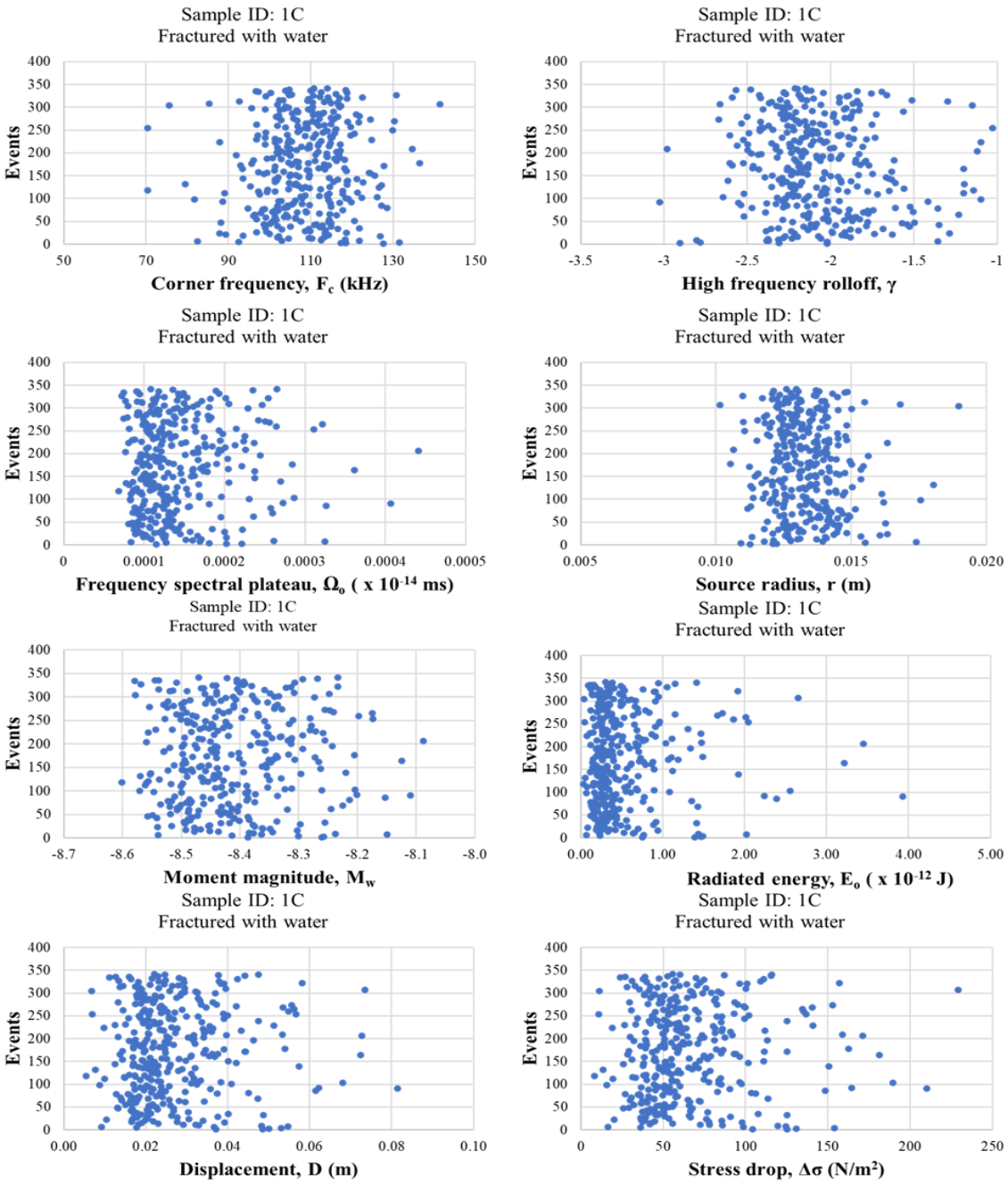

Figure D7. Source parameters for the shear events of S1C

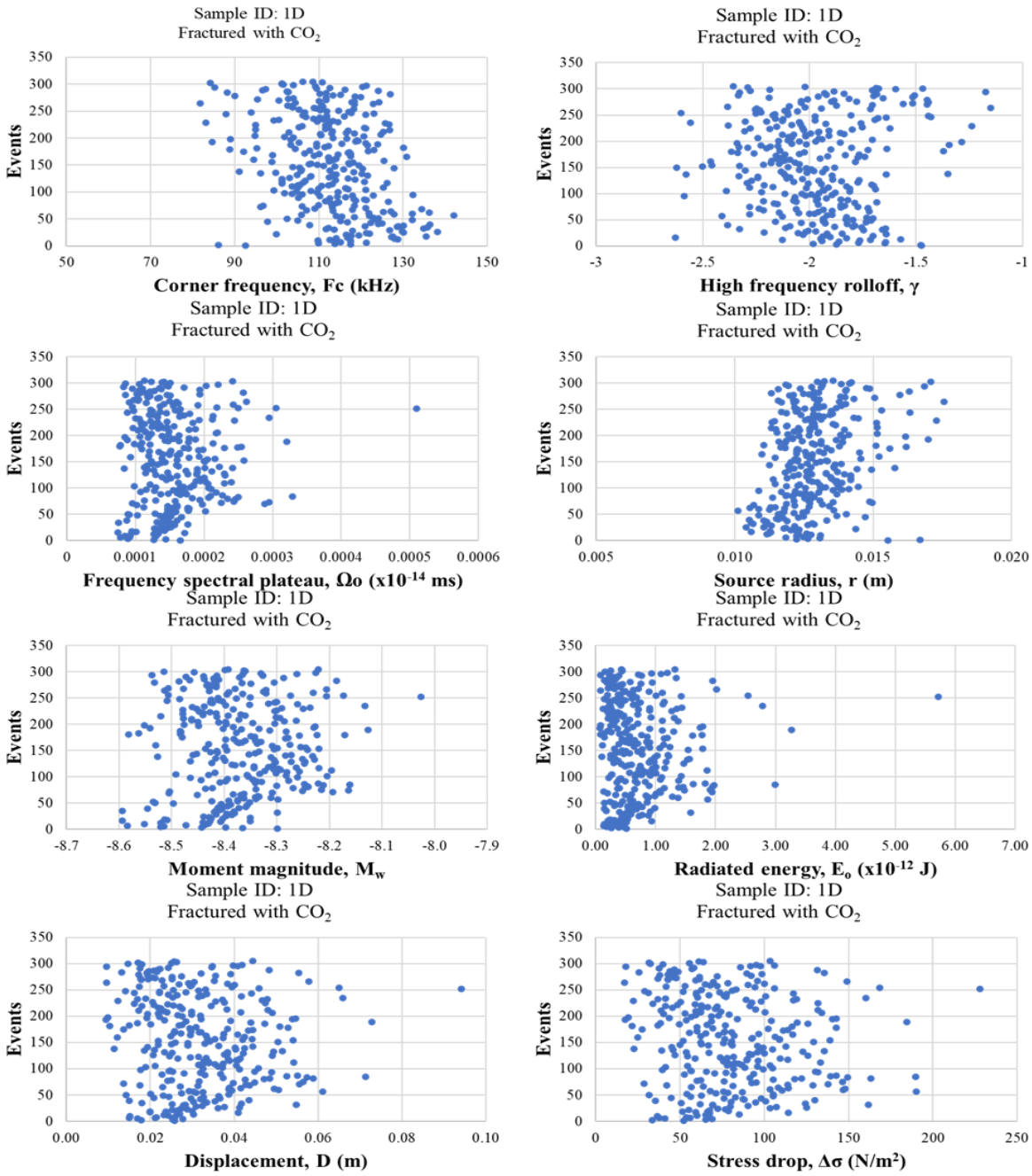

Figure D8. Source parameters for the shear events of S1D

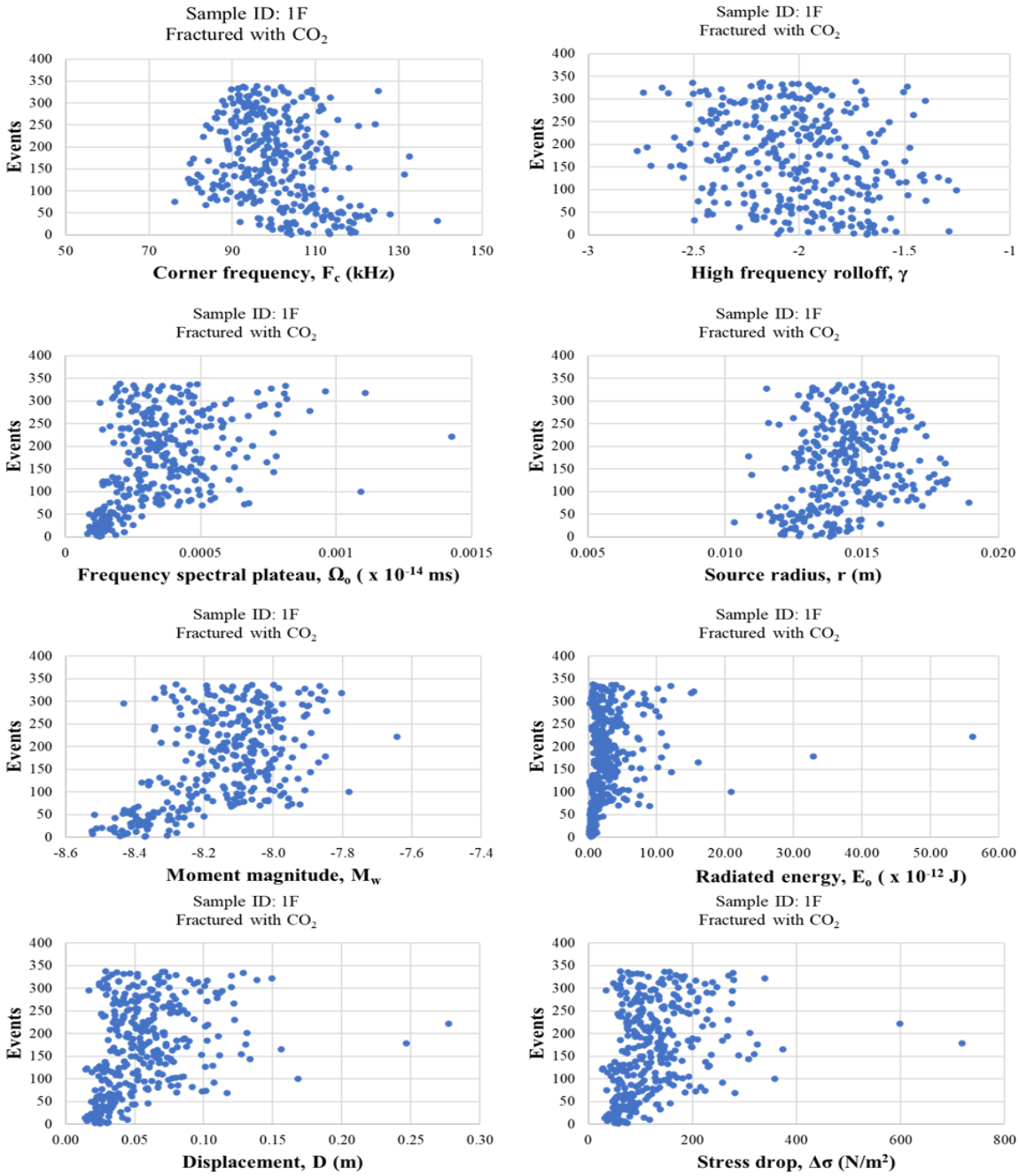

Figure D9. Source parameters for the shear events of S1F

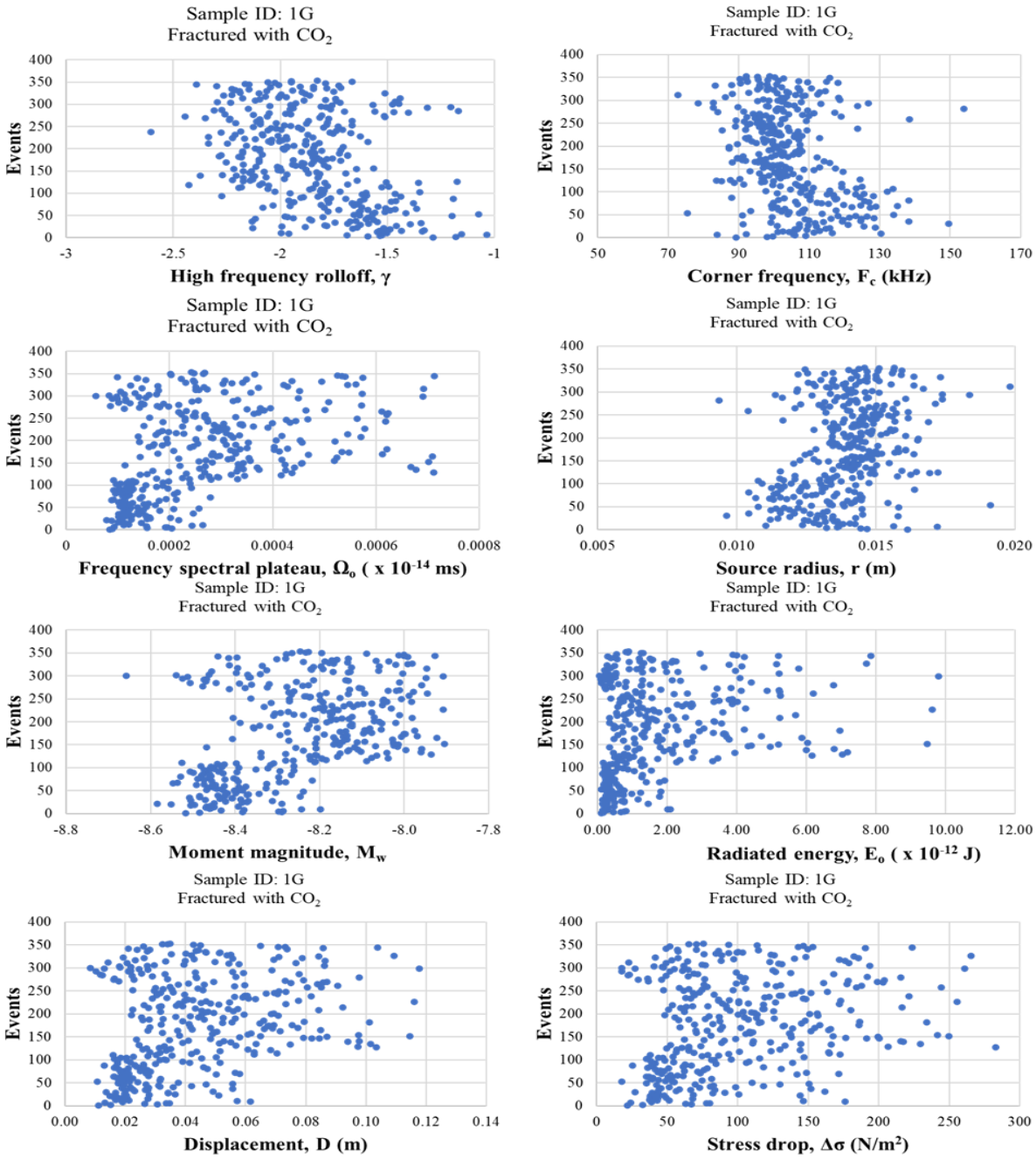

Figure D10. Source parameters for the shear events of S1G

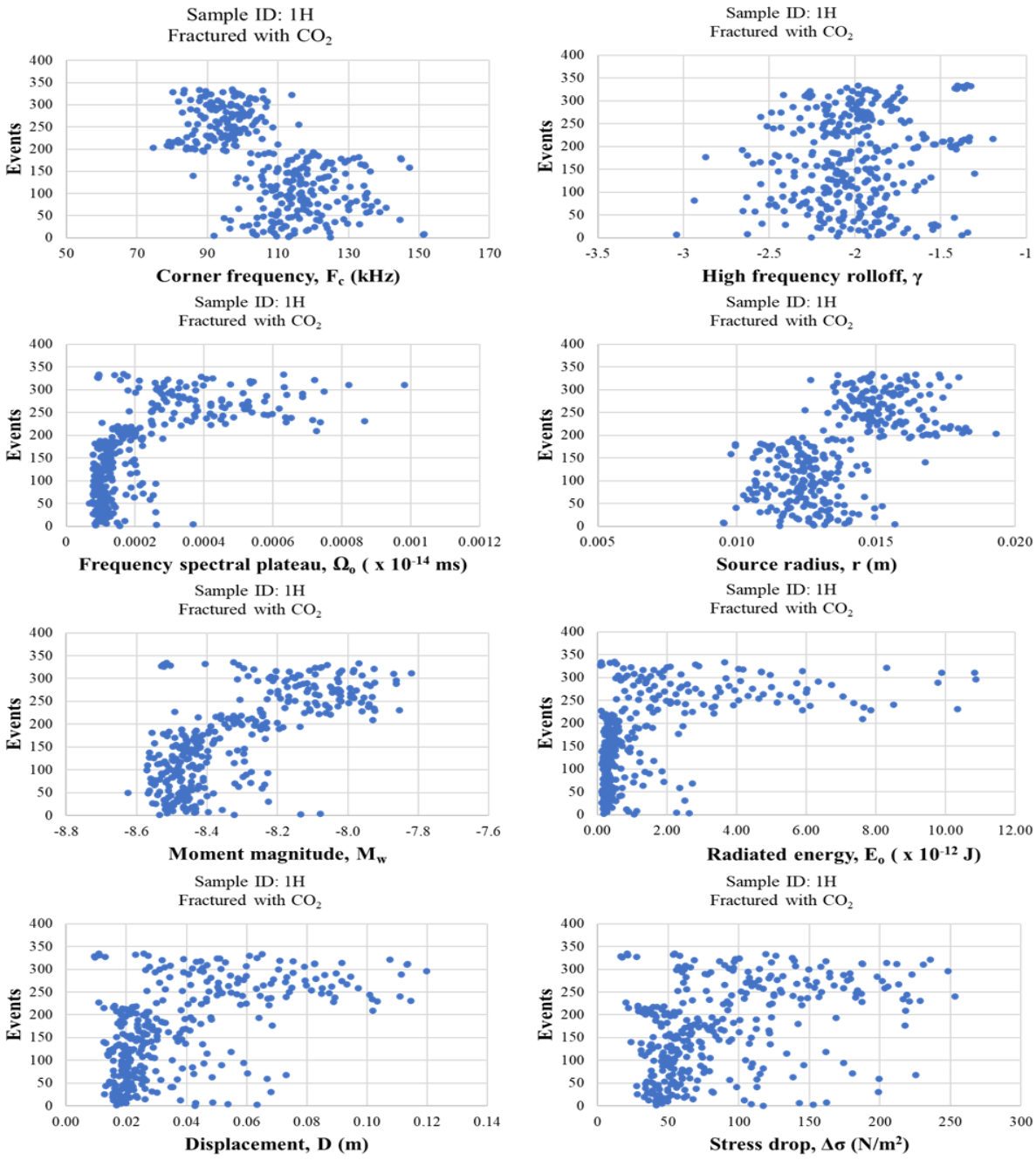

Figure D11. Source parameters for the shear events of S1G